Doctoral Thesis

EXTERNAL RADIOTHERAPY DOSIMETRY IN NONSTANDARD FIELDS

María Araceli Gago Arias

Departamento de Física de Partículas.
Universidade de Santiago de Compostela

September 2013


USC
UNIVERSIDADE DE SANTIAGO DE COMPOSTELA

D. Faustino Gómez Rodríguez, profesor titular de universidade do Departamento de Física de Partículas da Universidade de Santiago de Compostela e **D. Juan Pardo Montero**, Investigador Miguel Servet no Instituto de Investigación Sanitaria de Santiago de Compostela,

INFORMAN:

Que a presente memoria titulada *External radiotherapy dosimetry in nonstandard fields* recolle os resultados do traballo realizado por **Dña. María Araceli Gago Arias** baixo a súa dirección e supervisión, e constitúe a Tese de Doutoramento que presenta para a obtención do título de Doutor pola Universidade de Santiago de Compostela.

En Santiago de Compostela, a 17 de Setembro de 2013.

Faustino Gómez Rodríguez Juan Pardo Montero


USC
UNIVERSIDADE
DE SANTIAGO
DE COMPOSTELA

Agradecimientos

En primer lugar me gustaría empezar mostrando mi más sincero agradecimiento a mis directores de tesis, Faustino Gómez Rodríguez y Juan Pardo Montero, por su guía, paciencia, trabajo e ideas sin los cuales este trabajo no habría sido posible.

A todos los coautores de los artículos en los que he participado y a la gente con la que he trabajado directamente, que siempre han sido amables y me han dedicado su tiempo ante las innumerables dudas y preguntas que les he planteado (a algunos más que a otros, que espero, se den por aludidos).

Además de la gente con la que he colaborado más directamente para la realización de esta tesis doctoral, me gustaría mostrar mi agradecimiento a todas aquellas personas con las que compartí estos años, y que espero no se molesten por no incluír sus nombres en una larga lista que voy a resumir con un:

“A todos mis compañeros del Grupo de Investigación en Radiofísica”

No puedo olvidarme de ningún modo de mi familia y amigos, que me acompañaron cuando flaqueé y que siempre creyeron en mí, no estaría aquí sin vosotros.

El autor también agradece la concesión de un contrato predoctoral del Plan Galego de Investigación, Innovación e Crecemento (Plan I2C) de la Xunta de Galicia en el año 2011.


USC
UNIVERSIDADE
DE SANTIAGO
DE COMPOSTELA

Summary

The dosimetry of the small and intensity modulated fields employed in radiotherapy, with high dose gradients involved, is a quite demanding task. The need for reliable measurements in these beams responds not only to quality assurance requirements, but also to the legal regulations of Radiotherapy (in Spain, Real Decreto 1566/1998 sobre Criterios de Calidad en Radioterapia, and also EURATOM 97/43). The complexity of modern radiotherapy techniques led to an extensive incorporation of thorough treatment dosimetric verification in the hospital quality assurance programs. This verification, previous to the treatment, is performed in order to check that the dose distributions delivered by the radiotherapy machine match the corresponding planned dose distributions within the required tolerances. One work performed in this thesis project consists in the study of different commercial detector arrays, devices widely employed for dosimetric treatment verification. The response of the detectors involved in these devices is determined in order to study the impact of the detector size, technology and layout on the measurement of intensity modulated dose distributions. The capabilities of detector arrays for the detection of fluence variations is also studied, as this is one of the main objectives of treatment verification.

On the other hand, also related with the quality assurance of radiotherapy, a new dosimetry protocol is studied and applied to two modern radiotherapy machines, TomoTherapy and CyberKnife, for the determination of absorbed dose to water. Until now, dosimetry protocols ensured the traceability of dose to water through the measurement of 10 cm×10 cm radiation fields under charged particle equilibrium, following the recommendations of conventional dosimetry codes of practice, for example the TRS 398 of the International Atomic Energy Agency (IAEA). Modern radiotherapy techniques involve the use of small radiation fields and intensity modulated fluencies to achieve higher conformation of the dose to the tumour volume. Additionally, there was an increase in the radiotherapy machines involving this type of radiation fields that cannot reproduce the 10 cm×10 cm standard reference field. This situation increases the uncertainty associated to the determination of absorbed dose to water, compromising the quality of

treatment planning in these machines. This prompted the creation a Working Group of reference dosimetry on nonstandard fields through the collaboration of IAEA and the American Association of Physics in Medicine, which published recommendations for the development of a new dosimetry protocol: “A new formalism for reference dosimetry of small and non-standard fields” Medical Physics Volume 35, Issue 11, p. 5179-5186 (November 2008). The application of the new protocol to the above mentioned machines requires the definition of intermediate calibration fields and the measurement and simulation of correction factors associated to different ionization chambers under these radiation fields, being one of the scopes of this doctoral thesis.

Finally, alanine dosimetry is a secondary standard of absorbed dose to water in the therapy dose range (1 to 20 Gy), offered by primary laboratories like the National Physical Laboratory (NPL) in UK, the National Institute of Stantards and Technology (NIST) in US, or the Physikalisch-Technische Bundesanstalt (PTB) in Germany. This dosimetry system, which is tissue equivalent and exhibits small energy dependence, involves the use of small detectors, being widely used for small fields dosimetry and the calculation of ionization chamber correction factors. Another piece of work addressed in this thesis consists on the development of an alanine dosimetry system, unique in Spain, through the quantification of the dosimeters signal by electron spin resonance and with traceability to the secondary standard of absorbed dose to water of the Radiation Physics Laboratory at the Universidade de Santiago de Compostela.

Publications related with this work

A. Gago-Arias, L. Brualla-González, D. M. González-Castaño, F. Gómez, M. Sánchez García, V. Luna Vega, J. Mosquera Sueiro, and J. Pardo-Montero. Evaluation of chamber response function influence on IMRT verification using 2D commercial detector arrays. *Physics in Medicine and Biology*, 57(7):2005, April 2012. doi: 10.1088/0031-9155/57/7/2005

A. Gago-Arias, R. Rodríguez-Romero, P. Sánchez-Rubio, D. M. González-Castaño, F. Gómez, L. Nuñez, H. Palmans, P. Sharpe, and J. Pardo-Montero. Correction factors for A1SL ionization chamber dosimetry in TomoTherapy: machine-specific, plan-class, and clinical fields. *Medical Physics*, 39(4):1964–1970, 2012. doi: 10.1118/1.3692181

A. Gago-Arias, E. Antolín, F. Fayos-Ferrer, R. Simón, D. M. González-Castaño, H. Palmans, P. Sharpe, F. Gómez, and J. Pardo-Montero. Correction factors for ionization chamber dosimetry in CyberKnife: machine-specific, plan-class, and clinical fields. *Medical Physics*, 40(1):011721, 2013. doi: 10.1118/1.4773047

Other publications:

D. M. González-Castaño, J. Pena, F. Gómez, A. Gago-Arias, F. J. González-Castaño, D. A. Rodríguez-Silva, A. Gómez, C. Mouriño, M. Pombar, and M. Sánchez. eIMRT: a web platform for the verification and optimization of radiation treatment plans. Journal of Applied Clinical Medical Physics, 10(3), July 2009.

D. M. González-Castaño, L. González Brualla, M. A. Gago-Arias, J. Pardo-Montero, F. Gomez, V. Luna-Vega, M. Sanchez, and R. Lobato. A convolution model for obtaining the response of an ionization chamber in static non standard fields. *Medical Physics*, 39(1):482–491, 2012. doi: 10.1118/1.3666777

L. Brualla-González, F. Gómez, A. Vicedo, D. M. González-Castaño, M. A. Gago-Arias, A. Pazos, M. Zapata, J. V. Roselló, and J. Pardo-Montero. A two-dimensional liquid-filled ionization chamber array prototype for small-field verification: characterization and first clinical tests. *Physics in Medicine and Biology*, 57(16):5221, 2012. doi: 10.1088/0031-9155/57/16/5221

Contents

List of Figures

USC
UNIVERSIDADE
DE SANTIAGO
DE COMPOSTELA

List of Tables

Chapter 1

Introduction

1.1 Radiation therapy

By 2012, around 20% of deaths in the European Region are produced due to cancer, which constitutes the most important cause of morbidity and death in Europe after cardiovascular diseases, and involves more than 3 million new cases and 1.7 million deaths per year [1]. Among the different strategies currently followed to treat cancer, which include surgery, chemotherapy, hormone therapy and inmunotherapy, ionizing radiation is employed to kill or control malignant cells. This method, referred to as radiation therapy or radiotherapy, should be applied to approximately 52% of cancer diagnosed patients, as estimated by Delaney *et al.* [2], although the actual rate of radiotherapy treatments varies widely among different countries.

The interaction of ionizing radiation with biological tissues produces the ionization and excitation of their constituent atoms and molecules, leading to the formation of highly reactive radicals in the intracellular material that can chemically break bonds in DNA. Although most of this damage can be repaired by the cell, unrepaired damage to the cell DNA, consisting mainly in double strand breaks, can lead the cell to lose its ability to reproduce or die. This is due to the loss of genes with associated functions that are critical for survival, producing the death of the cell before reaching mitosis or after having undergone one or several cell cycles [3]. Quickly dividing tumor cells are generally more sensitive than other cells to ionizing radiation, being the objective of radiotherapy to deliver the amount of radiation needed to produce the desired cell killing and achieve tumor control, see Figure 1.1.

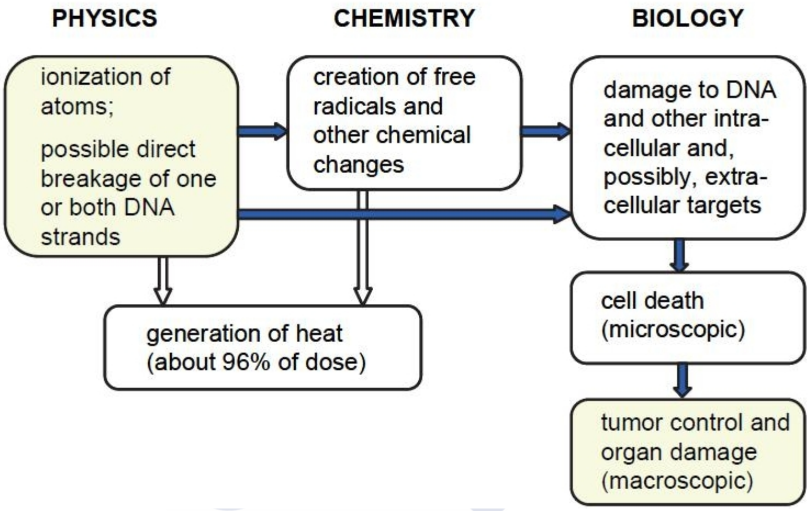

FIGURE 1.1: Scheme of the physical, chemical and biological effects of ionizing radiation in biological tissues [4].

Radiation Therapy can be classified by the type of ionizing particles employed (photons, electrons, protons or ion beams), by the energy of these particles (low, medium or high) and by the position of the radiation source with respect to the patient (external or internal), being the objective of this thesis centered in external radiotherapy of photon beams.

The amount of energy deposited in a medium by ionizing radiation per unit mass is quantified by a magnitude called absorbed dose. The effect of radiation on biological tissues is in turn related with the dose. The goal of radiotherapy will be to deliver certain amount of dose, prescribed by a radiation oncology doctor, to a planned target volume (PTV) surrounding the tumor region, while the dose to the healthy surrounding tissue (referred to as organs at risks, OARs) is maintained below certain levels of tolerance as to minimize side effects and preserve critical organs. For photon beams, and based on the knowledge achieved through the years about dose response and clinical error consequences, the International Commission of Radiation Units and Measurements established in 1993 a desired accuracy for the dose to the PTV lying within the range from 95% to 107% of the prescribed dose [5]. Taking into account the sources of uncertainty associated to the different steps that, as we will see, must be followed for the delivery of a radiotherapy treatment, the achievement of such an accuracy can result quite demanding.

1.1.1 The radiotherapy process.

The radiotherapy process begins with the patient being diagnosed (site and extent of the tumor, stage, etc) and the decision of treating the disease with radiotherapy. Patient anatomical information and tissue composition are then obtained through Computed Tomography (CT), where the delineation of OARs and treatment target volumes is performed[1]. The radiation oncologist prescribes the dose to be delivered to the PTV, OARs dose constraints and the radiation modality to be employed. A team of physicists addresses then the treatment planning, which consists, for external radiotherapy, in designing a combination of beams that fulfil the oncologist prescription [6].

For treatment planning, workstation software receiving the name of Treatment Planning Systems (TPS) is employed to optimize the beam directions, the geometrical shapes and the beam weights for the treatment. These tools use the information in the patient CT and some parameters describing the

---

[1] The position and extent of the tumor and neighboring healthy tissue can be assessed with other imaging techniques such as magnetic resonance imaging (MRI), single-photon-emission computed tomography (SPECT) and positron emission tomography (PET). These images can be correlated to improve the accuracy of volume delineation.

radiation source to compute the dose that an hypothetical treatment would deliver to the patient. Dose calculations are performed with different radiation transport algorithms depending on the TPS, the more recent ones including Monte Carlo calculation engines. The radiation source model inside the TPS is usually commissioned from ionometric measurements of dose deposition in a phantom with electronic density and atomic composition similar to tissue, usually water.

Once a certain radiotherapy treatment has been chosen for delivery, different verification procedures are adopted by clinical centers to check that the planned treatment will lead to the expected dose deposition, generally through the delivery of the radiotherapy plan in the treatment unit for the measurement of absorbed dose in one or several points of a phantom. Treatment replanning may be needed before proceeding to treatment delivery whenever the evaluation or verification of a treatment is not satisfactory. In some cases an analysis of the patient response between the fractions in which a treatment is divided, or the detection of patient geometry changes, may motivate treatment replanning for the improvement of tumor control probability. Patients are also followed after the radiotherapy treatment has been finished in order to analyze the outcome of the treatment.

1.1.2 Radiotherapy techniques

External radiotherapy has been always performed confronting the fact that the beam transport needed to deliver dose to the target locations in the patient involves also irradiation to healthy tissue, and thus important efforts have been focused on a better conformation of the dose to the PTV. For a megavoltage photon beam entering a material, the dose deposited with the depth of penetration exhibits a buildup region of increasing dose, maintained during the first millimetres of penetration until transient charged particle equilibrium is reached in the material and the maximum dose level is achieved (the depth of this maximum will depend, for the same material, on the energy of the beam). For larger depths, the deposited dose decreases following approximately an exponential attenuation law [7], see Figure 1.2.

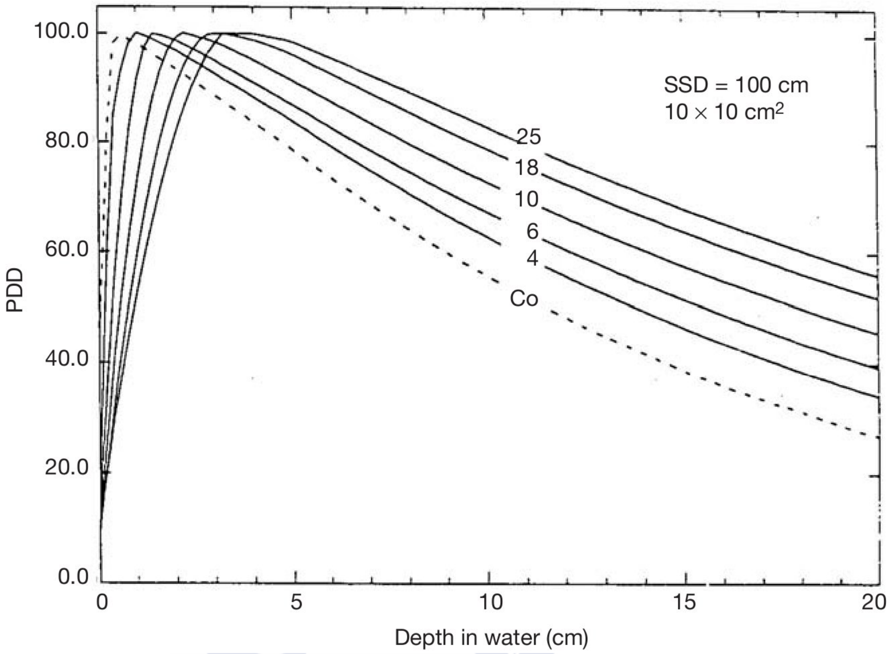

FIGURE 1.2: Percent depth dose distributions in water for a 10 cm×10 fields at 100 cm source to surface distance for a ^{60}Co beam and megavoltage photon beams from 4 to 25 MV [7].

Taking into account that the photon beam deposits energy all along its path through the patient, the strategy followed in radiotherapy involves the use of several beams entering from different directions. Beam incidences are performed to have the intersection of the beams located in the PTV region, where the desired dose will be achieved through the superposition of the beams. Under this radiation delivery scheme, the dose to the healthy surrounding tissue is minimized if compared with that obtained with one single beam irradiation reaching the same dose level in the PTV.

3D-Conformal radiotherapy

Rectangular beams were initially used for external radiotherapy, although dose conformation in these old modalities was very limited. Improvement in the conformation of the dose to the shape of the PTV was later achieved by adjusting the shape of the beams to the cross-section of the PTV in the incidence directions (beam eye view, BEV). This approach, receiving the name of 3D-Conformal Radiotherapy, was at the beginning addressed through the use of metal alloy patient-specific cast blocks, usually in ^{60}Co teletherapy units, see Figure 1.3, where the 1.25 MeV gamma emission of this radionuclide is employed as radiation source[2]. In these radiotherapy units, a gantry holding the radiation source rotates around a point, called isocenter, where all the possible beam propagation axes intersect.

FIGURE 1.3: Left: Theratron 780 ^{60}Co radiotherapy unit. Right: cerrobend blocks prepared from the beam eye view of the tumor of an specific patient

^{60}Co units were however progressively replaced by electron linear accelerators in developed countries. In a linear accelerator (Linac), electrons

---

[2] Kilovoltage X-ray units, useful for the treatment of superficial lesions, were the first equipment employed for external radiotherapy, playing an important role in its early development between 1910 and 1950. It was then when ^{60}Co units, which provide more penetrating gamma ray beams, were introduced becoming the predominant external radiotherapy for the next 30 years.

are accelerated by high power radio-frequency fields in straight accelerating cavities until they reach kinetic energies ranging from 4 to 25 MeV. These electron beams can be used for external electron radiotherapy or they can impinge a high atomic number target for the production, mainly by bremsstrahlung, of photon beams with different maximum energies. Linac photon beam modalities are usually named after the accelerating potential applied to the electron beam, leading to 4, 6, 9, 12, 15, 18 and 23 megavoltage photon beams.

In 1990 commercial linear accelerators begun to be equipped with computer controlled multileaf collimators, MLC. This devices consist in two sets of high atomic number metallic leaves that can move independently, blocking the radiation to achieve any beam shape subject to the width of the leaves, see Figure 1.4. This collimation system not only served to achieve a faster delivery of 3D-CRT treatments, it also favored the development and consolidation of a new delivery technique, the so called Intensity Modulated Radiation Therapy (IMRT).

FIGURE 1.4: Multileaf collimator made of several independently moving opposed leaf pairs made of tungsten, typically projecting a 1 cm shadow at the isocenter.

Intensity Modulated Radiation Therapy

The intensity modulated technique introduced the delivery of more complex fluence patterns on each direction of beam incidence. This allows the delivery of steeper dose gradients for a better dose conformation to the target volumes. Potential highly uniform coverages are thus feasible even for concave geometries, see Figure 1.5, leading to an improvement of TCP at fixed normal tissue complication probability. This treatment technique can involve field sizes being substantially smaller than those generally used in 3D-CRT, with areas, at 100 cm from the source, that can go down to 5 square centimeters whereas conformal radiotherapy fields usually range from 400 to 25 square centimeters. This and the steeper dose gradients achieved can make the dose measurements of IMRT fields to be affected by larger uncertainties. Since first proposed in the earlies 90s [8], the introduction of this technique in hospitals was a slow process due to the modern equipment required for both treatment planning and delivery as well as the demands of complex quality assurance procedures.

There are different operational modes that can lead to the delivery of an intensity modulated fluence, mainly:

- Segmented IMRT mode, or step-and-shoot mode: in this modality the intensity modulated fluence of every incidence is achieved by sequentially delivering open fields with different shapes (segments). The linac beam is turned off while the MLC leaves move to conform the fields of an incidence.
- Dynamic MLC mode, or sliding window mode: this modality involves the movement of the MLC leaves while the beam is on. Leaves change their speed in different regions to provide the modulated fluence desired for every incidence.

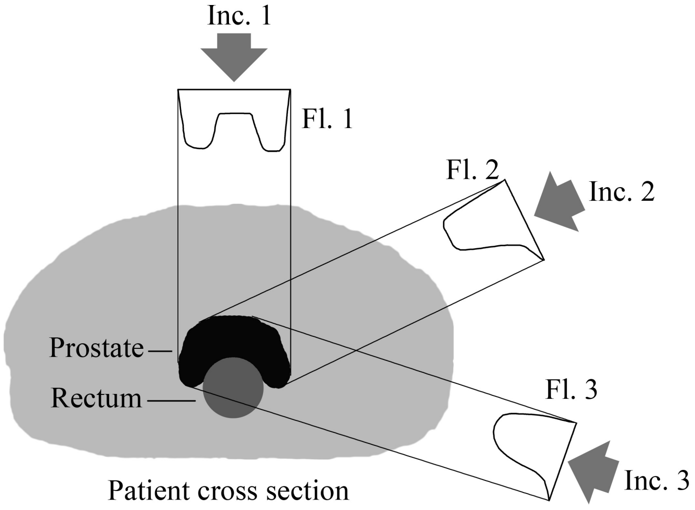

FIGURE 1.5: Example of IMRT treatment for a prostate cancer, where the PTV (prostate) and one OAR (rectum) are disposed in concavity. A fluence “castle" is constructed through superposition of beams involving inhomogeneous fluences (Fl.1 to Fl.3) coming from different incidence directions (Inc.1 to Inc.3).

- Intensity modulated Arc Therapy (IMAT): in this modality the radiation is delivered with the gantry moving continuously around the isocenter, in one or more rotating arcs, while the MLC yields segments in a dynamic mode (fields at different angles are defined to be connected geometrically). This modality involves higher costs both on hardware and software and increased complexity in planning and quality assurance than the latter two IMRT modalities. However, extending the discretized radiation incidence to a continuous arc can lead to a better dose conformation to the target with lower dose to OARs, and in the case of single arc IMAT, treatment delivery times can be reduced compared with other IMRT modalities [9].

  Different IMAT linacs are available from different manufacturers: RapidArc® (Varian Medical Systems Palo Alto, CA), SmartArc (Philips, Fitchburg, WI), and VMAT (Elekta AB, Stockholm, Sweden), all them allowing non coplanar arcs and some offering variable dose rate during treatment. Finally, developed in parallel with IMAT, TomoTherapy (Accuray Inc., Sunnyvale, CA) offers a different approach to the arc therapy [10]. This technique involves a compact linac, mounted on a CT ring, rotating around a patient coach that moves into the ring for an helical delivery of radiation. Conformation and modulation of a fan beam is in this case provided by a fast binary collimator.

Radiosurgery

Other relevant radiotherapy technique, employed to irradiate small regions with high accuracy is radiosurgery. Initially developed for the treatment of brain lesions in a single fraction delivery scheme through the use of very small field sizes (down to 0.1 cm^2), radiosurgery has evolved to treat other regions, like the lung or the spinal cord, in fractionated schemes, and with intensity modulated fluencies. Radiosurgery treatment units can be of different nature, like standard isocentric linacs equipped with special MLCs of tight mechanical tolerance (i.e. Novalis), or dedicated treatment units like GammaKnife® (which uses 201 stationary single-point-focused cobalt 60 sources) or CyberKnife® (a single modality linac mounted on a industrial robotic arm).

Finally, most modern units do not have a flattening filter in their linac head. Some of these units will be extensively studied in Chapter 4, where we will discuss the main differences between them and standard linacs using flattening filter.

1.2 Dosimetry

1.2.1 Physical basis

The term ionizing radiation is used to refer to both indirectly and directly ionizing radiation. Non-charged particles (neutrons, uncharged pions, neutrinos, etc) and short wavelength electromagnetic radiation (X rays and γ rays) are recognized as indirectly ionizing radiation as they transfer energy to materials in a two step process. In the first one, the non charged particles, for example photons, transfer energy to charged particles through different processes like photoelectric effect, Compton interaction, pair production, etc. Secondly, these charged particles produce further excitation and ionization in the material. On the other hand, directly ionizing radiation, conformed by charged particles (electrons, positrons, protons, ions) impart energy directly through excitation and ionization in the material, mainly through Coulomb collisions with electrons and nuclei. Regardless the type of ionizing radiation entering a material, the total imparted energy is equal to the addition of all the energy entering the volume corresponding to the mass m minus all the energy that goes out in different forms (Bremsstrahlung photons, annihilation photons and electrons or incident radiation going out). This balance must include all the conversion of mass to energy and energy to mass processes such as pair production and electron positron annihilation, leading to the expression [11]:

$$\epsilon = \epsilon_{in} - \epsilon_{out} + \sum Q \tag{1.1}$$

Where ϵ_{in} is the sum of the energies (excluding rest energies) of all the directly and indirectly ionizing particles entering the volume, ϵ_{out} is the sum of the energies (again excluding rest energies) of all the directly and indirectly ionizing particles leaving the volume and $\sum Q$ represents the net energy derived from rest mass (in any transformation of nuclei or elementary particles) in the volume.

Dosimetry is the metrologic discipline that studies the measurement of dose, a magnitude defined as the mean energy imparted by radiation to certain amount of mass, this is:

$$D = \frac{d\bar{\epsilon}}{dm} \tag{1.2}$$

Where $d\bar{\epsilon}$ is the mean energy imparted by ionizing radiation to a mass, dm, that should be as close a possible to a point although big enough to avoid statistical fluctuations affecting the mean energy[3]. Dose is expressed in gray (Gy), by definition a joule (J) per kilogram (kg). For clinical applications (radiology and radiotherapy), reference dose is evaluated in water, as there is a precise knowledge of radiation transport in this material that allows to obtain accurate results. Additionally, the human body, consisting in 70% water and with an average density close to 1 g cm^{-3}, has mass radiation interaction coefficients similar to those of water, being the dose to these two materials closely related.

The measurement of dose is performed with a dosimeter, an apparatus in which the effect of radiation can lead to a reading M that is linked to the dose D delivered to the dosimeter active volume V. The calibration of a dosimeter consists in the determination of a coefficient that converts the dosimeter reading M, which can require several corrections depending on the physical properties of the measurement system and conditions, into dose. Additionally, it may result necessary to evaluate, from the dose to the dosimeter sensitive medium, the dose to a material of interest, usually water. Under certain conditions and whenever the dosimeter does not

---

[3] While the energy imparted ϵ is a stochastic quantity, the dose can be considered in many situations as a non stochastic magnitude that can be described by a continuous point function in a volume of interest [12].

exhibit response variations with the radiation energy spectrum and irradiation conditions, dosimeter reading ratios, M_1/M_2, can result equal to dose ratios, D_1/D_2, being this methodology referred to as relative dosimetry. Absolute determination of dose in one of the points involved in a relative dosimetry study can serve to derive the dose in the rest of the distribution.

1.2.2 Dosimeters

Physical effects arising from the interaction of radiation and matter resulting useful for the measurement of dose are quite varied, and include temperature change, luminescence, different chemical changes, conductivity, etc. Besides the different physical detection principles, dosimeters can also be classified as active or passive depending on whether they can yield real time measurements or not, see Figure 1.6. Without going into much detail, the characteristics of an ideal dosimetry system have been recognized to be: repeatability and reproducibility, accuracy and precision, sensitivity, adequate dose range, linearity with accumulated dose, independence of response as a function of energy, spatial resolution, and insensitivity to influence quantities such as dose rate, temperature, pressure, etc. [3]. In practice all dosimeters will exhibit certain limitations, that should be always considered with respect to any specific application in order to choose the most adequate system for every measurement.

DOSIMETERS

PASIVE	**ACTIVE**
• **FRICKE** (absorbance)	• **CALORIMETER** (temperature)
• **FILM** (optical density)	• **SCINTILLATOR** (light)
• **TLD** (light)	• **IONOMETRIC** (electrical current):
• **ALANINE** (ESR transitions)	- **DIODE**
• **GEL DOSIMETRY** (NMR relaxation or CT assessment of polymerization)	- **DIAMOND**
	- **LIQUID-FILLED IONIZATION CHAMBER**
	- **GAS-FILLED IONIZATION CHAMBER**

FIGURE 1.6: List of dosimeter types, classified as active or passive in terms of their real time or delayed read out. The physical magnitude measured by every dosimeter type is shown in parentheses.

Primary standards of dose

Only three types of dosimeters are considered to be primary standards for absorbed dose, as they are widely acknowledged as having the highest metrological qualities, leading to values that are accepted without reference to other standards of the same quantity, under certain conditions and through the application of certain conversions and corrections. For a dosimetry system to be a primary standard, the measured magnitude arising from the radiation effect must be related to absorbed dose to water through a relationship involving fundamental quantities that can be known with a low uncertainty. To obtain absolute dose measurements, all other systems must be traceable to one primary standard of dose, which can be:

Calorimetry

This method is based on the heating effect of radiation in materials, using the temperature change of an absorber for the measurement of deposited energy. The main technical difficulty of this dosimetry system lies in the construction of a thermally isolated segment in which to measure the temperature change. The most extended absorbers or active mediums are water and graphite, a material with radiation absorption characteristics similar to those of water, being graphite calorimetry much extended due to the difficulties of working with a liquid system [13]. In water calorimetry, a direct measurement of absorbed dose to water is given by the temperature rise (after the application of some corrections related with heat defect due to water radiolysis and heat transport) and the knowledge of the specific heat capacity.

Frycke dosimetry

This a chemical dosimetry system where the dose is determined through the measurement of the chemical changes produced in the sensitive medium. Fricke solution can be prepared by combining 1 mmol/L ferrous ammonium sulphate with 1 mmol/L sodium chloride and 0.4 mol/L sulfuric acid in double distilled water. Irradiation of this solution will oxidize the ferrous ions Fe^{+2} into ferric ions Fe^{+3}, and concentrations of the latter will be proportional to the absorbed dose to water. Ferric ions exhibit a strong absorption in the near ultraviolet (λ=304 nm), and thus ferric ion concentration can be determined measuring the change in absorbance of the solution by spectrometry. In this technique the chemical radiation yield has some sensitivity to the beam quality. Additionally, water to Fricke mass energy absorption ratio varies significantly with photon energy ($\approx$ 2% for 0 to 10 MeV), consequently requiring delicate correction factors for the calculation of dose to water [14].

Air filled ionization chambers

Ionization chambers are the reference instrument most used in clinical routine for both absolute and relative dose measurements due to its accuracy, robustness, long term stability, negligible recombination losses and the deep knowledge that has been developed through the years about its response. It consists in a air filled cavity in which an electric field is applied between two electrodes to collect the ionization charge produced in the medium. There are basically two types of ionization cavity chambers, cylindrical (also known as thimble) chambers, represented in Figure 1.7, and plane parallel chambers. For thimble type ionization chambers the geometry consists of conductive outer walls and a central collection electrode, being these two elements separated by an insulator to reduce leakage currents when a polarizing voltage is applied. A guard ring is usually included to further reduce leakage and improve the field uniformity in the active volume of the chamber.

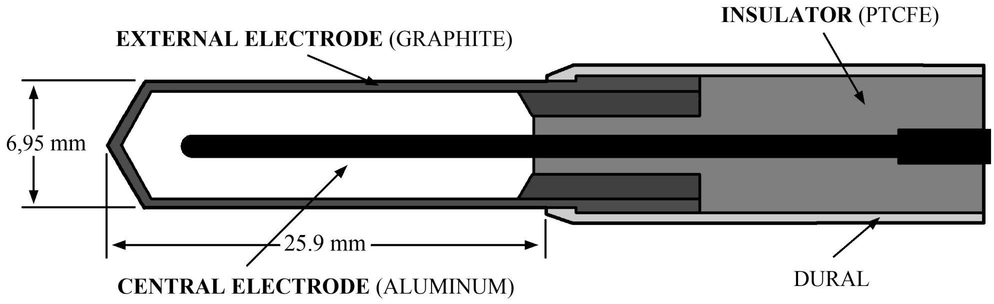

FIGURE 1.7: Sketch of a Farmer thimble type air ionization chamber showing typical length and diameter, PTCFE standing for polychlorotrifluoroethylene. The external electrode can be covered by a PMMA layer to make the detector waterproof.

The detection mechanism involves the ionization effect of radiation: an ionizing particle crossing the active volume produces electron-ion pairs along its path. The electric field produced through the polarization of the chamber electrodes makes these charge carriers to drift towards the electrodes, inducing a current that can be read out by an electrometer. Measurements are usually carried out with the ionization chamber placed in water and the collected charge can be related to dose to water. Details about this relationship are explained in Section 1.2.3.2. The Bragg-Gray cavity theory is employed to calculate dose to water from dose to air in the ionization chamber when the presence of the chamber does not perturb the fluence of electrons in the measurement medium[15]. This is fulfilled when the range of electrons in air is considerably larger than the dimensions of the cavity, which is generally the case in megavoltage photon and electron beams for regular size air ionization chambers and large field sizes[4]. However, actual measurements deviate from ideal Bragg-Gray conditions. Perturbations in the electron fluence usually arise, and certain corrections are necessary due to: the finite size of the chamber displacing some volume of the surrounding medium (water) and modifying the attenuation of the beam at the measuring point; the non water equivalence of the chamber wall and electrode materials; the presence of the chamber stem, etc.

Ionization chambers are usually vented, namely air is in contact with the exterior, which implies that temperature and pressure corrections have to be applied to account for changes in the mass of air inside the cavity arising from ambient condition changes.

Given that the sensitive medium is air at atmospheric pressure, with a mass density 700 times lower than water, the signal strength will be always smaller than that of solid-state detectors. For megavoltage beam dosimetry, the size of the ionization chambers active volume generally ranges from 0.01 to 1 cm^3, being the larger ones not suitable for small field measurements due to averaging effects, whereas the smallest ones exhibit lower signal to noise ratios, which affect the stability of the detector. Free air and air ionization chambers are one of the primary standards for air kerma in different beam

---

[4] Small cavity chambers, considered to be so with respect to the radiation field size, are well described by the Spencer-Attix modification of the Bragg Gray theory. The effect of high energetic electrons abandoning the cavity are here considered through the use of restricted mass stopping powers. Intermediate size cavities are better described by Burlin cavity theory. In this case, a factor is introduced to take into account the electron fluence generated by photon interactions occurring within the cavity [15].

qualities. Old dosimetry codes of practice were based on the measurement of air kerma for the ionization chamber calibration [16, 17]. However, additional uncertainties introduced for the determination of dose to water in clinical applications lead to use a new dosimetry protocol based on dose to water calibration [18, 19] within the medical physics community. For the measurement of this magnitude, difficulties arising in the determination of ionization chamber volumes with the required accuracy make ionization chambers to be generally used for radiotherapy purposes with a calibration factor obtained from cross calibration with other absolute dosimetry system [3].

Other dosimetry methods

Diode

These solid state semiconductor detectors are p-n union type diodes. In this case, electron-hole pairs induced by radiation in the bulk of the dosimeter diffuse to the depletion region, where they drift due to the intrinsic field leading to an inverse mode current in the diode. Diodes present the advantage of exhibiting high signal to noise ratios due to the high mass density of silicon. They can be thus built with very small sizes, $\approx 10^{-3}$ mm^3, providing good spatial resolution. The high atomic number of silicon make diodes to exhibit energy dependence, over responding at low energies, compared to water, due to the higher photoelectric effect in silicon. They present also dependence with temperature, dose rate and radiation incidence direction. The diode sensitivity changes with integrated dose due to radiation damage, reason for which these dosimeters are more commonly used for relative dosimetry than for absolute dosimetry purposes.

Diamond

Natural high purity type IIa diamonds are a dielectric material which can be used as dosimeters, usually working similar to air ionization chambers: electrons and positive holes are produced in the diamond by radiation, moving free through the crystal and producing a current proportional to dose when a polarization voltage is applied. Dosimeters are built by sandwiching the crystal with two electrodes and polystyrene capsule. Other diamond dosimetry method consists in measuring the thermoluminescence of this material after irradiation: light emitted in the UV range when the dosimeter is heated [20]. Diamonds exhibit high signal to dose ratios, being again constructed with small dimensions for the sake of spatial resolution. They are tissue equivalent, although 3.5 times denser than water, and present low energy dependence (compared to water), and high resistance to radiation damage. However, they exhibit certain dose rate dependence, require pre-irradiation and are certainly quite expensive[5].

Alanine

Alanine, $CH_3CH(NH_2)COOH$, is an amino acid with simple molecular structure. Highly stable radicals are induced in this dielectric and tissue equivalent material by ionizing radiation in a concentration that can be quantified by electron spin resonance. Alanine dosimeters are built in polycrystalline aggregate presentations including films, rods and small pellets ($v \approx 0.05$ cm^3), the latter resulting very useful for the measurement of small radiation fields. An alanine/ESR dosimetry system will be presented in Chapter 3.

Liquid ionization chamber

Ionization chambers using non-polar dielectric liquids as active medium, usually isooctane, present certain advantages. Liquid densities are closer

---

[5] Much progress has been achieved in the development of high purity single crystal diamonds by chemical vapor deposition, and synthetic diamonds exhibit now excellent electrical properties for their use as dosimeters [21].

to water, having a higher tissue equivalence and mass stopping power and energy absorption coefficient ratios, to water, that remain very constant in the range of energies used in standard radiotherapy. Furthermore, the higher mass density of the active medium compared to air increases the signal to noise ratio of these dosimeters, allowing the construction of active volumes down to 0.5 mm^3. Ion mobilities in liquid ionization chambers are however moderate, leading to important volume recombination effects [22], which imposes careful dosimetric characterizations for their use as absolute dosimeters.

1.2.3 Absorbed dose determination in external beam radiotherapy

1.2.3.1 Calibration

Megavoltage photon beams generated by electron linear accelerators (linacs) have become the most used clinical photon beams for external radiotherapy in developed countries. In electron linear accelerators, the calibration of a photon beam consists on the determination of the absorbed dose to water that corresponds to the delivery of one linac monitor unit (MU). This measurement is performed under certain prefixed conditions established as reference and described below in this section, Table 1.1. The MU is defined by the charge collected by two redundant transmission ionization chambers, called monitor chambers and located in the head of the linac, due to the ionization produced by the fluence of the linac in the chambers active medium. The monitor chamber signal is related with the absorbed dose to water in the above mentioned reference conditions, and the so defined MU is then used for the determination of the dose in radiotherapy treatment planning and delivery.

Ionization chambers can provide dose measurements with small associated uncertainties and are very easy to use, which has made them the dosimeter usually employed for photon beam calibrations and in clinical routine. Standard Dosimetry Laboratories (SDL) provide the clinical institutions with the ionization chamber calibration coefficients that are needed to convert chamber readings into absorbed dose to water under reference conditions. Determination of calibration coefficients at dosimetry laboratories involve the comparison of the detector reading and the known value of a certain magnitude, established as the dosimetry standard, through a high quality metrological instrument that allows its determination with a verified accuracy and traceability.

The detector traceability implies that an unbroken chain of comparisons relate the detector measurement and the dosimetry standard, what can be fulfilled through three main routes:

1. The dosimeter is directly calibrated by an Primary SDL (PSDL), which has experimentally developed the primary standard.
2. The dosimeter is calibrated by a Secondary SDL (SSDL) using a secondary standard that has been calibrated against the primary standard of a PSDL.
3. The dosimeter calibration coefficient is obtained by comparison with another dosimeter that has been in turn calibrated by a PSDL, a SSDL or an accredited dosimetry laboratory (ACDL), this procedure is commonly referred to as cross-calibration.

The reference beam employed for the development of dosimetry standards in high energy photon external beam radiotherapy is gamma radiation from a ^{60}Cobalt source. The suitability of this calibration lies on the reliability of the ^{60}Co radioactive decay and its gamma emission spectrum, with 1.17

and 1.33 MeV photons, which is close to the mean energy of 6 MV photon beams.

Additionally, dosimetry protocols or Codes of Practice (CoP) provide clinical institutions with standardized recommendations, including the information that is needed to measure absorbed dose to water in the user's beam from the calibration coefficient provided by the SDLs. These CoPs, which contribute with their recommendations to the accuracy of the measurement, are established to ensure that unified dosimetric methodologies are followed by clinical institutions, being published by organisms like the American Association of Physics in Medicine (AAPM) from the United States, the International Atomic Energy Agency (IAEA) and national institutions like the German Institute for Standardization (DIN).

To this date two dosimetry standards have been employed by SDLs for high energy photon radiotherapy: air kerma, adopted formerly, and absorbed dose to water, introduced more recently, both measured under certain prefixed geometrical conditions. According to this, two types of dosimetry protocols exist depending on the dosimetry standard employed: while AAPM TG-21 and IAEA TRS-277 CoPs were based on air kerma [16, 17], protocols like AAPM TG-51 and IAEA TRS-398 are based on absorbed dose to water standards [18, 19].

At hospitals, the measurement of absorbed dose to water using ionization chamber calibration coefficients of air kerma requires a series of steps that increase the final uncertainty of the measurement and involves chamber type dependent correction factors that do not account for differences between individual chambers of a certain type. The change in the standard employed for the dosimetry of high energy photon beams is justified by the lower uncertainties achieved in the measurement of absorbed dose to water (magnitude of interest at clinical institutions) when detectors are directly calibrated in terms of this magnitude. Primary standards of absorbed dose to water have been thus developed at SDLs from 1990 until now and dosimetry protocols based on this standard have been widely adopted by medical institutions.

1.2.3.2 Absorbed dose to water standard formalism

As we have seen, the calibration of a linac photon beam consists in the determination of the absorbed dose to water per MU under reference conditions. In this section we will describe the methodology recommended by the IAEA TRS-398 CoP [18] for the performance of clinical high energy photon beam calibration using the ionization chamber calibration coefficient provided by a standard dosimetry laboratory.

Reference conditions and influence quantities

The absorbed dose to water, measured under reference conditions at depth z_{ref} in a water tank, due to the delivery of a ^{60}Co reference beam represented by the beam quality index Q_0, is expressed as:

$$D_{w,Q_0} = M_{Q_0} \cdot N_{D,w,Q_0} \tag{1.3}$$

where M_{Q_0} is the ionization chamber reading, fully corrected for influence quantities such as pressure, temperature and relative humidity, and N_{D,w,Q_0} is the ionization chamber calibration coefficient, in terms of absorbed dose to water in the ^{60}Co reference beam and under reference conditions, that is provided by a SDL.

The calibration coefficient, N_{D,w,Q_0}, is determined in the SDL as the ratio of the dosimeter reading and the known value of the absorbed dose to water under reference conditions. This value, referred to as *conventional true value*, is developed as dosimetry standard through a dosimetric method of guaranteed accuracy. The accuracy of the method is ensured through the

Table 1.1: Reference conditions for the determination of absorbed dose to water in ^{60}Co and clinical high energy photon beams.

Influence quantity	**Reference value**
Phantom material	water
Chamber type	cylindrical (or plane-parallel, pp)$^{(a)}$
Measurement depth $z_{ref}^{(b)}$	10 g cm^{-2} or 5 g cm^{-2} if $TPR_{20,10}^{(c)}$ <0.7
	10 g·cm^{-2} if $TPR_{20,10} \geq 0.7$
Reference point of chamber	central axis at the cavity volume center
	pp chambers: window inner surface center
Position of chamber reference point	at the measurement depth z_{ref}
SSD or SCD$^{(d)}$	100 cm (or 80 cm)
Field size$^{(e)}$	10 cm×10 cm

$^{(a)}$Optional reference values allowed for calibration in ^{60}Co beams are included in brackets. $^{(b)}$Given the constancy of $N_{D,w}$ with depth, an ESTRO-IAEA report on Monitor Unit calculations [23] recommend the use of a single reference depth z_{ref}= 10 g cm^{-2} for all photon beam energies. However, the use of the z_{ref}= 5 g cm^{-2} reference depth used in the detector calibration in the ^{60}Co beam is also allowed by TRS-398 CoP. $^{(c)}$ $TPR_{20,10}$ is defined in Section 1.2.3.2. $^{(d)}$The reference Source to Surface or Source to Chamber Distance (SSD or SCD) should be that used for clinical treatments. $^{(e)}$The field size is defined at the surface of the phantom for a SSD type set-up, whereas for a SAD type set-up it is defined at the reference depth in the water phantom, at the isocenter of the machine.

fulfilment of the corresponding standard of the International Organization for Standardization[6], and through the existence of a network of calibration laboratories with intercompared standards.

Regarding the detector reading, M_{Q_0}, the effect of the above mentioned influence quantities has to be taken into account. Influence quantities refer to all the quantities that, not being the object of the measurement, can produce an effect on the measurement of the magnitude of interest. Dosimetry protocols set some of these influence quantities to certain values, establishing them as reference conditions, as this is the case, for example, with the size of the radiation field. These reference conditions, defined to

---

[6] The ISO/IEC 17025 establishes the general requirements for the competence of calibration laboratories.

keep fixed the maximum number of influence quantities as possible, serve as a common experimental frame for intercomparison between calibration laboratories, allowing traceability and providing a scenario for the use of dosimetry protocols in clinical institutions. In practice, reference conditions define the geometrical configuration of the measurement, the material and size of the phantom, the radiation field size and the source distance. The IAEA TRS-398 code of practice establishes the reference conditions presented in Table 1.1 for the measurement of absorbed dose in ^{60}Co beams and in clinical high energy photon beams, ensuring that conditions very close to CPE are achieved to guarantee a correct does determination.

The remaining influence quantities, not fixed as reference conditions, are of multiple nature and will be sometimes uncontrollable by the user, as for example the detector aging and the laboratory humidity, pressure and temperature. Examples of influence quantities controllable by the user are the ionization chamber polarization voltage, and in some cases, the dose rate and the beam quality. The use of correction factors associated to the influence quantities is required for the determination of absorbed dose to water whenever any of them vary from those established during the calibration coefficient evaluation. These factors are introduced in the dosimetry protocol as a set of multiplicative factors, $\prod_i k_i$, assuming that the associated influence quantities affect the measurement independently from each other, and thus the detector reading is corrected as indicated in Equation 1.4.

$$M = M_{raw} \cdot k_{TP} \cdot k_h \cdot k_s \cdot k_{elec} \cdot k_{pol} \tag{1.4}$$

The included factors correct for changes in temperature and pressure, k_{TP}, relative humidity, k_h, incomplete collection of charge (recombination effects) in the chamber, k_s, changes in the electrometers calibration factor, k_{elec}, and polarity effects associated to the chamber, k_{pol}.

Among all the influence quantities there is one, characteristic of every radiation field, that is considered separately in the formalism of dosimetry protocols due to its special relevance: the beam quality, related with the fluence spectral distribution of the photon beam. In order to summarize and represent the beam quality, a single quantity, referred to as beam quality index, Q, is used as beam quality descriptor, being defined and measured for every radiation beam. Dosimetry protocols include the correction factors associated to a wide range of ionization chambers as a function of the beam quality index, being employed for clinical photon beam calibration whenever the clinical beam quality differs from that employed for the detector calibration at the SDL. These correction factors, referred to as beam quality correction factors, will be presented in the following section.

Beam quality correction factors

Whenever an ionization chamber measurement is performed in a beam quality different from that in which the chamber calibration coefficient was obtained, a correction factor must be added to Equation 1.3 in order to obtain the absorbed dose to water as:

$$D_{w,Q} = M_Q \cdot N_{D,w,Q_0} \cdot k_{Q,Q_0} \tag{1.5}$$

where M_Q is the ionization chamber reading in the beam quality Q, N_{D,w,Q_0} is the ionization chamber calibration coefficient provided by the standard laboratory for the reference beam quality Q_0, under reference conditions, and k_{Q,Q_0} is the ionization chamber beam quality correction factor associated to the beam quality Q, different from the reference beam quality Q_0. In this expression, the ionization chamber reading M_Q is fully corrected for any influence quantity according to Equation 1.4.

For high energy photon beams, the beam quality index Q defined by TRS-398 is the tissue-phantom ratio, $TPR_{20,10}$, calculated as the ratio of absorbed dose in axis, at 20 cm and 10 cm depth in a water phantom, with a constant source to chamber distance (SCD) of 100 cm and a 10 cm×10 cm square field defined at the chamber plane, see Figure 1.8.

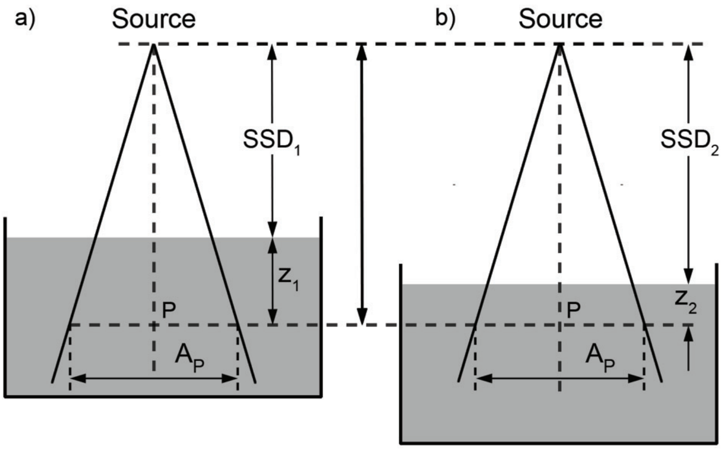

FIGURE 1.8: Geometry for measurement of $TPR_{20,10}$ under a square field of side, A_P, equal to 10 cm. (a) Geometry for the measurement of dose at point P and depth $z_1 = 20$ cm in a water phantom; (b) Geometry for the measurement of dose at point P at depth $z_2 = 10$ cm in a water phantom. The distance between the source and the point of measurement is $SSD1 + z1 = SSD2 + z2 = 100$ cm for both (a) and (b).

The $TPR_{20,10}$ gives, like the beam quality descriptors chosen by other dosimetry protocols, a measurement of the effective attenuation coefficient, characterizing the approximately exponential decrease of the photon depth-dose curve beyond the depth of maximum dose. The $TPR_{20,10}$ has been claimed however to present certain advantages over other quality descriptors, like the $\%\text{dd}(10)_x$, due to its independence on electron contamination in the incident beam, the simplicity of the measurement, and its low sensitivity to SCD changes arising from positioning errors [18].

If we take into account that the ionization chamber calibration coefficient at a beam quality Q can be defined as:

$$N_{D,w,Q} = D_{w,Q}/M_Q \tag{1.6}$$

The beam quality correction factor can be expressed as the ratio of calibration coefficients at the beam qualities under consideration, where Q stands again for the user beam and Q_0 for the calibration or reference beam:

$$k_{Q,Q_0} = \frac{N_{D,w,Q}}{N_{D,w,Q_0}} \tag{1.7}$$

The Spencer-Attix formulation of the Bragg-Gray theory expresses dose to water, D_w, as the product of dose to air in the ionization chamber, D_{air}, and the ratio of water to air restricted mean mass collision stopping power, $(\overline{L}/\rho)^{water}_{air}$, which depends on the beam quality. Under departure from ideal Bragg-Gray detector conditions, a perturbation factor that depends on beam quality and the ionization chamber model, p_Q, is needed to express dose to water as a function of dose to air. This factor accounts for fluence variations due to the presence of the cavity, p_{cav}, the effect of taking the chamber effective point of measurement at the center of the cavity, p_{dis}, the non water equivalence of the chamber wall, p_{wall}, and the effect of the central electrode, p_{cel}. The global perturbation factor is thus the product of all these contributions, $p_Q = p_{cav} \cdot p_{dis} \cdot p_{wall} \cdot p_{cel}$, and dose to water can be expressed as:

$$D_w = D_{air} \cdot (\overline{L}/\rho)^{water}_{air} \cdot p_Q \tag{1.8}$$

On the other hand, the dose to air can be obtained from the mean photon energy required to create an electron-ion pair in air, W_{air}/e, which is considered to remain constant for energy photons up to 25 MeV [24], and the exposition, X, or charge produced in air per unit mass, expressed by the corrected mass normalized detector reading M/m:

$$D_{air} = X\frac{W_{air}}{e} = \frac{M}{m}\frac{W_{air}}{e} \tag{1.9}$$

Equations 1.6, 1.8 and 1.9 lead to the expression of the beam quality correction factor as a function of the water to air restricted mass stopping power and perturbation factors ratios, which also vary with the beam quality:

$$k_{Q,Q_0} = \frac{D_{w,Q}/M_Q}{D_{w,Q_0}/M_{Q_0}} = \frac{[(\overline{L}/\rho)^{water}_{air} \cdot p]_Q}{[(\overline{L}/\rho)^{water}_{air} \cdot p]_{Q_0}} \tag{1.10}$$

Although the formalism here presented follows the methodology proposed by the TRS-398 CoP, other protocols like AAPM TG-51 follow very similar formalisms including the establishment of reference conditions and the application of beam quality correction factors. Slight differences, arising for example from differences in the definition of the beam quality index, are minimized through the well known relationships between them, which allows the CoPs intercomparison to test the protocols equivalence and consistency [25].

1.2.3.3 Nonstandard field dosimetry

As we have seen, IAEA TRS-398, and also AAPM TG-51, recommend the determination of absorbed dose to water in high energy photon beams using an ionization chamber calibrated in terms of absorbed dose to water in a reference beam quality Q_0 and under standard reference conditions, which are usually a 10 cm×10 cm square field and 100 cm source-to-surface distance (SSD) or source-to-axis distance (SAD), Table 1.1. These codes of practice established a robust path for the determination of absorbed dose to water in external radiotherapy standard beams during the decades of

1980's and 1990's, when conformal radiotherapy, involving large radiation field sizes compared with the range of secondary particles in water, was the predominant external radiotherapy technique employed in clinical institutions. However, the introduction in Europe and the USA of commercial multileaf collimators in 1990 [3] and the development and widespread in the clinic of IMRT by the late 1990's led to a huge increase in the use of small fields in clinical treatments. Additionally, a new generation of linear accelerators and special delivery techniques specifically designed for stereotactic deliveries and IMAT has been introduced, including treatment units like:

- Leksell GammaKnife® (Elekta Instrument AB, Stockholm, Sweden),
- CyberKnife® Robotic Radiosurgery system (Accuray Inc., Sunnyvale, CA)
- TomoTherapy® Hi-Art® (Accuray Inc., Sunnyvale, CA),
- VMAT (Elekta Instrument AB, Stockholm, Sweden).

The radiation delivery of these machines is mainly performed with non-standard fields, a term used to refer either to:

1. Small fields, with transversal sizes of the same (or less) magnitude as the range of secondary electrons in the medium, which present unfavorable measurement conditions whenever there is a partial occlusion of the radiation source or if the detector employed for the measurement is large compared with the field size.
2. Intensity modulated fields involving small fields, or extensive fields with steep dose gradients.

In these fields, departure from charged particle equilibrium conditions arise and volume averaging effects can become important for many detectors due to the steep dose gradients and multileaf collimator penumbras, substantially increasing the uncertainty and/or error associated to the measurement of absorbed dose to water when compared with measurements in standard fields.

Although reference conditions can be established in some of these modern treatment units and dosimetry protocols can still be applied, the departure from standard field dosimetric conditions in the clinical delivery raised considerable concerns in the medical physics community [26–29]. On the other hand, some new treatment units cannot fulfill the standard reference conditions defined in dosimetry protocols. Determination of absorbed dose to water was initially performed in these machines following the recommendations provided by the manufacturers and through the application of certain approximations.

Since the use of nonstandard fields became extensive in clinical practice in Europe and USA, a unified methodology for the measurement of absorbed dose to water under these fields was considered a necessary step for the quality assurance of the radiotherapy dosimetry chain. This situation prompted the collaboration of the International Atomic Energy Agency and the American Association of Physicists in Medicine Therapy Physics Committee for the creation of an international working group on reference dosimetry of small and nonstandard beams. A new formalism for small and composite fields reference dosimetry was proposed by Alfonso *et al.* [30] with the intention of complementing and extending the recommendations and methodologies contained in existing CoPs.

In this section, we present the new formalism for the dosimetry of nonstandard fields. The concept of intermediate calibration field is introduced in this formalism to define a field that can be delivered by the machine and stands close to the reference conditions or to the clinical delivery and the specific delivery technique associated to the machine. Two types of intermediate calibration fields, comprising both static and composite field dosimetry, are defined with their associated beam quality correction factors. These intermediate calibration fields are the machine-specific-reference field, f_{msr}, and the plan-class-specific-reference field, f_{pcsr}, that we proceed to briefly present here.

Intermediate calibration fields

Machine specific reference field

Whenever a measurement in reference conditions is not possible due, for example, to the geometrical design of the treatment unit, a static field, referred to as machine specific reference field, f_{msr}, is defined as close as possible to the conventional reference field. The f_{msr} field size should be larger that the range of secondary electrons in the medium (water), and the measurement should be performed with a relatively small ionization chamber to ensure effective lateral charged particle equilibrium in the volume of interest. Associated to the f_{msr}, an ionization chamber correction factor, $k^{f_{msr},f_{ref}}_{Q_{msr},Q}$, is then introduced in the previously explained reference dosimetry formalism, Equation 1.5, in order to account for the differences in geometry and beam quality between the machine specific measurement conditions and the conventional reference conditions denoted by f_{ref}. Absorbed dose to water in the machine specific reference field is then given by:

$$D^{f_{msr}}_{w,Q_{msr}} = M^{f_{msr}}_{Q_{msr}} \cdot N_{D,w,Q_0} \cdot k_{Q,Q_0} \cdot k^{f_{msr},f_{ref}}_{Q_{msr},Q} \tag{1.11}$$

Plan class specific reference field

The plan class specific intermediate calibration field, f_{pcsr}, is a composite field including unit-specific delivery features, defined with the purpose of reproducing dosimetric conditions similar to those of clinical treatments. This field would ideally deliver a homogeneous dose distribution to an extended and geometrically simple target volume, and the absorbed dose to water in this field can be expressed as:

$$D_{w,Q_{pcsr}}^{f_{pcsr}} = M_{Q_{pcsr}}^{f_{pcsr}} \cdot N_{D,w,Q_0} \cdot k_{Q,Q_0} \cdot k_{Q_{pcsr},Q}^{f_{pcsr},f_{ref}} \tag{1.12}$$

where $k_{Q_{pcsr},Q}^{f_{pcsr},f_{ref}}$ is a factor to correct between the differences between the *pcsr* and the conventional reference field.

This $k_{Q_{pcsr},Q}^{f_{pcsr},f_{ref}}$ factor can be also expressed as the product of the machine specific reference field correction factor and a factor correcting for the differences between the plan class specific and the machine specific reference field:

$$k_{Q_{pcsr},Q}^{f_{pcsr},f_{ref}} = k_{Q_{pcsr},Q_{msr}}^{f_{pcsr},f_{msr}} \cdot k_{Q_{msr},Q}^{f_{msr},f_{ref}} \tag{1.13}$$

Clinical dosimetry

Once intermediate calibration fields are defined, the determination of absorbed dose to water in nonstandard beams can be addressed. The dose of a clinical field can be obtained from the dose in either f_{msr} or f_{pcsr} through the introduction of a field factor Ω as:

$$D_{w,Q_{clin}}^{f_{clin}} = D_{w,Q_{msr(pcsr)}}^{f_{msr(pcsr)}} \cdot \Omega_{Q_{clin},Q_{msr(pcsr)}}^{f_{clin},f_{msr(pcsr)}} \tag{1.14}$$

where,

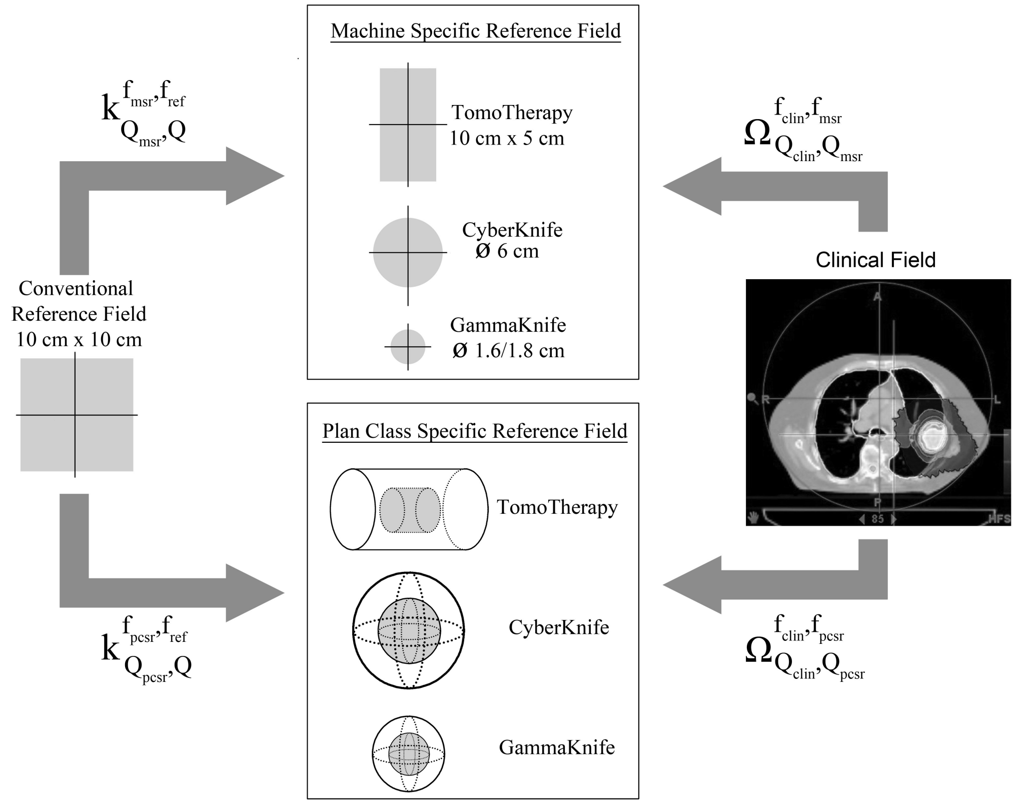

FIGURE 1.9: Scheme of the dosimetry routes introduced by the machine specific and plan class specific reference fields for the measurement of absorbed dose in nonstandard fields. Examples of possible intermediate calibration fields for machines like Tomotherapy, Cyberknife and GammaKnife. Plan class specific intermediate calibration fields are defined to deliver uniform dose distributions, in gray, with simple geometries (cylinders, spheres), to simple geometry phantoms represented by the white volumes.

$$\Omega^{f_{clin},f_{msr(pcsr)}}_{Q_{clin},Q_{msr(pcsr)}} = \frac{M^{f_{clin}}_{Q_{clin}}}{M^{f_{msr(pcsr)}}_{Q_{msr(pcsr)}}} \cdot k^{f_{clin},f_{msr(pcsr)}}_{Q_{clin},Q_{msr(pcsr)}} \tag{1.15}$$

If the intermediate calibration fields are representative of the clinical practice, $k^{f_{clin},f_{msr}}_{Q_{clin},Q_{msr}}$ and $k^{f_{clin},f_{pcsr}}_{Q_{clin},Q_{pcsr}}$ correction factors are close to unity and the field factors can be approximated as the ratio of chamber readings. On the other hand, in the practical case of a static field dosimetry, these $\Omega^{f_i,f_j}_{Q_i,Q_j}$

would be equal to the standard output factors.

Figure 1.9 shows a schematic representation of the paths proposed for the measurement of absorbed dose to water in nonstandard fields through static and dynamic intermediate calibration fields.

Scope of the nonstandard fields new formalism

The new formalism for the dosimetry of nonstandard fields was originally presented in Medical Physics [30] as a proposal for the standardization of the dosimetry procedures in the above mentioned IMRT and other special techniques. But the aim of that letter was not only to present the new dosimetry formalism but also to encourage the debate of the scientific community about the proposal. The working group on nonstandard fields also recalled that, although some static field dosimetry data were already available for many of the modern radiotherapy techniques, a lot of research work was to be done in composite field dosimetry in order to check the capabilities of plan class specific reference fields to study how they should be defined. Since then, several works about the dosimetry of nonstandard fields have been published [24, 31], and the topic is still subject of central attention in international medical physics conferences [32].

For the study of the new formalism, the experimental determination of ionization chamber correction factors associated to intermediate calibration fields is an important task that requires the measurement of absorbed dose to water under nonstandard conditions. Taking as an example the machine specific reference field, it directly follows from Equation 1.11 that the $k_{Q_{msr},Q}^{f_{msr},f_{ref}}$ correction factor can be obtained from the measurement of absorbed dose to water under the nonstandard field, $D_{w,Q_{msr}}^{f_{msr}}$, the fully corrected ionization chamber reading under the same field, $M_{Q_{msr}}^{f_{msr}}$, and the calibration coefficient at the reference beam quality and reference conditions, N_{D,w,Q_0}:

$$k_{Q_{msr},Q_0}^{f_{msr},f_{ref}} = k_{Q_{msr},Q}^{f_{msr},f_{ref}} \cdot k_{Q,Q_0} = \frac{D_{w,Q_{msr}}^{f_{msr}}}{M_{Q_{msr}}^{f_{msr}} \cdot N_{D,w,Q_0}} \tag{1.16}$$

Under nonstandard conditions, the lack of charged particle equilibrium and the importance of volume averaging effects in many detectors make the measurement of absorbed dose to water very demanding. A small volume dosimeter with good water equivalence and low energy dependence would be the most appropriate choice for this purpose. Alanine/ESR dosimetry, calibrated in terms of absorbed dose to water and traceable to a primary standard, has been widely employed in small field dosimetry studies and is recognized as a valuable independent dosimetry validation [33–35].

1.3 Quality assurance

Radiotherapy Quality Assurance (QA) is, according to World Health Organization (WHO), "concerned with all those procedures that ensure consistency of the medical prescription and the safe fulfillment of that prescription as regards dose to the target volume, together with minimal dose to normal tissue, minimal exposure of personnel and adequate patient monitoring aimed at determining the end result of treatmen" [36].

In order to ensure an optimized treatment delivery with maximized tumor control probability and minimum injury to normal tissue, QA aims the general reduction of uncertainties through the whole radiotherapy process, trying also to minimize and correct errors, and for this a series of actions must be followed. Guides for the implementation of radiotherapy quality assurance systems have been published by institutions like WHO, ESTRO and AAPM [36–38], usually suggesting the need for the definition of responsibilities and organization, documented procedures, accurate record keeping, system failure control, internal and external audit of procedures and education and training.

In the establishment of QA procedures, one key element is the definition of tolerance limits based on the clinical accuracy requirements. The analysis of dose effect relationships and tumor control probability models has lead to the establishment of these global requirements as[7]:

- 3% on the absorbed dose delivered to the specification point.
- 5% on the dose at all other points in the target volume.
- 4 mm on the position of field edges and shielding blocks in relation to the PTV.

It is important to note that whatever the required accuracy is, tolerance limits have to be established taking into account the real accuracy achievable in practical radiotherapy, which has been continuously improving through the years but has been observed to be some times lower than the limits stated above [39].

Radiotherapy QA programs are divided in individual QA steps affecting each contributing part of the whole radiotherapy process, and in these individual steps greater accuracies are required for the final recommended values to be achieved. Focusing on the tasks of the medical physicist staff, some of this steps are presented in the following subsections.

1.3.1 Treatment equipment quality assurance

Sophisticated equipment such as the treatment machine must undergo a commissioning phase and acceptance test before being clinically used. Measurements, adjustments and tests are performed taking into account the

---

[7] This accuracy requirements are given at the level of one standard deviation (k=1).

equipment specifications to optimize its performance and check the accuracy and capability of the system to meet the clinical requirements. Periodic QA checks and audits can later ensure that the original characteristics do not change inadvertently. Regarding megavoltage equipment, measurement of the radiation output and output stability is a fundamental step of QA. Beam calibration, or the determination of dose at reference conditions, plays a very important role here, where the required accuracy is 1.5% at a level of one standard deviation [18]. Ionization chambers are the recommended instruments for this purpose, and calibration coefficients have to be determined against SSDLs regularly (with 1 to 3 years intervals), stability checks have to be performed and beam quality correction factors determined with the highest possible accuracy.

1.3.2 Treatment planning quality assurance

This block includes the patient data acquisition systems, such as CT, and computerized treatment planning systems, which must both undergo the above mentioned commissioning processes and acceptance tests.

Regarding the CT QA, appropriate calibration on electronic density should be ensured, as well as its capability to reproduce actual dimensions of objects, absence of distortion, reproducibility and accuracy of the slice position and thickness, accuracy of gantry rotation and adequate alignment of positioning devices. Additionally, as data acquisition must allow the same patient position to be used in further steps of the process (delivery), immobilization and repositioning devices are of central attention.

In computerized treatment planning system, thorough commissioning of the beam has to be performed in order to ensure that TPS calculated dose distributions reproduce the output of the treatment machine. Special attention should be given to dose calculations in material inhomogeneities or whenever steep dose gradients are encountered [40, 41]. Correct interpretation of the patient data and accurate methods for the delineation of PTV and OARs is also required. TPS tolerance levels are typically set to 2-3 mm for geometry and 2-3 % for doses, although different criteria are applied depending on the clinical objective.

1.3.3 Treatment delivery quality assurance

This final step, usually referred to as treatment verification, is a global QA strategy trying to ensure that the treatment to be delivered matches the dose distributions of the planned treatment. In addition to all the procedures that check the treatment machine delivery and its consistency with the TPS, this QA step was extensively incorporated to QA programs with the introduction of IMRT in clinical institutions.

Highly conformed beams involved in IMRT techniques impose tighter controls in the MLC and patient positioning. Moreover, the higher demanding accuracy in TPS algorithms used for new treatment modalities imply more complex commissioning and sophisticated acceptance tests. Another complication is related with the small radiation fields and steep dose gradients involved in IMRT and other techniques, where transient charged particles equilibrium is not established and important volume averaging effects can arise in ionization chamber measurements. Moreover, as we commented before, ionization chamber beam quality correction factors are tabulated in dosimetry protocols for standard reference fields. Due to all these factors, the uncertainty of dose measurement of IMRT fields increases and errors up to 10% can arise [42].

From its introduction, many publications appeared discussing different aspects related with IMRT, and several institutions (ICRU, AAPM, ESTRO) published recommendations and guides for the clinical practice [43]. The

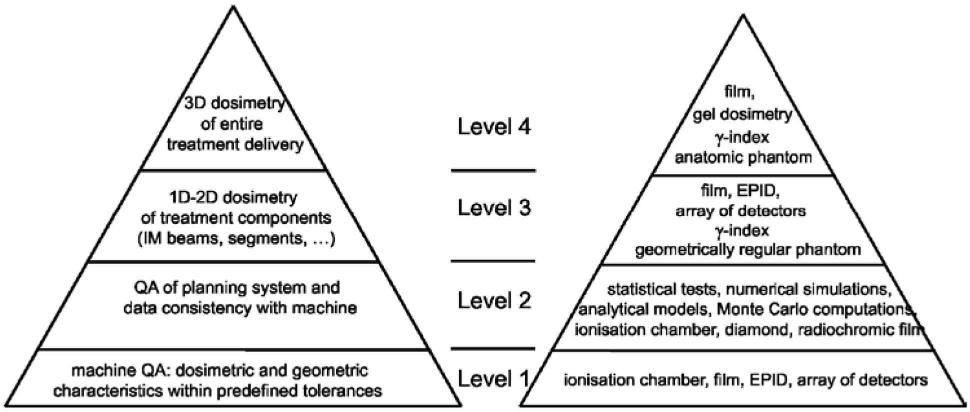

(a) **(b)**

FIGURE 1.10: (a) Conceptual pyramid including the different levels of treatment delivery QA, each level being based on the stability of the underlying levels. For the verification of one clinical treatment, the procedure could begin at the top of the pyramid through the performance of a 3D dosimetric verification, descending to lower pyramid levels whenever unacceptable discrepancies with treatment planning are encountered. (b) Methodology and dosimetry tools appropriate for every level [43].

variability and different complexity of the techniques implemented by different institutions makes however difficult the establishment of common procedures and criteria, and codes of practice have not been published establishing definitive procedures for this technique. This situation increases the importance and need for a pre-treatment verification to make a final evaluation of how the propagation of the different sources of uncertainly involved in the radiotherapy process affect the dose distribution finally delivered to the patient.

Departments applying complex radiotherapy techniques usually check individual plans by comparison between measurements and TPS dose distributions, at least until consistent accurate results are obtained in a center, and this can be performed in different ways. For each modulated beam, each beam setting can be applied with the gantry at 0° (in vertical incidence) to a rectangular phantom, where the dose distribution is measured and compared with that calculated by the TPS for the same setup. Another option is to compute and measure the dose delivered by all beams, again with the gantry at 0° or through the real delivery, using a simple geometrical phantom. It should be noted that individual beam measurements, where the detector may be only partially irradiated, can give results significantly different than those obtained through the combination of beams, where differences are usually smoothed.

Regarding dose measurements, different approaches can be also followed. Absolute dose measurements can be performed in one or several points (i.e. ionization chamber measurements in different points of a phantom or water tank). However, as the use of inhomogeneous fluencies is a relevant feature of IMRT, studying dose deposition in two or three dimensions results of particular interest. Two dimensional spatial dose distributions are measured with relative dosimetry using passive and active methods, usually combined with one absolute dose measurement from which absolute dose values can be obtained. Among the ideal characteristics of general dosimeters, detection systems used for IMRT verification will require good spatial resolution and low uncertainty in order to ensure effective treatment verification [3]. The types of dosimeters most employed for treatment verification will be summarized in the following sections.

1.3.3.1 Electronic portal imaging dosimetry (EPID)

Portal imaging systems consist of a radiation detector that is mounted opposite to the linac head, usually attached to the gantry, which detect the radiation transmitted through the patient and treatment couch. The detection mechanism varies with the system, being most extended the EPID systems based on fluoroscopic detectors, ionization chamber detectors and amorphous silicon detectors [7]. EPID systems produce two dimensional computer based images that are processed and analysed providing a representation of the attenuation properties of the different structures crossed by the radiation, being of central importance the contrast, resolution and noise of the device.

The use of EPID systems for treatment verification formerly included recording the integrated fluence from the treatment radiation beams and extracting information about the motion and position of the MLC leaves. EPID image information can be also used to derive the dose to the EPID, which is then compared with the calculation of the TPS at the EPID plane. Methods have been also developed to translate EPID images into primary fluence maps used as input in a TPS to recalculate 3D dose distributions using a phantom or patient CT data. Alternative approaches use backprojection algorithms to derive the dose to the patient from the EPID images [43].

1.3.3.2 Film dosimetry

Film dosimetry is in principle an ideal system for IMRT verification, registering two dimensional dose distributions with high spatial resolution. Films are usually placed in water equivalent phantoms at depths of interest, usually those of the PTV and OARS, see Figure 1.11. The relative dose distributions obtained can be scaled to absolute values through cross-calibration with a small ionization chamber measurement.

Radiographic film

Radiographic film consist on a radiation sensitive emulsion coated on a transparent polyester base. The emulsion contains silver halide crystals (95% silver bromide and 5% silver iodide suspended in gelatin for Kodak XTL and XV films), which under exposure to ionizing radiation undergo certain transformations related with the ionization of silver bromide and the accumulation of silver ions in impurity regions leading to the darkening of the film. Uncertainty levels with this dosimetry system depend on the irradiation conditions, the film processing, scanning, the calibration curve and the data analysis. One drawback is the non tissue equivalence of the dosimeter materials, which introduces energy dependency with over-response at low energy, inducing depth and field size dependent sensitivity. Radiographic film has been however the dosimeter most extensively employed for IMRT verification for many years, being considered an accurate system whenever appropriate procedures and careful sensitometric calibration are performed [44].

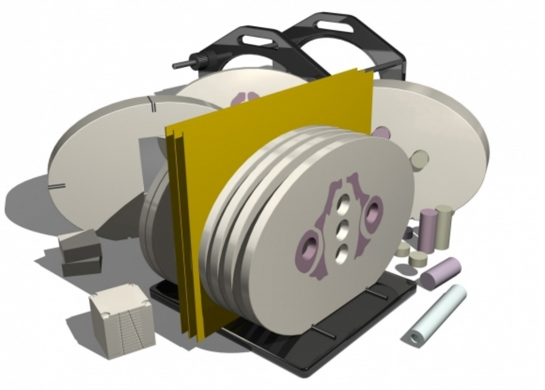

FIGURE 1.11: Sketch of an anthropomorphic phantom used for film dosimetry (CIRS IMRT Thorax Phantom, CIRS Norfolk, VA, USA), where film dosimeters are placed in the transversal planes of interest for the measurement of dose distributions.

Radiochromic film

Radiochromic films are made of several thin layers of plastic (mylar) sheet glued in sandwich with a radiosensitive gel that modifies the visible light absorbance with dose. It does not need chemical developing processing and presents some advantages as higher tissue equivalence and lower energy dependence. First radiochromic systems exhibited uniformity and reproducibility problems that have been improved in subsequent developments, although its cost remains quite high for massive clinical applications [45].

1.3.3.3 Detector arrays

Increase in the amount of patients being treated with a complex radiotherapy technique is a common situation encountered in clinical centers once that its implantation process is successfully achieved. Speeding up treatment verification procedures allows then to respond to the clinical demand, and getting dose distributions without the need of slow processing and scanning for their latter comparison with TPS dose distributions can greatly help to attain it. In this context detector arrays can result very useful, as these devices are easy to use and they are directly connected to computers allowing not only the fast measurement of one, two or three dimensional dose distributions but also its rapid incorporation into the clinical department computing network.

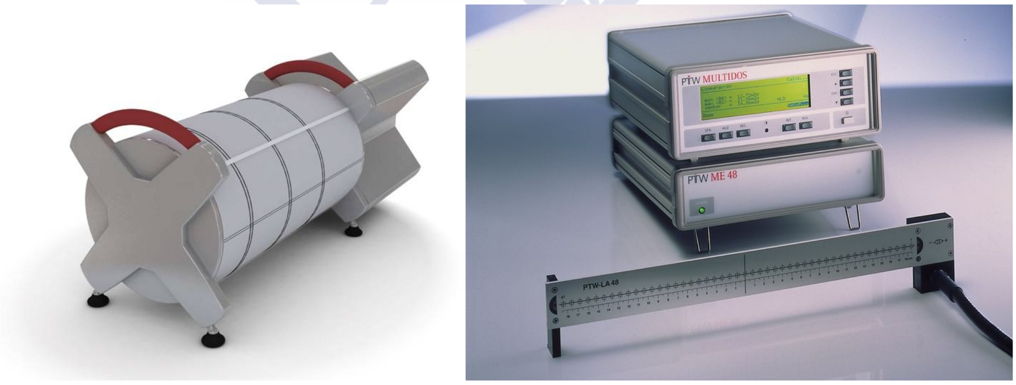

FIGURE 1.12: Two commercial detector arrays: Delta 4 detector array from Scandidos, Sweden, where diode detectors are arranged in a matrixx along two orthogonal planes to provide three dimensional dose distributions (left) and LA48 Linear Ion Chamber Array from PTW-Freiburg, Germany (right).

Different commercial detector arrays appeared through the last decade responding to the clinical demands and consisting usually in a number of detectors placed at fixed positions in a water equivalent phantom. The dosimetric mechanisms more extended in detection arrays are the ionization chamber and the diode, as they are robust, can be easily calibrated and can measure with low associated uncertainty. Different aspects related with these kind of detectors will be analyzed in detail in Chapter 2, where a study of different commercial solutions will be presented.

Chapter 2

2D detector arrays for IMRT verification: the influence of chamber response function

In this chapter we will study the use of two dimensional detector arrays for standard radiotherapy treatment verification. A detector response model will be presented that will allow us to reproduce the measurement of the detector under the incidence of an arbitrary fluence and quantify the effect introduced by such response. The performance of some of the most extended commercial solutions will be analyzed through the same methodology in order to compare their capabilities for IMRT verification and draw some conclusions about the optimal design for these kind of devices.

2.1 Introduction

The verification of complex treatments with composite fields, like those of IMRT, was initially performed using radiographic film dosimetry. The technological trend in dosimetry and medical imaging has imposed a limited availability of radiographic film for radiotherapy departments. Other passive alternatives, such as radiochromic film, present poor repeatability and dose uncertainty, and require time for film processing. Accordingly, in the last ten years most manufacturers of therapy dosimetry instruments have developed detector arrays for the measurement of dose distribution in planar and cylindrical geometries.

There are two main elements in the design of a detector array that determine the global performance of the device for treatment dosimetry verification, namely:

(a) The detection technology employed: semiconductor diode, air ionization chamber, diamond etc, together with the size of the detector.

(b) The spatial distribution of detectors in the array, referred to as detector sampling frequency.

Although measuring with an acceptable degree of accuracy also depends on some other factors like pre-irradiation requirements and long term stability, it is the choice of the detection technology, the design (size, shape and materials employed) and the array sampling what determines the intrinsic performance of the array, affecting:

i) Sensitivity to fluence variations: Depends on the signal to dose ratio exhibited by the detection technology, and the relationship between detector size and detector spacing in the array, which sets the smallest dose/fluence variation that can be detected by the device.

ii) Repeatability: Defined as the precision in repeated measurements performed under equal irradiation conditions.

iii) Accuracy: Defined as the degree of closeness of the array dose measurements to the true value of dose at the detectors reference points.

Other important characteristics of the device are, as for any dosimetry system, the linearity in the response with dose, the dose rate and energy dependence and the anisotropy in the response to radiation from different directions, which can be partially corrected for but is desired to be intrinsically minimal. The electronics acquisition time can also play a role for example in the verification of the collimator leaves movement in dynamic radiotherapy modalities.

Several commercial detector arrays were developed during the last years, which employ different combination of detection technology and spatial sampling, achieving considerable success for fast and accurate verification of complex treatments. Most of them can perform absolute dosimetry measurements through the use of a calibration coefficients, generally measured for the central detector, and an array of correction factors that compensate for the inter-detector response variations through the device [46].

Most detector arrays present a two dimensional, or planar, geometry, like PTW729 (PTW-Freiburg, Germany), MapCHECK (Sun Nuclear Corporation, Melbourne FL) or StarTrack and MatriXX (IBA Dosimetry, Louvain-La-Neuve, Belgium), while three-dimensional arrays, designed with their detectors distributed in several planes, have been later released, like ArcCheck (Sun Nuclear Corporation) and Delta4 (Scandidos, Uppsala, Sweden). By the time this study was conducted, planar arrays were more extended in clinical practice and it was by far easier to have them borrowed either from the vendor or from medical institutions than the three dimensional solutions. Given that the physical principles and factors affecting the performance of both two and three dimension detector arrays are the same, we decided to focus our study on different designs of planar arrays.

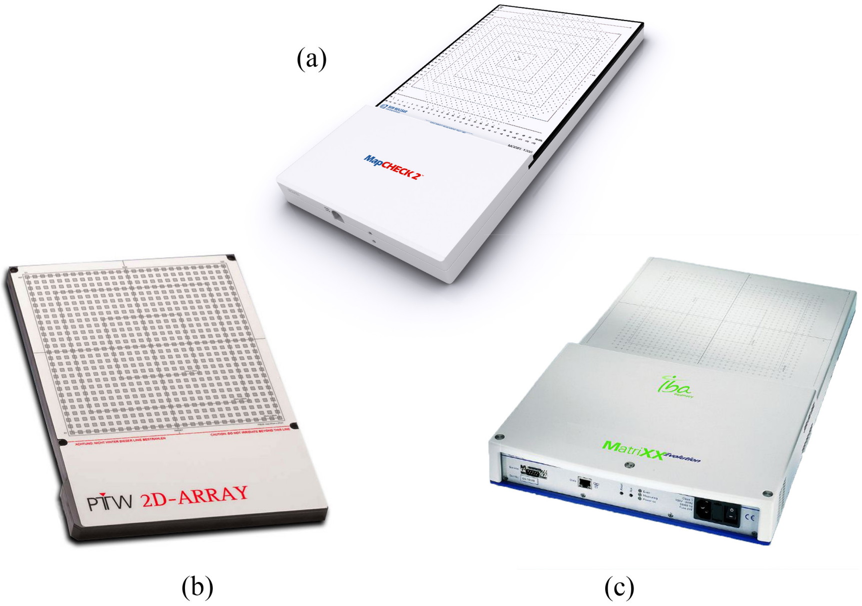

FIGURE 2.1: Commercial detector arrays studied in this chapter: a) MapCHECK2, b) PTW729 and c) MatriXX.

The detector arrays chosen for this study were:

a) MatriXX (IBA Dosimetry):

An array of 1020 cylindrical ionization chambers of 4.5 mm diameter and 5 mm height, arranged in a 32×32 grid with 7.62 mm center-to-center detector distances, covering an area of 24.4 cm×24.4 cm. The 0.3 cm thick buildup plate is made of Tecaran ABS (density 1.06 g cm^{-3}), while the backscatter plate is made of RW3 (98% Polystyrol, 2% TiO_2, density 1.045 g cm^{-3}) and has a thickness of 2.2 cm.

b) MapCHECK2 (Sun Nuclear Corporation):

An array made of 1527 n-diode detectors with a depletion region of 0.8 mm×0.8 mm transverse area. Detectors are distributed with a center-to-center detector distance of 1 cm in every row, with adjacent rows being laterally displaced by 0.5 cm, thus the shortest detector distance is 0.707 cm. The total area covered by the array is 36 cm×26 cm, and

Array	Field (cm×cm)	Detector Type	Detector size (mm)	Spacing (cm)
MatriXX	24.4×24.4	Ionization chamber	4.5 diam×5 height	0.76
MapCHECK2	26×32	Diode	0.8×0.8	0.71
PTW729	27×27	Ionization chamber	5×5×5	1

Table 2.1: Summary of the main characteristics of MatriXX, MapCHECK2 and PTW729 detector arrays.

the buildup and backscatter plates, of Polymethyl Methacrylate, have a mass thickness of 2 and 2.75 g cm^{-2} respectively.

c) PTW729 (PTW-Freiburg):

An array of 27×27 cubic ionization chambers of 5 mm side, embedded in a Polymethyl Methacrylate plate (density 1.12 g cm^{-3}) with 0.5 cm ridges between them. The center-to-center detector distance is 1 cm and thus the array covers a square area of 27 cm×27 cm side. The buildup and backscatter plates, also made of Polymethyl Methacrylate, have a thickness of 0.5 and 2 cm respectively.

2.1.1 Previous work and motivation

All the commercial detector arrays just presented are widely used for treatment verification in many clinical institutions, and had been thus object of thorough characterizations before our study. Amerio *et al.* and Stasi *et al.* [47, 48] dealt with the characterization of MatriXX initial versions, specifically studying the effect of the spatial resolution on the evaluation of the dose map. Spezi *et al.* [49] presented a characterization of PTW729, an array which was further studied by Poppe and collaborators [50, 51], showing a good performance and reliability. Jursinic and Nelms [52] presented a characterization study of the MapCHECK2 array and Banci Buonamici *et al.* [53] compared its performance with film dosimetry.

Other works have been more focused on the spatial response of these devices to radiation beams, as it can play a significant role in their use for dose verification. Ionization chambers spatial response functions were studied by Poppe *et al.* [50] through pencil-beam irradiation. A response maximum was observed when the beam impinges on the detector wall, or on the ridges between detectors, at a distance from the cavity surface within the range of secondary electrons, although the response function was finally approximated to a trapezoidal shape for the characterization of the device. Diode detectors, with a size smaller than the maximum range of secondary particles in the surrounding media, present a different response in shape and width than that of air ionization chambers [54]. Finally, other studies have used Fourier analysis and sampling theory to investigate the response functions of different detectors [51, 55].

The existing literature addressed the characterization of detection arrays, testing their suitability for treatment verification usually by comparison with film dosimetry. However, the different approaches followed in those investigations make inter comparison between devices difficult. In order to avoid this, our work simultaneously studies the aforementioned commercial solutions, covering both diodes and ionization chambers detection technologies and following a unified methodology (all devices under equal conditions), with the objective of providing comparable data to users and obtaining conclusions about the optimal design of detection arrays [56].

2.2 Detector fluence response function

The spatial response function of a detector can be characterized by the signal, S, registered when the detector, placed at a fixed depth z in a phantom, is irradiated with an infinitesimally narrow pencil beam of unit fluence, $\psi_\delta(x', y') \approx \delta(x' - x, y' - y)$, perpendicular to the phantom surface, at an incidence position (x, y) on this plane.

$$F_\psi(x,y,z) = S_\delta(x,y,z) \tag{2.1}$$

This response of the detector to an ideal perfectly collimated incident fluence function, referred to as energy fluence response function, F_ψ, allows to express the response of the detector to an arbitrary incident energy fluence through its convolution with the fluence distribution [57]:

$$S(x,y,z) = \int_{-\infty}^{\infty}\int_{-\infty}^{\infty} \psi(x',y')F_\psi(x-x',y-y',z)\;dx'\;dy' \tag{2.2}$$

For an air ionization chamber, the fluence response function depends on the cavity geometry and the properties of the materials surrounding it. The ionization signal is dominated by the fluence of secondary electrons generated in the plate above the active volume and the ridges between detectors [58] (usually chosen to be water equivalent), which leads to a lateral response peaking at the detector wall position, see Figure 2.2, as it was already observed for PTW729 detectors by Poppe *et al.* [50]. Diode detectors exhibit a much narrower lateral response due to their smaller size and higher density with respect to the surrounding materials. The diode detector signal drops thus more drastically when the pencil beam targets the rigdes between detectors with no response peaks associated to the change of material.

2.2.1 Measurements

The fluence response function of PTW729, MatriXX and MapCHECK2 were measured with a methodology resembling that adopted by Poppe [50]. Some differences in the collimation and scanning procedures were introduced with the objective of measuring narrower and more intense peaks at

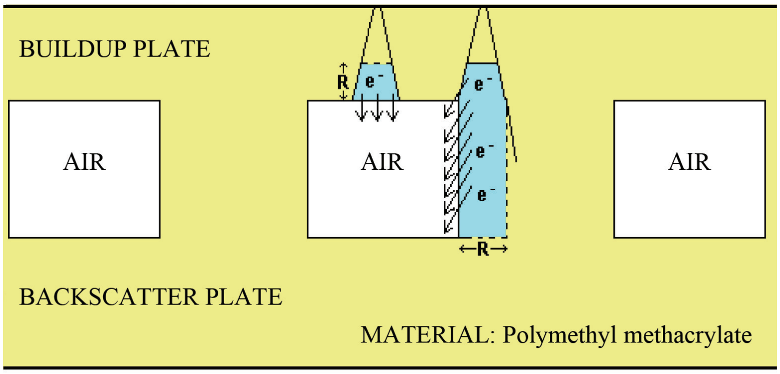

FIGURE 2.2: Schematic representation of the PTW729 array showing the contribution to the signal of the charged particles originated in the materials surrounding the air cavities. R stands for the electron range.

the ionization chamber walls as it would be expected from point-like pencil beams. Our collimated pencil beam, of 0.5 mm×0.5 mm size, was obtained from a 2 cm×2 cm radiation field of a 6 MV Siemens Mevatron linac by using two pairs of confronted cerrobend blocks (of 6 cm×5 cm×10 cm each) separated by 0.5 mm.

The spatial response of the detectors was measured with the array mounted on a stepper motorized platform. Detector arrays were placed on the platform with PMMA buildup plates on them to place all detectors at 5 g cm^{-2}. A PMMA plate was also placed below the arrays to ensure full backscatter contribution to the detectors. For the measurement of F_{ψ}, one single detector, usually the central one, was scanned with the pencil beam in 0.5 mm steps. Figure 2.3 shows a sketch of this experimental set-up and Figure 2.6 shows the measured fluence response functions under this method.

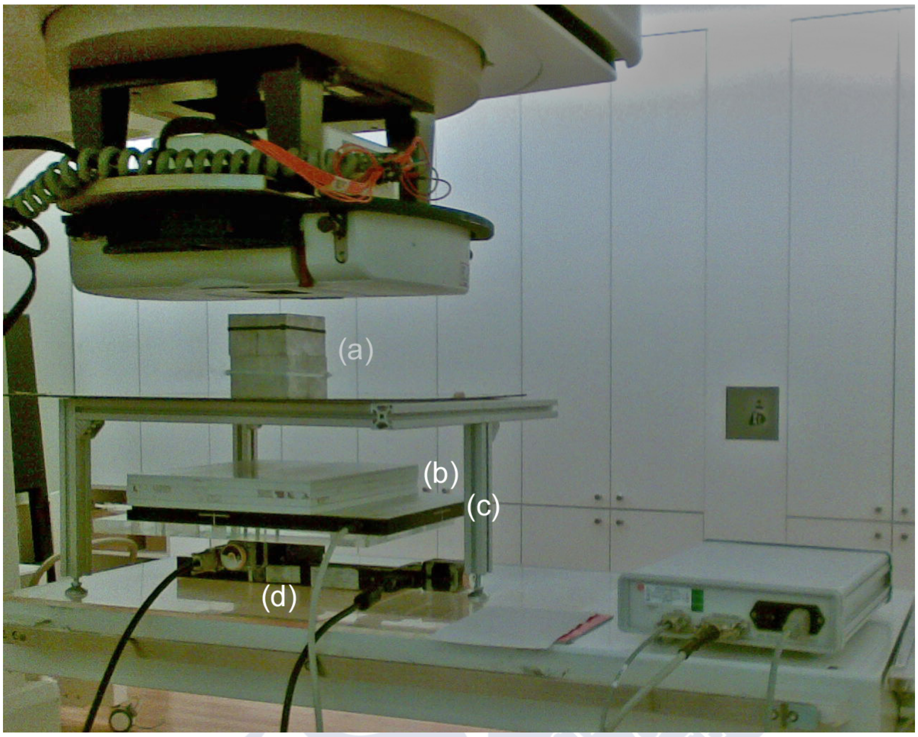

FIGURE 2.3: Experimental set-up for the measurement of the detector energy fluence response function F_ψ. The incident beam is collimated by two pairs of cerrobend blocks (a) conforming a 0.5 mm×0.5 mm pencil beam. The detector array (c) is mounted under slabs of water equivalent buildup slabs (b) on a stepper motorized platform (d) to scan one single detector and register F_ψ.

2.2.2 Monte Carlo simulation

The width of the measured fluence response function depends on the size and penumbra of the beam used to scan the detector, which should be as narrow as possible to reproduce the definition of Equation 2.1. The effect of measuring F_ψ for ionization chambers like those of MatriXX and PTW729 with a 0.5 mm×0.5 mm pencil beam is small due to the large size of these detectors. The peaks associated to the ionization chamber walls are softened, but the width of F_ψ is much closer to the real one than that obtained for a diode detector when using the same method, the reason being that in this case, the pencil beam size is not negligible compared with the detector size. The effect of the pencil beam size on the measurement of F_ψ was studied with Monte Carlo. The geometry used for the simulation of each detector array consisted in a set of 5×5 detectors located at a depth of 5 cm in a phantom. Ionization chambers were represented as simple air cavities within water for the simulation of MatriXX and within PMMA for the simulation of PTW729. For the simulation of the MapCheck2 array, geometry and materials of the diode detector were provided by the vendor, see Figure 2.4.

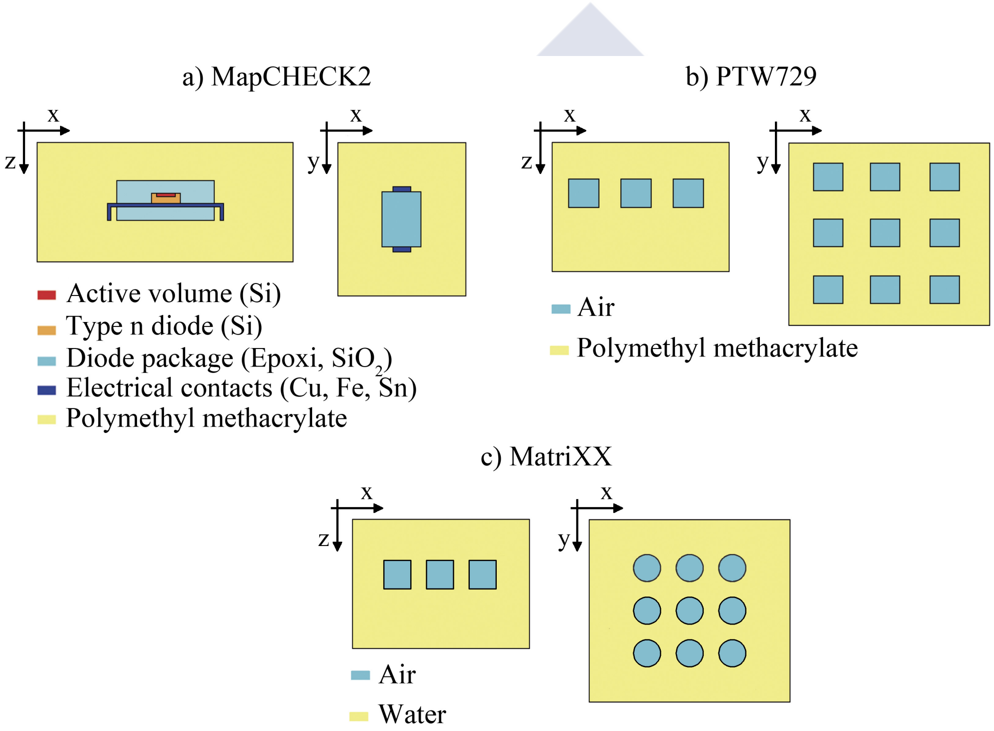

FIGURE 2.4: Scheme of the geometry and materials employed for the Monte Carlo simulation of a) the MapCHECK2, b) PTW729 and c) MatriXX (the buildup and backscatter plates of this device were approximated by water, given the similar mass and electronic density of Tecaran, RW3 and water).

Response functions were calculated, again for the central detector of our simulation geometries, using the EGSnrc code [59] and the C++ class library [60].

Transport Parameters

The range rejection variance reduction technique was applied to electrons with energies above 1 MeV, using 0.512 and 0.01 MeV cutoff energies for electrons and photons respectively. Presta I boundary crossing algorithm was employed with a skin depth of three elastic mean free paths, with the EXACT algorithm being employed beyond. Slowing-down of electrons was simulated through the condensed history method using the EGSnrc algorithm with a 0.5 default step-size and a maximum energy loss of a 25%. For the Bremsstrahlung processes, NIST cross-sections were employed together with the Koch-Moth photon angular sampling. The SIMPLE pair production angular sampling algorithm was chosen, while Rayleigh scattering, electron atomic relaxations and photo-electron angular sampling were neglected. Spin effects were considered for elastic scattering, and "Bound Compton scattering" activated to account for the electronic bounding effects and Doppler broadening according to the impulse approximation.

Response Functions

In a first step, fluence response functions were simulated with a source trying to reproduce the experimental pencil beam, which was represented by a bi-dimensional Gaussian spatially distributed photon source. EBT radiographic film dosimetry was used to estimate the size and penumbras of the pencil beams employed in the measurements, see Figure 2.5, yielding FWHM of (1.18 ± 0.11) mm and (1.49 ± 0.13) mm in the x and y axis respectively. The spectrum of the source was calculated at the axis of a 2 cm×2 cm field of a Siemens PRIMUS linac in 6 MV modality simulated with the BEAMnrc code [61] through the propagation of a monoenergetic electron source of 5.75 MeV and Gaussian focal spot of 1.5 mm FWHM. Fluence response functions calculated with this method found a good agreement with the experimental results, Figure 2.6, providing a verification

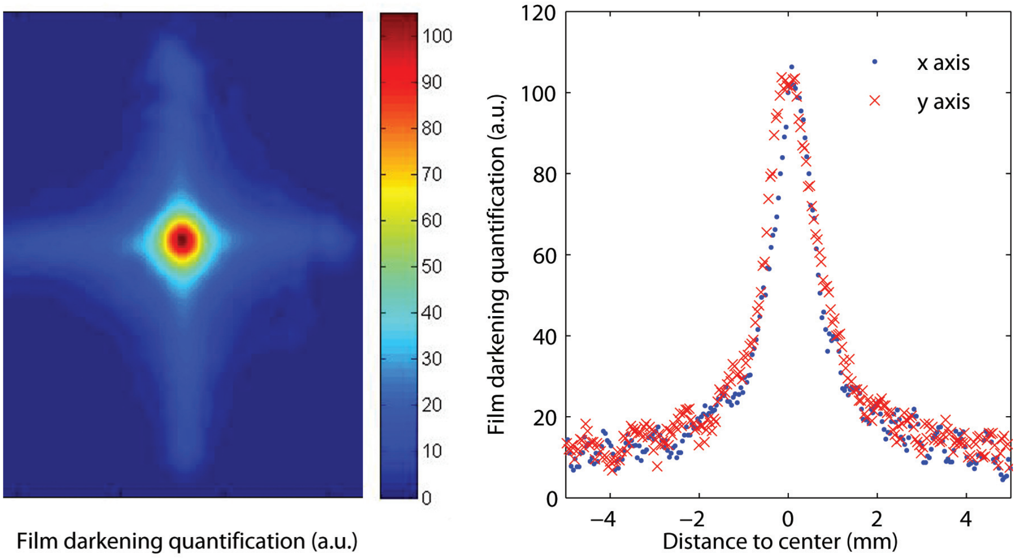

FIGURE 2.5: a) EBT gafchromic darkening under the irradiation of the 0.5 mm×0.5 mm pencil beam and b) film darkening quantification profiles, measured at the central x and y axis, for the determination of the collimated dose distribution.

for the Monte Carlo simulation procedure. The small discrepancies found around the ionization chambers wall are thought to be due to differences in the penumbra of the experimental and simulated radiation sources.

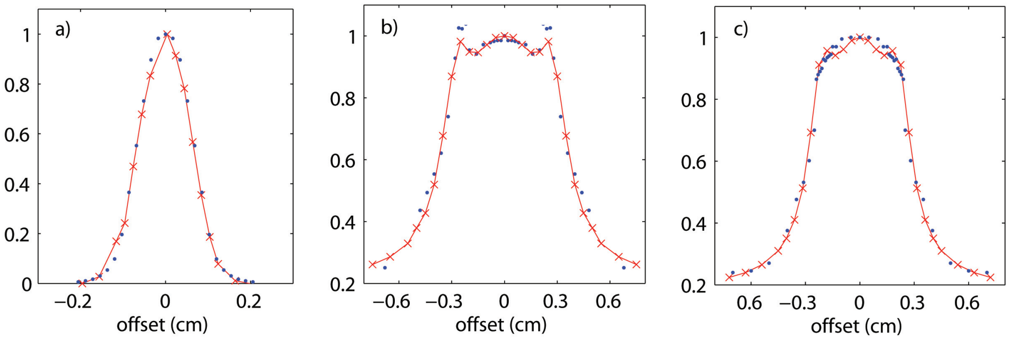

FIGURE 2.6: Measured (·) and Monte Carlo calculated (×), fluence spatial response functions from a 0.5 mm×0.5 mm pencil beam with a 6 MV modality in a Siemens PRIMUS linac spectrum, MapCHECK2 (a), PTW729 (b), and MatriXX (c).

The widening effect caused when measuring F_ψ with a 0.5 mm×0.5 mm pencil beam instead of an infinitesimal collimation was analyzed. Two dimensional F_ψ functions were calculated with a narrower radiation source: a square pencil beam of 0.1 mm side with the same 6 MV Siemens PRIMUS linac spectrum. Figure 2.7 (a) shows the response function obtained with this collimation for MapCHECK2 diode detectors in comparison with the measured F_ψ, while Figures 2.7 (b) and 2.8 (a) and (b) show the two dimensional response functions of the three detectors under study with a grid of 1 mm. The widths yielded by different measurements and simulations are summarized in Table 2.2, where we confirm the small but noticeable effect of the experimental 0.5 mm×0.5 mm pencil beam in the measurement of the ionization chambers response and an important widening in the diode response.

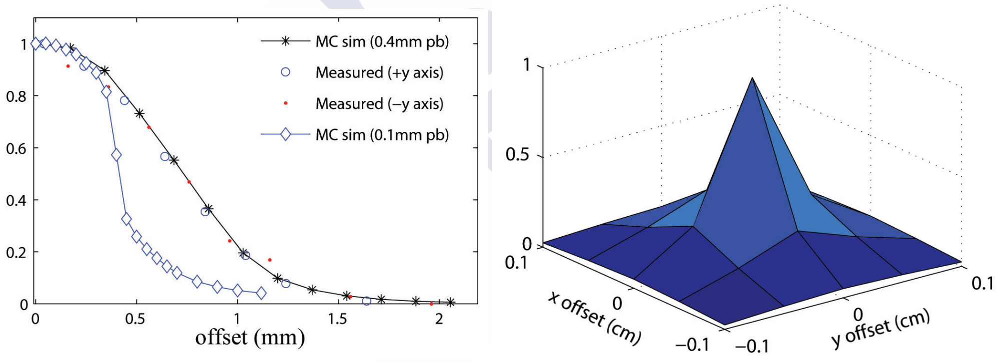

FIGURE 2.7: (a) Measured (○, ·) and Monte Carlo calculated (∗) MapCHECK2 F_ψ response function from a 6 MV Siemens PRIMUS 0.5 mm×0.5 mm pencil beam (pb). Monte Carlo calculated F_ψ from a 0.1 mm×0.1 mm pencil beam (⋄). (b) MapCHECK2 diodes two dimensional F_ψ calculated by Monte Carlo simulation with a square pencil beam source of 0.1 mm side.

Finally, a full Monte Carlo study was conducted on the energy dependence of the fluence response of air ionization chambers. An inverse relationship was observed between the energy of the beam and the height of the response peak associated to the ionization chamber wall, see Figure 2.9 (a).

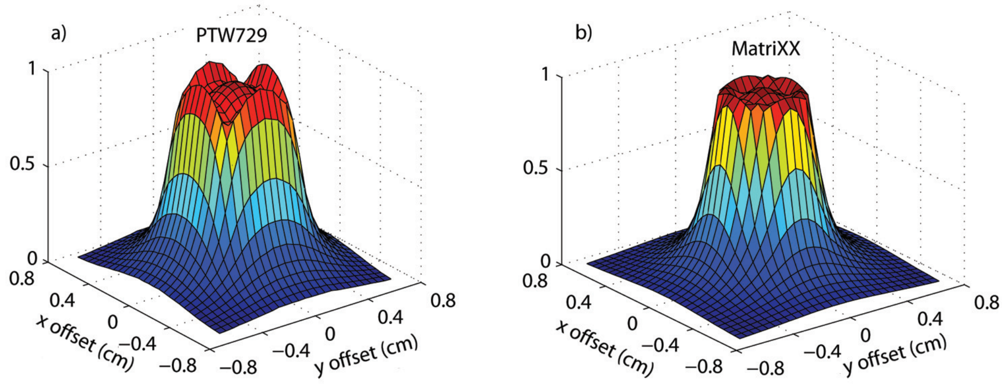

FIGURE 2.8: a) PTW729 and b) MatriXX ionization chambers F_ψ calculated by Monte Carlo simulation with a square pencil beam source of 0.1 mm side from a 6 MV Siemens PRIMUS linac.

F_ψ FWHM	**MapCHECK2**	**PTW729**	**MatriXX**
Measured (0.5 mm×0.5 mm)	0.146	0.872	0.665
Simulated (0.5 mm×0.5 mm)	0.140	0.821	0.648
Simulated (0.1 mm×0.1 mm)	0.083	0.700	0.640

TABLE 2.2: Width, expressed as FWHM in cm, of the detectors fluence response functions measured with a 0.5 mm×0.5 mm pencil beam, and width of the response functions simulated under the incidence of a 0.5 mm×0.5 mm and a 0.1 mm×0.1 mm pencil beams.

This behavior is understood to be a consequence of the decreased signal contribution from the secondary electrons released in the ridges between detectors (Figure 2.2) as the energy of the beam increases. We can also observe that the fluence response function F_ψ of an ionization chamber in a ^{60}Co beam and in a 6 MV linac beam are very close due to the similar average energy of these beam qualities. The relationship between the signal peak and the beam spectrum is also described in Figure 2.9 (b), where the normalized response peak is presented versus the inverse of the secondary electrons CSDA range for different spectra. A good linear correlation is observed between these two magnitudes.

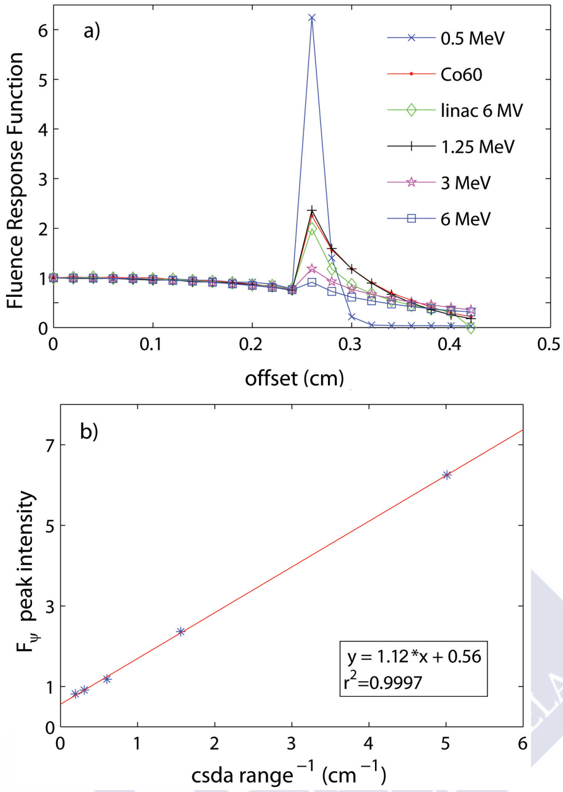

FIGURE 2.9: (a) F_ψ response function, normalized to central response, for a 0.5 MeV monoenergetic photon beam ($*$), ^{60}Co ($+$), 6 MV Siemens PRIMUS ($\circ$) and 1.25 MeV ($\cdot$), 3 MeV ($\times$) and 6 MeV ($\Box$) monoenergetic photon beams. (b) The response at the detector lateral wall position plotted against the inverse of the secondary electrons CSDA range.

2.3 Detector dose response function

Once the fluence response functions of MapCHECK2, PTW729 and MatriXX have been studied, we proceed to analyze the impact that using these detectors has on the measurement of dose distributions.

The dose deposition produced at a certain depth in a material under an incident photon energy fluence $\psi(x, y)$ can be written as the convolution/ superposition of that fluence with a dose deposition kernel $K(x, y, z)$ that accounts for photon scatter, primary and secondary electron transport and beam broadening with depth in the material.

$$D(x,y,z) = \int_{-\infty}^{\infty}\int_{-\infty}^{\infty} \psi(x',y')K(x-x',y-y',z)\,dx'\,dy' \tag{2.3}$$

If a detector is employed to measure this dose, the signal registered by the detector can be expressed as the convolution of the dose distribution at a depth z, calculated as in Equation 2.3, with a new detector response function $F_D(x,y)$, referred to here as 'dose response function'. If we note with the symbol $\otimes$ the convolution integral with respect to transversal coordinates, the response $S(x,y,z)$ of the detector is given as:

$$S = D \otimes F_D = \psi \otimes F_\psi = \psi \otimes K \otimes F_D \tag{2.4}$$

As the fluence response function F_ψ studied in the last section can be expressed as:

$$F_\psi = K \otimes F_D \tag{2.5}$$

The dose response function F_D can be obtained through the deconvolution of F_ψ with the dose deposition kernel, although it is important to observe that Equation (2.5) is only verified for realistic fluence response functions and dose deposition kernels.

In our work, the pencil beam dose deposition kernel was assumed to follow a single parameter Lorentz function, $K(x,y,z) = \frac{\lambda(z)}{2\pi}[x^2+y^2+\lambda^2(z)]^{-\frac{3}{2}}$ with $\lambda = 1.3$ mm for 6 MV photon beams at 5 cm in water [57]. F_D was then obtained with an iterative algorithm deconvolving the Monte Carlo calculated F_ψ functions (those obtained from the 0.1 mm×0.1 mm pencil

	MapCHECK2	**PTW729**	**MatriXX**
F_ψ	0.083	0.700	0.640
F_D	0.077	0.630	0.500

TABLE 2.3: Comparison of fluence and dose response functions widths, expressed as FWHM in cm.

beam exhibit more realistic widths and are thus more appropriate for the calculation of F_D) and the Lorentzian dose deposition kernel.

The dose response functions derived from the fluence response functions of MatriXX, MapCHECK2, and PTW729 detectors are shown in Figure 2.10. The dose deposition kernel corresponding to the measurement at 5 g cm^{-2} mass depth causes a reduction in the width of F_D compared to that of F_ψ, presented in Table 2.3.

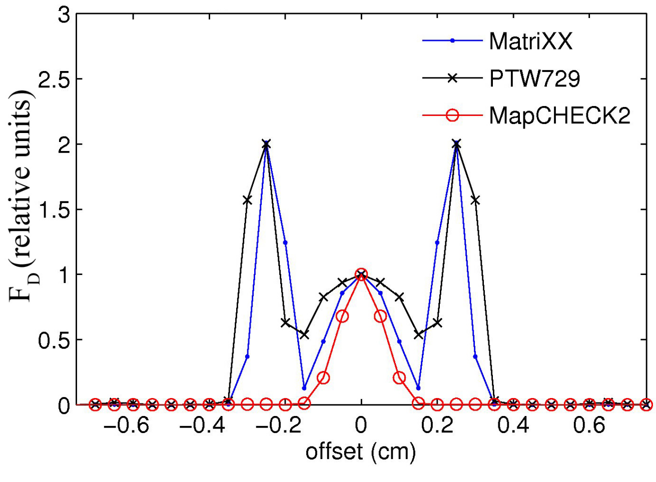

FIGURE 2.10: Dose detector response functions, F_D, obtained through the F_ψ dose kernel deconvolution for MapCHECK2 (○), MatriXX (·) and PTW729 (×) detectors.

Once the detector dose response function F_D has been calculated, the signal yielded by the detector for an arbitrary dose distribution can be modeled if a reference dose distribution with high spatial resolution is available [62].

2.3.1 Verification of the methodology

The methodology above presented can be used to test the capability of the devices to measure dose distributions with steep gradients, evaluating the importance of the volume averaging effect in ionization chambers. But before proceeding with this analysis for the three arrays under study, a consistency test was performed to check the presented formalism, trying to confirm that the convolution of the dose response function, F_D, of a detector with a reference dose distribution leads not only to an accurate representation of the detector signal, but also to a better result than what would be achieved through the use of F_ψ.

The F_D model was tested both in one and two dimensions using several radiosurgery radiation fields, with 1.8 cm×1.8 cm, 4.2 cm×4.2 cm and 11.2 cm×11.2 cm sizes, from a Siemens PRIMUS linac with a BrainLab MLC in 6 MV modality. Lateral profiles were measured with a PTW60016 diode detector in steps of 1 mm at 5 cm depth in water. These measurements were then used as reference dose distributions and convolved with the PTW729 ionization chambers F_D to obtain a model of the response of this device. The results, as well as those obtained through the convolution of the dose distribution with the F_ψ of the same detector, were then compared with real measurements of the PTW729 array for the same fields.

Figure 2.11 shows the results of these comparisons. The differences found between the models involving the convolution of F_ψ or F_D with the reference dose distribution are small, but we can observe an overestimation of the detector averaging effect when the convolution with F_ψ is performed. The accuracy achieved by the two models is quantitatively represented by

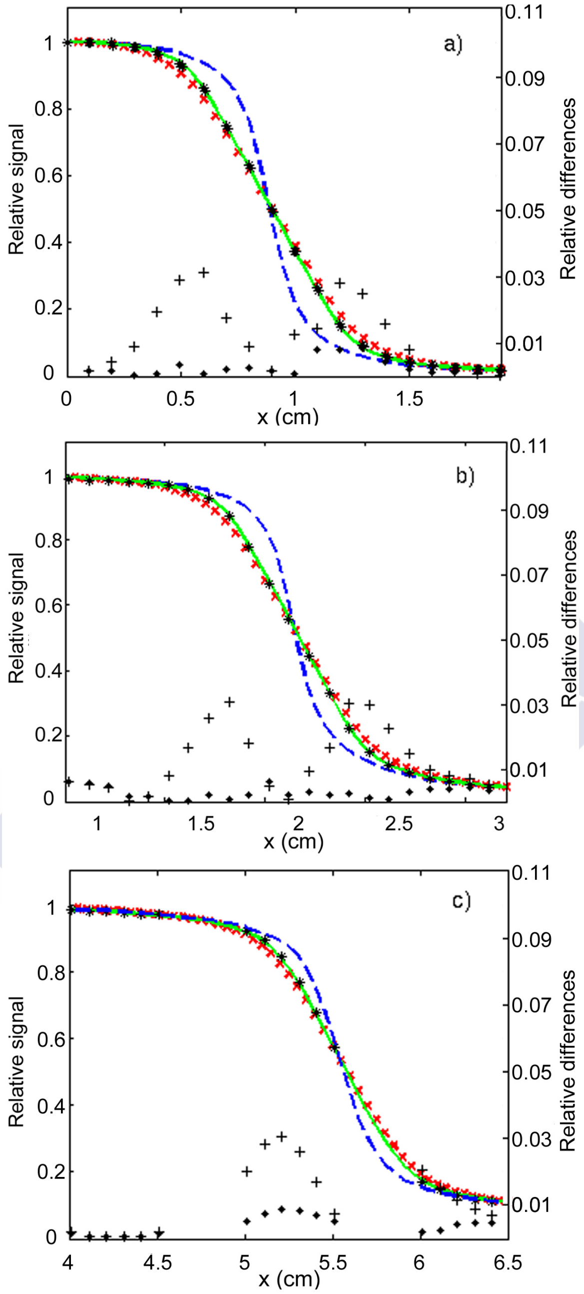

FIGURE 2.11: Radiosurgery lateral profiles for a) 1.8 cm×1.8 cm, b) 4.2 cm×4.2 cm and c) 11.2 cm×11.2 cm beam sizes. Measurements with PTW60016 diode (dashed line) are used as reference dose distribution to obtain detector response models through their convolution with F_D (solid line) and F_ψ ($\times$), for their comparison with PTW729 detector array measurements ($*$). Local relative differences for both convolution models F_ψ ($+$) and F_D ($\diamond$) are also shown.

the local percent dose differences between the models and the PTW729 measurements. These percent dose differences are also shown. A higher agreement was found in all the studied cases between the F_D model and the PTW729 measurements, with local relative deviations below 1%.

The same test was performed for a simple intensity modulated field made by superposition of three fields with the above mentioned field sizes, see Figure 2.12. In these case, the differences between the models involving the convolution of F_ψ or F_D with the dose distribution are smaller, probably due the positioning of the PTW729 array with respect to the radiation beam. In this measurement, the positioning of the PTW729 array caused the detectors to be placed either in flat dose zones or in the middle of penumbra regions, where the detector averaging effect is low and differences between the F_ψ and F_D convolutions are more difficult to detect. The discrepancies between the two models are minimal in these regions, as shown in Figure 2.11 for the single field study. A small but noticeable improvement is nevertheless observed for the convolution with F_D.

The tests here presented were considered to serve as a validation for the formalism presented in Section 2.3 for ionization chamber type detectors, and thus measurements were not repeated for the MatriXX array. Regarding MapCHECK2, this methodology should not be followed because the active area of PTW60016 diode (1 mm^2 circular) is bigger than that of MapCHECK2 detectors (0.8 mm×0.8 mm). We nevertheless rely on our methodology and use as diode F_D the function obtained from the Monte Carlo calculated F_ψ after deconvolution with the dose deposition kernel.

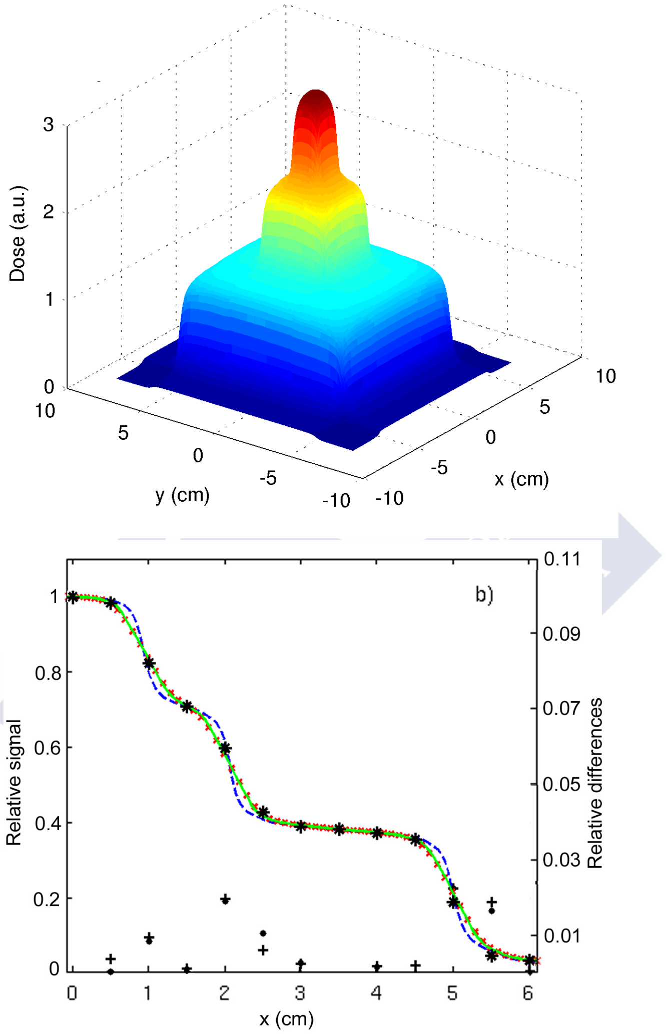

FIGURE 2.12: Radiosurgery IMRT beam created by the superposition of 1.8 cm×1.8 cm, 4.2 cm×4.2 cm and 11.2 cm×11.2 cm fields: a) Reconstruction of the beam in two dimensions as measured with a PTW60016 diode; b) Lateral profile measured with the PTW60016 diode (dashed line), PTW729 array measurements ($*$) and response models obtained through the convolution of F_ψ ($\times$) and F_D (solid line) response functions. Relative local differences between PTW729 measurements and F_ψ ($+$) and F_D ($\cdot$) models are also shown.

2.4 IMRT verification.

In this section we present a general study about the performance of the arrays for IMRT verification. We analyze how the response of the detectors affects the measurement of dose distributions, first disregarding the array detectors sampling and then taking it into account. Besides, we test the capability of the arrays to measure fluence variations arising from small leaf displacements in a treatment.

2.4.1 Effect of the detector F_D on IMRT verification.

The standard approach followed by clinical institutions for treatment verification consists in the comparison of a dose distribution obtained with a measurement system, here a detector array, with a reference dose map generally obtained from the Treatment Planning System. This comparison is usually performed through the Gamma function [63], a cost function that do not only considers relative dose differences between distributions but also their spatial matching. The Gamma function takes the following value:

$$\gamma(\boldsymbol{r_e}) = min\{\Gamma(\boldsymbol{r_e}, \boldsymbol{r_r})\} \ \ \forall\{\boldsymbol{r_r}\} \tag{2.6}$$

Where the Γ function is given by:

$$\Gamma(\boldsymbol{r_e}, \boldsymbol{r_r}) = \sqrt{\left(\frac{\mid \boldsymbol{r_e} - \boldsymbol{r_r} \mid}{\Delta d}\right)^2 + \left(\frac{D_e(\boldsymbol{r_e}) - D_r(\boldsymbol{r_r})}{\Delta D}\right)^2} \tag{2.7}$$

In the above equations $\boldsymbol{r_r}$ and $\boldsymbol{r_e}$ are the spatial coordinates of the reference and measured dose distributions, and ΔD and Δd are dose and distance tolerances. The matching of both distributions is measured by the percent of points with $\gamma < 1$.

The methodology of this section for the study of capability of the arrays on IMRT verification follows the clinical institutions' approach. Our analysis uses film dosimetry as reference dose distribution due to the higher resolution achieved with this dosimetry system, being more appropriate for its convolution with the dose response functions.

The effect that the response of the detectors has on the measurement of a dose distribution can be isolated from other effects, like the detector spacing in the array or the accelerator repeatability, through the comparison of the film dosimetry of an IMRT dose distribution with the model of the detector response for the same field. The response obtained through the convolution of the detector dose response function F_D and the film dosimetry leads to a detector model with the film sampling or grid, avoiding the effect introduced by the array discretization. The distribution so obtained would be equivalent to a set of array measurements displacing the device with the film grid step (*i.e.* 0.5 mm in our case) between consecutive measurements.

A demanding incidence of a real IMRT head-and-neck clinical treatment was chosen for this study. This modulated field consists of 38 different segments with sizes ranging approximately from 1 cm×3 cm or 0.5 cm×10 cm to 5 cm×20 cm, see Figure 2.13. This dose distribution includes steep gradients and flat regions, the maximum dose is 1.98 Gy and dose gradients range from 0 to 4.9 Gy/cm, being for our purpose considered as a representative IMRT dose distribution. A Siemens PRIMUS linac in 6 MV modality with an OPTIFOCUS multileaf collimator (MLC) was used to deliver the incidence at 0° fixed gantry position, with the detector arrays placed at 5 cm depth in a Solid Water phantom. The radiographic film dosimetry was performed at the same depth, leading to a dose distribution with 0.5 mm resolution suitable for the convolution with the detector dose response function, F_D, to evaluate the detector array measurement.

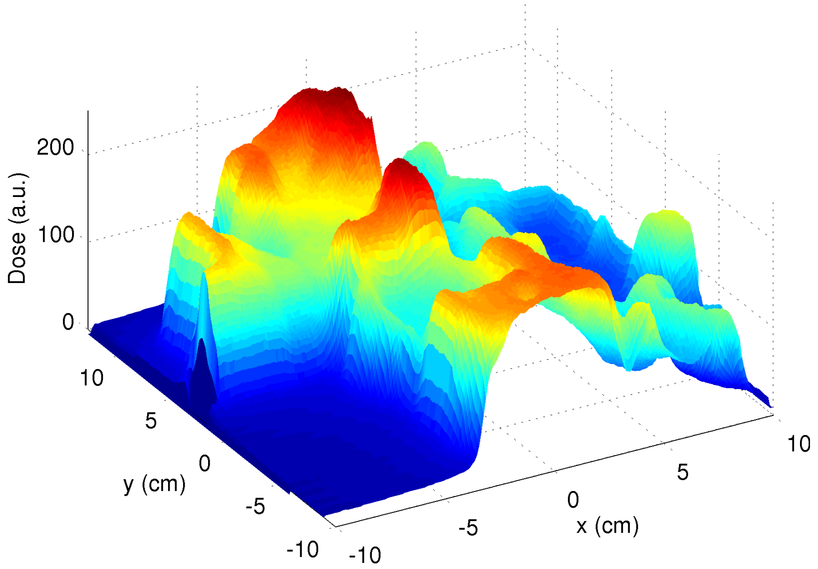

FIGURE 2.13: TPS Pinnacle 8.0h dose distribution calculated at a depth of 5 cm in water for the IMRT incidence used in our study (38 segments delivered at 0° gantry fixed position).

Models of the detector response to this incidence were obtained and compared with the film dosimetry by means of the Gamma function, see scheme in Figure 2.14 for clarification. This analysis allows uncoupling the effect of the detector response from other effects arising in the measurements with the real devices (noise from the film and array measurements, accelerator repeatability, etc) that can lead to reduced Gamma passing rates.

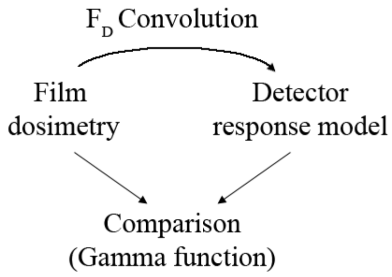

FIGURE 2.14: Scheme of the procedure followed to obtain a model of the detector response to the IMRT incidence. The effect of the detectors response is studied through the comparison of film dosimetry and the arrays response model by means of the Gamma function.

Figure 2.15 shows the percentage of points in the response models yielding Gamma values below one for different spatial and dose Gamma tolerances. A higher accuracy can be observed for the MapCHECK2 diode measurements, as expected given its narrow response function. On the other hand, the effect of MatriXX and PTW729 ionization chamber responses is higher, although it leads to passing rates above 96% for Gamma tolerances equal or above 1.5%-1.5 mm. We can here see how the detection type and active volume determine the behavior of a detector in the conditions of lack of lateral charged particle equilibrium found in IMRT. For the tolerance levels generally adopted in treatment verification programs, 1.5%-1.5 mm or higher, the ionization chamber averaging effect is however negligible when the overall fluence of an IMRT treatment incidence is analyzed.

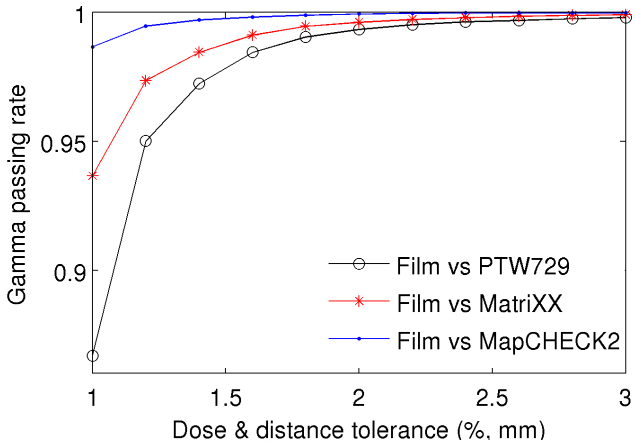

FIGURE 2.15: Gamma passing rates for different dose and distance tolerances, obtained from the comparison of the detector array response model of MapCHECK2 (·), MatriXX (∗) and PTW729 (∘) with the radiographic film dosimetry for the IMRT incidence under study.

The global performance of the detector arrays was also investigated through the comparison, again in terms of the Gamma function, of the arrays real measurements and the film dosimetry, which yields the passing rates presented in Figure 2.16(a). The effect of the above mentioned detector spacing and the linac, film and detectors repeatability are, in this way, included in the analysis. It is important to note that while Gamma evaluation in Figure 2.16 is restricted to the number of detectors in the array, values reported in Figure 2.15 were computed using a much higher number of points.

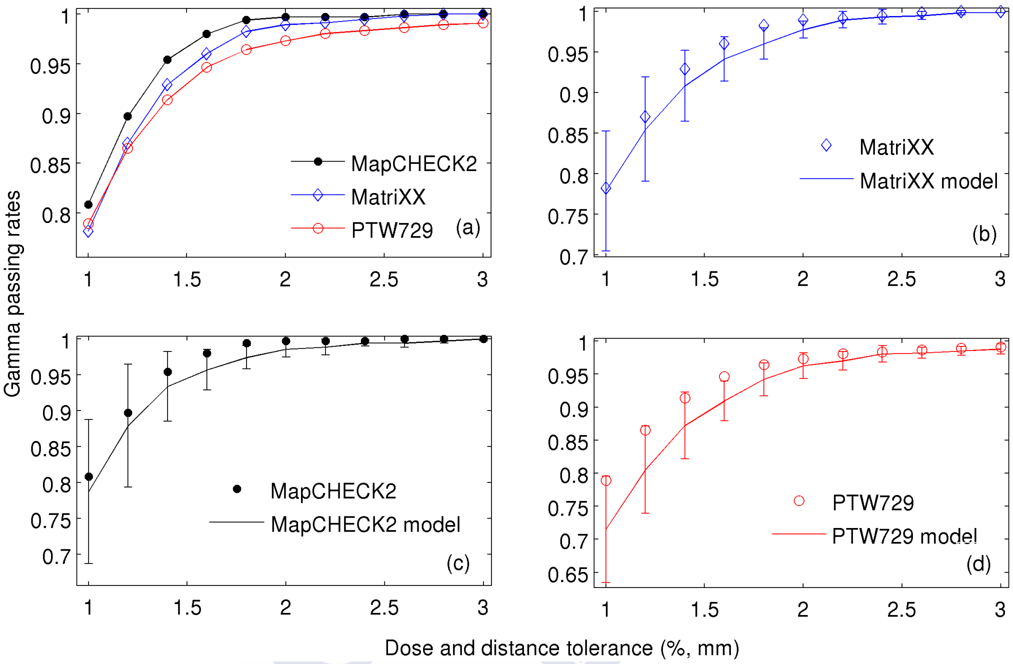

Figure 2.16: a) Gamma passing rates resulting from the comparison of the arrays measurement and film dosimetry for the studied IMRT dose distribution, MatriXX (◇), PTW729 (·) and MapCHECK (○). The arrays measurements are also compared with our response models, shown in full lines with uncertainty bars, for MatriXX b), PTW729 c) and MapCHECK2 d), respectively.

The arrays measurements were also compared with our response models, results shown in subplots b), c) and d) of Figure 2.16. Passing rates obtained for the film-array comparisons are included to serve as reference. Lower passing rates can be observed in the comparison of the arrays measurements and the response models. We should realize that Gaussian noise in film dosimetry, with an estimated 1.3% relative uncertainty, can contribute to increase the Gamma passing rates in Figure 2.16(a), as well as the sensitivity of the Gamma function to small spatial misalignments between dose distributions, with an uncertainty that was estimated to be around 0.5 mm. The uncertainty bars associated to the Gamma passing rates, which were obtained through the introduction of small displacements between dose distributions following a Gaussian distribution with 0.5 mm standard deviation, show that our response model is compatible with the detector array measurements. The reduced noise exhibited in the response model dose map compared to that of the original film map would explain the systematic slightly lower passing rates obtained for our models.

2.4.2 Sensitivity to fluence variations

As we have seen, dose verification consists in the comparison of a treatment planned dose with the dose distribution delivered by the linac to check whether the discrepancies encountered are relevant or not. Whichever it is the dosimetric system employed for that purpose, it is of major concern to study its capability to detect fluence variations, as this determines the thoroughness of the dosimetric verification performed with that dosimetric system.

In order to study the sensitivity to fluence variations of the detector arrays, different fluence changes were introduced in several segments of the IMRT head-and-neck treatment incidence presented in section 2.4.1. These intentional fluence variations were introduced mainly through leaf misplacements, an example of which is shown in Figure 2.17 (a), and changes in the monitor units of some of the segments. The fluence modifications, shown in Table 2.4 with the position of the fluence variations within the dose map, consisted on a leaf displacement of 4-5 mm in 5 of the 38 total segments, and a difference of 12 MU in one segment with no leaf displacement. TPS Pinnacle 8.0h dose calculations were performed to register the dose variations produced at 5 cm depth in water shown in Table 2.4.

X axis (cm)	Y axis (cm)	Monitor Units	ΔD_{max} (cGy)
$[-2, -1.5]$	$[9.5, 10.5]$	21	6.9
$[-0.5, 0.5]$	$[6.5, 11.5]$	12	19.0
$[5, 5.4]$	$[9.5, 10.5]$	53	18.4
$[7, 7.5]$	$[5.5, 6.5]$	34	8.2
$[-2, -1.6]$	$[1.5, 2.5]$	51	15.1
$[5.5, 5.9]$	$[-9.5, -10.5]$	57	17.9

TABLE 2.4: Position in the XY plane, change in Monitor Units and maximum dose difference registered by the treatment planning system for the fluence variations introduced in the IMRT incidence.

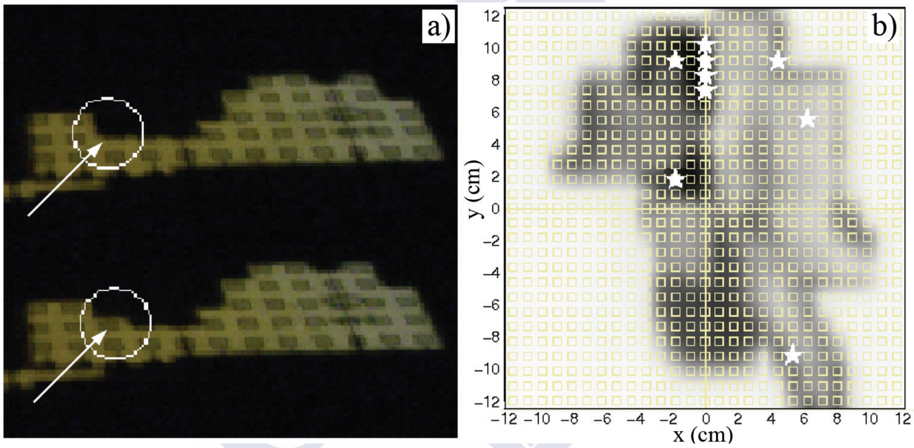

FIGURE 2.17: (a) MLC projection on the PTW729 surface showing a 5 mm leaf displacements in one segment, and (b) dose distribution, in gray scale, of the IMRT incidence under study: the stars positions indicate the spatial localization of the fluence changes introduced for the sensitivity study.

The sensitivity of the arrays to fluence changes was analyzed in a detector by detector basis. The signal variation registered in every detector when the array is irradiated by these two incidences (original and manually modified) was considered to be the most appropriate quantity to study, because the detector spacing in these commercial arrays does not allow the use of the Gamma function without dose interpolation, which we preferred to avoid. Several array measurements were acquired for the normal and modified incidences, to check the repeatability achieved in the signal changes arising from the intentional fluence perturbations. Although other perturbations were studied, only those summarized in Figure 2.17(b) and Table 2.4 are presented here due to the similar results obtained in all the studied cases.

The position of detectors exhibiting signal changes higher than 3% of the dose maximum are highlighted in Figure 2.18 for the three arrays. It can be observed that the fluence perturbations involve signal changes in a small number of detectors, and although a higher occurrence of signal variations can be noticed in MapCHECK2, not all these variations are located in positions where fluence perturbations were intentionally introduced.

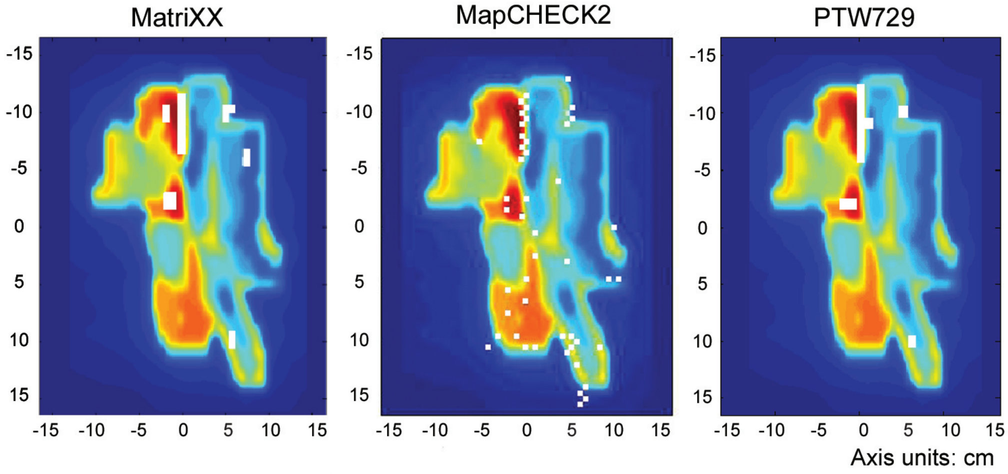

FIGURE 2.18: Comparison of arrays measurement for the normal and modified IMRT incidences. White squares show the position of the detectors exhibiting dose changes greater than 3% of the maximum dose.

On the other hand, the fraction of detectors having a threshold signal over the 10% of the array maximum signal and exhibiting signal variations greater than 1.5% of the maximum signal is 1.9% for MatriXX, 1.7% for PTW729 and 17% for MapCHECK2. This general analysis would not alert about the occurrence of critical perturbations, since many verification procedures consider as acceptable dose distributions exhibiting 5% of their total points in discrepancy with the reference distribution with a tolerance of 3% of the maximum dose [64, 65], something that would not happen in our case. The variation in the signal of the detectors was found to be clearly related with the fluence change, quantified by the product of the area in the segment suffering variations and the monitor units variation. This is shown in Figure 2.19, where the fluence perturbation is plotted against the change in array readout (the experiment was repeated twice for every device, and mean values are reported). We can see that the readout difference increases with the fluence change, although there seems to be an indication of a low sensitivity plateau for fluence perturbations below 20 MU×cm^2. A slightly higher sensitivity to the treatment fluence changes was observed for the air ionization chamber arrays, which is related with the larger effective (active) area covered by these devices, see Figure 2.20. The array fill factor was here quantified as the ratio of the area covered by the FWHM of the detector spatial response function F_ψ, referred to as active area in Figure 2.20, and the cell area defined by the detector grid. Fill factors amount to 55%, 44% and 8% for MatriXX, PTW729 and MapCHECK2 respectively.

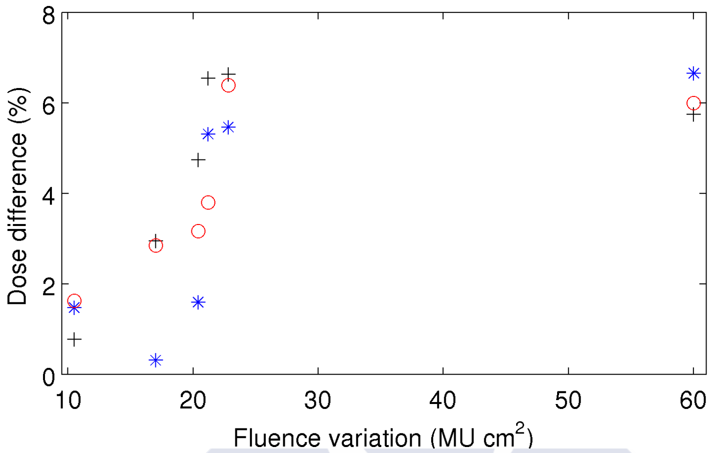

FIGURE 2.19: Percentage of change in detector response versus the magnitude of the induced fluence variations (mean value of repeated measurements) MapCHECK2 ($*$), PTW729 ($+$) and MatriXX ($\circ$).

Arrays with higher fill factors exhibit higher sensitivity to fluence variations which are not located at the detector center positions.

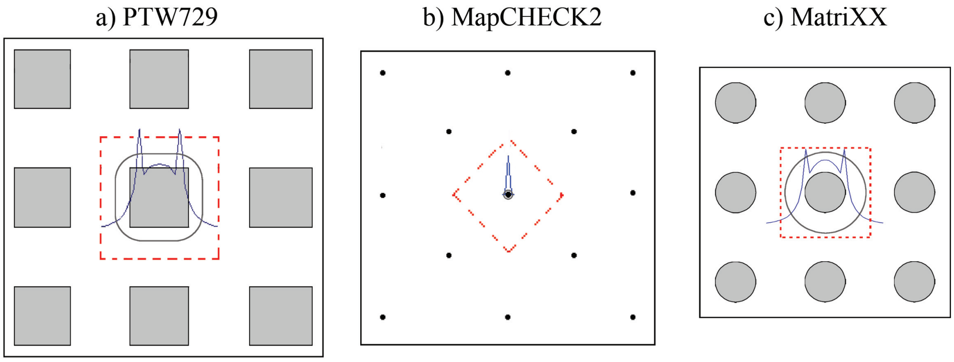

FIGURE 2.20: Schematic representation of the detectors active area and the array cell for the devices under study: a) PTW729 detectors represented by grey squares, b) MapCheck 2 detectors represented by points and c) MatriXX detectors represented by gray circles. The array cells are represented by dashed line squares and active areas are inscribed inside the solid line.

The sensitivity and predictivity of the arrays to fluence variations was also studied in terms of the Positive Predictive Value, PPV, a magnitude usually employed in radiology tests. The PPV is defined for a given threshold as the number of 'true' positives to total positives ratio. In our case, the 'true' positives stand for the number of detectors that register a signal change that is actually related with any of the intentionally introduced fluence variations, and the total positives is the number of detectors exhibiting readout variation above threshold.

Figure 2.21 shows the higher PPV values obtained for the ionization chamber arrays (as expected from Figure 2.18), while higher percentages of false positives were found for the diode array. It should be however noticed that for detectability thresholds above 5% of the maximum dose, the number of detectors included for MapCHECK2 PPV calculations is small: PPV values differing from unity are due to two or three detectors usually located at the beam penumbras. On the other hand, PPV values are observed to

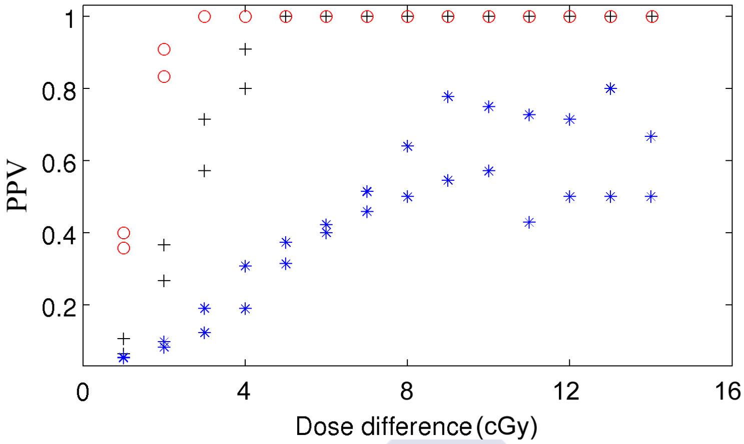

FIGURE 2.21: Positive Predictive Value obtained at different detectability thresholds for MapCHECK2 ($*$), PTW729 ($+$) and MatriXX ($\circ$).

decrease sharply when detectability thresholds are below 1%, 2% and 4% of the treatment maximum dose for MatriXX, PTW729 and MapCHECK2 respectively.

2.4.2.1 Sensitivity to MLC leaf displacements

The different results obtained for the ionization and diode arrays motivated a specific investigation about the MapCHECK2 'false' positives.

The hypothesis that these signal variations could due to (small) misspositionings of the multileaf collimator between measurements was investigated. The collimator employed in the treatment under study has a leaf positioning accuracy around ∼1 mm, which would lead to small fluence variations in the segments delivered within a treatment that could be detectable by the diodes.

In order to demostrate this, the MapCHECK2 array was irradiated with a 8 cm×12 cm Siemens PRIMUS linac field. The array was placed to have a row of diode detectors aligned with the penumbra of the beam to register the maximum signal variation arising from the MLC leaf positioning mechanical accuracy. Two sets of 10 measurements were performed, delivering 50 MU per irradiation, the first one maintaining the MLC leaf positions steady between measurements, and the second by moving the leaves to conform the field before each irradiation. This repeatability study also allowed discarding drastic miss-calibrations in any of the 1527 detectors.

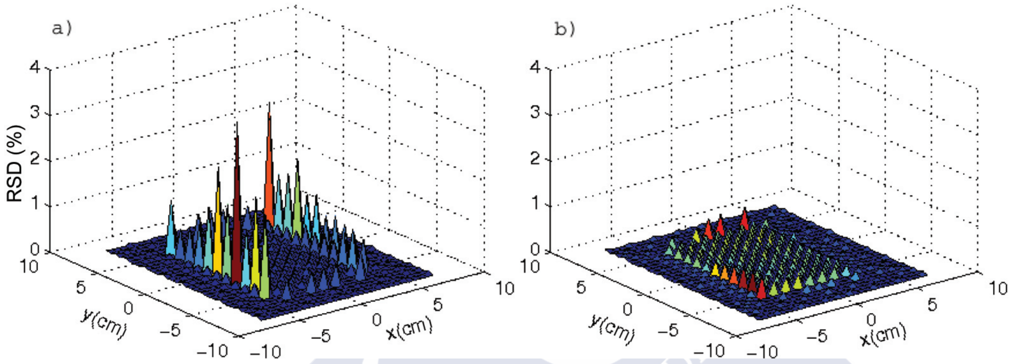

FIGURE 2.22: Relative standard deviation (rsd) obtained in 10 MapCHECK2 measurements of a 8×12 cm^2 Siemens PRIMUS field with 50 MU when: (a) the field is conformed before every irradiation and (b) leaves are kept in steady positions.

The set of measurements with the MLC leaves remaining steady exhibited a relative standard deviation, rsd, with respect to the maximum signal in the array for this field, that reached a 0.5%, while the measurements involving the leaves repositioning showed rsd values up to a 3.5% for the detectors located at the beam penumbra, as shown in Figure 2.22.

When sets of two measurements are compared, as it is done to obtain the signal difference registered when the array is irradiated by the normal and modified incidence, rsd values up to 0.9% are observed for the study with no MLC movements, while variations up to 7% are observed when leaves are moved to conform the same beam between measurements. The sensitivity of MapCHECK2 diode detectors to leaf position variations of ∼1 mm was thus confirmed, and the lower PPV values obtained for MapCHECK2 compared to ionization chamber arrays could be then associated with the detection of systematic small leaf displacements between segments employed in the repeated deliveries of the studied incidence. It could be then argued that the high resolution and sensitivity of the diode array can result counterproductive for treatment verification. The low fill factor of these devices can lead to important fluence changes involving large signal deviations in a small number of diodes, making difficult to distinguish these perturbations from 1 mm leaf positioning errors of lower relevance. This would be the case of the second modification, see Table 2.4, where only two diodes show a discrepancy higher than 3%, see Figure 2.18. On the contrary, ionization chambers volume averaging effect minimizes the signal variations originated from MLC displacements of ∼1 mm. The discrepancies exhibited by the ionization chambers located in regions without important fluence perturbations are thus smaller, leading to the higher PPV values observed in our study. This lower sensitivity to small leaf misplacements makes the ionization chamber arrays verification more predictive to important fluence perturbations.

2.5 Conclusions

In this chapter we have presented a study about detector arrays for dosimetric treatment verification, focusing on PTW729, MatriXX and MapCHECK2 commercial solutions.

Energy fluence detector response functions, F_ψ, were measured in water for the three arrays under 6 MV linac modality and with a 0.5 mm×0.5 mm scanning pencil beam. Monte Carlo response functions were also calculated reproducing the experimental measurements and allowing a Monte Carlo energy dependence study and the calculation of more realistic fluence response functions for narrower collimation. Dose detector response functions, F_D, were then calculated as the deconvolution of F_ψ and the dose deposition kernel for the depth at which the fluence response function was measured. A formalism was then presented to model the response of detector arrays to arbitrary incident fluences through the convolution of the corresponding reference dose distribution and the detector dose response function. This model, satisfactory validated in several radiosurgery beam measurements, was shown to avoid the overestimation of the detector effect that would result from the convolution of the dose distribution and the fluence response function.

Our model served to isolate and study the effect of the detectors response on the measurement of a representative IMRT dose distribution. The results show that highest accuracy is achieved with diodes, although the perturbations introduced by the ionization chambers due to volume averaging or the lateral wall response peak remain negligible for Gamma function tolerances higher than 1.5%-1.5 mm. The global performance of the devices including detector spacing was also analyzed, pointing out the impact on the Gamma test of small spatial misalignments and noise in the dose distributions under comparison.

Finally, the sensitivity of the arrays to treatment fluence changes was studied in a detector by detector basis. A correlation was found between fluence variation and detectors response above certain threshold. The Positive Predictive Value (PPV) indicator was also calculated showing a higher predictivity to fluence variations in the ionization chamber arrays for all detection thresholds. The larger sensitive area of ionization chambers would allow these devices to effectively detect fluence variations located at certain distances from the detectors positions. The point-like response of diode detectors, combined with the diode arrays sampling leads to a low fill factor that does not allow the detection of some fluence variations, depending on their position, which could be only avoided with a drastic decrease in the device detector spacing, a situation that might be technically unachievable. Diodes are however more sensitive to small leaf positioning errors, as those arising from the MLC mechanical accuracy, while ionization chambers cannot detect them due to their volume averaging effect. This sensitivity to smaller fluence variations lowers the predictivity of the MapCHECK2, with respect to that of ionization chamber arrays, to more important fluence variations, like the 0.4 cm×1 cm fluence perturbations studied in our work. It is worth pointing out that the high sensitivity of MapCHECK2 to small fluence leaf displacements would not be reflected in Gamma passing rates using standard tolerances, while its lower sensitivity to large fluence perturbations could have indeed consequences in Gamma passing rates for conventional tolerances.

Our results show that the ideal detector array for IMRT verification would not necessarily require point-like detectors, as the averaging effect of relatively large detectors, for example air ionization chambers, enhances the sensitive area of the device compared to that of the studied diode array. Although it is clear that small detectors yield a more accurate reproduction of dose in general IMRT conditions, the task of increasing the number of detectors in an array to obtain a high fill factor presents great design and production difficulties. On the contrary, the averaging effect of air ionization chambers implies that a high fill factor can be achieved in an array constructed with an affordable amount of detectors. Ionization chamber arrays can thus offer a good sensitivity to fluence variations across the whole area of a detector, which is the most important requirement of any dosimetry system employed for treatment verification.

The methodology followed in this work to study the arrays under the same conditions and through a common analysis allowed us to obtain comparable results to study the differences between them. With this work we have contributed to the understanding of IMRT QA requirements, helping to focus on the improvements that can lead to optimal detector array designs.

Considering our results, a detector array involving medium size detectors, for example ionization chambers with cross section areas of $\backsim$ 0.25 cm^2, and distance between detectors leading to fill factors around 50% or above would be an appropriate tool for IMRT treatment verification. Recent detection technologies, like LICs, may allow the construction of arrays with high sensitivity and fill factor. When our study was addressed, several works had been already published related with these kind of devices, first for a LICs linear array [66–68] and lately for a two dimensional LIC array covering a 100% sensitive area of 3 cm×2 cm [69]. Linear arrays involving LICs had been developed by PTW-Freiburg for field verification purposes [66] and by mid-2012, PTW-Freiburg also began to commercialize a 2D LIC array, the Octavius 1000 SRS®, with Stereotactic RadioTherapy and Radiosurgery verification purposes. The latter device covers a 10 cm×10 cm total area, with a 100% fill factor in an inner area of 5.5 cm×5.5 cm and a $\simeq$ 25% fill factor beyond. This device became commercially available well after this study was completed, and therefore could not be investigated here. Although only a few studies have been published to this date dealing with the characterization of this commercial solution [70–72], the knowledge currently available about this detection technology and the potential capability to build LIC arrays with small detectors size (cross section areas $\backsim$ 0.04 cm^2, active volumes $\backsim$ 0.002 cm^3) and full sensitive areas (100% fill factor) results very promising for the field of radiosurgery treatment verification.


USC
UNIVERSIDADE
DE SANTIAGO
DE COMPOSTELA

Chapter 3

Development of an ESR alanine dosimetry system for the study of nonstandard fields

3.1 Principles of alanine/ESR dosimetry

3.1.1 Introduction to alanine dosimetry

Alanine, an organic compound, is one of the simplest alpha amino acids present in nature regarding molecular structure, being $CH_3CH(NH_2)COOH$ its chemical formula[1]. Under the incidence of ionizing radiation, radicals are formed in alanine molecules, its number being proportional to the absorbed energy for a wide range of doses, and this property is the basis of alanine dosimetry.

There are several stable radical species that are now known to be present in irradiated alanine crystals. During many years the predominant radiation

---

[1] The amino acids that have both the amine and carboxylic acid groups attached to the first (alpha-) carbon atom have particular importance in biochemistry and they are known as alpha-, or α-amino acids.

induced reaction was thought to be the removal of the amine group, leading to the $CH_3CHCOOH$ radical with an unpaired electron. Additionally, a radical species formed by hydrogen abstraction from the central carbon atom and another minority radical species not yet unambiguously identified have been observed in irradiated alanine, Figure 3.1. Some aspects like the radicals radiation response, their thermal properties and differences in fading properties between radical species are still under study [73, 74].

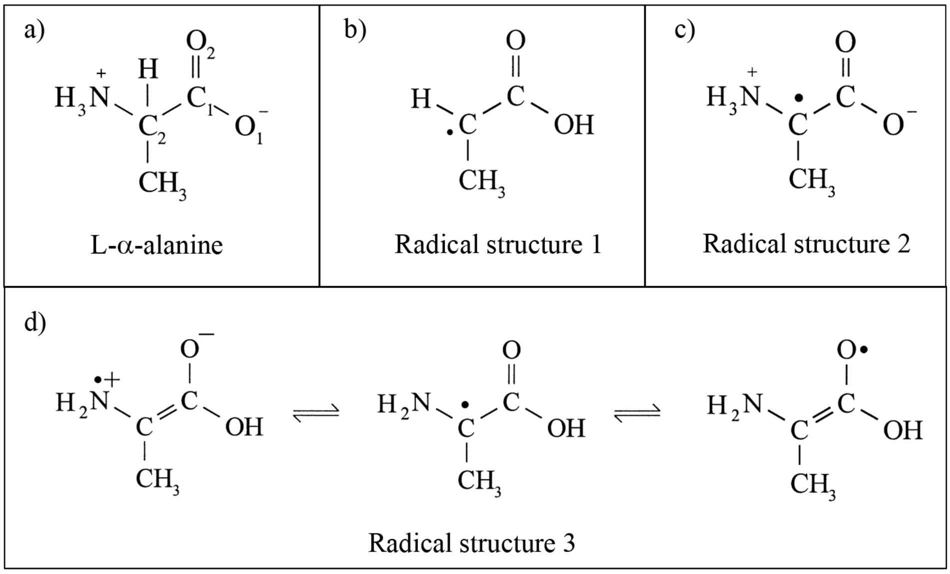

FIGURE 3.1: a) Alanine molecular structure, b) Alanine radical R1 formed by the deamination of alanine, c) Alanine radical species R2 and d) Alanine radical species R3 [73].

The presence of unpaired electrons in the alanine radical species can be measured by electronic spin resonance spectroscopy, ESR, which yields a signal consisting in the overlapping of the spectra from all the radical species present in the sample, with an amplitude proportional to the total number of radicals. The measurement of radical concentrations by ESR can be thus used for the determination of the absorbed dose in the alanine sample

$D_{al,Q}$.

$$(I_{ESR})_{Q,T} = K \cdot G_{Q,T} \cdot m \cdot D_{al,Q} \tag{3.1}$$

Where I_{ESR} is the intensity of the ESR alanine signal, K is a proportionality factor that depends on the spectrometer sensitivity, m is the mass of the dosimeter and $G_{Q,T}$ is the alanine radiation yield, defined as the number of radicals generated per unit of absorbed energy in the alanine for a certain beam quality Q and irradiation temperature T.

The demonstration around 50 years ago by Box and Freund, Bradshaw *et al.* and Rotblat and Simmons [75–77] that the alanine amino acid could be used as a solid state dosimeter by electronic spin resonance spectrometry was the first step of a successful research line that soon improved the technique for high precision measurement [78] and established the alanine/ESR system as a reference dosimeter for industrial irradiation applications in the kGy dose range. During the 1990s, several metrology institutions like the National Physical Laboratory, NPL, in the UK, and the National Institute of Standards and Technology, NIST, in the USA, developed the alanine/ESR technique as secondary standard for absorbed dose to water in the kGy dose range [79, 80].

The intrinsic properties that make alanine a good dosimeter for industrial applications also stand for its use as a reference dosimeter in radiotherapy. However, the signal to noise ratio exhibited by alanine dosimeters drops drastically in the therapy dose range (approximately from 1 to 20 Gy), increasing the sensitivity requirements of the spectrometer and making unavoidable to keep thoroughly controlled all the influence quantities that are involved in the alanine/ESR dosimetry.

As it was commented in the introduction, the recommendation of achieving a global accuracy of ±5% in the delivery of absorbed dose to water to target volumes of radiotherapy is usually established in the quality assurance documents emitted by international institutions. Taking into account the multiple steps conforming the radiotherapy chain and their contribution to the final uncertainty, this is usually translated into a desired uncertainty of 1-1.5% [18, 43] for the determination of absorbed dose to water in reference conditions. Lowering the uncertainty of the alanine dosimetry in the therapy dose range to the limits required by radiotherapy applications became the objective of the many studies performed during the last decade. These research efforts ended up successfully, being several the metrology institutes worldwide that nowadays use alanine/ESR dosimetry as secondary standard in the therapeutic dose range: NPL, NIST, Physikalisch-Technische Bundesanstalt, PTB, in Germany, etc. In Spain no laboratory or institute had yet developed an alanine dosimetry service, and the alanine dosimetry campaigns that are performed in this country must be sent abroad to get the dosimeters readout and certificates. The possibility of developing an alanine dosimetry service was opened in 2011 at the Universidade de Santiago de Compostela with the creation of a secondary standard laboratory of absorbed dose to water at the Radiation Physics Laboratory and the availability of an ESR laboratory in-house (Servicio de Resonancia Magnética, Rede de Infraestruturas de Apoio á Investigación e ao Desenvolvemento Tecnolóxico da Universidade de Santiago de Compostela).

The solid alanine dosimeters manufactured nowadays generally consist in a polycrystalline α-alanine aggregate sealed by a high melting point paraffin that serves as a partial binder. Dosimeters can be produced under different presentations including pellets, rods, cables, films and pure alanine powder without any binding process [81], being the pellets the physical presentation chosen for our work due to some advantages that will be later exposed.

Once a device has been demonstrated to be able to measure, either directly or indirectly, a magnitude related with ionizing radiation, in our case absorbed dose to water, the most important properties that characterize the dosimeter are: dose linearity, dose rate dependence, energy dependence, response isotropy and the resolution of the detector. All these properties, affecting the repeatability and global uncertainty of the measurement, will be presented here for alanine.

1. **Unusual stability of the radiation-induced radicals**

   The formation of radiation induced radicals in organic substances is quite a general process and there are many substances that could be investigated as potential dosimetry detectors. The temporal evolution of radicals in organic substances after irradiation is however an important characteristic that conditions the ESR signal acquisition procedure and affects the signal repeatability, and it is here where the alanine amino acid makes the difference. The discovery that polycrystalline alanine is among the organic substances with the highest stability in their radical species converted alanine in the most used molecule for ESR dosimetry. Alanine radiation induced radicals are nevertheless not perfectly stable and tend to recombine slowly, leading to a fading in the ESR signal with time. Radical recombination depends on several correlated parameters like the water content of the alanine probes (related to ambient air humidity) and the dosimeters storage temperature. Since the paraffin binding partially isolates the alanine aggregate from the ambient air, these effects vary with the dosimeters manufacturing process. As a guide, rates of fading of approximately a 4% over a 17 month period under normal laboratory conditions, 20 °C temperature and 55% relative humidity, have been reported for the alanine dosimeters in pellet presentation that are employed in this work [82].

2. **Linear signal response over a wide range of radiation doses.**

   The linear relationship between absorbed dose to water and the concentration of radicals in an alanine probe is a feature that further simplifies the use of alanine as a dosimeter. The calibration procedure that allows to measure absorbed dose to water from alanine

ESR signal intensities involves the determination of the proportionality factor linking these two magnitudes. In practice, this factor can be calculated as the slope, $C_{Q,T}$, of the linear fit of dose-ESR signal intensities for a batch of alanine dosimeters that have been irradiated to different values of dose to water, at temperature T and under a beam quality Q. The relationship between absorbed dose to water and absorbed dose to the alanine is directly obtained taking into account Equation 3.1:

$$D_{w,Q} = C_{Q,T} \cdot \frac{(I_{ESR})_{Q,T}}{m} = C_{Q,T} \cdot K \cdot G_{Q,T} \cdot D_{al,Q} \tag{3.2}$$

It should be noted that an exponential saturation in the concentration of radicals is well known to occur at high doses [77], but signal-to-dose linearity has been observed for dose values between 0.5 Gy and 5 kGy (residuals below 1%) [83], being thus guaranteed for the therapy dose range covered in this work.

3. **Small energy and dose rate dependence**

The response of a dosimeter can be generally defined as the ratio of the detector reading (noted by M in Chapter 1, here ESR signal intensity, I_{ESR}), and the value of the magnitude of interest, in our case absorbed dose to water, D_w. This response usually changes with the energy of the radiation beam, represented for high energy photons by the beam quality index Q (see Chapter 1). Since the detector is always calibrated at a certain energy/beam quality Q_0, correction factors have to be applied to determine the dose at different energies/beam qualities. The factor to correct for the change in the energy response at different beam qualities, calculated for the same value of absorbed dose to water at Q_0 and Q, can be expressed as:

$$F_{Q,Q_0} = \frac{(I_{ESR}/D_w)_Q}{(I_{ESR}/D_w)_{Q_0}} \tag{3.3}$$

This expression is equivalent to the first identity of Equation 1.10, with the beam quality correction factor k_{Q,Q_0} given by the inverse of F_{Q,Q_0}. But we can better understand the alanine energy dependence if we consider the proportionality between the detector reading, or ESR signal intensity, and the absorbed dose to alanine, Equation 3.1, which leads to the expression:

$$F_{Q,Q_0} = \frac{G_Q}{G_{Q_0}} \frac{(D_{al}/D_w)_Q}{(D_{al}/D_w)_{Q_0}} = \frac{C_Q}{C_{Q_0}} \tag{3.4}$$

We can here identify two effects contributing to the energy dependence and changing the slope in the alanine calibration curve, C_Q: one given by the change in the alanine radiation yield with the beam quality, and the other given by the change in the alanine to water absorbed dose ratio with the beam quality. Regarding this latter effect, and considering alanine dosimeters as medium size detectors when compared with the range of secondary electrons in that material, Burlin theory states that the deposition of energy in the detector is due to electrons generated both in the surroundings of the dosimeter and in the dosimeter itself [15]. Thus, stopping power of secondary electrons and mass absorption coefficients of the incident photons need to be considered when studying the energy dependence of alanine dosimeters. The energy dependence of alanine to water ratios of these two magnitudes is shown in Figure 3.2.

In practice, alanine to water dose ratios are usually calculated by Monte Carlo simulation, and the global energy dependence of the alanine is experimentally determined through the construction of calibration curves at different beam qualities. Variations in the alanine radiation yield with the beam quality can be thus inferred from them.

For X ray beams in the kV energy range, the alanine response is lower than that at ^{60}Co beams, ranging from 27% to 6.5% under-response for X ray beams from 50 kV to 200 kV [81]. Monte Carlo calculations

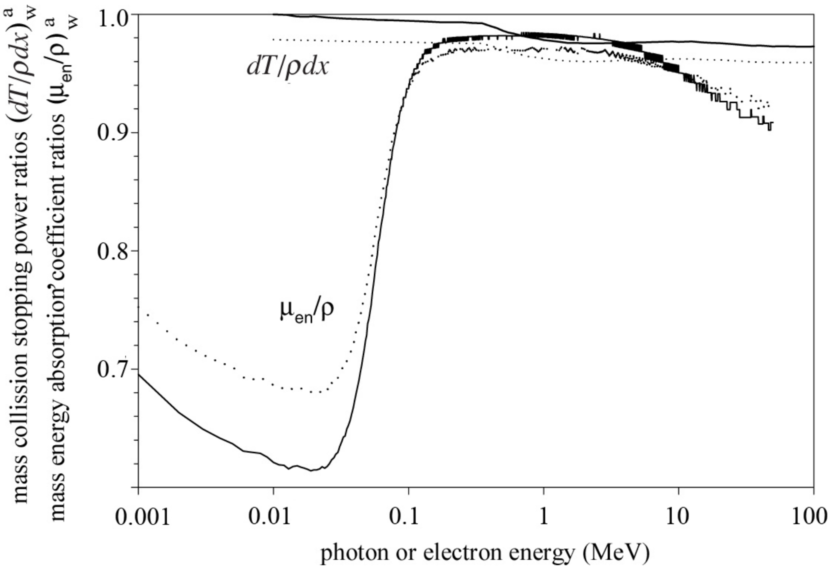

FIGURE 3.2: Alanine to water stopping power ratios and mass absorption coefficients ratios considering only alanine, solid line, and the dosimeter material including alanine and binder, dotted line. Results for alanine pellets manufactured by Bruker (Bruker Corporation, Billerica MA, USA) [84].

show that alanine to water mass energy absorption coefficients ratios cannot account for all the effect, and at least 5.7% of the under-response at 150 kV has been found to be due to variations in the radiation yield. Recent works offer however different results about the contribution of the two factors involved in the energy dependence to the global variation of the alanine response [85, 86].

On the other hand, in megavoltage photon beams from 6 to 25 MV, a global under-response of approximately a 0.6% is observed in alanine with respect to that in ^{60}Co beams, which is mostly due to variations in the radiation yield because no significant energy dependence is found between linac megavoltage modalities [87].

In summary, we can say that alanine can be considered to be nearly water equivalent for photons with energies above 100 keV. This energy dependence is small when compared with that of other detectors like ionization chambers, what will involve smaller uncertainties related with beam quality variations in alanine dosimetry.

On the other hand, no significant dose rate effects have been observed for alanine dosimeters irradiated to dose rates below 3 Gy/s [88]. The dose rate can be thus completely disregarded in alanine dosimetry campaigns performed in the therapy range.

4. **The relatively small physical size of the dosimeter.**

   Alanine dosimeters can be produced in many physical presentations, although manufacturers like Harwell Dosimeters Ltd., Gamma Service (Synergy Health Radeberg GmbH) and metrology institutes producing their own dosimeters like the NPL, have usually chosen cylindrical pellets of 0.5 cm diameter and 0.3 cm height. Even though smaller pellets are manufactured, this detector size, with a volume of 0.06 cm^3, is small if compared with many of the ionization chambers usually employed for radiotherapy measurements (Farmer type chambers $v \approx 0.6$ cm^3, Semiflex chambers $v \approx 0.3$ cm^3). Small detector sizes are required for measurements in the steep dose gradients that can be found in small and intensity modulated radiotherapy fields, so that field disturbance effects like volume averaging are minimized. In this context, alanine dosimeters can be appropriate detectors for measurements in new radiotherapy techniques where ionization chambers are the most operative detector for routine measurements. Alanine can provide here an alternative method for the determination of absorbed dose to water in, for example, dosimetry audits and intercomparisons. Additionally, alanine can be used for the determination of beam quality correction factors associated with ionization chambers in non standard fields, which has become a very important step of quality assurance now that many modern radiotherapy machines cannot deliver the 10 cm×10 cm field required for the establishment of conventional calibration reference conditions.

5. **Non-destructiveness of the ESR readout process.**

   Radiation induced radicals are not altered by the signal acquisition process of ESR spectroscopy, and this implies that alanine dosimeters can be read out as many times as desired provided that the dosimeters mass is controlled so that possible signal variations associated with mass losses can be corrected for. This is an advantage compared with other methods like thermo-luminescent dosimetry, which allows the performance of alanine dosimeter cumulative studies for in vivo dosimetry of fractionated treatments, representing important savings in the amount of pellets needed for some dosimetric studies.

6. **Small dependence on ambient conditions.**

   Ambient conditions like relative humidity during the dosimeters storage affect the fading of radicals in alanine. Other factor to be taken into account is the observed increase of the radiation yield with temperature. The effect is small and can depend on both the dosimeter manufacturing process and ambient conditioning. For L-α-alanine pellet presentations[2], the radiation yield exhibits a linear variation with a slope ranging from $+0.1\%\ ^{\circ}\mathrm{C}^{-1}$ to $+0.2\%\ ^{\circ}\mathrm{C}^{-1}$ for absorbed doses up to 50 kGy and temperature values between -10 °C and 50 °C [81].

   The radiation yield at a temperature T can be derived from the radiation yield at an arbitrary reference temperature, T_0, and the temperature coefficient c_T as:

   $$G_{Q,T} = G_{Q,T_0} \cdot [1 + c_T(T - T_0)] \tag{3.5}$$

   Where the slope, c_T, takes a value of $+0.11\%\ ^{\circ}\mathrm{C}^{-1}$, with an associated relative uncertainty of 2.9%, for the Harwell alanine dosimeters that are employed in this work [89].

---

[2] Among the two stereoisomers of alanine (D-α-alanine and L-α-alanine), L-α-alanine exhibits a temperature dependence 50% lower than D-α-alanine, being thus preferred for dosimetry [81].

> In order to correct for radiation yield variations that can arise between the different dosimeters involved in a measurement campaign, a temperature correction factor, k_T, is applied to the ESR signal. This temperature correction is needed whenever the pellets are irradiated at different temperatures. The correction will be simply given by the ratio of radiation yields at the dosimeter irradiation temperature T and another temperature that is taken as reference, T_0, and to which we will refer all our ESR signal intensities:
>
> $$k_T = \frac{G_{Q,T_0}}{G_{Q,T}} = \frac{1}{1 + c_T(T - T_0)} \simeq 1 - c_T(T - T_0) \tag{3.6}$$
>
> Additionally, alanine signal quantification through ESR spectroscopy is also affected by the water content of the pellet and the temperature and humidity of the laboratory, because the spectrometer sensitivity varies with the amount of water hold by the resonator cavity. Stability in the ambient conditions during ESR signal acquisition is required in order to minimize undesired sensitivity variations, and the pellets are usually stored open in laboratory conditions for some hours before proceeding with the measurements to reduce changes in the water content of the pellet during signal acquisitions.

The basic concepts just introduced are enough to identify the key factors that will condition the quality of the measurement of absorbed dose to water with an alanine/ESR system. We can classify these factors as being associated to any of the two steps that must be followed for the construction of the alanine calibration curve: a) irradiation of the alanine pellets and b) quantification of the dosimeters ESR signal.

On one hand, regarding the irradiation of the pellets, variations in the alanine dosimeters radiation yield and fading must be minimized in order to ensure that the same proportionality between radical concentration and absorbed dose to alanine is maintained for all the dosimeters involved in a measurement campaign. This can be done with a systematic control in the dosimeters ambient conditions before and after irradiation and through the application of a temperature correction factor if necessary. On the other hand, a good control on the ESR spectrometer is essential to ensure both signal repeatability and the proportionality between signal intensity and radical concentration. Taking into account that there are many parameters involved in the spectrometer operation, the principles of ESR spectroscopy have to be studied to ensure a proper understanding of the spectrometer operation.

3.1.2 Basic ESR spectroscopy theory

The study of the absorption and emission of radiation by matter provides information about energy differences between nuclear, atomic, molecular or crystallographic states, and has been historically employed to investigate the structure and dynamics of matter. In Electron Spin Resonance Spectroscopy, energy states are associated with the interaction between the magnetic moments of unpaired electrons in a substance and an external magnetic field.

The pairing of electrons that occurs spontaneously in most stable molecules due to Pauli exclusion principle can be disrupted by the presence of free radicals, which are induced for example by radiation. If these radicals remain stable with time, the material becomes paramagnetic due to the interaction between the intrinsic magnetic moment of the unpaired electrons and any external magnetic field. In the simplified case of a free electron system, the presence of a magnetic field, $\boldsymbol{B}$, aligns the electron intrinsic magnetic moment, $\boldsymbol{\mu}$, with the magnetic field, and the energy associated with this interaction can be expressed as:

$$E = \boldsymbol{\mu} \cdot \boldsymbol{B} \tag{3.7}$$

The intrinsic magnetic moment of the electron is in turn given by the product of the electron spin, $\boldsymbol{S}$, and the electron gyromagnetic factor $\gamma_e = e\, g_e/2m_e$, where e and m_e are the electric charge and mass of the electron and g_e is the g-factor of the electron, also known as Landé factor:

$$\boldsymbol{\mu} = \gamma_e \boldsymbol{S} = \frac{g_e e}{2m_e}\boldsymbol{S} \tag{3.8}$$

Due to the quantization of spin levels, the electron intrinsic angular momentum, $S = \hbar\sqrt{s(s+1)}$, can only have two projections in the direction of the magnetic field, chosen here (without loss of generality) to be aligned with the z axis, *i.e.* $s_z = \hbar m_s$, with $m_s = \pm\dfrac{1}{2}$ and $s = \dfrac{1}{2}$. In this way, the interaction between the external magnetic field, $\mathbf{B} = (0, 0, B_0)$, and the electron magnetic moment leads to two energy states, receiving this phenomenon the name of Zeeman effect:

$$E = \boldsymbol{\mu}\cdot\boldsymbol{B} = \mu_z B_0 = \frac{\hbar e}{2m_e} g_e m_s B_0 = \pm\frac{1}{2} g_e \mu_B B_0 \tag{3.9}$$

Where $\mu_B = \frac{\hbar e}{2m_e}$ is the Bohr magneton.

The object of ESR is to measure the energetic transitions between these two energy states, and for that purpose paramagnetic materials are placed in a magnetic field under the incidence of electromagnetic radiation with the appropriate frequency, as represented in Figure 3.3. The energy difference between the two states establishes a resonance condition for electronic transitions $\Delta E = h\nu = g_e \mu_B B_0$. In practice, ESR spectrometers involve the use of an electromagnetic radiation source with a frequency that is kept constant while the intensity of the magnetic field varies until the resonance condition is fulfilled and there is a net absorption of microwave radiation by the sample. For most spectrometers the incident radiation is within the microwave X band region, between 9 and 10 GHz, and the external magnetic

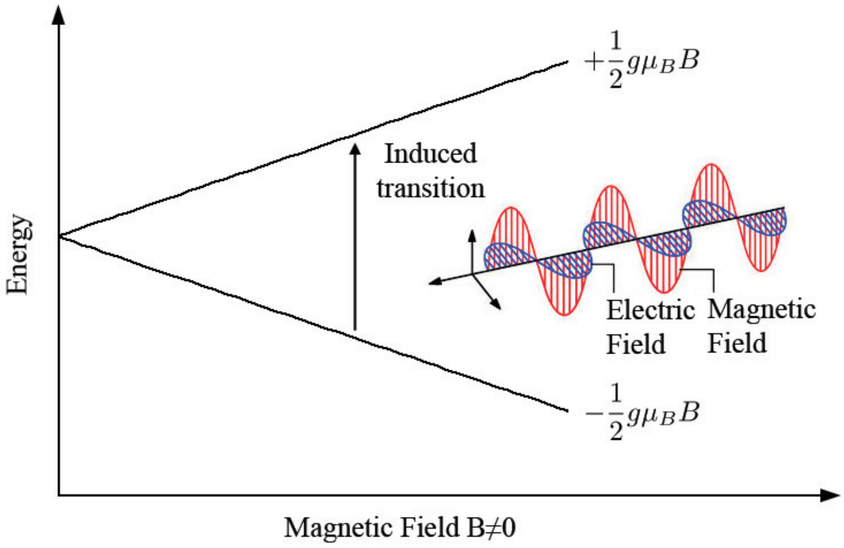

FIGURE 3.3: Energy splitting due to the two possible alignments of the electron magnetic moment and an external magnetic field. The state of lowest and highest energy occur when the moment of the electron μ is aligned with and against the magnetic field respectively. Transitions between these two states occur through the emission/absorption of microwave radiation with the appropriate frequency.

flux density ranges approximately between 0.32 T and 0.37 T (3200 to 3700 gauss) to fulfill the resonance condition. In order to fully understand paramagnetic spectroscopy we have to consider that an ESR sample contains many paramagnetic species and not a single electron. When a population of radicals is in thermodynamic equilibrium, the ratio of paramagnetic centers in the upper and lower energy states, $\frac{n_{upper}}{n_{lower}}$, can be described by the Maxwell-Boltzmann equation as a function of the energy gap between the two states, ΔE, the temperature, T and the Boltzmann constant, k_B, as:

$$\frac{n_{upper}}{n_{lower}} = \exp\left(-\frac{\Delta E}{k_B T}\right) \tag{3.10}$$

For the X-band microwave frequencies employed in most ESR spectrometers ($\nu \approx 9.75$ GHz), $h\nu = 40\mu$eV, and under standard conditions ($T = 298$ K),

$k_BT = 25.6$meV, the spins are almost equally distributed between parallel and anti-parallel with respect to the external magnetic field, $n_{upper}/n_{lower} \approx 0.998$.

Polarization excess can be then expressed by:

$$P = \frac{n_{upper} - n_{lower}}{n_{upper} + n_{lower}} = \frac{1 - \exp\left(-\Delta E/k_BT\right)}{1 + \exp\left(-\Delta E/k_BT\right)} = \tanh\left(\frac{\Delta E}{2k_BT}\right) \tag{3.11}$$

When thermal equilibrium is reached under a static magnetic field applied in the z axis, $\boldsymbol{B} = (0, 0, B_0)$, the equilibrium magnetization of the sample, $\boldsymbol{M_0}$, calculated as the addition of all the magnetic moments per unit volume v, is expressed as a function of this polarization excess:

$$\boldsymbol{M_0} = \frac{1}{v}\sum_i \boldsymbol{\mu}_i = \frac{1}{2}\hbar\gamma_e N P \boldsymbol{u_z} \tag{3.12}$$

Where N=$n_{upper} + n_{lower}$ is the total number of unpaired electrons.

Larmor theorem states that the rate of change in the magnetization, $\boldsymbol{M}$, of the sample is equal to the torque produced by the magnetic field:

$$\frac{d\boldsymbol{M}}{dt} = \gamma_e \boldsymbol{M} \times \boldsymbol{B} \tag{3.13}$$

Taking into account that we are considering the static magnetic field to be parallel to the z axis, we will use M_z for the longitudinal magnetization and M_x and M_y for the transverse components of the magnetization. Larmor theorem indicates that the longitudinal magnetization is constant and precesses around $\boldsymbol{B}$ with a frequency $\omega_0 = \gamma_e B_0$, usually referred to as Larmor frequency. If there is little interaction between the individual spins of the spin system, the phase of the precession is random and the sum of the individual magnet moments contributing to the transverse magnetization at equilibrium is zero.

In order to fully describe the motion of the magnetization vector, relaxation effects also need to be considered. Felix Bloch first derived the famous equation of motion which fully describes the evolution of the magnetization:

$$\frac{d\boldsymbol{M}}{dt} = \gamma_e\left(\boldsymbol{M} \times \boldsymbol{B}\right) - \boldsymbol{R}\left(\boldsymbol{M}(t) - \boldsymbol{M_0}\right) \tag{3.14}$$

Where $\boldsymbol{R}$ is the relaxation vector $\boldsymbol{R} = (T_2^{-1}, T_2^{-1}, T_1^{-1})$, expressing the rates at which the non-equilibrium magnetization, $\boldsymbol{M} = (M_x, M_y, M_z)$, approaches to its thermal equilibrium value $\boldsymbol{M_0} = (0, 0, M_0)$.

If $\boldsymbol{B}$ is a static field applied in the z axis, $\boldsymbol{B} = (0, 0, B_0)$, these equations reduce to:

$$\frac{dM_z}{dt} = -\frac{M_z(t) - M_0}{T_1} \tag{3.15}$$

With solution:

$$M_z(t) = M_0[1 - \exp\left(-t/T_1\right)] \tag{3.16}$$

And for the transverse components:

$$\begin{aligned} \frac{dM_x}{dt} &= \gamma_e B_0 M_y - \frac{M_x(t)}{T_2} \\ \frac{dM_y}{dt} &= -\gamma_e B_0 M_x - \frac{M_y(t)}{T_2} \end{aligned} \tag{3.17}$$

With solutions:

$$M_x(t) = \omega_0 \exp\left(-t/T_2\right)\cos(\omega_0 t); \;\; M_y(t) = \omega_0 \exp\left(-t/T_2\right)\sin(\omega_0 t); \tag{3.18}$$

Here we can see that if a static field is applied, the magnetization ends up reaching the equilibrium value M_0 in the direction of the applied field, and the transverse components of the magnetization will vanish. If the population balance of the sample is perturbed, the spin system's interactions with the surroundings results in an eventual return to thermal equilibrium. This process, called spin lattice relaxation, is characterized by the time constant T_1. On the other hand, if there is a net transverse magnetization caused by a perturbation of the system, the system relaxes back to zero transverse magnetization, a process characterized by the transverse relaxation time T_2, or spin-spin relaxation, quantifying the time during which individual moments contributing to the transversal magnetization remain in phase with each other.

In this situation, the magnetization is time invariant and cannot be detected. To allow detection, this alignment must be perturbed by applying a short oscillating field on the xy plane perpendicular to the static magnetic field in the z-axis, this is, a circularly polarized microwave pulse $\boldsymbol{B_1}$ $= (B_1 \sin(\omega t), B_1 \cos(\omega t), 0)$. The oscillating magnetic field will make the sample magnetization to nutate, as shown in Figure 3.4, and the spectrometer detector will then measure the emitted microwave signal created by the transverse components of the sample magnetization.

It is useful to define $\omega_1 = \gamma_e B_1$ and $\Omega_S = \omega_0 - \omega$. For on-resonant microwave irradiation, $\Omega_S = 0$, the effective nutation frequency ω_{eff} equals ω_1 and the magnetization vector precesses around an axis perpendicular to z. On the other hand, the magnetization vector is hardly affected when the microwave frequency is far off-resonant. After the pulse the magnetization returns to a state parallel to $\boldsymbol{B}$ through the spin-lattice relaxation, and the corresponding relaxation time needs to be considered when extracting signal from noise, where the experiment needs to be repeated several times, as fast as possible. In order to repeat the experiment, one needs to wait until the magnetization along the z-axis has recovered, because if there is no magnetization in z direction, then there is nothing to tip into the xy-plane to create a significant signal.

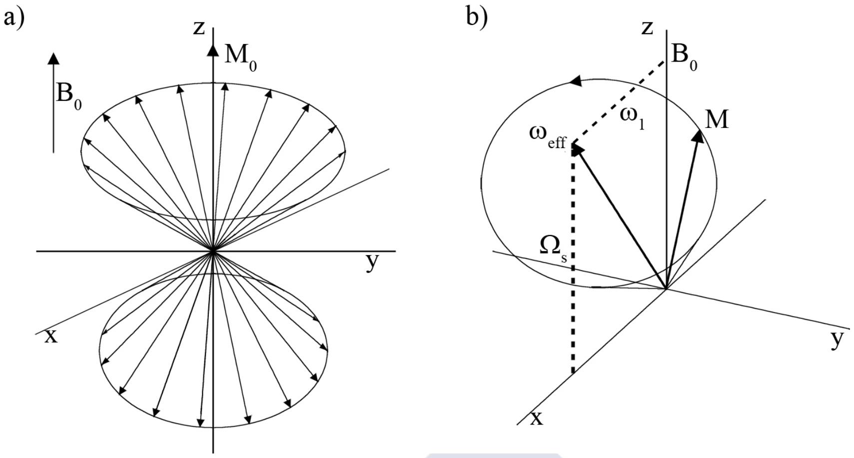

FIGURE 3.4: a) Precession of the magnetization vector M around an external magnetic field B_0 parallel to the z axis. b) Nutation of the magnetization vector during irradiation with a circularly polarized microwave field with amplitude $\omega_1 = \gamma_e B_1$, see text below.

Saturation is observed in the signal when the microwave power is higher than a given threshold. At the field-frequency resonance position, B_1 turns the spins in a very small amount, and a voltage proportional to the angle by which the spins were turned by B_1 is induced in the spectrometer detector. Under non saturating conditions T_1 and T_2 are short and relaxation back to the z axis is fast relative to the other time constants of the experiment, being the signal approximately at equilibrium. However, if the microwave power is too high relative to the relaxation rates, B_1 turns the spins so far from the z axis that relaxation cannot return the magnetization back to the z axis within the time range of the signal measurement. In this situation a saturation effect occurs.

During the microwave pulse, the total magnetic field applied to the sample is $\boldsymbol{B}(t) = (B_1 \sin(\omega t), B_1 \cos(\omega t), B_0)$, and the Bloch equations can be written as:

$$\begin{bmatrix} \frac{dM_x}{dt} \\ \frac{dM_y}{dt} \\ \frac{dM_z}{dt} \end{bmatrix} = \begin{bmatrix} \gamma_e[M_y B_0 - M_z B_1 \cos(\omega t)] - \frac{M_x}{T_2} \\ \gamma_e[M_z B_1 \sin(\omega t) - M_x B_0] - \frac{M_y}{T_2} \\ \gamma_e[M_x B_1 \cos(\omega t) - M_y B_1 \sin(\omega t)] - \frac{(M_z - M_0)}{T_1} \end{bmatrix} \tag{3.19}$$

It will be useful to change to a coordinate system rotating in the xy plane with frequency ω. If we define here the magnetization components as $U = M_x \cos(\omega t) - M_y \sin(\omega t)$ and $V = M_x \sin(\omega t) + M_y \cos(\omega t)$, deriving and using Equation 3.19, we can get:

$$\begin{bmatrix} \frac{dU}{dt} \\ \frac{dV}{dt} \\ \frac{dM_z}{dt} \end{bmatrix} = \begin{bmatrix} (\omega_0 - \omega)\, V - \omega_1 M_z - U/T_2 \\ -\,(\omega_0 - \omega)\, U - V/T_2 \\ \omega_1 V - (M_z - M_0)/T_1 \end{bmatrix} \tag{3.20}$$

After a sufficiently long continuous microwave irradiation, the magnetization will reach a stationary state and the time derivatives of the magnetization vector vanish. The Bloch equations will then become a linear system of equations, with solutions:

$$U = -M_0\, \omega_1\, \frac{T_2}{1 + \Omega_S^2 T_2^2 + \omega_1^2 T_1 T_2} \tag{3.21}$$

$$V = M_0\, \omega_1\, \frac{\Omega_S T_2^2}{1 + \Omega_S^2 T_2^2 + \omega_1^2 T_1 T_2} \tag{3.22}$$

$$M_z = M_0 - \frac{M_0 \omega_1^2 T_1 T_2}{1 + \Omega_S^2 T_2^2 + \omega_1^2 T_1 T_2} \tag{3.23}$$

The transverse magnetization components can be measured simultaneously in a quadrature-detection scheme with two microwave reference signals phase-shifted by 90° with respect to each other, which yields a complex signal $S = -U\ + i\, V$.

For low microwave powers, $\omega_1^2 T_1 T_2 << 1$, the transverse components are proportional to ω_1. The real part of S can be recognized as a Lorentzian absorption line with an amplitude given by the sample magnetization under equilibrium, M_0, and the oscillating magnetic field intensity ($\omega_1 = \gamma_e B_1$), and a width given by the inverse of the spin lattice relaxation time T_2:

$$U = -M_0 \omega_1 \frac{T_2^{-1}}{T_2^{-2} + \Omega_S^2} \tag{3.24}$$

On the other hand, the imaginary part V will correspond with a dispersion Lorentzian line:

$$V = M_0 \omega_1 \frac{\Omega_S}{T_2^{-2} + \Omega_S^2} \tag{3.25}$$

Since the dispersion line suffers from broad flanks and decreased amplitudes, only absorption lines are recorded, which offer a better signal to noise ratio (SNR) and a better resolution in presence of multiple lines.

For a free electron system, the ESR absorption and dispersion curves would have thus the shape represented in Figure 3.5, and the ESR spectra is commonly acquired as the first derivative of the absorption curve. However, real samples are not electron free systems, and the shape of the ESR spectral line presents rather complicated structures. Electrons, normally associated with one or more atoms, will have nonzero orbital angular momenta and the value of their g-factors will differ from g_e. Moreover, interactions with the nuclear spin of the atoms will lead to hyperfine couplings, splitting the ESR resonance signal into doublets, triplets, etc.

Additionally, if a sample has different radical species, this is, unpaired electrons in different environments, the observed ESR spectrum is the overlapping of the ESR spectra from the different radicals species. This is the case of the alanine, for which the existence of the three radical species mentioned in Section 3.1.1 produces the overlapping of three ESR lines conforming the final alanine spectrum shown in Figure 3.6.

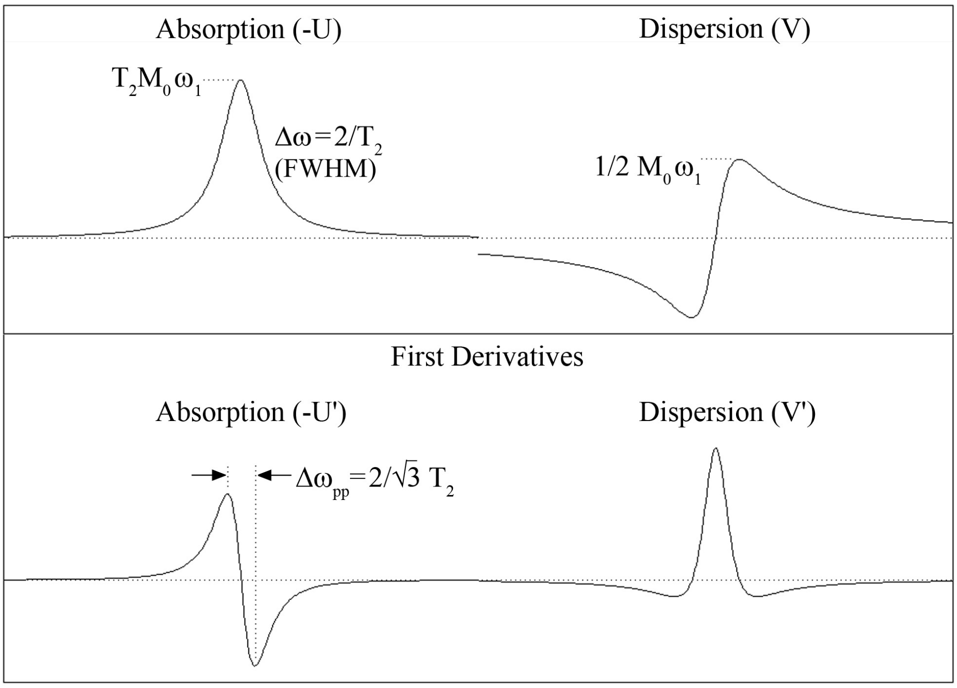

FIGURE 3.5: ESR energy absorption and dispersion lines of a free electron system, top, and their first derivative as acquired by the spectrometer, bottom.

Regarding alanine dosimetry applications, it is the ESR signal intensity exhibited by the dosimeters what becomes the quantity of interest as it is proportional to the total amount of radicals in the sample. For high doses, this quantification is usually done through the analysis of the peak-to-peak intensity of the ESR spectrum, widely demonstrated to be a good estimator for the concentration of radicals [90]. The ESR signal intensity measured by a spectrometer is strongly dependent on the spectrometer sensitivity, which is affected by several parameters like the microwave power, the modulation amplitude, etc. Other aspects of vital importance for the quality of the measurement, like the noise in the signal and the stability of the instrument, will also depend on the choice of some operation parameters.

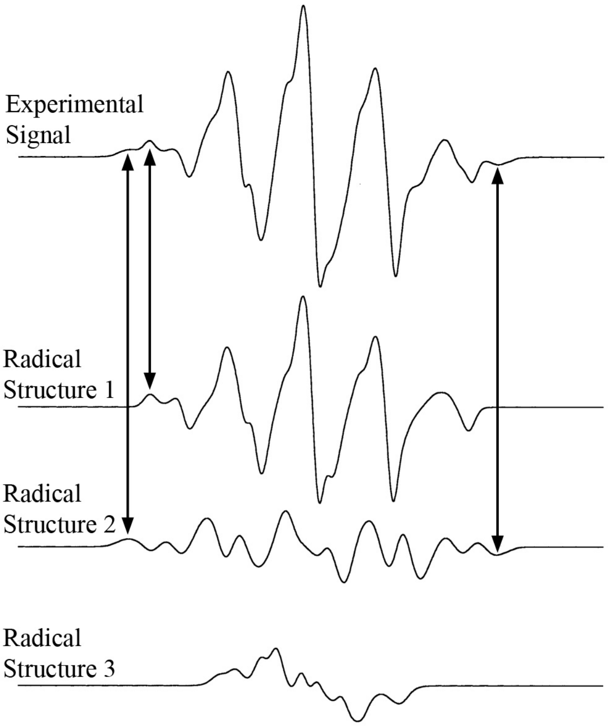

FIGURE 3.6: Alanine ESR spectrum, top, consisting in the superposition of the ESR spectra for the three radicals species R1, R2 and R3 that are induced by radiation in the alanine [74].

3.1.3 Spectrometer operation

All ESR spectrometers comprise four main components, namely a microwave radiation source, a magnet, a microwave resonant cavity where the samples are placed, and a diode detector that measures the amount of radiation absorbed or emitted by the samples. Most ESR spectrometers can be classified as reflection spectrometers because they measure changes in the amount of radiation that is reflected back from the cavity containing the sample when the spectroscopic transitions occur. Figure 3.7 shows a schematic representation of the spectrometer, and their main components are described below.

Microwave bridge:

The electromagnetic radiation source and the detector are in a box called the microwave bridge.

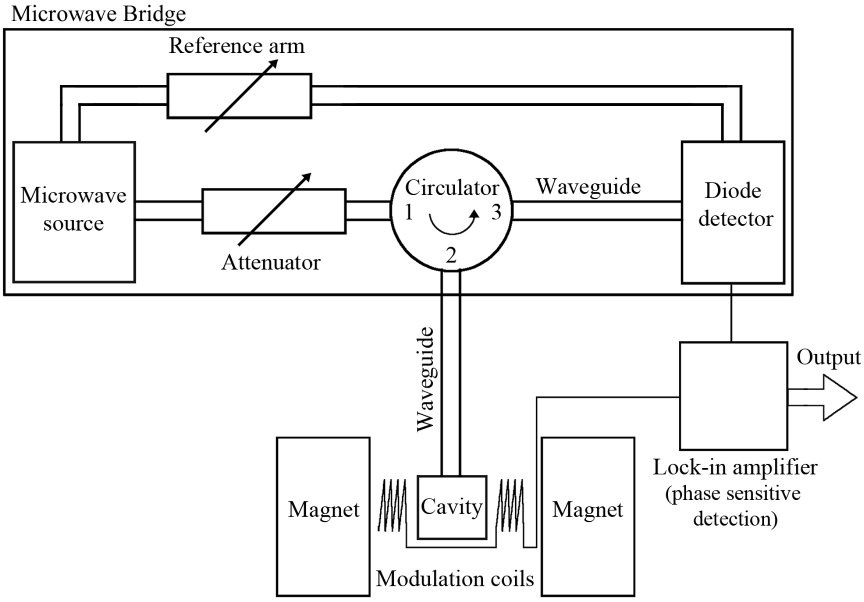

FIGURE 3.7: Schematic representation of the main components conforming the ESR spectrometer.

At the output of the microwave source there is an attenuator that controls the flow of microwave radiation, so that the microwave power entering the cavity can be accurately tuned. Microwave radiation will then enter a circulator, which ensures that the radiation coming from the microwave attenuator is only directed to the cavity, while the radiation that is reflected from the cavity is only directed to the detector.

The detector is a Schottky barrier diode that converts the microwave power reflected from the cavity into an electrical current. The relationship between diode current and the microwave power is known to vary from a linear proportionality to a square root dependence as the microwave power increases [91]. The optimal sensitivity required for signal intensity quantification is achieved when the diode operates in the region of square root dependence, usually achieved for incident powers higher than 1 milliwatt.

The remaining component in the microwave bridge is a reference arm, which supplies the detector with an extra microwave power to ensure that the diode operates in the adequate region.

Cavity:

The sample to be studied by ESR spectroscopy is located inside of a microwave cavity consisting in a metal box with a rectangular shape that resonates with the microwaves, amplifying weak signals from the sample. In order to couple the microwaves into the cavity, there is a hole, called iris, with a screw that can be moved up and down to control the amount of microwaves entering the cavity, see Figure 3.8.

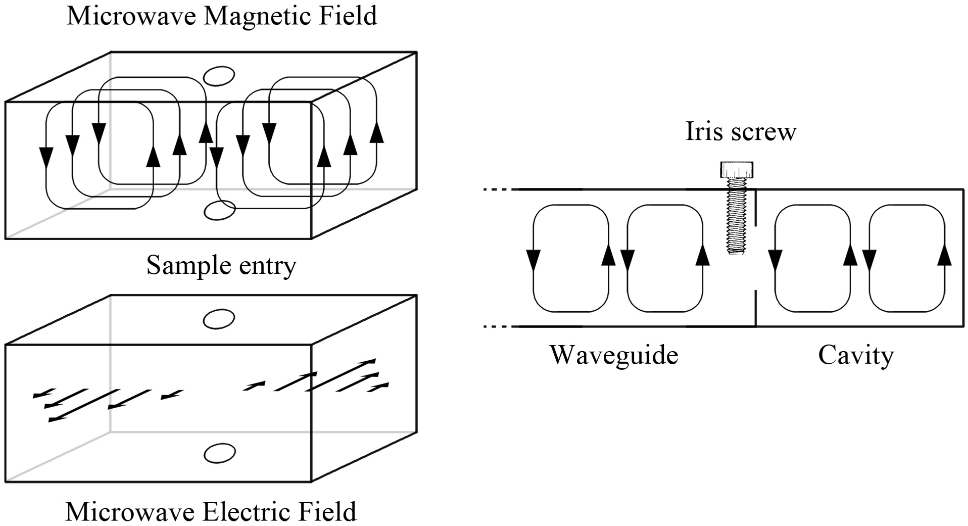

FIGURE 3.8: Sketch of the magnetic and electric field patterns in a microwave cavity, left, and scheme of the iris screw controlling the entrance of radiation in the cavity from the waveguide, right.

Although we will not elaborate this in much detail, resonance in the cavity is achieved when a certain condition related with the iris aperture, and the losses in the microwave source, cavity walls and sample, is fulfilled. Under resonance conditions the cavity is critically coupled and microwaves remain inside the cavity conforming standing waves, being the amount of microwaves that are reflected from the cavity minimized. The efficiency of every cavity to store the microwave energy is expressed by its quality factor, QF, which is defined as the ratio of energy stored and dissipated in the cavity per cycle, being also related with the above mentioned parameters of iris aperture, and the cavity and microwave source impedances.

When paramagnetic transitions occur, the absorption of a net microwave energy by the sample changes the effective impedance of the cavity, which will be no longer critically coupled. The microwaves are then reflected back to the circulator, reaching the diode detector, which yields an electrical current conforming the ESR signal.

It is worth to note that the presence of water, a microwave absorber, in the cavity lowers the QF and affects the spectrometer sensitivity. Although some amount of water inside the cavity is unavoidable due to the non zero relative humidity of the air, changes in this water content should be minimized during measurements for the sake of stability.

Regarding the positioning of the samples in the cavity, it must be taken into account that most paramagnetic samples do not exhibit resonant absorption of microwaves via the electric field, and as the electromagnetic waves have their electric and magnetic components in opposite phase, samples must be placed at a position of maximum magnetic field. The non uniformity of the modulated magnetic field and the distribution of standing microwaves within the cavity leads to a drastic variation of sensitivity over the intracavity space. The sensitivity usually reaches the maximum at the cavity center, decreasing for points displaced either upwards or downwards from there. Due to this, the same paramagnetic sample placed at different positions inside the cavity leads to signals of different intensities. As alanine dosimeters are not point like samples, different portions of the pellet are located in regions of the cavity with different sensitivities, contributing differently to the total signal [83].

Signal channel, phase sensitive detector:

A strategy to separate ESR signal from noise and interferences, thus improving the SNR, is usually employed in ESR spectrometers. This strategy consists in introducing a sinusoidal modulation of the magnetic field strength that is seen by the sample.

When a spectroscopic transition occurs, the field modulation sweeps the signal and the microwaves reflected from the cavity are also modulated in amplitude with the frequency of the modulated magnetic field. The ESR signal, which would be linear over a magnetic field interval as wide as the modulation amplitude, will instead have a sinusoidal shape with an amplitude proportional to the signal slope. A lock-in amplifier (phase sensitive detector) suppresses then all the signals that do not have the frequency and phase of the magnetic field modulation, so that both noise and electrical interference signals are effectively suppressed. Additionally, a low pass filter is coupled to the detector to remove some of the remaining high frequency noise.

In Figure 3.9 we can see that the amplitude of the oscillating detected signal increases with the slope of the absorption signal in the signal channel (difference between the absorption at the extremes of the modulated field), being this the reason why ESR spectra are acquired as the first derivative of the absorption signal.

Among all the factors affecting the spectrometer operation, the spectrometer sensitivity is mainly determined by the resonator QF, the magnetic field modulation amplitude and the magnetic component of the microwave field.

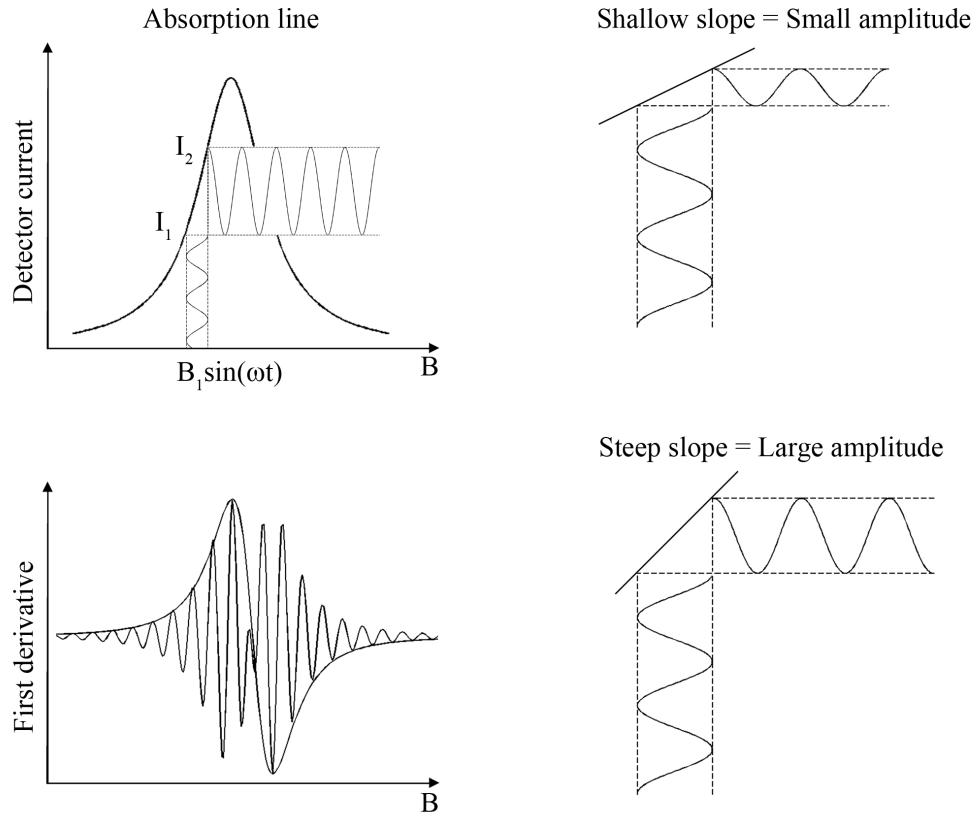

FIGURE 3.9: Schematic representation of the effect produced by the field modulation employed for phase sensitive detection of the ESR signal.

3.2 Development of an Alanine/ESR dosimetry system

3.2.1 Materials and experimental setup

The construction of an alanine calibration curve for the performance of alanine dosimetry involves two main steps: the irradiation of the dosimeters and the alanine signal ESR read out. In this section we will describe the experimental setup that was employed for the performance of these two tasks. The alanine dosimeters employed in our work will be presented, including some further considerations about how to manage the influence that ambient conditions have in the dosimeters and the spectrometer. Then, the irradiation setup will be described, and we will conclude with a description of the ESR spectrometer and a system that was specifically developed for the alanine pellets positioning inside the ESR cavity.

3.2.1.1 The alanine pellets

The alanine dosimeters employed in this work are the cylindrical shaped pellets manufactured by Harwell Dosimeters Ltd, see Figure 3.10, consisting in 90.9% in mass of an alanine polycrystalline aggregate and a 9.1% of high melting point paraffin. The diameter of the pellets is (4.83 ± 0.01) mm, the height is (2.8 ± 0.1) mm and a nominal mass of (60 ± 2) mg is ensured within a production batch.

One of the advantages of Harwell dosimeters is their low sensitivity to changes in the environmental conditions when compared with the alanine dosimeters from other manufacturers, which is thought to be due to the high paraffin content of these pellets. The low porosity of Harwell dosimeters keeps the alanine rather isolated, minimizing variations in their water content related with their exposure to ambient conditions. Additionally,

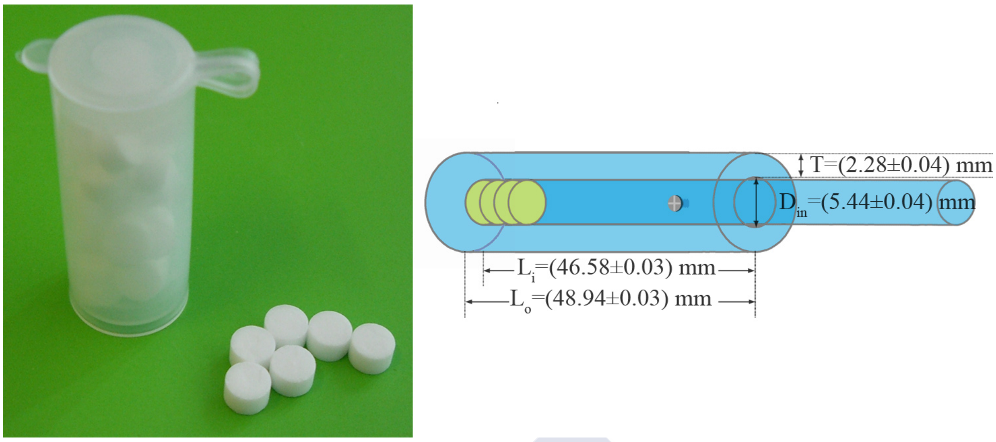

FIGURE 3.10: Harwell alanine pellets, left, and Perspex irradiation holder, right.

these pellets also further contribute to seal the quartz tube that holds the pellet inside the ESR cavity reducing the air flow through the cavity during measurements, which minimizes perturbations in cavity sensitivity due to changes in air temperature and relative humidity [92].

Another advantage of these dosimeters, shared with other manufacturers that produce alanine pellets with similar dimensions, is the relative small size of the pellets, which allows them to fit in the region of uniform sensitivity of the ESR cavities. Although one Harwell alanine pellet can fit inside this region, the positioning of the dosimeter in the cavity has to be accurately controlled to ensure that they are all read out in the same sensitivity region of the cavity. Besides, pellets with masses significantly deviating from the average can produce outlying mass-normalized signals. Corrections consisting in mass normalization will only be valid in the volume of approximately uniform sensitivity that extends up to 2 mm from the cavity center in each direction [83].

The formation of radiation induced radicals in alanine is temperature dependent and this can have an effect both on the construction of the calibration curve and on subsequent determinations of absorbed dose to water with those alanine dosimeters. In order to correct the ESR signal for radiation yield variations, the temperature of the dosimeters during irradiation must be known. All the pellets involved in a measurement campaign and the pellets holder are placed at the irradiation room for temperature stabilization some hours before irradiation. The temperature of the irradiation water tank where the pellets are irradiated is then recorded in every measurement, and it is later employed to correct the radiation yield by arbitrarily choosing one of the pellets temperature as a reference.

Radiation induced radicals present also a short-term evolution after irradiation that varies depending on the total dose absorbed in the pellet [93]. Variations are observed to become minimal approximately 72 hours after irradiation for most dose levels. This period of time, after which high-precision ESR measurements can be performed, is always respected in our campaigns before proceeding with the dosimeters readout.

The moisture content of the pellets is another issue that needs to be controlled, as water is a substance that absorbs microwaves and affects the resonator QF. Due to this, alanine pellets with different moisture content will lead to different signal amplitudes. Variations in water content from pellet to pellet, or even changes in the relative humidity of a single pellet during ESR measurements, must be thus taken into account. The water content of a pellet depends only on the ambient humidity of the environment where it is stored, and thus all pellets included in a measurement campaign should be stored together or under identical conditions. In order to control the pellets relative humidity, a saturated aqueous solution of a particular salt is usually placed in a sealed recipient where the pellets are stored, as for certain salts the relative humidity of the ambient air in the recipient remains constant or varies slightly with temperature [94, 95].

In our work, a preconditioning was performed to the pellets employed in the measurement campaigns: a saturated solution of sodium hydrogen sulfate was placed inside a sealed desiccator where the pellets were stored for a month before irradiation, Figure 3.11. The air enclosed in the desiccator was in this way maintained under a relative humidity of 65%.

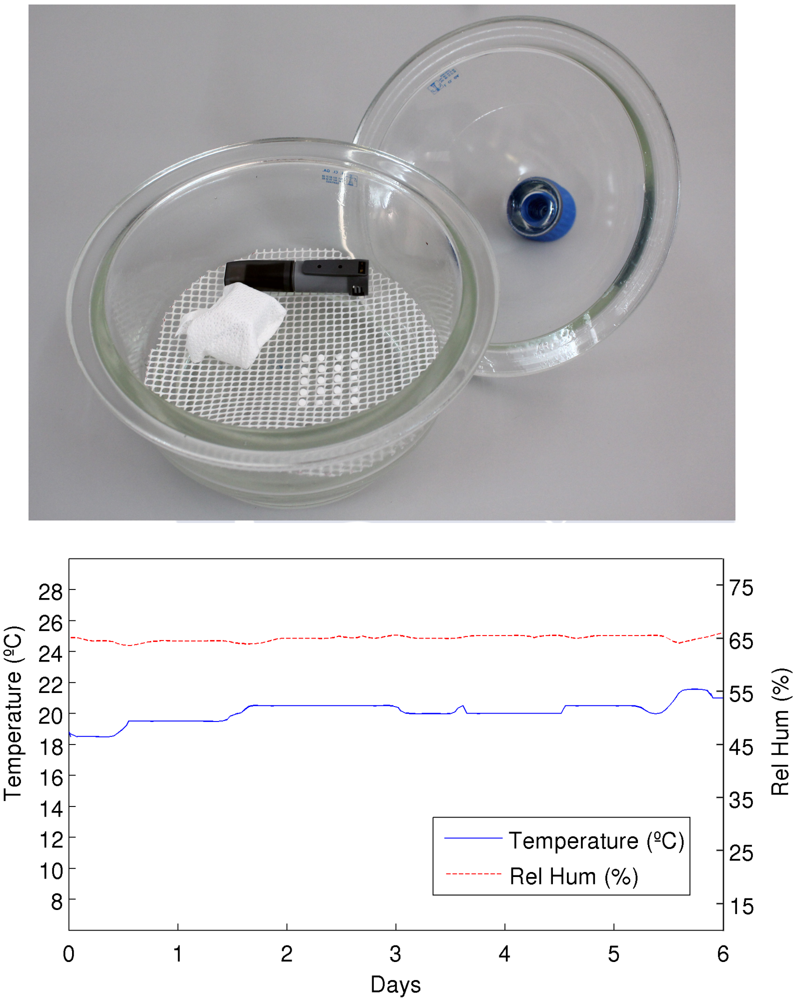

FIGURE 3.11: (Top) Desiccant vessel containing 300 ml of a saturated solution of sodium hydrogen sulfate, the alanine pellets are held on a plastic grid. To get an airtight environment inside the desiccant, a silicon grease is applied to the cap to get the vessel properly sealed. (Bottom) Temperature and relative humidity were monitored by a data logger.

Additionally, variations in the alanine moisture during ESR measurements will arise if the relative humidity of the dosimeters and the ambient humidity of the ESR room differ. As this would affect the cavity QF, pellets are conditioned over-night for moisture content stabilization at the ESR room conditions. The relative humidity in the ESR room should be kept as constant as possible during ESR measurement campaigns, avoiding changes in the laboratory air flow (doors or windows openings, changes in the air conditioning, etc).

3.2.1.2 Irradiation of the alanine pellets

The irradiation of the alanine pellets is an essential step in the alanine dosimetry work-flow for the construction of a calibration curve.

All the irradiations involved in this work were performed at the ^{60}Co facility of the Radiation Physics Laboratory of the Universade de Santiago de Compostela, a Secondary Standards Dosimetry Laboratory with ISO 17025 implanted and traceability to the PTB. For the construction of the calibration curve, the ESR signal amplitude of every irradiated alanine pellet has to be associated with the dose that would be deposited in water under the same incidence of radiation. In this way, the amount of radiation delivered to the alanine pellets is quantified in terms of absorbed dose to water, which is obtained from the dose rate of the ^{60}Co unit under reference conditions.

Before the irradiation of the pellets, the dose rate of the ^{60}Co unit is measured with a PTW TM30013 ionization chamber calibrated in terms of absorbed dose to water. This dose rate measurement was performed with the setup used for the calibration of ionization chambers in the laboratory: a water tank prepared for horizontal radiation incidence with the gantry position at 90°, as it is shown in Figure 3.12. A 10 cm×10 cm radiation field defined at a SSD = 75 cm and a SCD = 80 cm was employed for this irradiation, and a dose rate of (0.349 ± 0.001) Gy/min (uncertainty expressed with k=1) was determined under these conditions.

The irradiation of the alanine dosimeters is performed under the same conditions, holding the pellets in a cylindrical water-tight Perspex insert

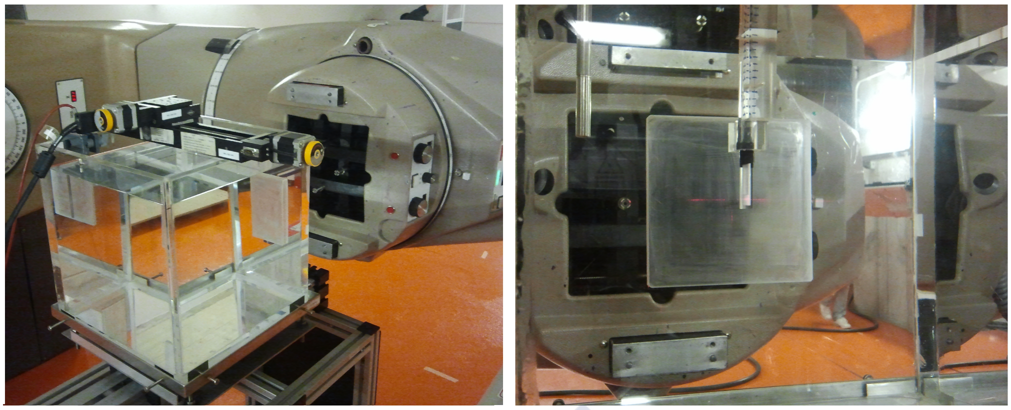

FIGURE 3.12: ^{60}Co unit irradiation setup involving a water tank and horizontal radiation incidence (left) and alanine insert positioning inside the water tank (right).

specifically machined for this purpose with the dimensions specified in Figure 3.10. The symmetry axis of the insert is placed perpendicularly to the direction of the beam propagation and three alanine pellets are always allocated in the holder to be irradiated together for repeatability studies. The insert holding the pellets is placed with two motorized stepper platforms to have the central pellet positioned at the position where the dose rate has been determined in the water tank. The time needed to achieve the desired value of absorbed dose to water is then calculated from the unit dose rate and selected as irradiation time.

3.2.1.3 ESR setup

The spectrometer employed in this work is a Bruker EMX ER073 with a standard st4102 cavity. Although other cavities with higher sensitivities exist, st4102 seems appropriate for alanine dosimetry as it has been demonstrated to be less affected by changes in the environmental conditions than high sensitivity cavities [92].

As we introduced in Section 3.1.3, for alanine dosimetry applications in the therapy dose range, the sensitivity of the spectrometer should be kept constant to allow calibration and maximal given the low signal intensities of alanine dosimeters at these dose levels. Considering these requirements, a specific positioning setup aiming to provide a reproducible positioning of the dosimeters in the cavity was developed based on the setups designed by other dosimetry laboratories like the NPL [79].

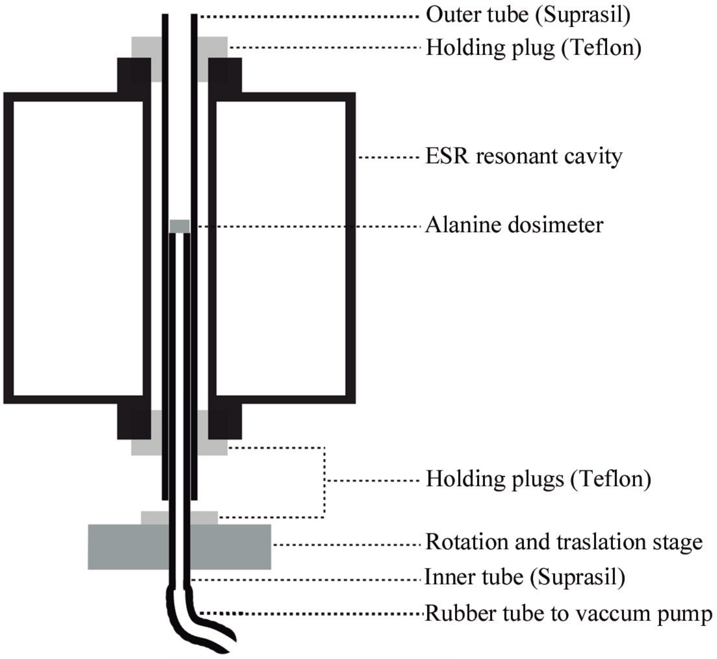

FIGURE 3.13: Sketch of the setup employed for the positioning of the pellets inside the ESR cavity. Concentric Suprasil tubes cross the cavity: the outer tube is fixed to the cavity while the inner tube can be displaced with a motorized stage to place the alanine pellet at the cavity center to acquire spectra. A vacuum pump ensures the pellets immobilization with respect to the inner tube during rotation.

To hold the alanine pellet inside the cavity, two concentric tubes of high purity fused quartz (Suprasil) are employed. The inner tube has an outer diameter of $D_{inner,o} = (4.2065 \pm 0.0065)$ mm, slightly smaller than the diameter of the pellet, $D_{pellet} = (4.83 \pm 0.01)$ mm, so it can rest at the tube top. The outer tube has an internal diameter of $D_{outer,i} = (5.0041 \pm 0.0065)$ mm, slightly wider than the pellet diameter so it fits inside the tube without friction but being not much wider than the pellet to control its lateral positioning inside the cavity. One of the ends of outer tube was flared during the manufacturing process to broaden its diameter and allow an easier positioning of the pellet on the inner tube, as shown in Figure 3.13. The tubes go through the cavity along its vertical axis, being the outer tube fixed to the top of the cavity with a Teflon screw piece.

The positioning in the cavity is as follows: the pellet is placed on the inner tube at the top of the cavity with vacuum tweezers. The inner tube is then displaced along the cavity by a linear motorized stepper stage to place the pellet at the cavity center. The position of the pellet inside the cavity is controlled with a precision of 0.025 mm. Studies of signal intensity versus dosimeter position are then performed to find the position of maximum sensitivity where all spectra will be acquired with the required positioning reproducibility. Additionally, the inner tube is coupled to a goniometer that rotates the dosimeter inside the cavity to enable the acquisition of spectra at different orientations of the pellet. This is due to the anisotropy of the alanine dosimeter signal, which will be studied in the next section. A weak vacuum is applied to the inner tube to attach the pellet to it and avoid relative movements between them during measurement.

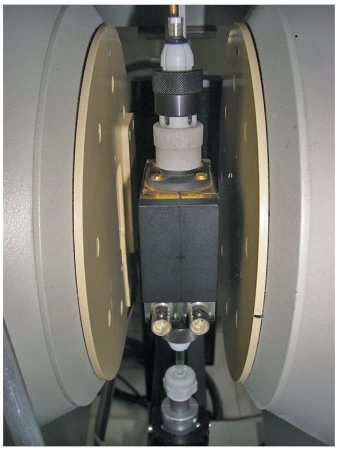

FIGURE 3.14: Picture of the ESR positioning setup fixed to the spectrometer frame.

Figure 3.14 shows the positioning setup, being the motorized stepper stage mounted on a structure that is fixed to the spectrometer frame. The use of materials presenting ESR signal was avoided inside the cavity, so that the empty cavity presents a signal sufficiently weak compared with the signal of a pellet irradiated to 50 Gy, see Figure 3.15.

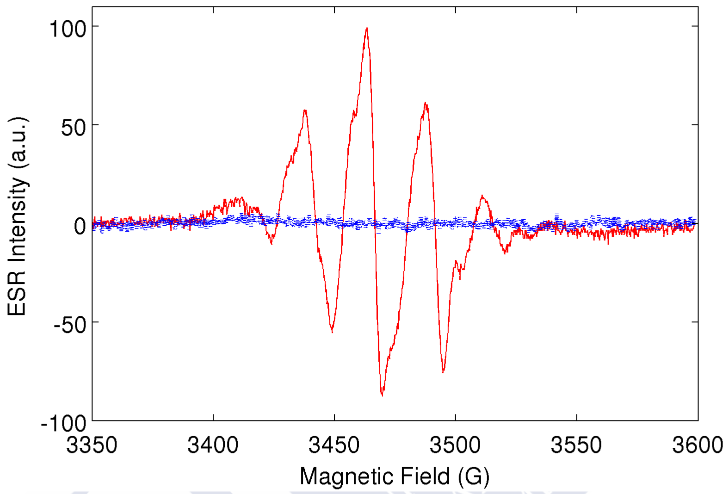

FIGURE 3.15: Comparison of ESR signals of an alanine pellet irradiated to 50 Gy (solid line) and the ESR background signal exhibited by the positioning setup itself, with no alanine pellet inside (dots).

3.2.2 ESR parameters optimization

Alanine dosimetry in the therapy dose range faces as major difficulty the rather low ESR signal to noise ratio exhibited by the dosimeters, which requires the spectrometer yielding maximum sensitivity in order to achieve the highest signal quality. This requirement is not as strict in other applications where the study is focused in the shape of the sample ESR spectrum, and thus the optimal spectrometer parameters in alanine dosimetry can differ from those used in other applications.

As we already introduced, there are many tunable parameters related with the spectrometer operation that affect not only the sensitivity but also the stability of the equipment. The spectrometer sensitivity will be determined by the magnetic field modulation amplitude, the magnetic component of the microwave field and the QF of the resonator, which is in principle a characteristic of every cavity but becomes also affected by the presence of the sample.

On the other hand, variations in the spectrometer sensitivity can arise during measurements due to changes in the laboratory ambient conditions, variations in the water content of the dosimeters or the use of excessively high microwave power and modulation amplitudes, which can lead to overheating in the cavity.

The first step addressed for the development of an alanine/ESR dosimetry system was to study the spectrometer operational parameters in order to find an optimal combination of them and to establish our measurement protocol for alanine dosimetry applications. Increasing the signal to noise ratio and determining the lowest achievable uncertainty associated to the alanine dosimeters signal with our spectrometer was the main objective of this optimization process. Pellets irradiated to 50 were employed in most of these measurements. Signal quantification through the peak-to-peak intensity was adopted after subtraction of any possible slope in the alanine baseline and after having applied a noise filter suppressing the high frequency noise components of our spectrum.

3.2.2.1 Cavity positioning

First of all, a study of the cavity sensitivity versus the position of the alanine samples inside cavity was performed. A reference position was chosen by leveling the pellet, already placed on the top of the inner tube, with the outer tube. Then, several spectra were acquired at different positions of the pellet along the vertical axis of the cavity using the motorized stage. As expected, the ESR signal intensity exhibits a maximum around the cavity center, diminishing with the square of the distance to this position, as it can be observed in Figure 3.16.

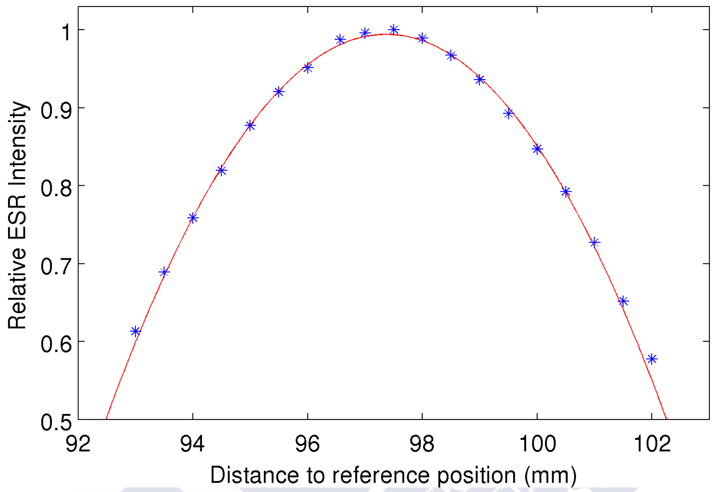

FIGURE 3.16: ESR signal intensity versus the position of the alanine dosimeter inside the cavity. The position of the pellet is expressed by the distance to a reference position established by leveling the pellet with the outer quartz tube of the positioning setup.

A parabolic fit to the experimental data yielded the solution, with x in millimeters:

$$y = 1 - 0.0207 \cdot (x - 97.34)^2 \tag{3.26}$$

Where y is the relative peak-to-peak signal normalized to the maximum value. This fit served for the determination of the position of maximum sensitivity, found at 97.34 mm from the reference position of the pellet.

Measurements are performed at the position of maximum sensitivity in all experiments. Although the data used for the fit exhibits certain scatter and the determination of the position with maximum sensitivity would have an associated uncertainty, it does not affect measurements providing that all the pellets involved in a campaign are measured at the same position, which only depends on the stage repeatability. The uncertainty in the determination of the maximum affect our capability to maximize the spectrometer sensitivity in our measurements. It should be noted that since the positioning setup of the alanine pellets is sometimes removed from the spectrometer for measurements related with other ESR applications, positioning recalibration is performed in every measurement campaign.

3.2.2.2 Sweep time

The sweep time, or time spent by the spectrometer to acquire a spectrum, is the product of conversion time, *ct*, which is the diode integration time at every value of external magnetic field intensity, and the number of magnetic field intensities employed to acquire the spectrum.

The number of points acquired by the spectrometer can be set to 512, 1024, 2048, 4096 or 8192, and recommendations are usually given to have at least 10 data points within the narrowest line of the spectrum to be resolved. In our case, for the 9.75 GHz frequency of the microwaves entering the cavity, the alanine spectrum is centered at an external magnetic field intensity of approximately 3465 gauss, spanning for an interval of 125 gauss. As the peak-to-peak intensity is employed for signal quantification, signal peaks are placed at the center of the alanine spectrum acquisition. We must however acquire the alanine signal in a wide range of magnetic field to correct for possible slopes in the spectrum baseline, which can distort the peak to peak intensity. Taking into account the sweep widths employed for spectrometer operation at other institutions like the PTB and the NPL, we decided to choose a sweep width of 250 gauss around the center of the alanine spectrum. For this sweep width, the number of points acquired per spectrum was set to 1024, which leads to approximately 25 data points from peak-to-peak.

Regarding the conversion time, the spectrometer allows setting it to 20.48 ms, 40.96 ms, 81.92 ms, 163.84 ms, etc. The impact of the conversion time on the signal repeatability was studied by acquiring seven spectra of an alanine pellet irradiated to 50 Gy at different values of conversion time to calculate the relative standard deviation of the signal intensities measured at different *ct*.

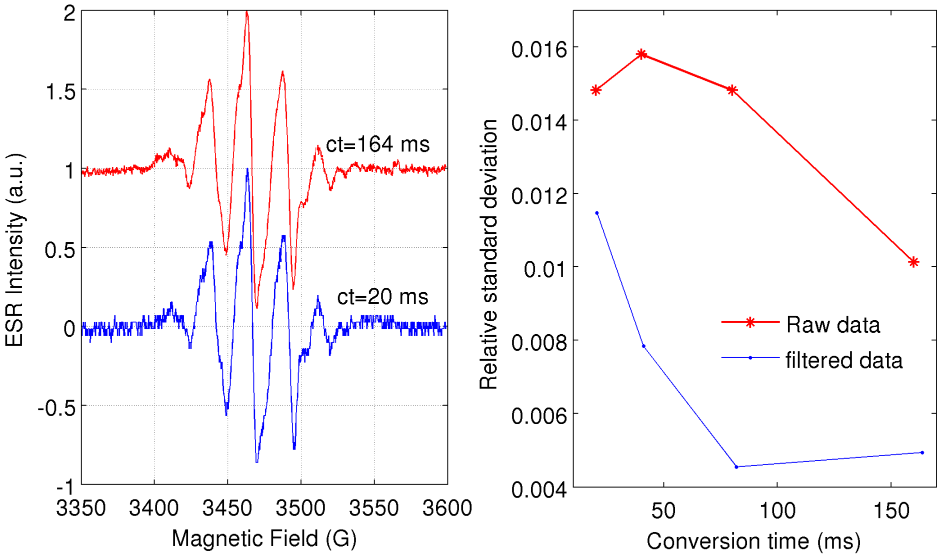

FIGURE 3.17: Improvement in the signal to noise ratio of the ESR spectrum as the conversion time increases (left) and impact of the conversion time in signal repeatability (right).

We can see in Figure 3.17 that as the conversion time increases, the signal to noise ratio of the spectrum and the repeatability improve, a behavior which was rather expected. However, if the conversion time is too long, possible instabilities occurring in the spectrometer can only affect a small part of the spectrum, being difficult to detect if they arise, for example, during the acquisition of the narrow but most intense peaks of the spectrum. In a visit to the alanine dosimetry laboratory of the NPL we were recommended to avoid these kind of effects by choosing a short conversion time, and thus we decided to choose a *ct* of 20.48 ms. The election of both these conversion time and number of data points per spectrum determines a sweep time of 20.97 s per acquisition.

3.2.2.3 Time constant

The time constant, tc, is a parameter associated to the low-pass filter that is coupled to the diode detector to suppress high frequency noise. This filter basically slows down the spectrometer response time, being the signal less affected by noise as the time constant is increased. However, if the time constant is too long with respect to the conversion time, signal distortions and shifts in the magnetic field of resonance can arise, and closely spaced signal structures can be excessively filtered presenting apparent lower intensities.

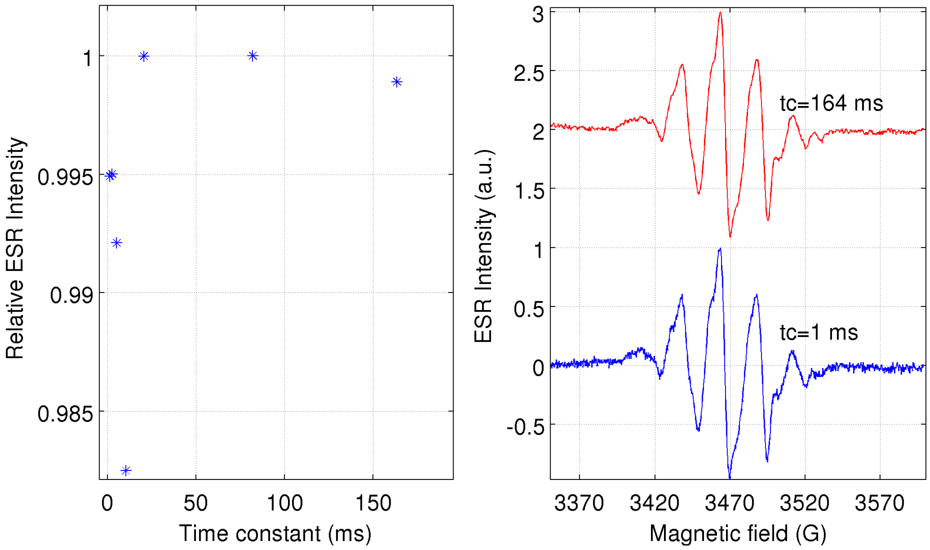

FIGURE 3.18: Relative ESR signal intensity (normalized at $tc = 20.48$ ms) versus the spectrometer time constant (left). Decrease in the noise exhibited by the ESR spectra measuerd at $tc = 163.84$ ms with respect to that at $tc = 1.28$ ms, no signal distortion is appreciated (right). The conversion time was 20.48 ms in both cases.

The optimization of time constant for the alanine dosimeters readout was performed by measuring the ESR signal intensity of the pellet spectrum with a conversion time of 20.48 ms and different time constants ranging from 1.28 ms to 163.84 ms. Excessive filtering could be detected by the decrease the peak to peak intensity of the alanine spectrum, but as we can see in Figure 3.18, this was not the case in our measurements even for the highest time constant studied, neither we observed any shifts in the field of resonance of the sample.

Trying to find the best methodology for the data analysis, the application an off-line noise filter to delete the high frequency components of the spectrum was studied, but changes in the frequency cut-off were observed to introduce variations of around a 0.1% in the signal repeatability. As any of the investigated time constants can be chosen without compromising the quality of our ESR measurement, we decided thus to choose a 163.84 ms *tc*, a rather long time constant, so we could suppress any further noise filtering from our data analysis.

3.2.2.4 Microwave power

The ESR signal intensity measured by the diode increases with the microwave power. However, if the microwave power is too high, the magnetization relaxation times become longer than the time between microwave pulses and the signal saturates, being its intensity lowered and experimenting a broadening distortion. Moreover, at high microwave powers, heating effects in the resonant cavity can adversely affect the machine stability and produce changes in the moisture content of pellets during measurement. This implies that in order to measure spectral lineshapes, linewidths and intensities accurately, the spectrometer should not operate in the saturation regime. For power values below 1 mW the signal is proportional to the microwave power, while a square root dependence is observed above that value until the saturation regime is reached. A compromise to get good signal to noise ratios without signal distortion or spectrometer instabilities is ensured through the spectrometer operation in the upper part of the square root dependence region.

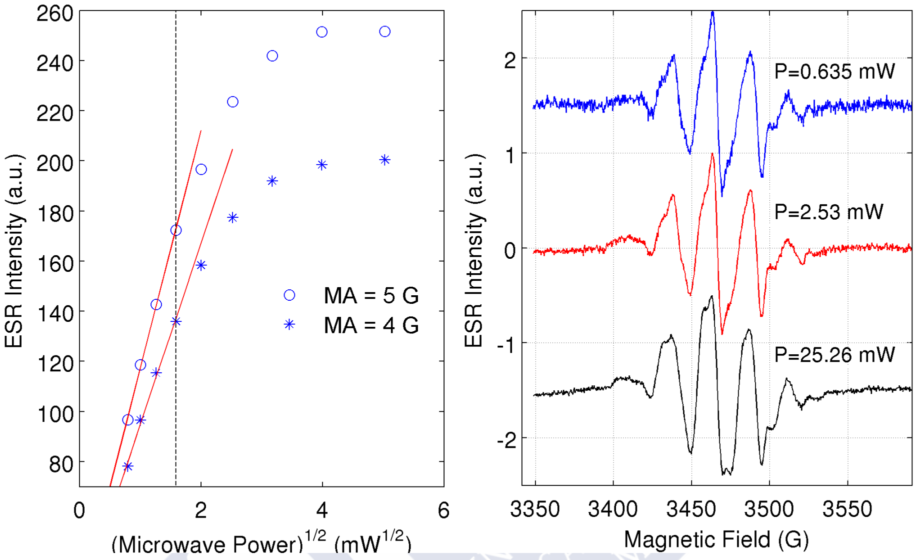

FIGURE 3.19: (Left) Peak-to-peak intensity of alanine ESR spectra versus the square root of the spectrometer microwave power, the linear fit performed with low values of microwave power shows the departure from the square root regime for power values above 2.53 mW, MA stands for modulation amplitude. (Right) Improvement in the signal to noise ratio of the ESR spectrum from P=0.6 mW to P=2.53 mW and distortion of the signal for P=25.26 mW.

An experimental determination of the optimal microwave power was addressed by measuring the signal intensity of a pellet irradiated to 50 Gy for different values of microwave power. Two values of modulation amplitude, close to that employed for alanine dosimetry in the therapy dose range at the NPL laboratory, were considered in this study given the correlation between these two parameters.

Figure 3.19 shows the dependence of signal intensity on microwave power as well as the improvement in the signal to noise ratio as the microwave power increases and the eventual distortion in the signal shape at very high microwave powers.

As a high microwave power within the square root regime ensures a good SNR with no signal distortion, consecutive linear fits of signal intensity versus the microwave power square root were performed, progressively including higher microwave power values, in order to evaluate the departure from the linear regime in the spectrometer operation. A microwave power of 2.53 mW was considered to ensure optimal spectrometer operation avoiding saturation and was thus chosen for future measurements.

3.2.2.5 Modulation amplitude

The magnetic field modulation employed in the phase sensitive detector to filter electrical interference and noise affects also the ESR signal intensity. As the modulation amplitude (MA) increases so does the intensity of the ESR signal, although above a certain threshold comparable to the signal linewidth the signal broadens and becomes distorted. Undesired heating effects can also arise in the cavity at high modulation amplitudes, leading to spectrometer instabilities and the drying of the dosimeters during measurements. Modulation amplitude should be kept under the width of the narrowest ESR structure that we want to resolve, noted here as ΔB (which in the case of alanine dosimetry is the central peak-to-peak width). Taking into account that our alanine signals have $\Delta B \approx 8$ G, spectral acquisitions were performed with modulation amplitudes below 7 G, to check whether the level of signal distortion remained acceptable. This study was underwent for two values of microwave power due to the correlated contribution of both parameters to the signal intensity.

As it can be seen in Figure 3.20, substantial decrease in the noise is observed as the modulation amplitude increases, and no important distortions were

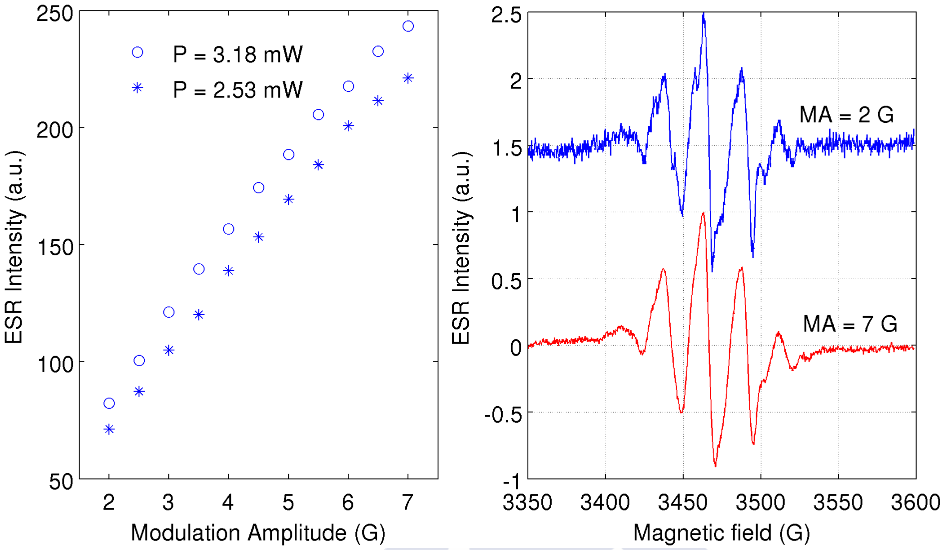

FIGURE 3.20: (Left) Peak-to-peak intensity of alanine ESR spectra for different values of magnetic field modulation amplitude. (Right) Improvement in the signal to dose ratio of the ESR spectrum from $MA = 2$ G to $MA = 7$ G, no signal distortion can be appreciated.

detected even for the largest value of modulation amplitude investigated here.

3.2.2.6 Signal isotropy

Alanine is an orthorhombic crystal that exhibits different ESR spectra depending on its orientation relative to the three axes of the crystalline structure. Alanine polycrystalline powder made of randomly oriented small crystals, with low granulometry (average grain size $< 200\ \mu$m) and a sufficiently high number of grains, behaves as a liquid sample with stable radicals and exhibits a sinusoidal theoretical intrinsic anisotropy with period π [96]. Variations from this angular response arise however in alanine dosimeter pellets (60 mg samples). On one hand, the number of grains is not high enough and the sample does not behave as truly polycrystalline. Deviations from the periodic sinusoidal response are supposed to be also due to inhomogeneities in the alanine-binder admixture and to the instability of radicals at the surface of grains: rearrangements and transformations from one radical into another are observed, being increased when the distance between grain surfaces is decreased in the powder compacting process performed during manufacturing [97]. This implies that different anisotropies can be found depending on the pellet manufacturing process.

The anisotropy of the alanine pellets is considered for ESR signal quantification through the acquisition of several ESR spectra at different orientations of the sample, by rotation of the dosimeter around the vertical axis of the cavity. The intensity corresponding to different orientations is then averaged. The time required to acquire several spectra at different orientations per pellet is however a limiting factor, as it is preferable to complete a measurement campaign, involving tens of dosimeters, in one single day to avoid effects in the measurements due to changes in ambient conditions.

Two pellets respectively irradiated to 90 and 60 Gy were investigated to assess the anisotropy of our dosimeters. Several spectra were acquired at 18 different orientations per dosimeter (from 0° to 360 ° in steps of 20°)[3]. The variation observed in the peak-to-peak signal intensity with the orientation of the pellets is shown in Figure 3.21, where type A uncertainties were calculated at each orientation from the standard deviation of five repeated measurements. We can observe deviation from the theoretical sinusoidal shape with period π in the response of our pellets, although a certain symmetry persists in the pellet irradiated to 90 Gy, which has lower associated uncertainties. The effect of using the average intensity from the signal amplitude measured at a different number of pellet orientations was then analyzed considering two angular samplings, 180° or 360°.

---

[3] We should note here that the orientations are relative to the initial positioning of the pellet, which is totally arbitrary.

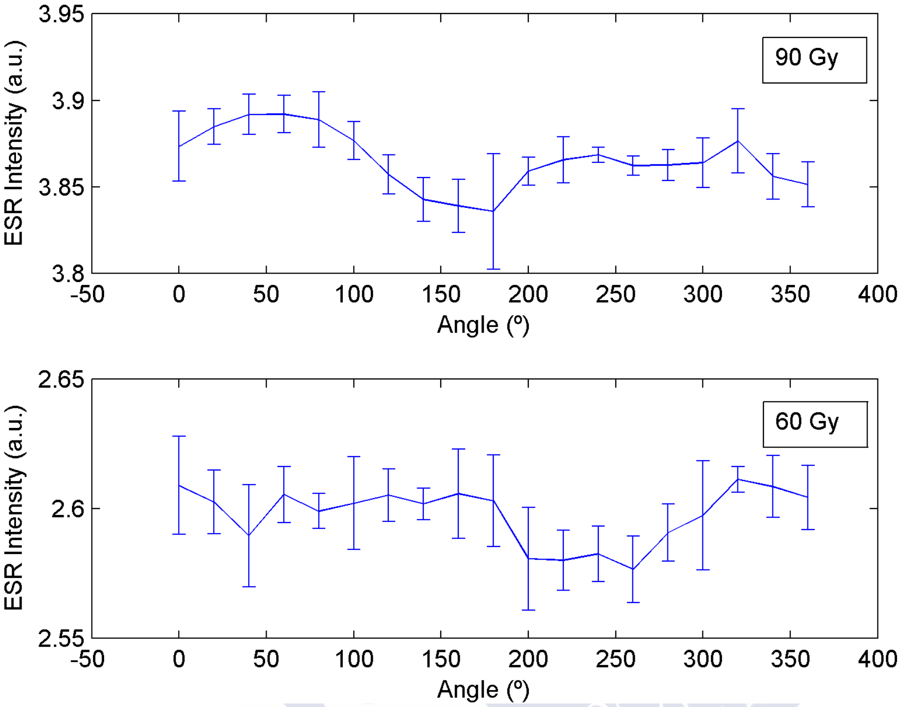

FIGURE 3.21: Signal intensity of two alanine pellets irradiated to 90 and 60 Gy, top and bottom respectively, versus their orientation inside the ESR cavity.

Different samples of average amplitudes were calculated considering up to 9 investigated angles. From a random initial position, the angular sampling was performed considering from 2 to 9 equally spaced positions in a 180° or 360° interval. The average amplitude was then computed from the signal intensity corresponding to every sampled position through interpolation from the measured signal, taking into account the type A uncertainty of the measurements. This procedure was repeated 1000 times to calculate the standard deviation associated to the average amplitude calculated for the different number of orientations, Figure 3.22. We can see how the standard deviation of the mean amplitude decreases as the number of orientations increases. An overall smaller standard deviation is achieved when the sampling is performed in the 360° interval. When two pellet orientations are considered the result is however different, as here the 180° sampling leads to a smaller standard deviation, probably due to the persistence of certain periodicity with π in the anisotropy of the pellets.

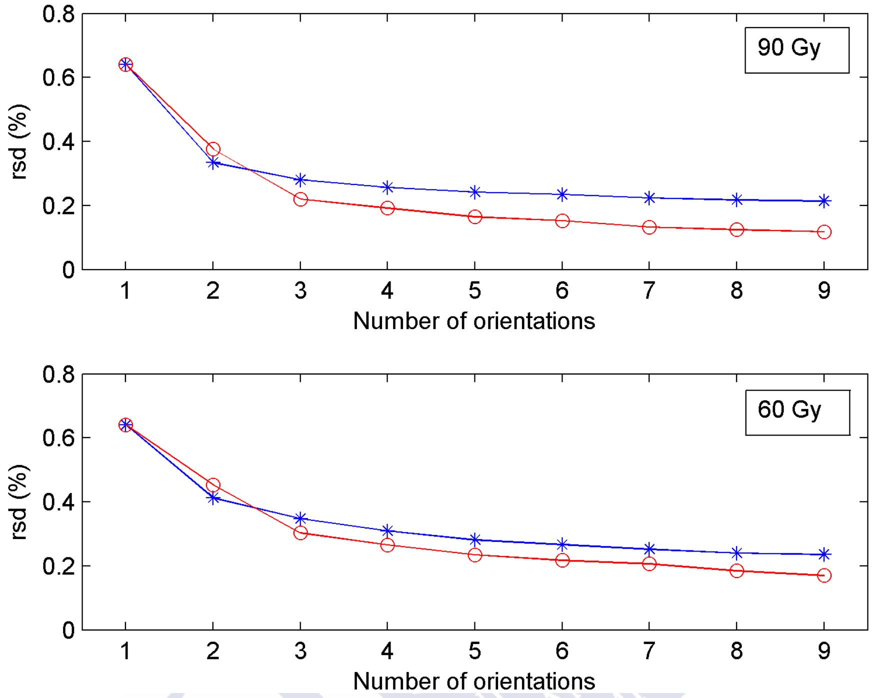

FIGURE 3.22: Relative standard deviation of the average peak-to-peak signal intensity of two alanine pellets, irradiated to 90 and 60 Gy respectively, versus the number of pellet orientations employed for the signal quantification, two angular samplings are employed, 360° (○) and 180° ($*$).

As we said time is a limiting factor in the measurement of ESR signals from a high number of alanine dosimeters, and thus we decided to include in our measurement protocol the acquisition of spectra at two perpendicular orientations per pellet. This is also the procedure at other alanine dosimetry services [79, 98], although the acquisition of spectra at a higher number of orientations is usually preferred [99]. If the time required for the measurement process could be reduced, for example through the installation of an automated sample changer in the spectrometer, the acquisition of spectra at a higher number of orientations may be addressed.

Spectrometer Parameters	Before Optimization	After Optimization
Sweep width	500 G	250 G
Resolution	2048 points	1024 points
Conversion time	81.92 ms	20.48 ms
Time constant	40.96 ms	163.8 ms
Microwave Power	1.006 mW	2.53 mW
Modulation Amplitude	5 G	7 G
Number of pellet orientations	1	2

Table 3.1: ESR spectrometer parameters employed before and after optimization for alanine dosimetry applications in the therapy dose range.

3.2.2.7 Measurement protocol

A basic co-addition method for signal to noise ratio enhancement is also included in the measurement protocol, involving the acquisition of three spectra at each of the two orientations of the alanine pellet inside the cavity. The spectrometer automatically averages the three values of adc counts related with the absorption of microwaves by the sample at every level of magnetic field strength, yielding an average spectrum per pellet orientation. Considering the resolution and conversion times selected, six spectra are acquired in a total time of 125.82 s per pellet, although some time is required for the rotation, re-coupling of the cavity, an data saving.

The optimization of spectrometer parameters addressed in this section allows a substantial improvement, of a factor of approximately 7.7, in the signal to noise ratio of the ESR alanine spectra, see Figure 3.23. Table 3.1 summarizes the changes introduced in the spectrometer parameters in comparison to the initial ones, which would be appropriate for other applications where spectrometer sensitivity and stability are not that critical, for example when the interest is focused in the shape of the ESR spectrum, or even for alanine dosimetry applications at higher dose ranges (of the order of kGy) that involve more intense alanine dosimeter signals.

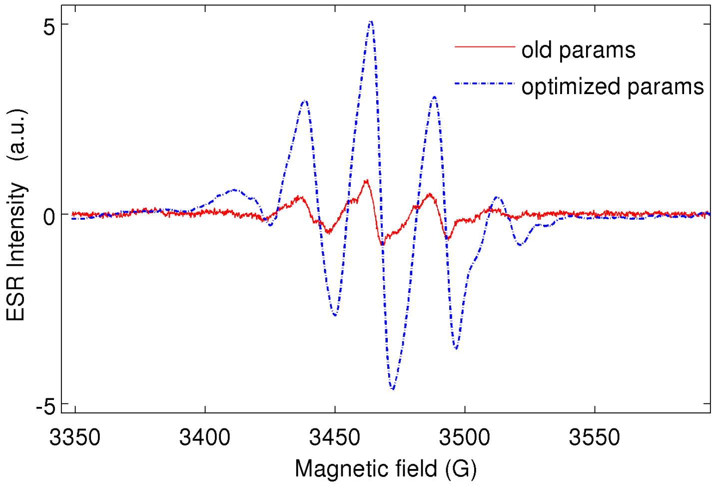

FIGURE 3.23: Improvement in the signal to noise ratio of the alanine ESR spectrum obtained through the optimization of the spectrometer parameters.

3.2.3 Construction of the alanine calibration curve

Once the optimal ESR parameters for alanine dosimetry applications at the therapy dose range are determined, we can proceed to construct the first calibration curve, which in this case included seven calibration points. Alanine dosimeters were irradiated in the cobalt unit to achieve the desired values of absorbed dose to water: 10, 20, 30, 40, 50, 60 and 90 Gy. Three pellets were irradiated at every dose level for repeatability purposes, leading to a total of 21 irradiated pellets. The recommended 72 h period was respected before proceeding to the measurement of the ESR signals to allow radical stabilization in the dosimeters. Measurements in the ESR spectrometer were then carried out following the above mentioned measurement protocol. Six spectra were acquired per pellet with a 90° rotation of the pellet inside the cavity between the third and the fourth acquisition, and spectral acquisitions alternating pellets with different values of absorbed dose were performed in order to avoid possible changes in the ambient parameters of the laboratory to affect only one part of the calibration curve.

3.2.3.1 Alanine background signal

The presence of a background signal in the alanine dosimeters spectra must be taken into account for the construction of the calibration curve.

Several contributions are responsible for this background signal, also referred to as baseline. On one hand, the components of the setup placed inside the cavity are made of materials specifically chosen to yield no ESR signals, like the high fused quartz tubes. Measurable ESR signals can however arise associated to them and to the presence of small amounts of contamination inside the cavity. Additionally, unirradiated alanine dosimeters also exhibit a measurable ESR signal due to the existence of alanine endogenous radicals, usually related with the dosimeters manufacturing process. The signal of unirradiated dosimeters is observed to vary between manufacturers and, to a much lesser extent, between dosimeters from the same manufacturer.

The quantity of interest in alanine dosimetry is the signal intensity corresponding only to radiation induced radicals thus subtraction of the background signal from the spectra of irradiated alanine dosimeters has to be performed. Measurements of this weak background signal are highly affected by spectrometer instabilities arising from temperature and humidity variations, small differences in the water content of the pellets, and the alanine dosimeters anisotropy, contributing all these factors to potential discrepancies between the signal measured for different unirradiated dosimeters. The measurement of the background signal was performed through the acquisition of several spectra from three unirradiated pellets. Two orientations and six acquisitions per pellet were again considered. A fourth order polynomial fit to the average of these background spectra was employed to model the baseline as shown in Figure 3.24.

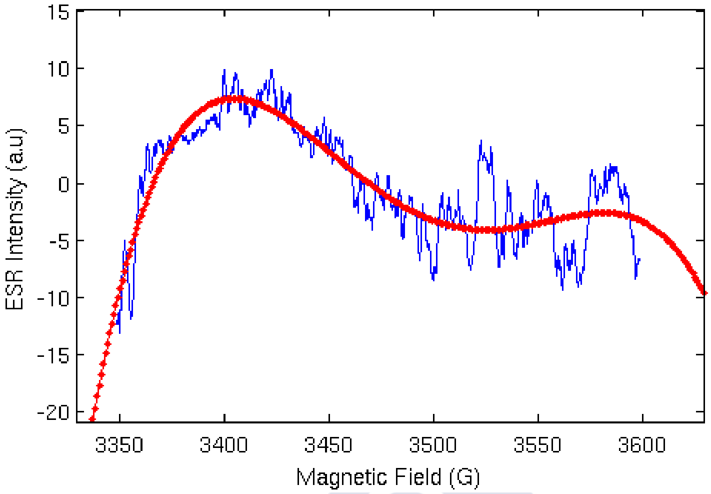

FIGURE 3.24: Average alanine background spectrum, calculated from three unirradiated alanine dosimeters (solid line) and 4th degree polynomial fit employed for the modelization of the alanine baseline (·).

3.2.3.2 Alanine ESR signal quantification

After the measurement of the pellets ESR spectra, which was performed with the spectrometer parameters detailed in Table 3.1 and spectrometer gain equal to 1.002 10^4, quantification of the dosimeters ESR signal intensity was performed in two different ways. On one hand, the peak-to-peak signal intensity was calculated after simple subtraction of the baseline from the average spectrum of each dosimeter at each of the investigated orientations. The other method used to quantify signal intensities involved the comparison of a reference alanine spectrum with the signal of every dosimeter involved in the calibration for the calculation of the proportionality factor existing between them through a least squares minimization. The reference spectrum here employed is the signal of an alanine dosimeter irradiated to a high value of dose, 90 Gy in our case, exhibiting a high signal to noise ratio. The baseline was also subtracted to this reference spectrum before comparison with other spectra.

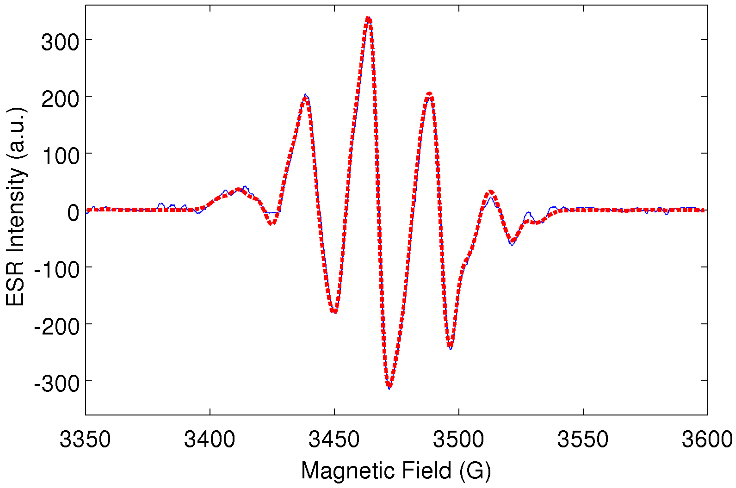

FIGURE 3.25: Comparison of the reference spectrum obtained from a pellet irradiated to 90 Gy, in dashed line, and the renormalized signal of a dosimeter irradiated to 20 Gy, solid line. The normalization factor minimizing the reduced Chi square is employed for signal quantification.

This method, proposed by Sharpe *et al.* [79] and exemplified in Figure 3.25, lies on the assumption that the alanine spectral shape is the same independently of the dose deposited in the dosimeter. Comparison with a clean reference signal can be thus of great help for signal quantification when the dose decreases below 10 Gy and the dosimeters signals become more affected by noise.

As the resonant frequency can vary between measurements due to differences in the cavity QF arising from changes in the dosimeters water content or laboratory ambient humidity [92], x-axis alignment with respect to the reference signal is performed for all the dosimeters spectra by finding the translation that maximizes the correlation between both signals.

For signal quantification, the peak-to-peak ratio between the investigated signals and the reference spectrum is initially employed as an approximated proportionality factor, being this value varied until the reduced Chi-square of the fit, expressed by Equation 3.27, is minimized.

$$\chi^2_{red} = \frac{1}{n-2} \sum_{i=1}^{n} \frac{(f_i - a s_i)^2}{\sigma_i^2} \tag{3.27}$$

In this equation s_i and f_i are the signal intensities of the investigated and reference spectra respectively, and σ represents the noise amplitude, obtained as the standard deviation of the experimental signal over 100 points in a region with no significant ESR signal.

For the construction of the calibration curve, some transformations have to be still applied to the alanine dosimeter intensities determined through any of the methods above described. First of all, and considering Equation 3.2, normalization of the ESR intensities by the mass of the pellets has to be performed. Taking into account that two orientations of every pellet with respect to the cavity were investigated for every set of the three dosimeters irradiated at each dose level, the mean, mass normalized ESR intensity would be expressed as:

$$\overline{\left(\frac{I_{ESR}}{m}\right)} = \frac{1}{3} \sum_{i=1}^{3} \frac{(I_{ESR})_{i,0^\circ} + (I_{ESR})_{i,90^\circ}}{2m_i} \tag{3.28}$$

Additionally, our calibration curve has to be referred to a single irradiation temperature, T_0, see Equations 3.5 and 3.6, arbitrarily chosen as reference. Since the pellets corresponding to the different dose levels were irradiated at slightly different temperatures, a temperature correction k_T, described by Equation 3.6, has to be applied to the mean value of the mass normalized ESR intensities, leading to the expression:

$$D_{w,{}^{60}Co} = C_{{}^{60}Co,T_0} \overline{\left(\frac{I_{ESR}}{m}\right)}_{{}^{60}Co,T_0} = C_{{}^{60}Co,T_0} k_T \cdot \overline{\left(\frac{I_{ESR}}{m}\right)}_{{}^{60}Co,T} \tag{3.29}$$

Corrections related with the dosimeters signal fading do not have to be applied as long as all the dosimeters, not only those employed to construct the calibration curve but also those employed to measure absorbed doses to water through the calibration curve, were irradiated the same day, kept in identical ambient conditions and measured in the ESR spectrometer within the same day. Besides the fading, this methodology intends to minimize spectrometer sensitivity variations related with changes in the laboratory ambient parameters that are difficult to correct. Other solutions have been developed that involve the use of a sample, made of a reference substance, that is placed in the cavity during the alanine dosimeter measurements to correct for the spectrometer instabilities, as they can be detected by the changes exhibited by the intensity of the reference sample [100].

3.2.3.3 Calibration uncertainty budget

All the uncertainties involved in this work were evaluated according to the Guide to the Expression of Uncertainty in Measurement [101] and are here expressed at one standard deviation (k=1). The sources of uncertainty that have to be considered in the construction of the alanine calibration curve can be easily classified as being associated to the determination of the absorbed dose to water corresponding to the pellets irradiation or to the quantification of the ESR signal intensities.

Determination of absorbed dose to water associated uncertainties:

Regarding the deposition of dose in the pellets during their irradiation in the ^{60}Co unit, the uncertainty mainly comes from:

a. **Dose rate determination.**

   The ionization chamber employed for the determination of the ^{60}Co unit dose rate was calibrated at the PTB primary standard, with a relative uncertainty associated to the calibration coefficient of 0.25%.

After appropriate corrections to the ionization chamber measurement, due to polarization and ambient condition changes (k_{TP}), the global uncertainty associated to the determination of dose rate is 0.3%.

b. **Detectors positioning.**

An estimated accuracy of 0.2 mm is considered for the positioning of both the alanine holder and the ionization chamber in the beam propagation axis, which will involve a corresponding standard uncertainty u_{pos} equal to 0.16 mm considering a rectangular distribution. Additionally, the insert where the pellets are placed for irradiation has an inner diameter of (5.435 ± 0.037) mm, and the pellets have a diameter of (4.82 ± 0.01) mm, variations in the position of the pellets inside the holder were thus supposed to follow a rectangular distribution with full width (0.614 ± 0.038) mm. The total uncertainty associated to positioning, obtained through propagation of the uncertainty in the position of the pellets inside the insert and the positioning of the insert itself, amounts to 0.39 mm. The ^{60}Co dose gradient at 5 cm depth, of 0.50% mm^{-1}, can be used to calculate the impact of the positioning uncertainty in the determination of absorbed dose to water in every pellet, estimated to be 0.2%. In the axis that are perpendicular to the direction of beam propagation, the effect of the positioning accuracy is neglected given the high uniformity of the 10 cm×10 cm field dose profile.

c. **Irradiation time.**

The irradiation times needed to achieve the desired values of absorbed dose to water involved in the calibration curve were calculated from the unit dose rate, 0.349 Gy/min for this calibration, once the ^{60}Co source is already placed at the irradiation position in the unit head. An uncertainty of 0.5 s is estimated for the determination of the irradiation time, leading to an uncertainty in the dose of 2.9 $\times 10^{-3}$ Gy (0.03% in 10 Gy).

Additionally, it has to be taken into account that the path travelled by the source from its shielded position at rest to the irradiation position at the unit head has an associated dose rate that is not zero. The pellets, already positioned in the water tank for irradiation during the source transit, will receive an extra dose that has to be considered. Assuming a linear increase in the dose rate during the source transit, which lasts 2.4 seconds on average, this extra dose can be calculated as the dose rate divided by the source transit time. This quantity, amounting to a 0.14% in 10 Gy for the 0.349 Gy/min dose rate of the ^{60}Co during this calibration, could be included for the calculation of the total absorbed dose to water. However, the time of transit of the source can fluctuate depending on the pressure of the pneumatic system moving the source, and this extra dose to the pellets will be thus considered as a maximum uncertainty for its inclusion in the budget.

d. **The radioactive decay of the ^{60}Co source.** Finally, the unit dose rate decreases during an irradiation campaign due to the radioactive decay of the ^{60}Co source, half life (1925.20±0.25) d, diminishing approximately a 0.04% per day, independently of the dose rate [102]. The contribution of the source decay to the uncertainty in the determination of absorbed dose to water is negligible when compared with the other sources of uncertainty, and it was therefore not taken into account.

ESR signal quantification associated uncertainties:

Regarding the quantification of the ESR signals, the sources of uncertainty will mainly come from:

a. **Pellets temperature during irradiation.**

The concentration of radicals in the alanine dosimeters depends on the irradiation temperature. The preconditioning addressed in order to control the temperature of the pellets during irradiation was described in Section 3.2.1.1 and consists in letting the pellets stabilize to the irradiation room temperature. The water tank temperature is registered during every irradiation and employed to correct the ESR signal intensities for relative radiation yield variations. The temperature of the water tank is however between 0.7°C and 1°C lower than that of the air in the room when both are in thermal equilibrium, but we cannot let the pellets reach the thermal equilibrium with the water tank since this would take hours and the time needed for a measurement campaign would be unaffordable. Due to this, we can expect variations within 1°C in the temperature of the pellets with respect to the temperature in the water tank during irradiation, which would imply an uncertainty in temperature of a 0.29°C. The uncertainty associated to the temperature correction, k_t, that is applied to the ESR readings, amounts in this case to 0.05%, a value that is obtained from the uncertainty associated to the measurement of the temperature and the uncertainty associated to the temperature coefficient, c_T, by applying the laws of error propagation.

b. **The mass of the pellets.**

The alanine pellets were weighted with a microscale with 0.1 mg precision after having performed the ESR spectrometer measurements in the first calibration campaign. The relative standard deviation in the distribution of masses within the 24 measured pellets was found to be 0.3%, a value that is considered to be low enough to discard the need of preselecting the pellets by mass for the construction of the calibration curve. This check should have been done before irradiation to avoid possible outliers, and that was the procedure implanted since then. The uncertainty associated to the measurement of the mass of the pellets was quantified from the precision of the micro scale and the standard deviation of the mass measurements for every single pellet, obtained by measurement repetition, which amounted on average to a 0.15% of the mass of the pellet. This lead to a total uncertainty associated to the mass of the pellets of 0.16%.

c. **The spectrometer.**

The uncertainty associated to the measurement of the alanine ESR signals in the spectrometer is due to different contributions like the positioning of the pellets in the vertical axis of the cavity, anisotropies in the dosimeters remaining after having averaged the signal from two positions of the pellet inside the cavity, Section 3.2.2.6, and the stability of the spectrometer, which is affected by the ESR parameters, the water content of the pellets, and the temperature of the magnet and bridge water cooling system. As separation of these contributions would be rather complicated, they have been evaluated altogether by performing several measurements and computing their standard deviation. At each dose level, the size of a statistical sample made of only six signals, two spectra corresponding to each of the three pellets involved, could be questionable. However, the methodology followed in this work was designed to obtain an alanine calibration curve on one day of ESR measurements, and increasing the number of replicate pellets to four at each calibration point would be excessively time-consuming.

Table 3.2 presents a summary of the different sources of uncertainty that are considered for the construction of this alanine calibration curve.

Uncertainty source	**Type**	u_r (%)
1. Pellets irradiation		
Dose rate determination	B	0.3%
Positioning	B	0.2%
Irradiation time	B	2.9×10^{-3} Gy (0.03% in 10 Gy)
^{60}Co source transit	B	0.014 Gy (0.14% in 10 Gy)
2. ESR signal quantification		
Irradiation temperature	B	0.05%
Mass of the pellets	A	0.16%
Spectrometer	A	0.9% or 0.6% in 10 Gy*

TABLE 3.2: Summary of the sources of uncertainty involved in the construction of the alanine calibration curve, k=1. * The two uncertainties associated to the measurement of the ESR signal are respectively obtained through the peak-to-peak method for signal quantification and through the method involving a reference signal.

3.2.3.4 Calibration fit

The calibration curve was constructed through a least squares linear fit to the several pairs, 6 in this case, of absorbed dose to water values, D_w, and mass normalized and temperature corrected ESR intensities $\overline{(I_{ESR}/m)}_{^{60}Co,T_0}$, noted here by A_{esr} for abbreviation.

$$A_{esr} = a + b \cdot D_{w,^{60}Co} \tag{3.30}$$

Regarding the linear fit, the ordinary least squares method assumes that the abscissa values (dose to water here) have no associated uncertainty and the ordinate values (ESR intensity) follow a normal uncertainty distribution. In our case, however, the uncertainties associated to the ESR intensities increase, even when considered relative to dose, as the dose in the dosimeters decreases.

At high dose levels the uncertainty associated to the ESR signal of alanine dosimeters has been observed to remain constant relative to dose [83], but at low dose levels, specially below 10 Gy, this is no longer observed. In this regime, measured signals are more importantly affected by the spectrometer high frequency noise, and the signals baseline becomes affected by low frequency distortions arising from the cavity/holder and the dosimeter itself, being this latter contribution variable from dosimeter to dosimeter [79]. These contributions make the relative uncertainty associated to the ESR intensity to increase as the dose level decreases.

Under this situation, the application of a weighted least squares method for the fit of the calibration curve would be adequate. Moreover, as the uncertainties associated to the absorbed dose to water and to the ESR intensities are of the same order of magnitude, a method weighting both sources of uncertainty was considered to be the most appropriate strategy. The least squares method proposed by York *et al.* [103] was followed for the determination of the slope, intercept, and standard errors of our alanine calibration fit.

The alanine calibration curves that were built with the two studied methods of signal quantification are shown in Figure 3.26. Signal intensities corresponding to 60 Gy are normalized to unity for both methods to allow comparison in the figure, although fitting parameters, presented in Table 3.3, were obtained without such a normalization.

Very similar results are obtained in the fits corresponding to the two methods of signal quantification. The intercepts, a, yielded values compatible with zero in both cases, $u(a)/a$=180% and $u(a)/a$=240% for the method involving the reference signal and the peak-to-peak respectively, indicating that an effective baseline subtraction was applied to the pellets for the quantification of the ESR signals. Errors associated to the slope are however slightly lower for the method involving the comparison with the reference signal, $u(b)/b$=0.76%, compared with the value $u(b)/b$=0.84%

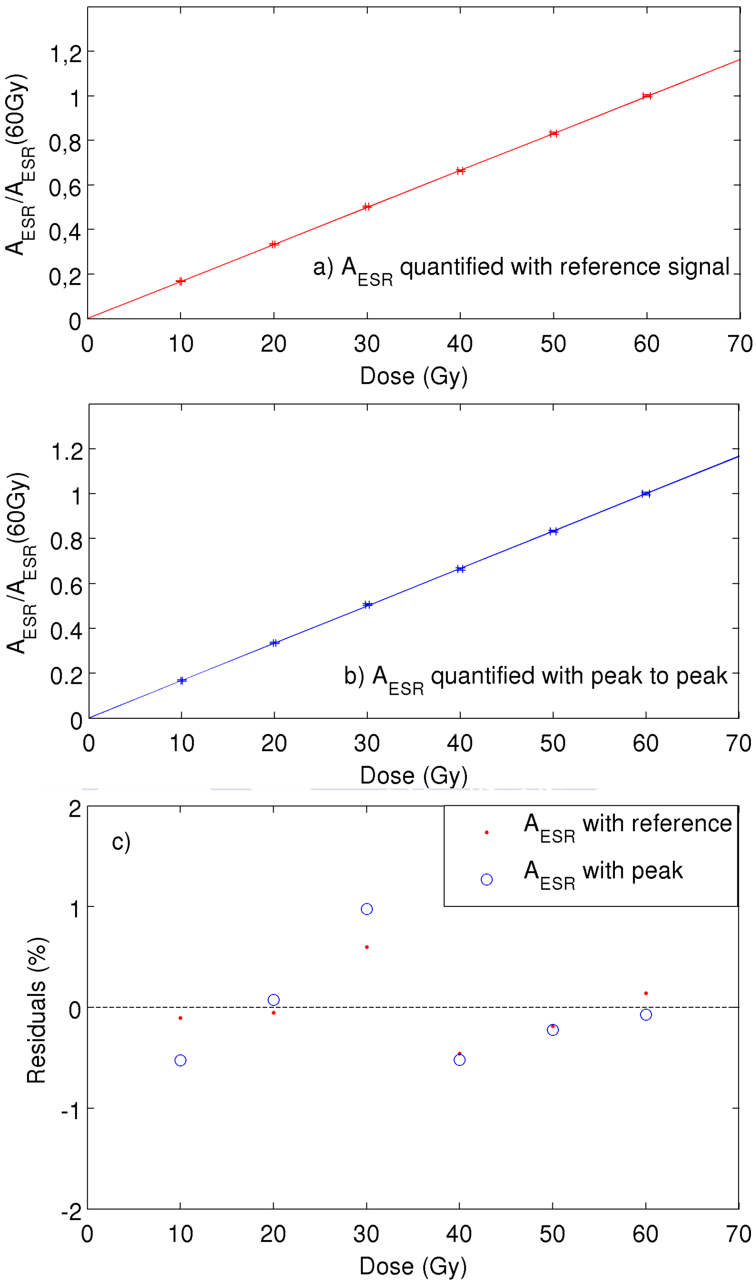

FIGURE 3.26: Calibration curves constructed from the two methods for ESR signal quantification a) proportionality factors existing between the signals and the reference signal f_{ref} and b) the peak-to-peak intensity of the signals. c) Residuals obtained from the two linear fits, expressed relative to the value of A_{ESR} obtained with each respective fit at every dose level.

Signal Quantif. Method	Peak-to-peak	Prop. factor f_{ref}
a	66 adc	1.5×10^{-2}
$u(a)$	121 adc	3.5×10^{-2}
b	537.6 adc Gy^{-1}	$1.871\times10^{-1}\mathrm{Gy}^{-1}$
$u(b)$	4.5 adc Gy^{-1}	$0.014\times10^{-1}\mathrm{Gy}^{-1}$
$\mathrm{cov(a, b)}$	-4.64×10^{-2} adc Gy^{-1}	$-4.17\times10^{-5}\mathrm{Gy}^{-1}$

TABLE 3.3: Parameters from the calibration obtained through the two methods of ESR signal quantification.

obtained with the peak-to-peak method. This is due to the lower scatter achieved in the signal quantification through this method.

A check of the alanine signal-to-dose linearity can be performed through the analysis of the residuals corresponding to these fits, where a sample of residuals following a normal distribution centred at zero would indicate a good agreement between the linear fit and the calibration data. Being our sample rather small to perform a valid normality test, the distribution of residuals is directly presented in Figure 3.26, with residuals lying below and above zero from point to point and no systematic deviations observed. Furthermore, a χ^2 test performed to study the goodness of the fit yielded χ^2 values equal to 0.72 and 1.25 for the calibration methods involving the reference signal and the peak-to-peak intensities respectively. From them, reduced χ^2 values (χ^2 over the number of degrees of freedom) of 0.18 and 0.31 can be obtained considering the four degrees of freedom in our fit. As the reduced chi square would be close to one whenever the estimated uncertainties are an accurate representation of the error in the data, the results here obtained, both below one, would suggest a small overestimation in our uncertainties.

Determination of dose

Once a calibration curve has been established, the values of absorbed dose to water corresponding to the ESR signal exhibited by irradiated alanine dosimeters can be directly calculated using the fit parameters a and b:

$$D_{w,^{60}Co} = \frac{1}{b} \cdot A_{esr} - \frac{a}{b} \tag{3.31}$$

The uncertainty associated to this indirect measurement of absorbed dose to water can be expressed according to the laws of error propagation as:

$$u(D_{w,^{60}Co}) = \frac{1}{b}\sqrt{u(A_{esr})^2 + u(a)^2 + D^2_{w,^{60}Co} \cdot u(b)^2 + 2 \cdot D_{w,^{60}Co} \cdot \mathrm{cov(a, b)}} \tag{3.32}$$

From our best linear fit, uncertainties in the determination of absorbed dose to water using irradiated alanine pellets and this alanine calibration curve are estimated to range from 1.2% at 50 Gy to 2.8% at 10 Gy, although this can slightly vary for other dosimeters, as for them the quantification of ESR signal would be affected by slightly different uncertainties.

3.2.3.5 Improvements in the system

After the construction of the first calibration curve, several actions were identified that could be addressed in order to reduce the uncertainty of the measurement system.

a. **The spectrometer.**

One of the largest contributions to the uncertainty in the determination of dose with the alanine/ESR system comes from measurement of the ESR signal, see Table 3.2, and enhancing the stability of the spectrometer can contribute to improve the quality of the ESR measurement. The water cooling system used to avoid overheating in the spectrometer magnet and bridge plays an important role in alanine dosimetry applications, as changes in the temperature of the water can affect the spectrometer sensitivity. Due to this, many departments install heat exchangers to control the temperature of the cooling water [92, 104]. In our institution, the water for this cooling system came from the building main water supply, passing through the instrument and being not recirculated. The water flow changed depending on the building water demands, leading to uncontrollable temperature variations in the magnet and bridge that unavoidably affected the spectrometer stability. In order to minimize this, a new water cooling system was installed for the recirculation of water from a water tank of 75 L and a temperature control with a precision of 0.5°C.

b. **Irradiation time.**

Regarding the determination of the dose delivered to the pellets during irradiation in the ^{60}Co unit, another reduction of uncertainties can arise from the quantification of the dose delivered to the pellets during the transit of the ^{60}Co source from its shielded position at rest to the irradiation position at the unit head. In last section, an approximated estimation of this extra dose was considered as an uncertainty associated to the dose, but including this quantity as dose to the pellets, with the corresponding associated uncertainty, would be a most accurate determination of the dose. Repeated measurements of the dose at the reference point during the source transit were performed with an ionization chamber located at that point under reference conditions. The ionization chamber current was measured every 0.5 second, registering the dose curve associated to the source transit. The integration of the current curve over the time of source transit multiplied by the dose rate with the source at the full unshielded position leads to the dose associated to the source transit. This measurement was repeated several times and an average value of (0.017 ± 0.002) Gy was determined.

This is of special importance because the ^{60}Co source of the Radiation Physics Laboratory was replaced on November 2012 by one with an activity two times higher than that of the old source. The dose rate was, by the 7th of August 2013, equal to (0.758 ± 0.002) Gy/min under reference conditions, what would have lead to an uncertainty associated to the source transit equal to 0.031 Gy (0.3% in 10 Gy) if the estimations addressed in Section 3.2.3.3 were repeated.

c. **The mass of the pellets.**

The uncertainty associated to the determination of the mass of the pellets is another factor to take into account. For the first calibration curve, a microscale with 0.1 mg precision was employed, exhibiting a repeatability of 0.15% in the measurement of 60 mg samples (mass of the pellets). A microscale with the same precision but higher repeatability became available for subsequent campaigns, leading to 0.09% relative standard deviations in the measurement of the pellets. Pellets to be used in the measurement campaign were chosen before irradiation leading to a relative standard deviation in the distribution of masses equal to 0.2%. The uncertainty associated to the measurement of the mass, quantified from the precision of the microscale and the standard deviation of the measurements of every single pellet, lead to a total uncertainty associated to the mass of the pellets of 0.09%.

A new calibration curve was established to check the effect of the changes introduced in the system to reduce the uncertainty. Groups of three pellets were irradiated under reference conditions to dose levels similar to those involved in the first calibration curve: 8.017, 10.017, 20.017, 30.017, 40.017, 50.017, 60.051 and 90.034 Gy (60 and 90 Gy dose levels were achieved in repeated irradiation and thus the dose contribution from the transit source has to be considered several times). The calibration point at 8 Gy was additionally introduced to check the quality of the system at this lower dose level. Moreover, a blind test was included to check the alanine/ESR calibration. This test consisted in the irradiation, by the Radiation Physics Laboratory staff, of two groups of three pellets to different dose levels, whose values were not revealed until the determination of dose was performed through the calibration curve. The total number of pellets involved in the campaign amounted now to 33, organized in 11 groups of 3 pellets each, being seven the groups of pellets used as calibration points, other group used for the 90 Gy reference signal, two groups corresponding to the blind tests and another group of unirradiated pellets employed for ESR background signal determination.

The method addressed for the measurement of the dosimeters in the ESR spectrometer was analogous to that presented in Section 3.2.2.7, involving the optimized operational parameters detailed in Table 3.1. However, the spectrometer gain was now set to 4.48 10^5, instead of the 1.002 10^4 used in the last calibration, being this value low enough to avoid saturation in the most intense ESR spectra exhibited by the pellets irradiated to 90 Gy. The quantification of the ESR signal intensity was determined through the two methods (peak-to-peak and proportionality factor to the reference signal) presented in Section 3.2.3.2.

The uncertainty budget associated to this calibration is detailed in Table 3.4, where we can observe an improvement in the repeatability of the spectrometer after the installation of the recirculated water cooling system.

Uncertainty source	**Type**	u_r (%)
1. Pellets irradiation		
Dose rate determination	B	0.3%
Positioning	B	0.2%
Irradiation time	B	6.3×10^{-3} Gy (0.06% in 10 Gy)
Source transit	B	2.8×10^{-3} Gy (0.03% in 10 Gy)
2. ESR signal quantification		
Irradiation temperature	B	0.05%
Mass of the pellets	A	0.09%
Spectrometer	A	0.6% or 0.4% in 10 Gy*

Table 3.4: Summary of the sources of uncertainty involved in the construction of an improved alanine calibration curve, k=1, after improvement of the system. * The two uncertainties associated to the measurement of the ESR signal correspond to the peak-to-peak method for signal quantification and the method involving a reference signal.

Figure 3.27 shows the results of this calibration, with signal intensities normalized to the signal at 60 Gy to allow comparison in the figure. Fitting parameters, presented in Table 3.5, were again obtained without such a normalization.

Signal Quantif. Method	Peak-to-peak	Prop. factor f_{ref}
a (a.u.)	3.2×10^{3} adc	3.1×10^{-2}
$u(a)$ (a.u.)	3.1×10^{3} adc	1.8×10^{-2}
b Gy^{-1}	2.363×10^{4} adc Gy^{-1}	1.866×10^{-1} Gy^{-1}
$u(b)$ Gy^{-1}	0.015×10^{4} adc Gy^{-1}	0.011×10^{-1} Gy^{-1}
$cov(a,b)$ Gy^{-1}	-3.7×10^{5} adc Gy^{-1}	-1.5×10^{-5} Gy^{-1}

Table 3.5: Parameters from the calibration obtained through the two methods of ESR signal quantification after improvement of the system.

We can observe an important difference between the fitting parameters associated to the peak-to-peak quantification method in the two campaigns

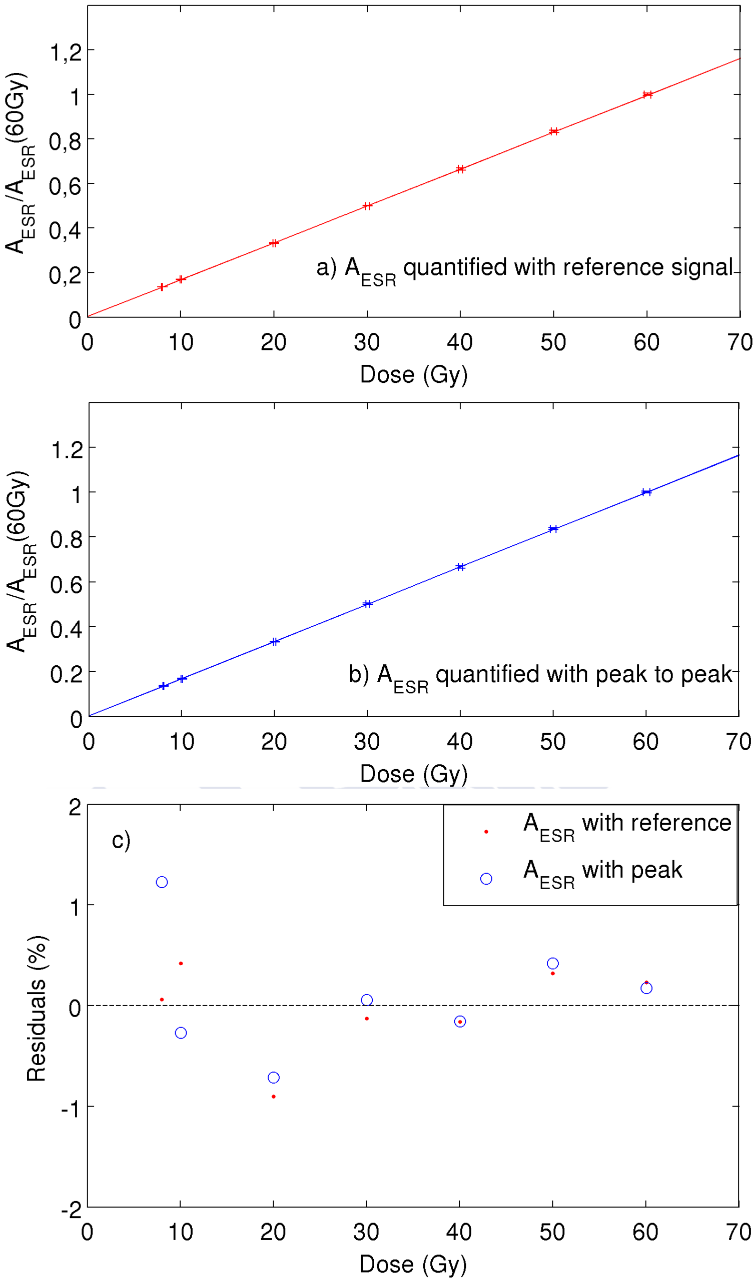

FIGURE 3.27: Calibration curves constructed from the two methods for ESR signal quantification after improvement of the system a) proportionality factors existing between the signals and the reference signal f_{ref} and b) the peak-to-peak intensity of the signals. c) Residuals obtained from the two linear fits, expressed relative to the value of A_{ESR} obtained with each respective fit at every dose level.

(first column of Table 3.5 and Table 3.3). This is due to the change in the spectrometer gain between the two campaigns, being the ratio of gains, equal to 44.7, very close to ratio of the slopes associated to the two calibration curves, which is 44. This values are not equal due to the deviation from one in the slope of signal intensity versus the spectrometer gain.

On the other hand, the errors associated to the fitting parameters are again slightly smaller for the method involving the comparison with the reference signal ($u(b)/b$=0.57% and 0.64% for the methods involving the reference signal and the peak-to-peak respectively).

Intercepts, a, associated to the new calibration curves are not compatible with zero, with relative uncertainties equal to 57% and 95% for the reference signal and the peak-to-peak method respectively, reflecting that the subtraction of background signal from the irradiated dosimeters was not completely effective in this case. The difficulties for background subtraction are however only encountered in the lower dose levels, as it was observed that intercepts compatible with zero are obtained when the calibration point corresponding to 8 Gy is not included to fit the data. This is thought to be due to the low signal exhibited by the dosimeter for dose levels below 10 Gy, where radiation induced radicals become more drastically affected by the background signal. Background subtraction difficulties at low dose levels are confirmed by the work of Sharpe *et al.* [79], where an iterative method is applied to subtract dosimeter dependent base line distortions, claimed to be of main importance at low dose levels. A similar approach to suppress base line distortions could be applied in the future to ensure that only random noise remains when the radiation induced signal and the background signal are subtracted.

Residuals associated to the fit, including the 8 Gy calibration point, are distributed above and below zero, and no systematic deviations are observed, being all below 1% except that associated to the 8 Gy calibration point in the fit corresponding to the peak-to-peak signal quantification. Finally, the χ^2 test performed to study the goodness of the fit yields now χ^2 values equal to 1.0 and 1.3 for the calibration methods involving the reference signal and the peak-to-peak intensities, with corresponding reduced χ^2 values of 0.17 and 0.21 respectively, suggesting again a small overestimation in our uncertainties.

From these calibration, relative uncertainties in the determination of absorbed dose to water can be estimated to range, for the reference signal quantification method, from 1.7% to 0.8% for dosimeters irradiated from 10 Gy to 50 Gy. The peak-to-peak quantification yielded estimated uncertainties ranging from 2.2% to 0.9% for dosimeters irradiated from 10 Gy to 50 Gy.

Regarding the blind test, dose values were estimated from the two calibration curves. When the calibration curve obtained from the reference signal quantification method is employed, dose values amounted to (13.25 ± 0.18) Gy, 1.4% relative uncertainty, and (15.02 ± 0.19) Gy, 1.3 % relative uncertainty. Using the peak-to-peak calibration curve, dose values amounted to (13.39 ± 0.22) Gy, 1.6% relative uncertainty, and (15.10 ± 0.27) Gy, 1.8% relative uncertainty, uncertainties being expressed with k=2. All values are compatible with the dose delivered to the pellets as registered by the Radiation Physics Laboratory staff, which were (13.341 ± 0.082) Gy and (15.190 ± 0.092) Gy respectively.

In the determination of dose through the peak-to-peak quantification method a larger uncertainty was achieved for the blind test with the higher dose, 15.19 Gy, although the relative uncertainty of the alanine dosimetry system is expected to decrease with dose. This was due to the higher type A uncertainty associated to the peak-to-peak quantification for the dosimeters involved in this test, which amounted to 0.55%, while for the first blind test, of 13.34 Gy, remained of 0.23%. The use of a reference signal for the quantification of dose is mainly useful when applied to dosimeters with low dose levels, which is confirmed through the proportionality encountered between dose level and the type A uncertainty associated to this ESR quantification method at the lowest dose levels involved in our study.

The estimation of the uncertainty associated to the ESR signal quantification using the standard deviation from the measurement of three pellets has been demonstrated to be an adequate approach leading to consistent results [92]. A repeated construction of calibration curves, similar to that addressed in the work by Anton *et al.*, would serve to check that the variations obtained in the determination of dose are repeatedly compatible with the uncertainty estimates.

3.3 Conclusions

In this chapter, a thorough study about alanine/ESR dosimetry systems in the therapy dose range has been performed. An approximation to the theoretical foundations of ESR detection has been addressed, as well as a study about the ESR spectrometer operation.

The spectrometer sensitivity and stability required to achieve uncertainties below 1% in the quantification of ESR signal from alanine dosimeters irradiated in the therapy dose range are quite demanding. The parameters ensuring optimal spectrometer operation can deviate from those employed in other ESR applications where the interest lies in the determination of ESR spectral shapes instead of ESR signal intensity quantification. Several tests were performed to determine the combination of spectrometer operation parameters resulting optimal for the measurement of the alanine dosimeters, maximizing the spectrometer stability and sensitivity. The development of a specific custom motorized system to accurately control the position of the dosimeters in the cavity, as well as the study of the anisotropy exhibited by the ESR signal of alanine dosimeters, allowed the definition of an ESR measurement protocol.

A first calibration of alanine ESR signal intensity in terms of dose to water was addressed through the irradiation of a batch of dosimeters to six levels of dose to water in ^{60}Co, serving for the investigation of two methods of ESR signal quantification and to study the subtraction of alanine background signal from unirradiated alanine dosimeters. A general uncertainty budget was established to estimate the uncertainty associated to this calibration, which amounted to 1.2% for dosimeters irradiated to 50 Gy and 2.8% for dosimeters irradiated to 10 Gy.

Improvements related with the stability of the spectrometer (installation of a recirculated water cooling system in the spectrometer with a heat exchanger to control the temperature) and a more accurate determination of the dose to water delivered to the dosimeters were introduced in the system to reduce the uncertainty. Calibration of dose to water from alanine ESR signal performed after these improvements yielded a relative associated uncertainty estimated to amount to 0.8% for dosimeters irradiated to 50 Gy and 1.7% for dosimeters irradiated to 10 Gy. Two alanine dosimetry blind tests were used to check the consistency of the system at 13 and 15 Gy. The determination of dose to water from the calibration curve yielded for these pellets values compatible with the reference values of dose delivered to the pellets, with relative uncertainty levels amounting to 1.4% at 13 Gy and 1.3% at 15 Gy.

This Chapter described the first steps for the development of an alanine dosimetry system at the Universidade de Santiago de Compostela. The work here addressed served for the construction of an alanine calibration curve with associated uncertainties below 2% (k=2) at 10 Gy, low enough for applications like the determination of ionization chamber correction factors or their use for dosimetry audits.

Some improvements could be still introduced in the system to further reduce the uncertainty in the determination of dose to water from alanine ESR signal, being related with the positioning of the pellets during irradiation and the subtraction of background from the dosimeters ESR signal at low dose levels. Before offering an alanine dosimetry service to external users, a repeated construction of calibration curves would serve to definitively check that the variations obtained in the determination of dose in different calibrations are compatible with the uncertainty estimates.

Chapter 4

Ionization chamber correction factors in nonstandard fields: TomoTherapy and CyberKnife

In this chapter we will apply the dosimetric formalism presented in Chapter 1 to two modern radiotherapy techniques, TomoTherapy® Hi-Art® and the CyberKnife® Robotic Radiosurgery system, both machines from Accuray Inc., Sunnyvale, CA. For these two machines, intermediate calibration fields will be defined for the calculation of ionization chamber correction factors following the proposal of Alfonso *et al.*. Clinical treatments will be also measured to evaluate the suitability of the intermediate calibration fields for the clinical practice.

4.1 Introduction

4.1.1 Flattening filter free linear accelerators

Although there are many differences between the two radiotherapy techniques here chosen to investigate the applicability of the new dosimetry protocol, they both share the peculiarity of using flattening filter free (FFF) accelerators. Modern linacs that operate without flattening filter became available during the last years, like Elekta Precise® (Elekta AB, Stockholm, Sweden), and TrueBEAM®, Trilogy® and Clinac® linacs from Varian (Varian Medical Systems Palo Alto, CA), or TomoTherapy® Hi-Art® and the CyberKnife® Robotic Radiosurgery system, both machines from Accuray Inc., Sunnyvale, CA, which shows a sustained trend in the evolution of radiotherapy machines industry.

A flattening filter (FF) is basically a conical shaped piece made of a high-Z material that is introduced in the head of medical accelerators to compensate the forward peaked angular distribution of the photons that are generated by bremsstrahlung in the linac target. Its thickness, of several centimeters, is chosen to provide flat dose profiles at 10 cm depth in water, and depends on the linac megavoltage modality. Flat dose profiles were used in radiotherapy treatments as they substantially simplified treatment planning dose calculations when computers were not available. However, the development of dose calculation engines and the emergence of radiotherapy techniques like stereotactic radiotherapy (SRT) or IMRT, with the delivery of fluence patterns that vary across the beam yielding inhomogeneous dose distributions, set some questions about the need of this component in the linac heads. Then, progressively during the last 10 years, the main linac vendors began to release Flattening Filter Free (FFF) accelerators.

The characteristics of a linac with or without this component present some differences in the photon beam output regarding:

1. **Dose rate**

   The attenuation suffered by the forward peaked distribution of photons crossing the FF involves a strong decrease in photon fluence. The dose rate delivered by a FFF beam is therefore higher than that of flattened beams. Under these increased dose rates, that can reach 2400 cGy/min, differences in the radiobiological effect of photons with respect to conventional rates are however not observed [105], neither the measurement of dose with air ionization chambers, film dosimetry, semiconductors or alanine dosimeters requires the introduction of any correction factor.

   This dose rate increment of FFF beams cannot be however directly translated into substantial treatment time reductions as gantry and MLC movements constitute a significant fraction of the total treatment time. Improvements in the MLC designs to get higher leaf speeds, increasing the efficiencies of treatment delivery, will help to take full advantage of the higher dose rates in FFF beams.

2. **Beam spectrum (beam quality)**

   The attenuation suffered by the photons crossing the FF produces a hardening in the photon spectrum that makes FFF beams to present a softer spectrum when compared to that of flattened beams operating under the same accelerating potential, see Figure 4.1 (a) and (b). This softening in the spectrum makes FFF beam percent depth dose distributions to fall more steeply than those of FF beams, leading to lower $TPR_{20,10}$ and %dd(10) beam quality indexes than that exhibited for the same megavoltage modality in FF linacs. In practice, 6 and 18

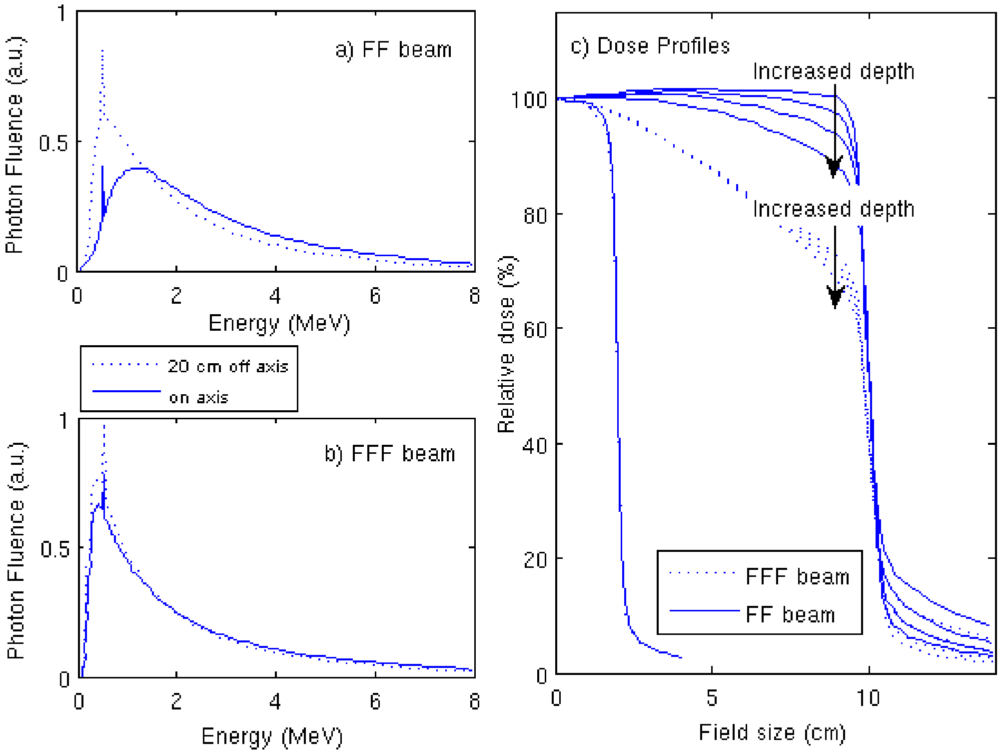

FIGURE 4.1: Normalized energy fluence in the central axis (solid line) and field edge (points) of a flattened (a) and unflattened (b) 6MV 40 cm×40 cm field from a Elekta Precise linac, Monte Carlo simulation [106]. (c) Lateral dose profiles of a 4 cm×4 cm and a 20 cm×20 cm field from a flattened (solid line) and unflattened (points) 6 MV beam from a TrueBeam linac [107]. 20 cm×20 cm field dose profiles at a depth of 1.5, 5, 10 and 20 cm in water are included to show the lower variation with depth found for unflattened beams.

MV unflattened beams exhibit beam quality indexes that are typical of 4 and 15 MV standard FF beams respectively.

The flattening filter produces also an off-axis softening in the spectrum, and unflattened beams will thus present smaller energy variations across the beam. This will be translated into smaller variations in the lateral dose profiles with depth and lower differences between axis and off-axis depth dose profiles, which can be considered as a simplification for dose calculations. The lower off-axis softening in the FFF beams spectrum will also affect phantom scatter ratios, a parameter sensitive to the photon beam quality, irradiated area and field shape. Namely, changes amounting to a 4% have been found between phantom scatter ratios of FF and FFF beams with the same beam quality indexes, and although more studies should be performed to verify this effect, this may suggest that kernel parameters employed in convolution-superposition dose calculation algorithms of FFF beams could differ from those of FF beams [108].

3. **Lateral dose profiles**

   As we just mentioned, the spectral variation associated to the removal of the flattening filter produces certain differences between FFF lateral dose profiles and those yielded by conventional flattened beams. FFF lateral dose profiles exhibit a central peak that becomes increasingly pronounced at higher energy modalities due to the predominant smaller scattering angles. Under 6 MV modalities, this peak is noticeable at large and medium field sizes, while dose profiles of field sizes smaller than 4 cm×4 cm are very similar to those of flattened beams, Figure 4.1 (c). Variations in the shape of lateral dose profiles with depth, this is, the horns and pronounced shoulders typically observed in flattened beam profiles at depths respectively lower and higher than 10 cm, are minimized in unfflatened beams due to the smaller radial energy variation. Regarding the penumbra of dose profiles from FF and FFF beams, axis rescalation using the inflection point of the FF and FFF field profiles is needed to enable their comparison [109], and only slightly smaller penumbras, with ≈ 1 mm differences, are obtained for the FFF beam profiles.

4. **Scatter from the linac head**

   The flattening filter is the element in the treatment head that contributes the most to the photon scatter from the linac head, in an amount that depends on the material, shape and size of the flattening filter. Output ratios in air, usually employed to characterize the variations in photon fluence with field size, are a good parameter to compare differences in the scatter produced in the head of FF and FFF linacs. Taking as an example a Varian Clinac 2100, output ratios of 6 and 18 MV flattened beams increase respectively a 8% and a 7% when the field size varies from 3 cm×3 cm to 40 cm×40 cm, while these values are lowered to 1% and 3% when the FF is removed from the linac head, giving a measure of the amount of scatter that is produced in the flattening filter [110].

5. **Radiation Protection**

The removal of the flattening filter has also certain impact in some aspects related with radiation protection. On one hand, electron contamination is reduced in FFF beams in an amount that increases with the energy. This causes and improvement in the accuracy of treatment planning system (TPS) dose calculations in the first centimeters of material, as most of them employ rather simple electron contamination models. Regarding the dose to the surface due to photons, the softening in the spectrum contributes to enhance it, an effect that is partially balanced with the lower electron contamination to yield a total dose to the surface that is higher than that of flattened beams for small field sizes, and equal or slightly lower for large field sizes.

Regarding the peripheral, or out of field, dose to the patient, the reduction in photon leakage from the linac head, amounting from 50% to 60% in 10 MV FFF beams from Elekta Precise linacs [111], will contribute to reduce it. Additionally, removal of the FF also causes a reduction in photoneutron production[1], with neutron fluences

---

[1] The production of neutrons through the interaction of photons with the linac head components is an undesired effect that contributes to the peripheral dose to the patient. The neutron production increases with the energy above certain production threshold around 6 MeV and varies strongly with the vendor depending on the materials employed in the linac head [112].

> being 50% to 60% lower than those produced by flattened beams from Varian Clinac 2100 linacs at 18 MV and open square fields from 10 to 30 cm [113].
>
> The high radiobiological effectiveness of neutrons motivated some discussion about the hazards of high energy IMRT treatments [114], being several the clinical centers that renounced to deliver IMRT treatments at 18-25 MV modalities with standard linacs. The global reduction attained in the neutron and photon leakage with the removal of the flattening filter implies lower risk of radiation-induced secondary cancers, a result that is clearly advantageous for IMRT treatments.

Some of the above mentioned differences between flattened and unflattened beams have some implications that are worth to comment. First of all, redefinition of some of the parameters usually employed in the quality assurance of linacs, like field flatness, penumbra and homogeneity is required. More related with the work addressed in this thesis, the differences in the shape of dose distributions and spectra from these beams will have certain impact on the determination of beam quality correction factors associated to FFF linacs. On one hand, differences in the water to air stopping power ratios amounting to 4% have been reported between flattened and unflattened beams of equal beam quality indexes [115]. This implies certain deviations in the beam quality correction factors of FFF beams with respect to those tabulated in conventional dosimetry codes of practice as a function of the beam quality descriptor. Additionally, the dose distribution gradient that is due to the central peaked fluence of unflattened beams affects the suitability of some detectors for beam calibration. The average volume effect can lead to under-responses in some ionization chambers under large field sizes, an effect that can amount to 1% for Farmer type chambers [116, 117].

These two differences between FF and FFF beams imply that the determination of FFF beam quality correction factors using the data from conventional dosimetry CoPs will have a larger associated uncertainty, as values in these tables were derived for flattened beams. Moreover, as commented in Section 1.2.3.3, if the standard reference conditions proposed by current dosimetry protocols cannot be established by these machines, the definition of new conditions for the measurement of beam quality descriptors and associated ionization chamber correction factors becomes an imperative task for the continuation with the quality assurance procedures followed until now for the determination of absorbed dose to water. This is the case in TomoTherapy and CyberKnife units, that we will proceed to describe next.

4.1.2 TomoTherapy

The TomoTherapy unit, developed during the 90's by Mackie *et al.* [10], consists in a 6 MV compact linear accelerator mounted on a ring gantry similar to that employed in Computed Tomography (CT), see Figure 4.2. In this machine, the rotation of the linac around the ring, which has a radius of 85 cm, is combined with the continuous movement of the treatment couch to perform a helical radiation delivery, while the use of a binary multileaf collimator enables the modulation of the beam.

The collimation elements in the TomoTherapy linac head include a standard primary collimator, a jaw, which blocks the beam in the y direction to yield a fan beam with a length of 40 cm along the x-axis and a maximum width of 5 cm in the y-axis (the direction of couch movement), and a binary multileaf collimator, see Figure 4.2. The jaw aperture defines the *slice width*, a term used to refer to the maximum field size in the y-axis, typically set to 1, 2.5 or 5 cm for treatment delivery (sizes given at the isocenter). Below the jaw, a 64 leaf collimator is employed to modulate the beam in the x direction, with leafs disposed in two separate banks traveling in the y direction to

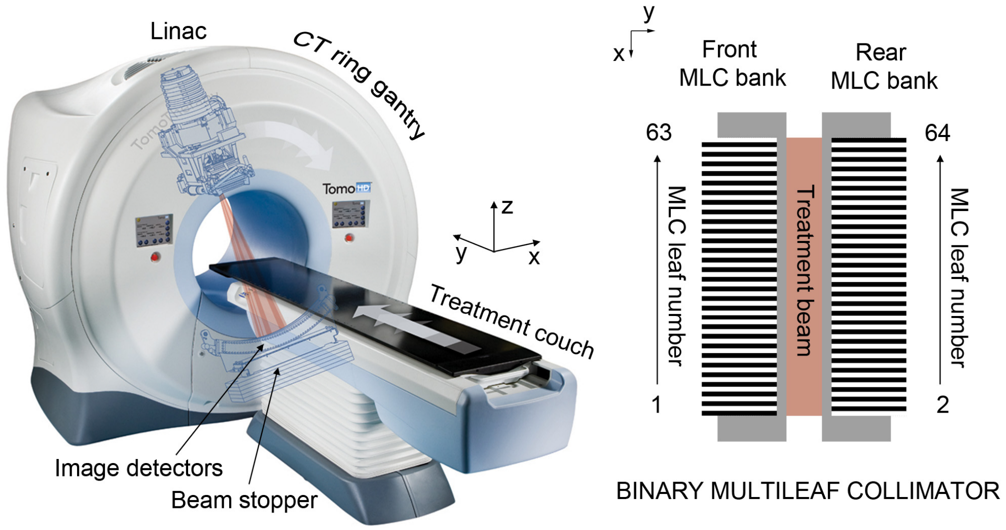

FIGURE 4.2: TomoTherapy unit design (left) and beam eye view of the TomoTherapy binary multileaf collimator (right).

be totally opened or totally closed, Figure 4.2. A pneumatic system is employed to move the leafs of this binary MLC in very fast transitions of approximately 20 ms. The modulation of the beam is provided through the selection of specific opening times during the arc segments of the rotational delivery.

Beam modulation and treatment time are controlled through the so called *modulation factor*, a parameter defined as the longest leaf opening time divided by the average opening time of all nonzero leaf opening times [118]. Another parameter used in treatment planning is the *pitch*, defined as the ratio of distance traveled by the couch in a complete linac rotation and the slice width.

TomoTherapy also takes advantage of its CT structure for imaging, and it has a detection system mounted opposite to the linac, at a distance from the source of 145 cm, for the acquisition of pretreatment megavoltage computed tomographies. Computed tomographies are performed under 3.5 MV linac operation, being employed in addition to the room laser references to ensure correct patient positioning in the couch, further corrected if changes in the patient's anatomy arise between treatment fractions. The tomography system is also employed for dose reconstruction and the performance of image guided radiotherapy.

TomoTherapy units operate at about 888 MU/min with no servo control for the dose rate. There is however an interlock that terminates the beam if there is more than 5% dose rate variation in the monitor chambers of the linac head.

Regarding the dosimetric calibration of TomoTherapy, the definition of the 10 cm×10 cm field size required for the establishment of reference conditions in TRS-398 and TG-51 protocols cannot be set due to the collimation characteristics of the machine. Additionally, the measurement of dose at source to detector distances larger than 110 cm, needed for the measurement of standard beam quality descriptors $TPR_{20,10}$ and $\%\mathrm{dd}(10)_x$, is not allowed in the machine, as the maximum distance from isocenter to the lowest position of the couch is 28 cm and there is not enough phantom material to achieve the required backscatter contribution. Under this situation, several approximations can be made to determine the values that standard beam quality descriptors would have on the machines [119, 120], all increasing to some extent the uncertainty associated to the measurement of dose in these machines.

4.1.3 CyberKnife

The CyberKnife unit consists on a compact x-band linear accelerator mounted on an industrial robotic arm, operating together with two orthogonal X-ray imaging systems to ensure good patient positioning and provide image guidance during the treatment process. The image guidance is performed by the Synchrony® Tracking System, which uses a CCD camera to track some optical markers (light emitting optical fibers) attached to the patient during treatment. The combination of both the optical and X-ray imaging systems enables the robotic manipulator to track the motion of tumors during irradiation.

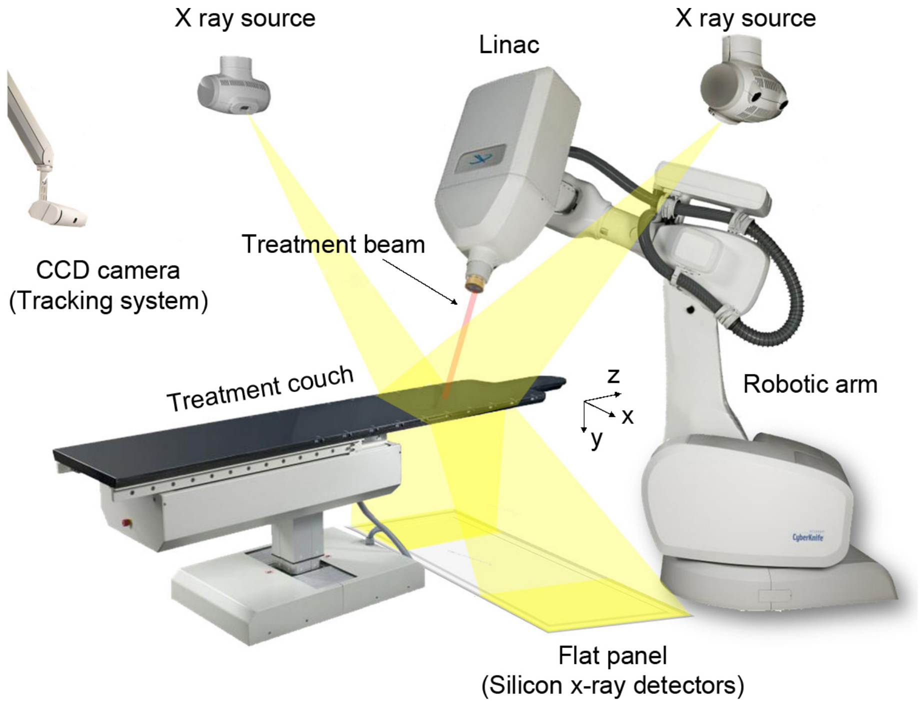

FIGURE 4.3: Diagram of the main components of a CyberKnife unit.

For treatment delivery, the robotic arm directs the linac beam to the region of the imaging X-ray beams intersection, where the target to treat is placed by a robotic automated patient couch, see Figure 4.3. All the movements of the linac head and the treatment coach are controlled by a computer supervised by the radiation therapist. This radiotherapy delivery scheme, employing independently targeted (non-isocentric) and non-coplanar treatment beams from different directions, is used for both extracraneal and frameless intracraneal image guided radiosurgery.

The CyberKnife linac operates in 6 MV modality and it has a compact design with neither bending magnet nor flattening filter, like TomoTherapy.

Besides the standard elements (primary collimator and jaws) employed in the linac head to collimate the photon beam, the secondary collimation is achieved in this unit through the use of twelve fixed interchangeable conical collimators, which yield circular fields with diameters from 0.5 to 6 cm (defined at 80 cm source-to-axis distance). Typically, several collimators are used in a treatment to achieve highly conformal dose distributions. The collimators are changed either manually or automatically if the unit is equipped with the Xchange® Robotic Collimator Changer. Other solutions are available for the CyberKnife secondary collimation: the Iris$^{\text{TM}}$ Variable Aperture Collimator can provide the same set of twelve field sizes avoiding the need for collimation swap during treatments, and lately, in the CyberKnife M6$^{\text{TM}}$ series, linacs can be equipped with the InCise$^{\text{TM}}$ Multileaf Collimator, which uses 41 tungsten leaf pairs to shape the beam, yielding a maximum field size of 10 cm×12 cm at 80 cm SAD. All CyberKnife units equipped with this multileaf collimator could be calibrated following standard dosimetry protocols, although the absence of FF would increase the uncertainty as mentioned above. On the other hand, most of the CyberKnife machines available in clinical institutions can only deliver a maximum field size of 6 cm diameter at 80 cm SAD, with the Iris or with the largest fixed conical collimator, not fulfilling the reference conditions established in AAPM TG-51 and IAEA TRS-398 and becoming candidates for the application of the nonstandard fields dosimetry protocol.

4.2 Correction factors determination

In the next sections, the determination of ionization chamber correction factors associated to TomoTherapy and CyberKnife is presented. Intermediate calibration fields (machine and plan class specific reference fields) are for that purpose specifically defined and measured following the proposal of the new formalism, presented in Section 1.2.3.3. Additionally, the suitability and usefulness of the dosimetric paths introduced by the intermediate calibration fields is tested through the study of some clinical treatments.

The measurement of absorbed dose to water required for the determination of correction factors was performed with alanine dosimetry in collaboration with the National Physical Laboratory (Teddington, Middx, United Kingdom) under the IAEA Coordinated research Project No. 15647/RO "Correction Factors for Ionization Chamber Dosimetry in Small Field and Non Standard Conditions" Our alanine/ESR dosimetry system was at that time under development and thus both the supply of dosimeters as well as their ESR readout was performed by the NPL alanine dosimetry service.

The dosimeters provided by the NPL consist of 90.9% by weight L-α-alanine and 9.1% high melting point paraffin wax. Their average density is 1.23 g cm^3 and they have a nominal diameter of (5.026 ± 0.013) mm and a nominal thickness of 2.5 mm, although the real thickness is 2.3 mm on average. The alanine dosimeters were read out at the NPL following their standard procedure for radiotherapy level alanine dosimetry, described in detail by Sharpe *et al.* [82]. The spectrometer employed at the NPL is exactly the same model (Bruker ESX with a standard Bruker ST4102 rectangular cavity) available at the University of Santiago de Compostela (Chapter 3). Pellets were introduced in the spectrometer using an automated loading system with a specially constructed sample holder that provides highly accurate positioning [121]. The spectrometer total acquisition time per dosimeter was 120 s, consisting of six scans of 20 s with a 90° pellet rotation performed between the third and fourth scan. The average ESR signal from each pellet is then compared with that of a set of pellets, from the same batch, irradiated by a 10 cm×10 cm ^{60}Co field to an interval of dose levels arranged by the NPL with traceability to their primary standard of absorbed dose to water. As commented in Chapter 3 Section 3.1.1, a correction factor of 1.006 is applied to obtain absorbed dose in the high-energy photon beam to account for the difference in the alanine signal under linac photon megavoltage beams and ^{60}Co beams. The dose deposition in both intermediate calibration fields and clinical treatments was planned to be higher than 10 Gy, the dose level above which the lowest uncertainty associated to the NPL alanine dosimetry system, 1.6%, can be achieved.

4.2.1 TomoTherapy

4.2.1.1 Experimental setup

The TomoTherapy unit employed in this work was a TomoTherapy® Hi-artII® machine installed at Hospital Puerta de Hierro, Madrid, Spain. For the application of the new protocol, the election of a detector being representative of the clinical practice in TomoTherapy units is the most practical approach. The Exradin A1SL ionization chamber (Standard Imaging, Middleton, WI), supplied by the vendor with the TomoTherapy unit, is the detector most widely used for the dosimetry of this machine. Measurements were thus performed with this detector, of 0.053 cm^3 active volume, at an operation voltage of 300 V using a TomoElectrometer (Standard Imaging, Middleton, WI) for the study of the new protocol.

Two phantoms, both supplied by Accuray, Inc., were used for the measurements:

1. A rectangular phantom made of 15 cm×55 cm Virtual Water™ slabs (Med-Cal, Verona, WI), used for the measurement of *msr* fields.
2. A Virtual Water™ cylindrical water phantom (TomoPhantom) with 30 cm diameter and 18 cm length, used for the measurement of the *pcsr* and the clinical fields. This phantom, which is available in all TomoTherapy facilities, was used instead of the NPL polystyrene

phantom adopted in previous investigations [122, 123] to ensure reproducibility and allow the performance of measurements under the same conditions by other institutions.

For the alanine dosimetry, a virtual water insert was machined to hold groups of three cylindrical alanine pellets inside the mentioned phantoms.

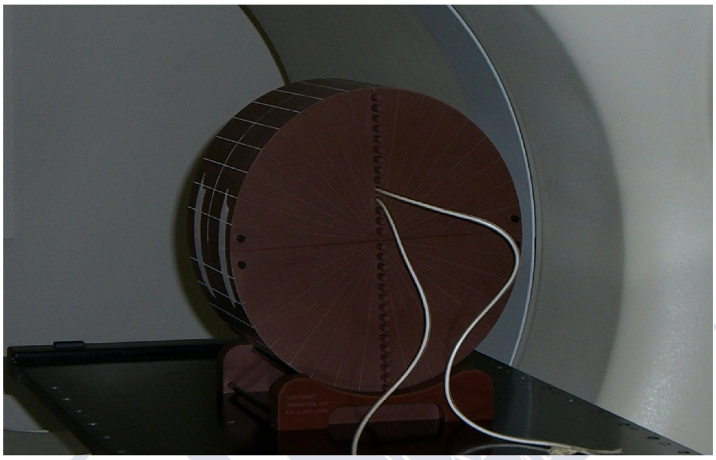

FIGURE 4.4: Cylindrical Virtual Water^{TM} phantom employed for the measurement of the *pcsr* field and clinical treatments in TomoTherapy. Two A1SL chambers employed for the measurements and for machine monitoring respectively are placed at a distance of 1 cm.

The phantoms, as well as the ionization chambers stem and alanine insert, were oriented along the y-axis according IECt coordinate system [124], see Figure 4.2. During the measurement of all the investigated fields, an additional A1SL chamber was placed at 1 cm from the alanine or investigated chamber position to monitor and correct for possible output variations during the treatment, see Figure 4.4. For the static field measurements, the linac parallel-plate monitor ion chambers located above the jaws were used to provide an independent measurement.

Temperature and pressure were monitored during the measurements in order to apply *T*-*P* corrections for the ionization chambers, k_{TP}, and T corrections for the alanine, k_T (Section 3.1.1). Chamber leakage was carefully measured and treatment times were considered in order to subtract such contribution from the chamber readings.

4.2.1.2 Investigated fields

Machine Specific Reference Field

Following previous works [125–127] and TG-148 recommendations [118], a 10 cm×5 cm beam size (defined at SAD of 85 cm) was chosen as the TomoTherapy machine specific reference field. Absorbed dose measurements were performed on axis at 5 cm depth in the rectangular Virtual Water phantom previously described. The dose delivered to the chamber/alanine position was planned to be above 18 Gy.

Plan Class Specific Reference Field

The plan class specific reference field was chosen, also following TG-148 report recommendations [118], to deliver a uniform dose of 2 Gy to a cylinder of 8 cm diameter and 10 cm length, oriented along the axis of the Virtual Water cylindrical phantom. Treatment planning parameters included a slice width of 5 cm, a pitch of 0.287 and a modulation factor of 1.807.

Measurement positions were located within a volume of homogeneous dose, being this verified with the TPS dose distribution. As there is no chamber insert along the phantom axis, detectors were located slightly off-axis, at a distance of 0.5 cm in the x direction from the phantom geometric center, see Figure 4.5. For the irradiation of the alanine pellets, the treatment was repeated eight times to deliver a total dose of 16 Gy to the detectors and decrease the dose uncertainty.

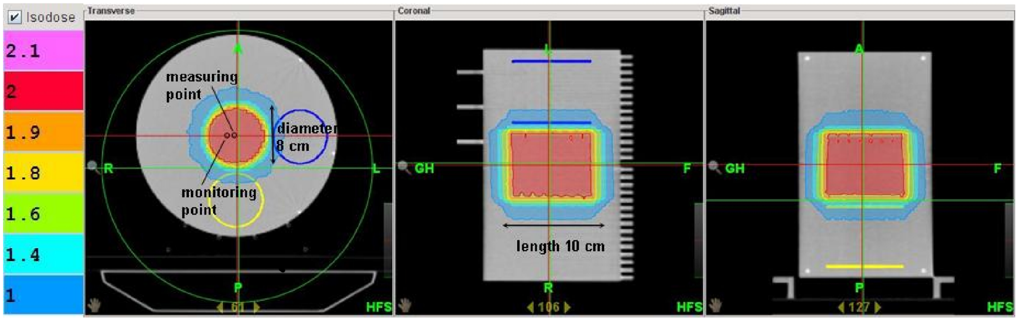

FIGURE 4.5: Dose distribution for the plan class specific reference field (isodoses given in Gy). The positions of the investigated chamber/alanine and the monitor chamber are shown in the left panel.

Clinical Treatments

Two clinical plans were studied in order to investigate the applicability of the intermediate calibration fields to the relative clinical dosimetry:

- A hypofractionated lung treatment using a 2.5 cm slice width, planned with 1.322 modulation factor and 0.100 pitch to deliver 18 Gy per fraction.
- A head-and-neck treatment, also involving a 2.5 cm slice width, delivering 2 Gy per fraction with 2.167 modulation factor and 0.287 pitch.

It should be noticed that some of these planning parameters are different from those used in the *pcsr*.

The dose to the planned target volume (PTV), calculated in the cylindrical phantom by the TPS, was determined to be 16 Gy and 1.6 Gy for the lung and head-and-neck treatments respectively. For the irradiation of the alanine pellets, the head-and-neck treatment was repeated seven times in order to enhance the dose up to 11.2 Gy and improve dose uncertainty. In all cases, investigated dosimeters and monitor ionization chambers were placed at homogeneous PTV dose regions, as shown in Figure 4.6.

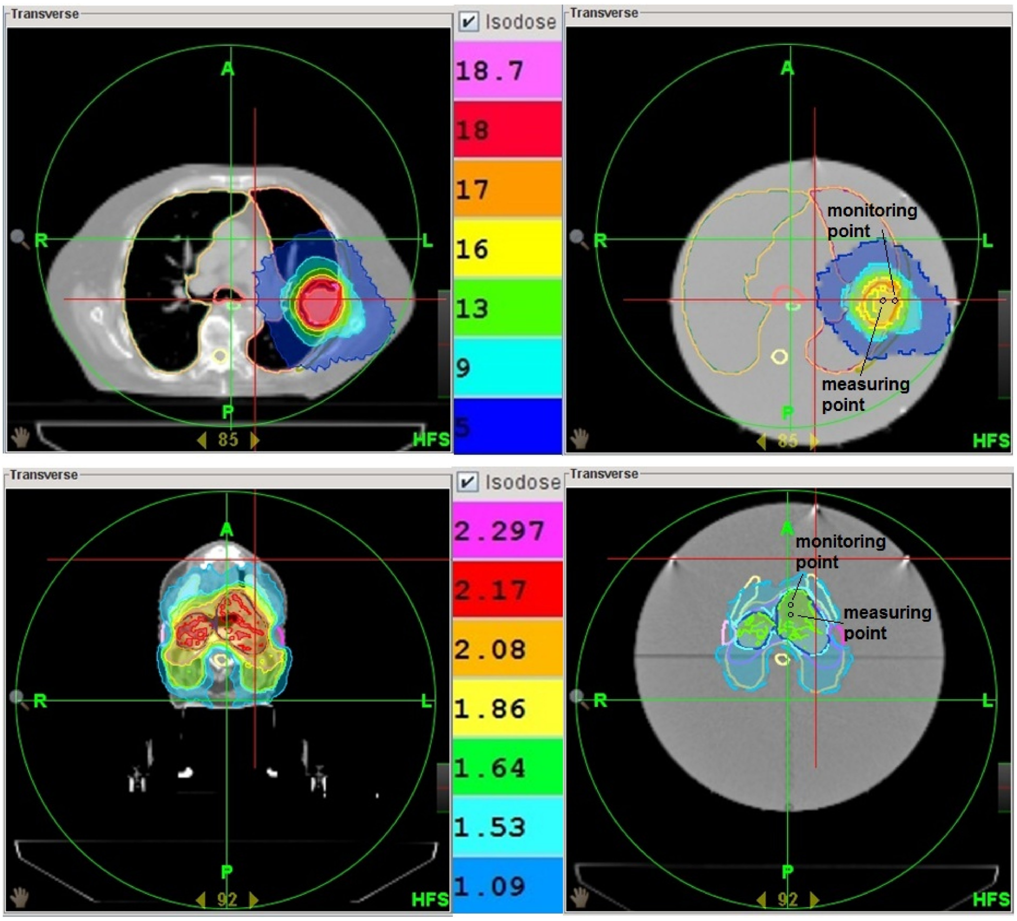

FIGURE 4.6: Dose distributions for lung (top panels) and head-and-neck (bottom panels) in the patient (left panels) and the cylindrical phantom (right panels). Isodoses are given in Gy, and the positioning of the ionization chamber/alanine and the monitor chamber in the cylindrical phantom is shown with open circles.

4.2.1.3 Reference beam quality correction factor

Although measurements with the A1SL ionization chamber and alanine dosimeters in intermediate calibration fields and ^{60}Co would suffice to derive global correction factors $k^{f_{\mathrm{msr}},f_{\mathrm{ref}}}_{Q_{\mathrm{msr}},Q_0}$, $k^{f_{\mathrm{pcsr}},f_{\mathrm{ref}}}_{Q_{\mathrm{pcsr}},Q_0}$ and $k^{f_{\mathrm{clin}},f_{\mathrm{ref}}}_{Q_{\mathrm{clin}},Q_0}$, the formalism proposed by Alfonso *et al.* [30] was conceived to appear as an extension of previous formalisms. In this context, values of $k^{f_{\mathrm{msr}},f_{\mathrm{ref}}}_{Q_{\mathrm{msr}},Q}$, $k^{f_{\mathrm{pcsr}},f_{\mathrm{ref}}}_{Q_{\mathrm{pcsr}},Q}$ and $k^{f_{\mathrm{clin}},f_{\mathrm{ref}}}_{Q_{\mathrm{clin}},Q}$ should be provided, appearing multiplied by the standard correction factor k_{Q,Q_0} and the calibration coefficient N_{D,w,Q_0} for the determination of absorbed dose, as presented in Equation 1.11.

Since standard beam quality descriptors $TPR_{20,10}$ and $\%\mathrm{dd}(10)_x$ cannot be directly measured in TomoTherapy machines, other strategies must be followed for the determination of k_{Q,Q_0}. Several works have been published reporting both Monte Carlo calculated beam quality descriptors and correction factors through simulation of TomoTherapy units with modified geometries that reproduce reference conditions [125, 126]. Thomas *et al.* obtained an expression to compute standard %dd(10) values from the percent depth dose at 10 cm depth in TomoTherapy conditions, $\%\mathrm{dd}(10)_{\mathrm{HT}}$, defined as a 5 cm×10 cm field-size and 85 cm SSD. A third-order polynomial was then used to fit these two magnitudes for $\%\mathrm{dd}(10)_{\mathrm{HT}}$ values ranging from 58.8% to 60.8%. However, the TomoTherapy unit at Puerta de Hierro Hospital presents a softer beam quality, $\%\mathrm{dd}(10)_{\mathrm{HT}}=58.5\%$, and so the expression derived by Thomas *et al.* has to be used with caution because our $\%\mathrm{dd}(10)_{\mathrm{HT}}$ value lies off range. A direct application of such polynomial leads to %dd(10)=57.6% for this TomoTherapy unit, with a corresponding k_{Q,Q_0} value of 0.9994 obtained by extrapolation of TG–51 data of the A1SL ionization chamber.

Alternatively, in a previous work performed at Puerta de Hierro TomoTherapy unit [119], a methodology that draws some analogies with the work

Estimation of standard beam quality correction factor			
Method	Thomas *et al.*	Rodriguez-Romero *et al.*	Palmans
Beam Quality	%dd(10)=57.6%	$TPR_{20,10}$=0.629	$TPR_{20,10}$=0.631
k_{Q,Q_0}	0.9994	0.9994	0.9993

TABLE 4.1: Summary of the results obtained through the different approaches followed for the estimation of the A1SL standard beam quality correction factor k_{Q,Q_0} in the TomoTherapy unit under study.

of Sauer [128] was developed for the determination of k_{Q,Q_0}. Rodríguez-Romero and Sánchez-Rubio demonstrated that TomoTherapy-to-LINAC $TPR_{20,10}$ ratios remain constant for equivalent square field sizes ranging from 5 cm to 8.9 cm. From this, an extrapolation to a 10 cm×10 cm field in the TomoTherapy unit yielded a $TPR_{20,10}$ value of 0.629, with a corresponding k_{Q,Q_0} value of 0.9994 obtained from the TRS-398 CoP.

More recently, following the work of Sauer, Palmans presented a reformulated expression for the calculation of standard beam quality descriptors, $TPR_{20,10}$ and %dd(10), from the values that these magnitudes yield under square fields of a different size, s, $TPR_{20,10}$(s) and %dd(s) [120]. Palmans proposed that the uncertainty associated to the standard beam quality descriptors determined through the method of Sauer could be reduced if the range of energies and field sizes chosen to fit the BJR25 experimental data [129] were restricted to (4-12) MV and (4-12) cm. When the method of Palmans is applied to our TomoTherapy unit, with a $TPR_{20,10}(6.7)^2$ of 0.611, the standard $TPR_{20,10}$ yields a value of 0.631, leading to a 0.9993 k_{Q,Q_0} value from the TRS-398. Although the $TPR_{20,10}(6.7)$ was measured at a SCD of 85 cm instead of the 100 cm recommended, this beam quality descriptor has been demonstrated to be insensitive to the SCD.

---

[2] Using the empirical relation $s = 2ab/(a + b)$, employed by the ICRU for the calculation of equivalent square fields from rectangular fields of a cm×b cm [130], a field of 10 cm×5 cm would be equivalent to a square field size of 6.7 cm.

The k_{Q,Q_0} values estimated by these three methods exhibit a very close agreement, and its mean value will be considered for the determination of $k_{Q_{\mathrm{msr}},Q}^{f_{\mathrm{msr}},f_{\mathrm{ref}}}$, $k_{Q_{\mathrm{pcsr}},Q}^{f_{\mathrm{pcsr}},f_{\mathrm{ref}}}$ and $k_{Q_{\mathrm{clin}},Q}^{f_{\mathrm{clin}},f_{\mathrm{ref}}}$ nonstandard fields correction factors.

4.2.1.4 Uncertainty budget and corrections

The relative uncertainties associated with the measurement of A1SL ionization chambers and alanine dosimeters in the TomoTherapy measurements campaign are summarized in Table 4.2 with coverage factor k=2, and the details about their evaluation are described next.

Regarding ionization chamber measurements, type B uncertainties are dominated by the calibration coefficient uncertainty, which amounts to a 0.8%. Atmospheric pressure and temperature conditions were monitored for the application of the corresponding correction factor accounting for air density changes. A 0.2% uncertainty associated to this correction has been considered. The saturation effect was found to be less than 0.3% for a 40 cm×5 cm static field using the two-voltage method (k_s=1.0029). However, recent studies suggest that this value might be lower, and that recombination under helical delivery is significantly reduced when the slice width decreases [131]. We decided to neglect this correction, although a 0.2% associated uncertainty was conservatively included in the analysis. The polarization

Uncertainty source	Uncertainty type	A1SL(%)	Alanine (%)
Calibration coeff	B	0.8	1.7
Ambient conditions	B	0.2	0.1
Positioning	B	0.2 or 0.4	0.2 or 0.4
Repeatibility	A	0.1 to 0.7	0.6 to 0.8
Total uncertainty	A & B	0.87 to 1.0	1.7 to 1.8

TABLE 4.2: Relative uncertainty contributions to ionization chamber and alanine measurements with coverage factor k=2. Positioning uncertainty is 0.2% in f_{msr} and 0.4% in helical deliveries.

effect was found to be lower than 0.04% (k_{pol}=0.9996) and was neglected. Chamber leakage current was measured to amount to 0.09 pA, leading to a systematic effect that ranged from less than 0.05% for the *msr* field to up to 1.4% for the head-and-neck treatment and was corrected for. No uncertainty was assigned to this correction because the leakage current was found to be very stable. On the other hand, type A uncertainties accounting for chamber and machine repeatability were estimated by repeating each measurement three times. Values ranging from 0.1% to 0.7% were obtained for the different intermediate calibration fields and clinical treatments.

The NPL alanine/ESR dosimetry methodology has an expanded relative uncertainty associated with the calibration of the alanine dosimeters in ^{60}Co of 1.6% at doses above 10 Gy. Type A uncertainties associated with the variation between individual alanine pellets are estimated by statistical methods at the NPL to be 0.1 Gy or 0.6%, whichever is larger. An independent estimation of alanine type A uncertainty was obtained by performing three measurements, of three pellets each, for every field/treatment, and consistent results were found. Finally, the correction for the alanine temperature dependence was considered to contribute with a 0.1% uncertainty.

An additional uncertainty associated to both chamber and alanine measurements was assigned to account for possible relative mispositionings of the chamber and the alanine dosimeters, which was determined to be 0.2% in the static *msr* field and 0.4% in helical deliveries.

4.2.1.5 Dose values and correction factors.

Absorbed dose values measured by the ionization chamber and the alanine dosimeters are shown in Table 4.3 for the fields under investigation, where it can be seen that the dose values measured with the A1SL chamber are systematically higher than those measured with alanine. This result leads to overall correction factors lower than unity, as can be seen in Table 4.4

Field	A1SL $[M_Q \cdot N_{D,w,Q_0}](Gy)$	Alanine Dose (Gy)
f_{msr}	19.90 ± 0.17	19.54 ± 0.34
f_{pcsr}	2.023 ± 0.021	1.981 ± 0.035
Lung clin treatment	15.98 ± 0.15	15.67 ± 0.028
H&N clin treatment	1.647 ± 0.015	1.620 ± 0.030

Table 4.3: Exradin A1SL ionization chamber dose measurements, alanine dose measurements and global correction factors. Associated uncertainties are expressed with a coverage factor k=2.

and Figure 4.7, with $k^{f_{msr},f_{ref}}_{Q_{msr},Q_0}$=0.982, $k^{f_{pcsr},f_{ref}}_{Q_{pcsr},Q_0}$=0.979 and $k^{f_{clin},f_{ref}}_{Q_{clin},Q_0}$=0.980, 0.984 for the lung and the head-and-neck treatments respectively. Although each single factor is compatible with unity within uncertainties (around 2% at k=2, with uncertainties dominated by the chamber and alanine calibration factor uncertainty), this behavior seems to be significant when considered altogether, p = 0.02 for a hypothesis test performed assuming a t-student distribution.

<table>
<tr><th>Calibration field</th><th colspan="2">$k^{f_{\mathrm{msr}},f_{\mathrm{ref}}}_{Q_{\mathrm{msr}},Q_0}$</th><th colspan="2">$k^{f_{\mathrm{msr}},f_{\mathrm{ref}}}_{Q_{\mathrm{msr}},Q}$</th></tr>
<tr><td>f_{msr}</td><td colspan="2">0.982(19)</td><td colspan="2">0.982(19)</td></tr>
<tr><th>Calibration field</th><th colspan="2">$k^{f_{\mathrm{pcsr}},f_{\mathrm{ref}}}_{Q_{\mathrm{pcsr}},Q_0}$</th><th>$k^{f_{\mathrm{pcsr}},f_{\mathrm{ref}}}_{Q_{\mathrm{pcsr}},Q}$</th><th>$k^{f_{\mathrm{pcsr}},f_{\mathrm{msr}}}_{Q_{\mathrm{pcsr}},Q_{\mathrm{msr}}}$</th></tr>
<tr><td>f_{pcsr}</td><td colspan="2">0.979(20)</td><td>0.980(20)</td><td>0.997(10)</td></tr>
<tr><th>Clinical treatment</th><th>$k^{f_{\mathrm{clin}},f_{\mathrm{ref}}}_{Q_{\mathrm{clin}},Q_0}$</th><th>$k^{f_{\mathrm{clin}},f_{\mathrm{ref}}}_{Q_{\mathrm{clin}},Q}$</th><th>$k^{f_{\mathrm{clin}},f_{\mathrm{msr}}}_{Q_{\mathrm{clin}},Q_{\mathrm{msr}}}$</th><th>$k^{f_{\mathrm{clin}},f_{\mathrm{pcsr}}}_{Q_{\mathrm{clin}},Q_{\mathrm{pcsr}}}$</th></tr>
<tr><td>Lung</td><td>0.980(20)</td><td>0.981(20)</td><td>0.9981(93)</td><td>1.001(11)</td></tr>
<tr><td>H&N</td><td>0.984(20)</td><td>0.984(20)</td><td>1.0017(98)</td><td>1.004(12)</td></tr>
</table>

Table 4.4: Measured correction factors for intermediate calibration fields f_{msr}, f_{pcsr} and clinical treatments. Associated uncertainties affecting last decimals are shown in brackets with two significant digits and coverage factor k=2.

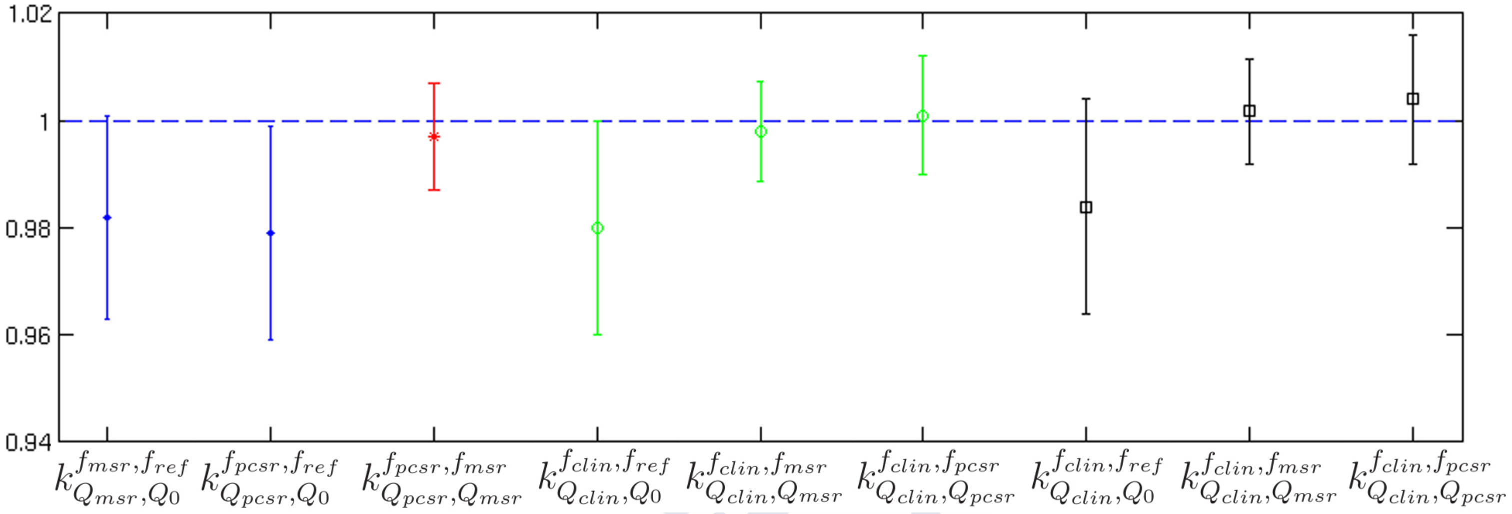

FIGURE 4.7: Measured correction factors for intermediate calibration fields f_{msr}, f_{pcsr} and clinical treatments, lung (○) and head-and-neck (□). Associated uncertainties are shown with a coverage factor k=2.

Regarding the dosimetric differences between the studied intermediate calibration fields, the $k^{f_{pcsr},f_{msr}}_{Q_{pcsr},Q_{msr}}$ correction factor was found to be very close to unity (with a value of 0.997 and 1% uncertainty), suggesting that the dynamic delivery does not introduce important changes in the determination of absolute dose with the A1SL chamber. We can observe that the main contribution to global correction factors comes from the intermediate calibration fields and it seems to be independent of the route followed (f_{msr} or f_{pcsr}) for the determination absorbed dose to water ($k^{f_{msr},f_{ref}}_{Q_{msr},Q} = 0.982 \pm 0.019$ or $k^{f_{pcsr},f_{ref}}_{Q_{pcsr},Q} = 0.980 \pm 0.020$).

On the other hand, $k^{f_{clin},f_{pcsr}}_{Q_{clin},Q_{pcsr}}$ and $k^{f_{clin},f_{msr}}_{Q_{clin},Q_{msr}}$ correction factors, which account for the differences between intermediate calibration fields and the investigated clinical treatments, also yielded values compatible with unity, ranging from 0.9981 to 1.004 with relative uncertainty values around 1% (k=2). In these clinical treatments, field factors for relative clinical dosimetry, Equation 1.15, could therefore be easily computed from chamber readings ratios, using either the *msr* or the *pcsr*:

$$\Omega^{f_{clin},f_{msr(pcsr)}}_{Q_{clin},Q_{msr(pcsr)}} \simeq \frac{M^{f_{clin}}_{Q_{clin}}}{M^{f_{msr(pcsr)}}_{Q_{msr(pcsr)}}} \tag{4.1}$$

This should be considered with caution though, as only two clinical treatments have been studied here and other publications present treatments that behave differently.

4.2.1.6 Review

Once that the results yielded by our study [132] have been analyzed, comparison with those from other works dealing with the application of the new dosimetric formalism to TomoTherapy will help us to draw more realistic conclusions about the role that the intermediate calibration fields can play for TomoTherapy.

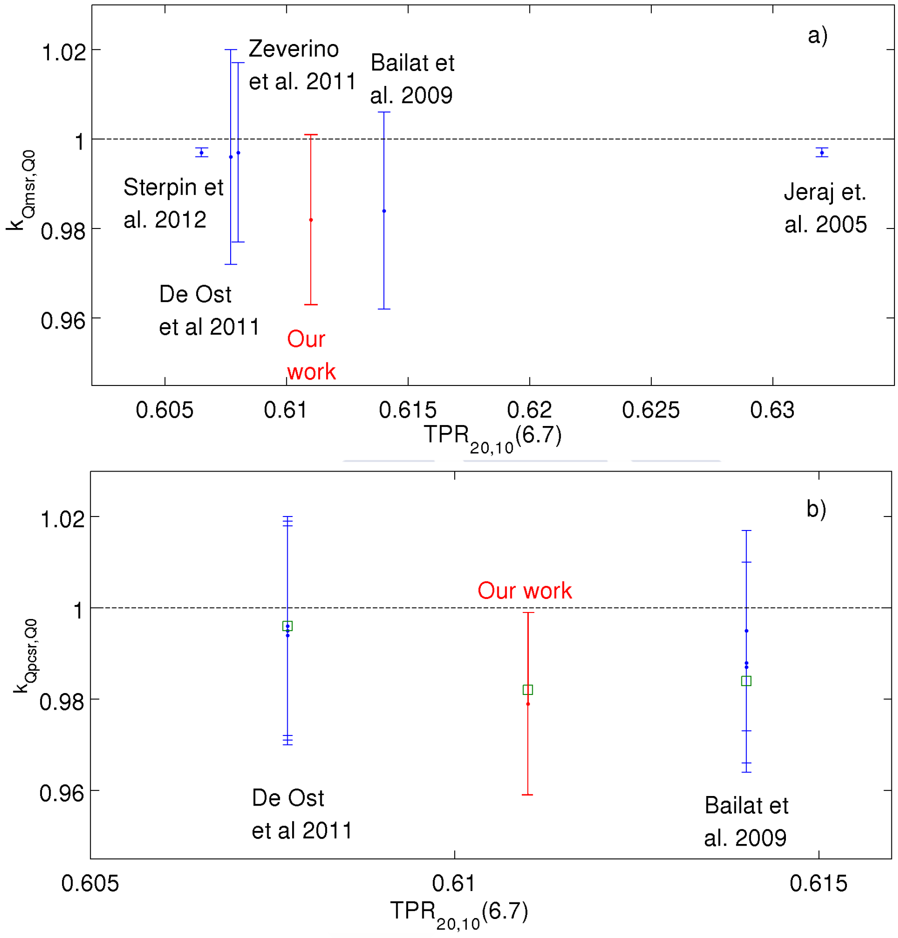

FIGURE 4.8: Summary of A1SL beam quality correction factors $k^{f_{\mathrm{msr}},f_{\mathrm{ref}}}_{Q_{\mathrm{msr}},Q_0}$ (a), and $k^{f_{\mathrm{pcsr}},f_{\mathrm{ref}}}_{Q_{\mathrm{pcsr}},Q_0}$ (b), published to this date versus the $TPR_{20,10}$ value yielded by every TomoTherapy unit under nonstandard conditions (10 cm×5 cm field and 85 cm SAD). Squares are included in subplot (b) showing the $k^{f_{\mathrm{msr}},f_{\mathrm{ref}}}_{Q_{\mathrm{msr}},Q_0}$ factors measured by every author for comparison.

Figure 4.8 collects the results of the published (updated by Spring of 2013) global correction factors, $k^{f_{\mathrm{i}},f_{\mathrm{ref}}}_{Q_{\mathrm{i}},Q_0}$, associated to TomoTherapy *msr* and *pcsr* fields as a function of the beam quality of the units where the different works were performed, uncertainties given with a coverage factor k=2. The beam quality descriptor chosen for the comparison is the $TPR_{20,10}(6.7)$ mentioned in Section 4.2.1.3, which can be directly measured in the machine.

If we focus on the calibration through static intermediate fields, Figure 4.8 (a), all the works defined as f_{msr} a 10 cm×5 cm field, although measurement conditions slightly varied from work to work: Sterpin *et al.* [133], SSD= 85 cm and SCD= 95 cm; De Ost *et al.* [134], SSD= 75 cm and SCD= 85 cm; Zeverino *et al.* [135], SSD= 85 cm and SCD= 95 cm; Bailat *et al.* [127], SSD= 80 cm and SCD= 85 cm and Jeraj *et al.* [126], SSD= 85 cm and SCD= 95 cm. The resulting $k_{Q_{msr},Q_0}^{f_{msr},f_{ref}}$ A1SL correction factors do not follow a clear trend with the $TPR_{20,10}(6.7)$, which may be to some extent related with the different measurement conditions. The correction factors relative uncertainties, around 2% for all the experimental measurements (smaller uncertainties were obtained in full Monte Carlo simulations), make all the values to be compatible among them, making impossible the establishment of any trend. Chung *et al.* also published a study about TomoTherapy $k_{Q_{msr},Q_0}^{f_{msr},f_{ref}}$ correction factors [136], which has not been included here as correction factors were determined in this study through the measurement of the conventional reference field (10 cm×10 cm) in a standard linac and no information is given about the beam quality of this unit or that of the Thomotherapy unit. Correction factor values presented in the work of Chung *et al.* are also compatible with those included in this review. Regarding the plan class specific calibration fields, different helical deliveries were chosen as f_{pcsr} candidates in the different works. Again, some work has been also performed by Chung *et al* on this matter [137], also involving the measurement of the conventional reference field in a standard linac but giving no information about the linacs beam quality. Chung planned a cylindrical *pcsr* field with some avoidance structures defined within the cylindrical phantom and different *pcsr* fields were planned exhibiting different levels of dose homogeneity within the *pcsr* PTV. $k_{Q_{msr},Q}^{f_{msr},f_{ref}}$ values ranging between 0.980 and 1.002 were obtained for the A1SL chamber in this study. Bailat *et* *al.* [127] defined the f_{pcsr} as a cylindrical dose distribution with 8 cm diameter and 10 cm length (same size of ours), delivered to the TomoPhantom. The dependence of $k_{Q_{msr},Q_0}^{f_{msr},f_{ref}}$ correction factors with the slice width (2.5 and 5 cm slice widths were employed for *pcsr1* and *pcsr2*), as well as the effect of delivering the dose distribution 13 cm off axis (*pcsr3*) were investigated in this study. Equivalent $k_{Q_{pcsr},Q_0}^{f_{pcsr},f_{ref}}$ correction factors were obtained for *pcsr1* and *pcsr2* (0.987 and 0.988 values respectively), while *pcsr3* yielded a correction factor closer to unity, 0.995. Finally, the work of De Ost *et al.* [134] included three *pcsr* plans being delivered to a cylindrical water phantom with 20 cm diameter and 30 cm length. The *pcsr1* was defined as a rotational delivery of the 10 cm×5 cm *msr* field, while for *pcsr2* and *pcsr3* cylindrical dose distributions were planned, with 8 cm diameter, 10 cm length and 2.5 cm slice width in *pcsr2* and 10 cm diameter, 5 cm length and 2.5 cm slice width in *pcsr3*. Correction factors associated to these three *pcsr* fields exhibited very similar values. Figure 4.8 (b) shows that all correction factors associated to these *pcsr* fields are again compatible among them within uncertainty.

This compatibility can be also found when all the correction factors, associated to both *msr* and *pcsr* fields, are compared, which indicates a small dosimetric difference between them. Moreover, the *pcsr* fields studied by every author led to correction factors lying very close (much closer than the 2% tolerance due to uncertainty) to the values obtained by that same author for the *msr* fields, as shown Figure 4.8 (b), further supporting the equivalence of *msr* and *pcsr* fields for TomoTherapy. In spite of the need for more measurements in clinical treatments, these results would pose some doubts about the necessity of defining a composite intermediate calibration field for TomoTherapy, as the *msr* fields yield a dosimetry route that is equivalent to that obtained with the *pcsr* fields, only much more simple.

On the other hand, the systematic 2% overestimation of dose in A1SL measurements at TomoTherapy was also observed by Bailat *et al.* [127]

and Duane *et al.* [138], although no numerical values are available for this work. Other studies reported A1SL measurements closer to absorbed dose to water, leading to corrections factors closer to unity, either through the experimental approach based on radiochromic film by Zeverino *et al.* [135], or through Monte Carlo simulation, Sterpin *et al.* [133] and Jeraj *et al.* [126]. Trying to find an explanation for a systematic departure from unity of nonstandard beam quality correction factors, Bouchard *et al.* [139] suggested that by taking into account that CPE re-establishment should be achieved in a time-averaged sense for plan class specific reference fields, both $k_{Q_{pcsr},Q}^{f_{pcsr},f_{ref}}$ and $k_{Q_{pcsr},Q_{msr}}^{f_{pcsr},f_{msr}}$ correction factors could be reduced to the inverse of the gradient perturbation effect in the ionization chamber [139]. This would lead to correction factors higher than one, contrary to the 0.980 and 0.997 values obtained in this study. Our values are however in agreement with other previous measurements, Figure 4.8, and a theoretical study on CPE violation in composite fields lately presented by Bouchard *et al.* [29] demonstrated that the conditions for CPE re-establishment in a time-averaged sense are not met and the expression of the correction factor given in [139] is not applicable.

4.2.2 CyberKnife

Regarding CyberKnife machine study, the work addressed in this case included an experimental and a Monte Carlo determination of correction factors associated to the fields proposed by the new formalism and two clinical treatments. Two ionization chambers were chosen for the study, and the measurement of absorbed dose to water was again performed through alanine dosimetry. The experimental work will be first here presented, proceeding next to describe the Monte Carlo simulation and compare the results obtained.

4.2.2.1 Experimental setup

The CyberKnife unit employed in this work for the application of the new dosimetry protocol is a CyberKnife® G4® machine installed at Hospital Ruber International in Madrid, Spain. Regarding the choice of appropriate detectors for this study, the AAPM report TG-106 on accelerator beam data commissioning, equipment and procedures recommends the use of microchambers for the measurement of small fields in radiosurgery because of the volume averaging effects that can arise in detectors with large active volumes [140]. According to this, the ionization chambers chosen for the determination of correction factors in the CyberKnife machine were the PTW31014 (PTW-Freiburg, Germany) and Scanditronix-Wellhofer CC13 (IBA Dosimetry GmbH, Schwarzenbruck, Germany), with active volumes of 0.015 cm^3 and 0.13 cm^3 respectively, being these detectors used in many radiotherapy departments for the dosimetry of small fields.

On the other hand, the alanine dosimeters employed for the determination of absorbed dose to water were again provided and read out by the NPL as described in section 4.2.1.1. Perspex and Solid Water inserts were machined to hold groups of three cylindrical alanine pellets in the different fields and phantoms.

Ionization chambers were operated at a voltage of +400 V with a PTW T10009 UNIDOS E electrometer (PTW-Freiburg, Germany). Room temperature and pressure were monitored during the measurements in order to apply T-P corrections to the ionization chambers readings and T corrections to the alanine readings. The chamber leakage current was again carefully measured and subtracted from the chamber measurements. Polarity and saturation correction factors were also measured according to the recommendations of IAEA TRS-398.

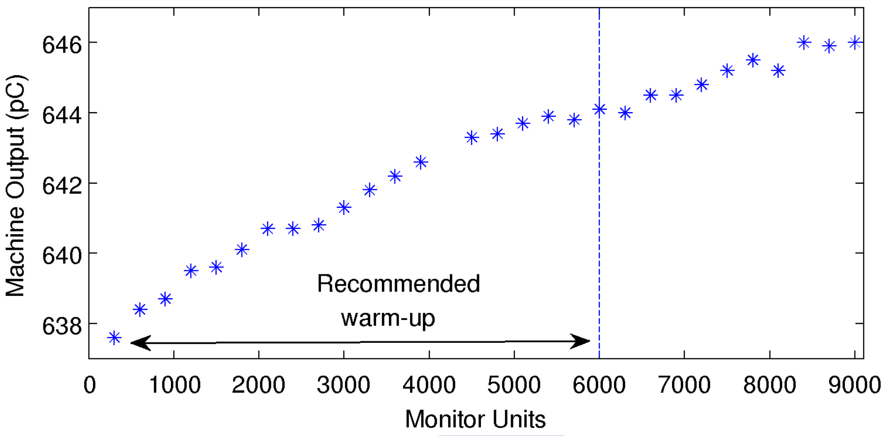

FIGURE 4.9: Changes registered in the CyberKnife machine output due to heating effects in the linac head and open (vented) monitor chambers, measurements performed with PTW31014 chambers in steps of 300 MU.

Regarding the stability of the linac, the CyberKnife G4 unit is equipped with vented monitor ionization chambers. This implies that changes in the temperature of the monitor chambers due to the machine warm-up and changes in pressure in the treatment room can induce machine output variations. This type of unit has to go through a warm-up of approximately 6000 MU to achieve a stable temperature and output before clinical use [141]. Our unit was given such warm-up before every set of measurements, however small output variations still arise due to pressure changes and residual machine warm-up, see Figure 4.9. Such small changes may lack clinical significance, but they can affect the determination of chamber correction factors.

In order to minimize this, a multiplicative factor, p/p_0, was used to correct the machine output, where p is the measured pressure and p_0 is the reference pressure at which the unit was calibrated. Temperature variations in the head of the CyberKnife unit were monitored with a PT100 probe inserted between the primary and secondary collimators (off-field to avoid fluence perturbations). Correlations between the machine output, registered with an external ionization chamber placed at 5 cm depth in a water phantom, and the gantry temperature were measured to have a positive slope of a 0.5% per degree after the warm-up irradiation. This output correction factor was applied to all the measurements with a successful reduction of the relative standard deviation in the measurements of absorbed dose with both ionization chambers and alanine dosimeters within every investigated field.

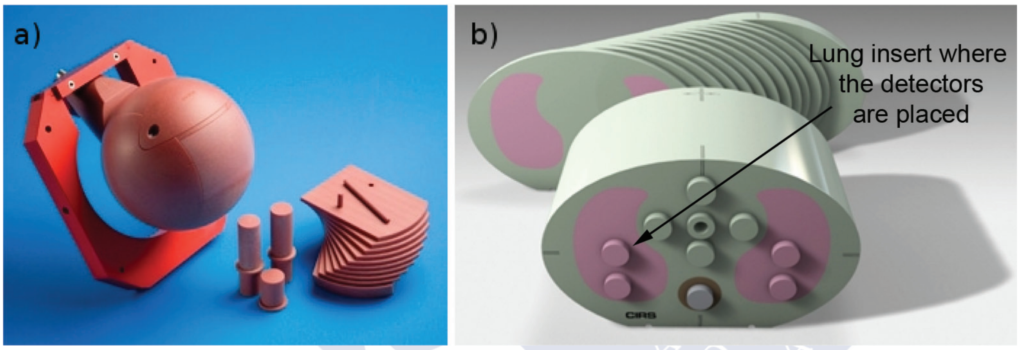

FIGURE 4.10: a) Spherical Solid Water Leksell® Gamma Knife Dosimetry Phantom employed for the measurement of the *pcsr* fields and one of the clinical treatments and b) Anthropomorphic CIRS IMRT Thorax Phantom employed for the measurement of one clinical treatment, the ionization chamber was placed inside the upper insert of the left lung.

Three phantoms were used depending on the field to be studied:

1. The 3D Blue Phantom water tank (Wellhofer, IBA Dosimetry GmbH, Schwarzenbruck, Germany) of 67.5 cm×64.5 cm×56 cm, used for the measurement of the *msr* field in water.
2. The 8 cm radius spherical Solid Water Leksell® Gamma Knife Dosimetry Phantom [142] (Elekta AB, Stockholm, Sweden), used for measurements in the *pcsr* fields and one of the clinical fields.
3. The anthropomorphic CIRS IMRT Thorax Phantom Model 002LFC (CIRS Norfolk, VA, USA), used for measurements in the other clinical field.

DICOM orientation standards [143] were adopted here for the specification of the coordinate system by considering head-first supine (HFS) patient position and [100, 010] image orientation; i.e. when the patient is positioned HFS on the couch, +x points to the patient's left side, +z points to towards the patient's head, and +y points to the patient's posterior side, see Figure 4.3. The orientation of the detectors depended on the phantom used. In the spherical phantom the detector stem as well as the alanine insert were on the sagittal plane, oriented at an angle of 44° with the z axis. The detectors reference point was placed at the phantom center; specific inserts had to be manufactured for this purpose as this phantom does not support PTW31014 nor CC13 detectors. The anthropomorphic phantom was placed head-first supine on the couch, with the detectors placed along the z axis with their reference points at 10 cm from the bottom of the phantom.

4.2.2.2 Investigated Fields.

Machine specific reference field.

Considering that achievement of lateral charged particle equilibrium is a desired condition for the measurement of *msr* fields, the widest collimator available for the CyberKnife machine, defining a 6 cm diameter circular field at 80 cm SAD, was chosen as machine specific reference field for this unit. A dose of approximately 14.5 Gy was delivered to the alanine/chamber position at a SSD of 75 cm and a SCD of 80 cm in a water phantom, following the setup of previous publications for the sake of comparison [144, 145].

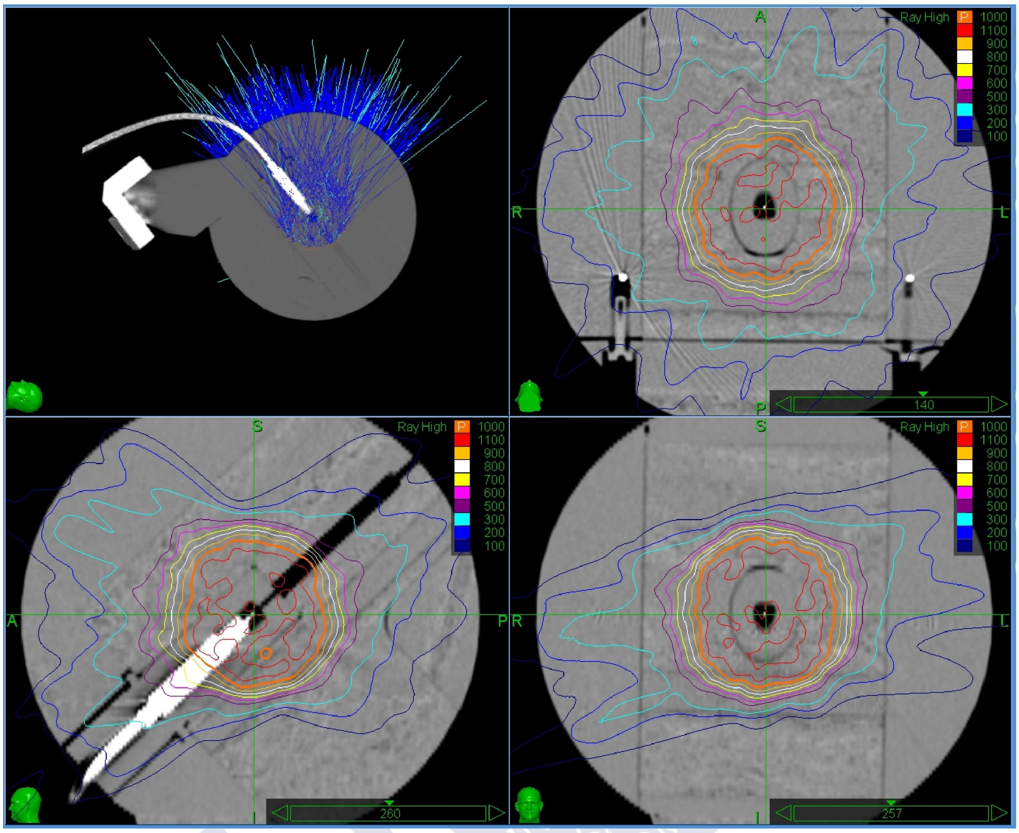

FIGURE 4.11: Plan class specific reference field scheme: beam incidences on the spherical phantom, top left panel, and transversal, sagittal and coronal isodoses map on the ionization chamber/alanine plane (top right, bottom left and bottom right panels respectively) for the *pcsr*2 field.

Plan class specific reference fields.

Regarding composite field dosimetry, two plan-class-specific reference fields were proposed, both of them delivering a spherical dose distribution to the spherical Solid Water Leksell® Gamma Knife Dosimetry Phantom (Elekta AB, Stockholm, Sweden).

- In *pcsr1*, the 1.5 cm diameter collimator was employed to deliver a homogeneous dose to a 32 mm diameter sphere centered in the phantom. The treatment involved 174 fields and a total delivery time of 42 minutes.

- For *pcsr2* (Figure 4.11), the 1.25 and 2 cm diameter collimators were chosen to deliver a spherical dose distribution with 48 mm diameter, also centered in the phantom. The plan involved 140 fields from the 1.25 cm collimator and 80 fields from the 2 cm collimator in a total delivery time of 61 minutes.

These *pcsr* fields match the set of collimators and PTV sizes of the investigated clinical treatments (see following section) but with a simpler geometry, which allows us to explore a possible dependence of correction factors on the set of collimators used in *pcsr* fields. Both treatments were planned to deliver a dose of 11.3 Gy by CyberKnife Multiplan® TPS.

Clinical treatments

The usefulness of intermediate calibration fields for the relative clinical dosimetry of CyberKnife was investigated for two representative clinical treatments, chosen among real treatments employed at the clinical institution.

- Firstly, a clinical brain treatment of 192 fields involving the use of the 1.5 cm collimator was chosen. The dose delivered to the spherical Solid Water phantom at the detectors reference point was 12.1 Gy, calculated by the TPS, being the dosimeters placed to have their reference point at the phantom center.
- Secondly, a lung clinical treatment of 250 fields was studied. For this treatment, the CIRS anthropomorphic phantom was irradiated using the 1.25 cm collimator in 141 fields and the 2 cm collimator in 109 fields. The detectors were placed in a rod insert available to perform measurements in the right lung of the phantom, receiving a dose of approximately 12 Gy, Figure 4.12.

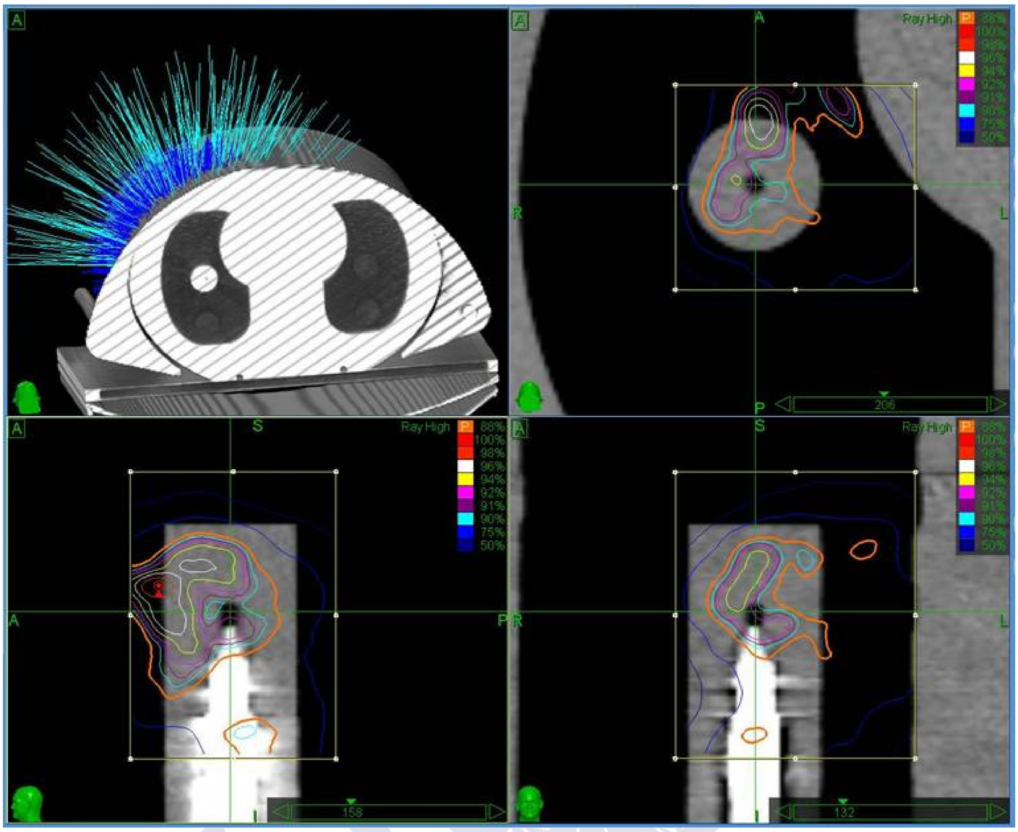

FIGURE 4.12: Scheme of the lung clinical treatment: Beam incidences on the anthropomorphic phantom, top left panel, and transversal, sagittal and coronal isodoses map on the ionization chamber/alanine plane (top right, bottom left and bottom right panels respectively).

4.2.2.3 Reference beam quality correction factor

The estimation of the values that standard k_{Q,Q_0} correction factors associated to the two studied ionization chambers would have if reference conditions could be achieved in our CyberKnife unit was performed by three different methods:

- On one hand, a measurement of the %dd(10) at 100 cm SSD was performed using the largest collimator available[3], yielding a value of 64.5% at 80 cm SCD. From this value, tables in Supplement 25 of the British Journal of Radiology [129] can be used to calculate the %dd(10) for the 10 cm×10 cm^2 standard field size, yielding a value of 66.6%. PTW31014 and CC13 chambers are however not considered in TG-51 dosimetry protocol and TRS-398 has to be consulted instead. Using the expression included in TRS-398 to derive $TPR_{20,10}$ values from %dd(10), we can obtain the $TPR_{20,10}$ for this CyberKnife unit, which is 0.665, leading to correction factors of 0.994 and 0.996 for PTW31014 and Scanditronix-Wellhofer CC13 respectively, calculated through interpolation from the values tabulated in TRS-398 for these chambers.

- If the expression of Palmans [120] is employed to calculate the %dd(10) for the 10 cm×10 cm field, a value of 67.1% is obtained, leading to a $TPR_{20,10}$ value of 0.669 using the expression from TRS-398, and 0.993 and 0.996 correction factors for the PTW31014 and Scanditronix-Wellhofer CC13 respectively.

- Finally, a direct measurement of the $TPR_{20,10}$ at SCD 80 cm with the 6 cm collimator field yielded a value of $TPR_{20,10}(5.4)$ equal to 0.637, which can be again converted to a value of $TPR_{20,10}(10)$ of 0.663 using the expression of Palmans. This value of beam quality descriptor leads to correction factors amounting to 0.994 and 0.996 for the PTW31014 and Scanditronix-Wellhofer CC13.

We can see in Table 4.5 that the different procedures followed for the estimation of correction factors consistently lead to very similar values, 0.994

---

[3] Following the formula of Sauer for the calculation of equivalent square field for circular fields, s=0.9×2×r [128], the 6 cm diameter circular field defined at 80 cm would be equivalent to a square field size of 5.4 cm at 80 cm SAD, or 6.75 cm at 100 cm SAD.

Estimation of standard beam quality correction factor

Method	BJR Supp. 25	Palmans	Palmans
Beam Quality	%dd(10)=66.6%	%dd(10)=67.01%	$TPR_{20,10}$=0.663
Chamber	PTW31014/CC13	PTW31014/CC13	PTW31014/CC13
k_{Q,Q_0}	0.994 / 0.996	0.993 / 0.996	0.994 / 0.996

Table 4.5: Summary of the results obtained through the different approaches followed for the estimation of the PTW31014 and CC13 standard beam quality correction factor k_{Q,Q_0} in the CyberKnife unit under study.

and 0.996 mean values will be taken for the calculation of intermediate correction factors for PTW31014 and Scanditronix-Wellhofer CC13 ionization chambers respectively.

4.2.2.4 Uncertainty budget and corrections

The relative uncertainties associated to the measurement with CC13 and PTW 31014 ionization chambers and alanine dosimeters in the CyberKnife unit are summarized in Table 4.6. Details about their evaluation will be described next.

Uncertainty source	Unc. type	CC13(%)	PTW31014(%)	Alanine (%)
Calibration coeff	B	0.8	1.4	1.7
Ambient conditions	B	0.2	0.2	0.1
Positioning	B	0.08 to 0.36	0.06 to 0.54	0.09 or 0.50
Machine Output	B	0.2	0.2	0.2
Repeatability	A	0.12 to 0.39	0.03 to 1.1	0.4 to 0.6
Total uncertainty	A & B	0.86 to 0.94	1.4 to 1.9	1.7 to 1.8

Table 4.6: Relative uncertainty contributions to ionization chamber and alanine measurements with coverage factor k=2.

Regarding the ionization chamber measurements, uncertainties are again dominated by the uncertainty of calibration coefficients, 0.8% and 1.4% for Scanditronix-Wellhofer CC13 and PTW31014 detectors respectively, determined in the Radiation Physics Laboratory at the Universidade de Santiago de Compostela.

Atmospheric pressure and temperature conditions were monitored and the correction factor accounting for air density changes was applied. The uncertainty associated to this correction has been considered to amount to a 0.2%. The polarization effect was found to be negligible for Scanditronix-Wellhofer CC13 and $\simeq$ 0.5% for PTW31014 in a 10 cm×10 cm field of a linac, although variations of approximately 0.5% are observed for smaller field sizes [146]. In composite fields, ionization chambers are irradiated under different conditions (in and off-field) and with smaller field sizes, which can involve changes in the polarity effect that cannot be properly corrected for. However, the overall effect is expected to be negligible and was therefore ignored.

Measurements of the saturation effect k_s were performed (the effect of charge multiplication, which can be important for the operation voltages here used [147], was included in the analysis), yielding values of unity within estimated uncertainties for both ionization chambers in the 60 mm collimator machine specific reference field measurements. Taking into account the lower dose rates associated with smaller field sizes and off-axis positioning, saturation corrections were considered to be also negligible for each of the investigated fields. The chamber leakage current was measured to be 5 fA for Scanditronix-Wellhofer CC13 and 15 fA for PTW31014. This contribution would lead to a systematic effect ranging from 0.002% to 0.04% for the measurements with the CC13 and from 0.04% to 1.2% for PTW31014 for the different fields under study. The leakage current was found to be very stable and was substracted off-line to the ionization chamber readings, with an associated uncertainty below 0.02% that was therefore neglected.

Type A uncertainties were estimated by repeating each measurement three times. Values ranging from 0.05% to 0.2% for Scanditronix-Wellhofer CC13 and from 0.01% to 0.6% for PTW31014 were obtained for the different calibration fields and clinical treatments.

The uncertainies associated to the NPL alanine/ESR dosimetry methodology are the same than those presented in Section 4.2.1.4. The independent estimation of alanine type A uncertainties was again obtained by performing three measurements, of three pellets each, for every field/treatment.

Finally, the uncertainty associated to alanine dosimeters and ionization chamber positioning has to be included. For the static *msr* field, this uncertainty was estimated to be $\simeq 0.2\%$ for lateral detector displacements of 0.1 mm. For composite fields, the effect of small dosimeter spatial mispositionings on the detector readings was evaluated from the TPS dose distributions and the geometry of the detectors. Dose deposition in the detectors was calculated for detector mispositionings following a $\sigma = 0.1$ mm Gaussian distribution, which corresponds to the positioning accuracy of the CyberKnife X-ray imaging system. Relative standard deviations in the average dose to the detectors ranging from 0.08% to 0.36%, from 0.06% to 0.54% and from 0.08% to 0.5% were obtained for Scanditronix-Wellhofer CC13, PTW31014 and the set of three alanine pellets respectively. These values were assumed as positioning uncertainties for the composite fields.

4.2.2.5 Dose values and correction factors.

Dose values measured with ionization chambers and alanine dosimeters are shown in Table 4.7. No systematic trends are observed between any of the detectors and the alanine dosimeter measurements and thus corrections factors are below or above unity depending on the studied field. However, larger discrepancies with respect to alanine are encountered in the PTW31014 measurements, probably due to the different volume averaging

Field	CC13	PTW31014	Alanine Dose
f_{msr}	14.51 ± 0.13	14.73 ± 0.21	14.43 ± 0.25
f_{pcsr1}	11.64 ± 0.11	11.74 ± 0.19	11.83 ± 0.21
f_{pcsr2}	11.82 ± 0.11	11.77 ± 0.22	11.90 ± 0.21
Lung clin treatment	13.21 ± 0.12	13.00 ± 0.24	13.21 ± 0.24
Brain clin treatment	11.92 ± 0.11	12.01 ± 0.20	11.86 ± 0.21

TABLE 4.7: Ionization chamber $[M_Q \cdot N_{D,w,Q_0}]$, and alanine measurements of absorbed dose to water expressed in Gy. Associated uncertainties are expressed with a coverage factor k=2.

effect of this detector compared to that of the alanine dosimeters and the CC13.

Table 4.8 shows experimental correction factors obtained for the CC13 and PTW31014 ionization chambers for the intermediate calibration fields and clinical treatments under study, with expanded uncertainties expressed with a coverage factor k=2.

For the intermediate calibration fields, overall correction factors are compatible with unity within uncertainties. Small differences are however encountered between static and composite field dosimetry, and correlation is observed for the behavior of the two detectors, with associated correction factors being above or below unity for both chambers depending on the investigated field. While f_{msr} exhibits a correction factor lower than one ($k^{f_{\mathrm{msr}},f_{\mathrm{ref}}}_{Q_{\mathrm{msr}},Q_0}$ equal to 0.979±0.022 and 0.994±0.020 for PTW31014 and CC13 detectors respectively) correction factors associated with composite calibration fields are higher than one ($k^{f_{\mathrm{pcsr}},f_{\mathrm{ref}}}_{Q_{\mathrm{pcsr}},Q_0}$ equal to 1.008±0.025 and 1.012±0.026 for PTW31014 in f_{pcsr1} and f_{pcsr2}, and 1.016±0.020 and 1.007±0.020 for the CC13 detector in f_{pcsr1} and f_{pcsr2} respectively).

PTW31014			
Calibration	$k^{f_{\mathrm{msr}},f_{\mathrm{ref}}}_{Q_{\mathrm{msr}},Q_0}$	$k^{f_{\mathrm{msr}},f_{\mathrm{ref}}}_{Q_{\mathrm{msr}},Q}$	–
f_{msr}	0.979(22)	0.985(22)	–
	$k^{f_{\mathrm{pcsr}},f_{\mathrm{ref}}}_{Q_{\mathrm{pcsr}},Q_0}$	$k^{f_{\mathrm{pcsr1\&2}},f_{\mathrm{ref}}}_{Q_{\mathrm{pcsr}},Q}$	$k^{f_{\mathrm{pcsr}},f_{\mathrm{msr}}}_{Q_{\mathrm{pcsr}},Q_{\mathrm{msr}}}$
f_{pcsr1}	1.008(25)	1.014(25)	1.029(12)
f_{pcsr2}	1.012(26)	1.018(26)	1.033(15)
Treatment	$k^{f_{\mathrm{clin}},f_{\mathrm{ref}}}_{Q_{\mathrm{clin}},Q_0}$ – $k^{f_{\mathrm{clin}},f_{\mathrm{ref}}}_{Q_{\mathrm{clin}},Q}$	$k^{f_{\mathrm{clin}},f_{\mathrm{msr}}}_{Q_{\mathrm{clin}},Q_{\mathrm{msr}}}$	$k^{f_{\mathrm{clin}},f_{\mathrm{pcsr1\&2}}}_{Q_{\mathrm{clin}},Q_{\mathrm{pcsr1\&2}}}$
brain	1.016(27) – 1.022(27)	1.037(16)	1.008(17) & 1.005(19)
lung	0.987(24) – 0.993(24)	1.008(12)	0.980(14) & 0.976(16)

CC13			
Calibration	$k^{f_{\mathrm{msr}},f_{\mathrm{ref}}}_{Q_{\mathrm{msr}},Q_0}$	$k^{f_{\mathrm{msr}},f_{\mathrm{ref}}}_{Q_{\mathrm{msr}},Q}$	–
f_{msr}	0.994(20)	0.998(20)	–
	$k^{f_{\mathrm{pcsr}},f_{\mathrm{ref}}}_{Q_{\mathrm{pcsr}},Q_0}$	$k^{f_{\mathrm{pcsr}},f_{\mathrm{ref}}}_{Q_{\mathrm{pcsr}},Q}$	$k^{f_{\mathrm{pcsr}},f_{\mathrm{msr}}}_{Q_{\mathrm{pcsr}},Q_{\mathrm{msr}}}$
f_{pcsr1}	1.016(20)	1.020(20)	1.0220(92)
f_{pcsr2}	1.007(20)	1.011(20)	1.0124(94)
Treatment	$k^{f_{\mathrm{clin}},f_{\mathrm{ref}}}_{Q_{\mathrm{clin}},Q_0}$ – $k^{f_{\mathrm{clin}},f_{\mathrm{ref}}}_{Q_{\mathrm{clin}},Q}$	$k^{f_{\mathrm{clin}},f_{\mathrm{msr}}}_{Q_{\mathrm{clin}},Q_{\mathrm{msr}}}$	$k^{f_{\mathrm{clin}},f_{\mathrm{pcsr1\&2}}}_{Q_{\mathrm{clin}},Q_{\mathrm{pcsr1\&2}}}$
brain	1.000(21) – 1.004(21)	1.005(10)	0.984(11) & 0.993(11)
lung	0.995(20) – 0.999(20)	1.000(10)	0.979(10) & 0.988(10)

TABLE 4.8: Measured correction factors for intermediate calibration fields f_{msr}, f_{pcsr1} and f_{pcsr2} and clinical treatments. Associated uncertainties affecting last decimals are shown in brackets with two significant digits and coverage factor k=2.

Focusing on the clinical treatments, Figure 4.13 is included to facilitate the interpretation of results. Scanditronix-Wellhofer CC13 yielded overall correction factors being very similar among them and close to unity for both treatments: $k^{f_{\text{clin}},f_{\text{ref}}}_{Q_{\text{clin}},Q_0}$ equal to 1.000±0.021 and 0.995±0.021 for the brain and lung treatments respectively. In this case, the f_{msr} field is the intermediate calibration field leading to clinical to intermediate field correction factors closer to unity, $k^{f_{\text{clin}},f_{\text{msr}}}_{Q_{\text{clin}},Q_{\text{msr}}}$ equal to 1.000±0.010 and 1.005±0.010, although compatibility with unity is also found for $k^{f_{\text{clin}},f_{\text{pcsr2}}}_{Q_{\text{clin}},Q_{\text{pcsr2}}}$, with 0.993±0.011 and 0.988±0.010 values for the brain and lung treatments respectively. The *pcsr1* field leads to $k^{f_{\text{clin}},f_{\text{pcsr1}}}_{Q_{\text{clin}},Q_{\text{pcsr1}}}$ equal to 0.984±0.010 for the brain treatment and, departing more drastically from unity, 0.979±0.010 for the lung treatment.

Deviations from unity in correction factors associated to clinical treatments arise more often for the PTW31014 detector, although given the uncertainties, results are again compatible with unity: $k^{f_{\text{clin}},f_{\text{ref}}}_{Q_{\text{clin}},Q_0}$ equal to 1.016±0.027 and 0.987±0.027 for the brain and lung treatment respectively. In this case, *pcsr* fields would remain closer to the brain treatment: $k^{f_{\text{brain}},f_{\text{pcsr}}}_{Q_{\text{brain}},Q_{\text{pcsr}}}$ equal to 1.008±0.017 and 1.005±0.019 for *pcsr1* and *pcsr2*, while $k^{f_{\text{brain}},f_{\text{msr}}}_{Q_{\text{brain}},Q_{\text{msr}}}$ is equal to 1.037±0.016. For the lung treatment, the *msr* field would be the intermediate calibration field closer to the treatment, $k^{f_{\text{lung}},f_{\text{msr}}}_{Q_{\text{lung}},Q_{\text{msr}}}$ equal to 1.008±0.012, while the correction factors associated to the *pcsr* fields would deviate more importantly from unity: $k^{f_{\text{lung}},f_{\text{pcsr}}}_{Q_{\text{lung}},Q_{\text{pcsr}}}$ equal to 0.980±0.014 and 0.976±0.016 for *pcsr1* and *pcsr2*.

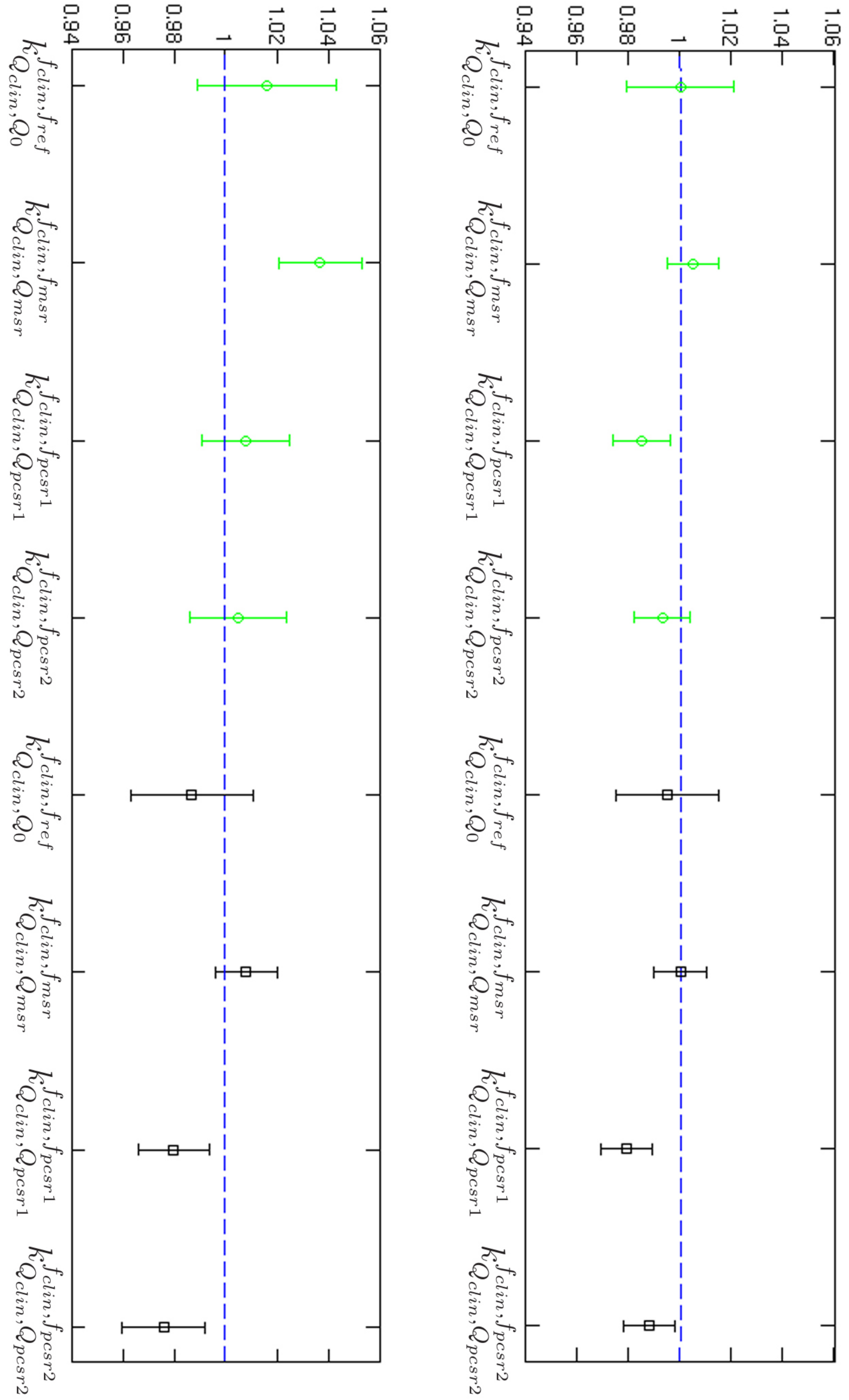

FIGURE 4.13: Scanditronix-Wellhofer CC13 (top) and PTW31014 (bottom) measured correction factors associated to the brain (○) and lung (□) clinical treatments in CyberKnife, uncertainties are shown with a coverage factor k=2.

4.2.2.6 Monte Carlo Simulation

Monte Carlo simulation of the CyberKnife machine treatment head was performed with the BEAMnrc code [61], using the information about geometry and materials provided by the manufacturer, see Figure 4.14, while the deposition of dose was simulated with the DOSXYZnrc code and the C++ based EGSnrc code *cavity* [59, 148].

Transport Parameters.

All simulations were performed considering spin effects, bound Compton scattering, photoelectron angular sampling, Rayleigh scattering, atomic relaxations, triplet production and radiative Compton corrections. NIST cross sections were employed for bremsstrahlung interactions and Koch Motz for bremsstrahlung angular sampling.

BEAMnrc simulations were performed to score, at a distance of 70 cm from the electron source, particle phase spaces registering information about the energy, position and velocity of the particles propagated through the linac geometry. The objective of these simulations is to obtain a phase space with a number of statistically independent particles high enough to later yield statistical noise free Monte Carlo calculated values of absorbed dose. The number of phase space particles estimated to suffice for this purpose was considered to be 600000 cm^{-2} in this work. The Directive Bremsstrahlung Splitting (DBS) technique was employed with an splitting number of 1000 in order to to generate the maximum number of statistically independent particles from the minimum number of initial particles. The DBS radius was changed from field to field being, at 80 cm SAD, equal to the radius of the field plus 1.5 times the continuous slowing down approximation (CSDA) range of an electron of maximum energy, so that field penumbras were lying inside the bremsstrahlung splitting region. The range rejection (RR) variance reduction technique was applied, through the whole geometry, to electrons with energies below 1 MeV, and photon and electron transport cut-off energies of 0.01 MeV and 0.7 MeV were respectively used (electron rest mas, 0.511 MeV, is not substracted from electron energies), see Table 4.9.

Particles from BEAMnrc phase spaces were then propagated through different phantoms in which absorbed dose was calculated. DOSXYZnrc simulations of absorbed dose to water were performed using again the RR variance reduction technique on particles with energies below 1 MeV and photon and electron transport cut-off energies of 0.01 MeV and 0.7 MeV respectively, through the whole geometry. Water slabs were placed around calculation voxels using *dsurround* variables to avoid an excessive number of regions in the geometry, and the photon splitting variance reduction technique was applied with a splitting number of 10.

Monte Carlo transport or Variance Reduction Technique			
	BEAMnrc	DOSXYZnrc	cavity
Maximum energy for RR	1 MeV	1 MeV	1 MeV
Electron transport cut-off energy	0.700 MeV	0.700 MeV	0.521 MeV
Photon transport cut-off energy	0.010 MeV	0.010 MeV	0.010 MeV
DBS number	1000	–	–
Photon splitting number	–	10	80
Medium to calculate ranges for RR	That of every region		Air

TABLE 4.9: Monte Carlo transport and variance reduction parameters used to simulate the CyberKnife linac (BEAMnrc), to calculate absorbed dose to water during the linac commissioning process (DOSXYZnrc) and to calculate absorbed dose to water, to ionization chambers and to alanine for the determination of beam quality correction factors (cavity).

EGSnrc calculations of dose delivered to water, to ionization chambers and to alanine were performed using photon and electron transport cut-off energies of 0.01 MeV and 0.521 MeV respectively through the whole geometry. The photon splitting variance reduction technique was applied with a splitting number of 80. Additionally, electron RR was applied outside the cavity with a survival probability of 1/125, using air as the medium to calculate the ranges. Simulation efficiencies, defined as $1/(t\sigma^2)$, with t standing for the CPU simulation time in seconds and σ the relative standard deviation of the simulation, were calculated for the composite field simulations, obtaining values ranging from 0.01 s^{-1} to 0.74 s^{-1} depending on the cavity volume and dose deposition medium.

Machine Commissioning

Simulation of the treatment unit requires a commissioning process to fine-tune the sensitive parameters of the X-ray beam, which are [149]:

- Energy of the electron beam impinging the linac target.
- Spatial distribution of the electron beam.

Monoenergetic spectra and Gaussian spatial distributions of different full widths at half maximum (FWHM) were employed in the BEAMnrc simulation of the treatment head for the scoring of phase spaces with at least 8×10^4 particles per square cm. DOSXYZnrc calculated dose distributions were then obtained for different combinations of beam parameters and compared with measured dose distributions in order to select the optimum beam parameters. The dose distributions employed for comparison with Monte Carlo simulations were measured with a PTW60012 diode detector (PTW-Freiburg, Germany) as recommended by Accuray Inc. for commissioning procedures.

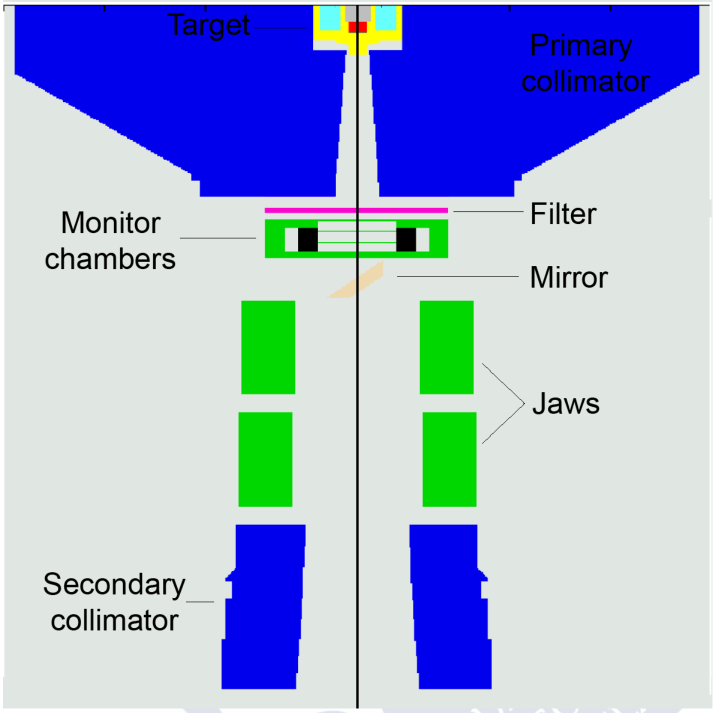

Figure 4.14: Geometry of the CyberKnife linac head in the xz plane as seen with the BEAMnrc graphical user interface. Dimensions are not realistic and materials are not given due to the non disclosure agreement signed with Accuray to preserve this information.

For the election of the optimal source parameters, a procedure based on the method of Pena *et al.* [150] was followed, in which two cost functions are defined comparing measured and simulated dose distributions. A first cost function, given by the distance between field edges, DBFE, of measured and simulated profiles is employed for the determination of the size of the electron source that results optimal at different energies. DBFE is calculated as the sum of the squared difference between the position of 80%, 60%, 50%, 40% and 20% dose levels, with respect to the maximum, from measured and simulated profiles.

This first step involved in our case the comparison of lateral profiles from collimators, col_i, of 1, 1.5 and 3 cm diameters, measured and simulated at 1.5, 5 and 10 cm depth in water. Electron spatial distributions with 1.5, 2 and 2.5 mm FWHM were tested in these simulations for electron source energies, E_j, of 6.3, 6.5, 6.6 and 6.7 MeV, an energy range similar to that reported in other works of Monte Carlo simulation of CyberKnife units [28, 145, 151]. The FWHM yielding the minimum cost function is obtained for every energy and field size, as:

$$FWHM_{col_i}(E_j) = \underset{FWHM_k}{\arg\min}\, DBFE_{col_i}(E_j, FWHM_k) \tag{4.2}$$

A weighted average is then obtained for each energy E_j as:

$$FWHM(E_j) = \sum_{col_i} \omega_{col_i} FWHM_{col_i}(E_j) \tag{4.3}$$

In our case, weight factors, ω_{col}, of 3, 3 and 1 were chosen for 1 cm, 1.5 cm and 3 cm collimators respectively. Higher weights were given to the smaller collimators due to the small field sizes that are involved in the simulation of *pcsr* and clinical fields. The average FWHM took the same value, 0.197 mm, for all the investigated energy values. In order to build the second cost function, measured lateral and percent depth dose profiles are compared, now in terms of the Gamma function [63], with the simulations obtained at each energy using the optimal electron source spatial dose distribution, with 0.197 mm FWHM, as calculated above. The Γ function has the following form:

$$\Gamma_{E_j} = \sum_{col_i} \omega_{p_{col_i}} \gamma_{p_{col_i}} + \omega_{d_{col_i}} \gamma_{d_{col_i}} \tag{4.4}$$

Where $\gamma_{p_{col_i}}$ and $\gamma_{d_{col_i}}$ represent the sum of Gamma values for the lateral and depth dose profiles comparisons respectively, and ω_p and ω_d are their weight factors (here set to one). The optimal energy is the one that minimizes Equation 4.4.

DBFEs and values of the global cost function obtained for the different combinations of energy and FWHM are shown in Figure 4.15. The optimal combination of source parameters was determined to be 6.5 MeV and a 0.197 mm FHWM.

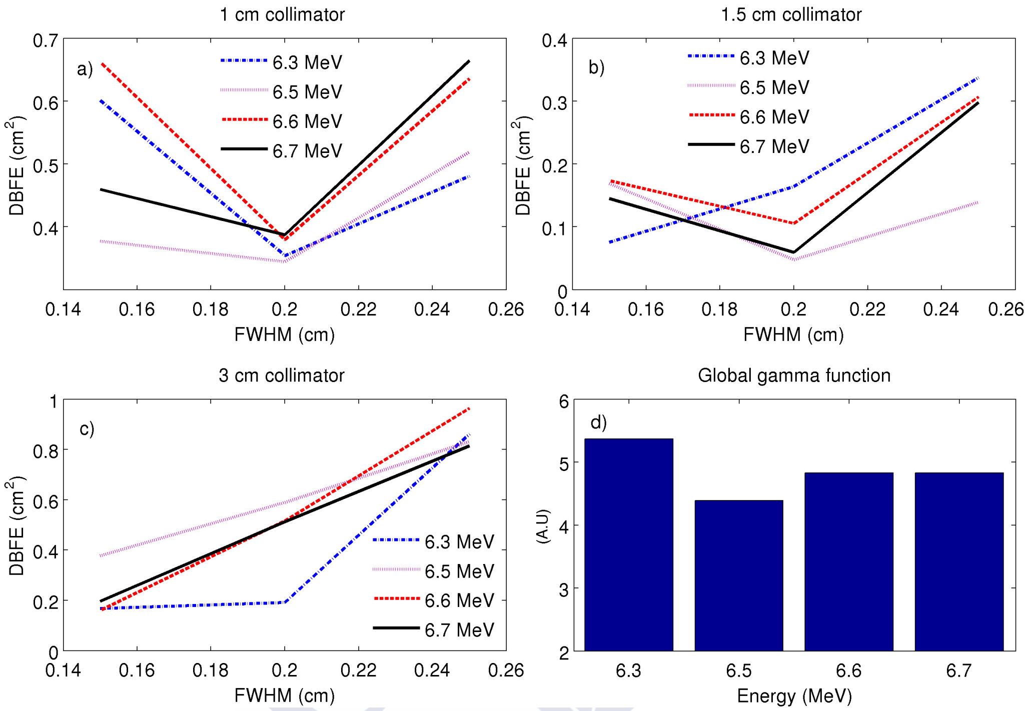

FIGURE 4.15: Distance between field edges of measured and simulated lateral profiles calculated for different electron source energies and FWHM for the collimators with 1cm (a), 1.5 cm (b) and 3 cm (c) diameters. d) Global Gamma function obtained from the comparison of measured and simulated lateral and depth dose profiles for 6.3, 6.5, 6.6 and 6.7 MeV electron sources with 0.196 FWHM.

Finally, an additional test for the beam energy was performed through the comparison of measured and calculated tissue phantom ratios for the above mentioned collimators at 1.5, 5 and 10 cm depths for 6.5, 6.6 and 6.7 MeV beam energies, obtaining again better agreement with the experimental measurements through the simulation involving a 6.5 MeV electron source.

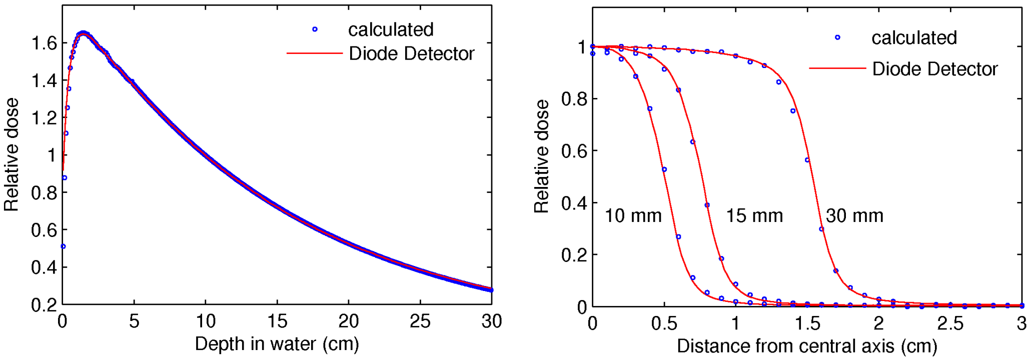

a) 60 mm collimator

b) z= 1.5 cm

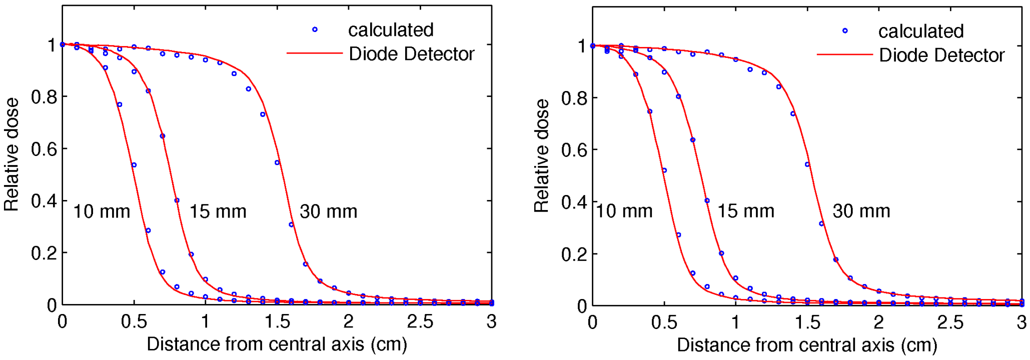

c) z= 5 cm

d) z= 10 cm

FIGURE 4.16: Comparison of the dose distributions measured with a PTW 60012 diode detector in the CyberKnife unit of the Hospital Ruber International with Monte Carlo calculated dose distributions simulated with an electron source of 6.5 MeV and 0.197 mm FHWM. Comparison of central axis depth dose profile for the 60 mm collimator field a), and lateral profiles for 10 mm, 15 mm and 30 mm fields at 85 cm SAD and 1.5 cm b), 5 cm c) and 10 cm d) depth in water.

Figure 4.16 shows the comparison of measured and Monte Carlo calculated lateral and percent depth dose profiles for an electron beam incident on the X-ray target with an energy of 6.5 MeV and 0.197 mm FWHM Gaussian spatial distribution. Under these beam parameters, the Monte Carlo calculated $TPR_{20,10}$ at 80 cm source to detector distance for the 60 mm collimator yielded a value of 0.640±0.012 (k=2), which is in agreement within uncertainties with the measured value of 0.637.

Correction factors calculation

Monte Carlo correction factors were obtained after treatment unit commissioning by calculating the dose imparted to the detectors by the intermediate calibration fields, *msr* and *pcsr*, a ^{60}Co conventional reference field and the brain clinical treatment. The geometry of the anthropomorphic phantom is much more complicated, and since the detailed geometry was not available, the clinical lung treatment was not simulated. A geometrically detailed simulation of detectors and phantoms was performed with the EGSnrc code and the C++ class library [60], see Figure 4.17. Dose to water was also calculated in a spherical voxel of 1.5 mm radius for the determination of correction factors and in three cylindrical voxels emulating the alanine pellets' geometry for the study of volume averaging effects and alanine to water stopping power ratios.

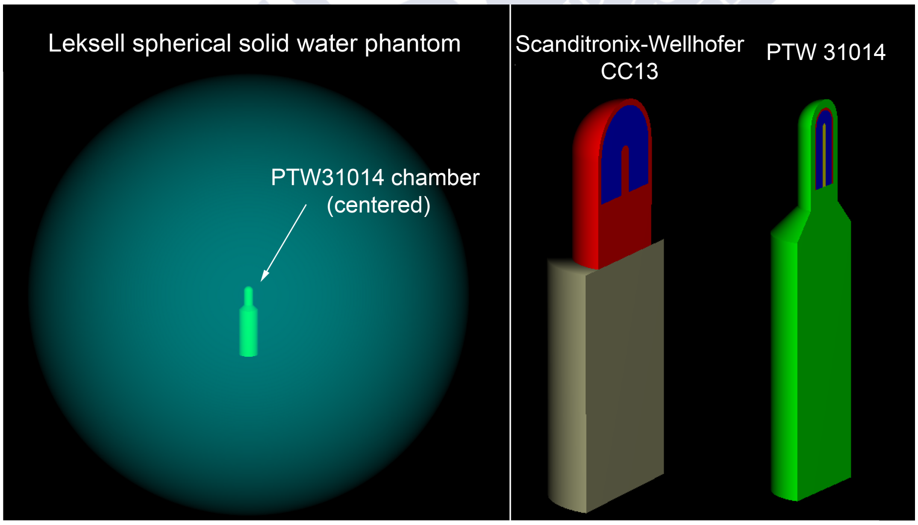

FIGURE 4.17: Scheme of the phantom and ionization chamber geometries employed for the Monte Carlo simulation of correction factors. Left, Solid Water spherical phantom with the ionization chamber (here PTW31014) reference point placed at the center of the sphere. Right, geometry and materials employed for the simulation in cavity of Scanditronix-Wellhofer CC13 and PTW31014 ionization chambers.

Additionally, Monte Carlo simulation of a conical collimator defining a field of 8.88 cm diameter, d, at 80 cm SAD, which is equivalent to a square field size of 10 cm at SSD = 100 cm ($S_{\mathrm{eq}} = 0.9 \times d \times 100/80$) [128], was performed to crosscheck the values of k_{Q,Q_0} estimated in Section 4.2.2.3. Dose to water and dose to ionization chambers under this 8.88 cm circular beam and the standard ^{60}Co reference field served for the calculation of k_{Q,Q_0} correction factors, yielding values of 0.991±0.016 and 0.996±0.011 (k=2) for the PTW31014 and the Scanditronix-Wellhofer CC13 ionization chambers, which are in good agreement with the 0.994 and 0.996 values estimated in section 4.2.2.3.

Composite field simulation.

The simulation of composite fields involved a procedure similar to that adopted by Ma *et al.* [151]. Information about composite fields, such as monitor units, collimator size and beam incidence direction per beam were obtained from Accuray CyberKnife treatment plan XML files.

Beams were propagated with the EGSnrc code and the C++ library along the z axis, and thus for each beam the whole geometry (phantom and detectors) was rotated to align the beam propagation with the simulation z axis. Rotation matrices were calculated, for each beam propagation axis, from the position of two points, node and target, provided in the treatment XML file in the patient CT coordinate system [141].

Dose to water and dose to air in the cavity of the ionization chambers were then calculated to compute correction factors as described in Equation 1.16. The large number of segments involved in composite fields made simulations very costly in terms of computation time and thus uncertainty levels, ranging from 0.28% to 0.94% (k=2) were set as a compromise between simulation time and the level of accuracy desired for the correction factors calculation. Monte Carlo correction factors associated with the intermediate calibration fields and the brain treatment field, shown in Table 4.10 and Figure 4.18, present associated uncertainties ranging from 0.8% to 1.4% (k=2).

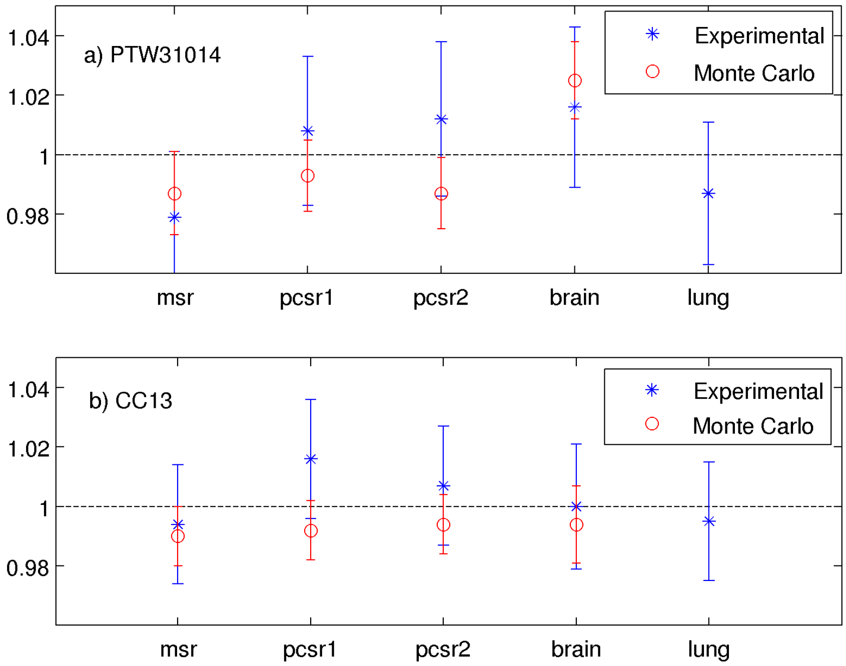

FIGURE 4.18: Experimental and Monte Carlo overall correction factors, $k^{f_i,f_{\text{ref}}}_{Q_i,Q_0}$, relating intermediate calibration fields and clinical fields, f_i, and conventional reference conditions, f_{ref}, for a) PTW31014 and b) CC13 ionization chambers. Uncertainty bars are presented with a coverage factor k=2.

Monte Carlo calculated correction factors are in agreement with the measured values within measurement uncertainties for both PTW31014 and Scanditronix-Wellhofer CC13 ionization chambers, with the exception of *pcsr1* for CC13, where a discrepancy of 2.4% is found, being the uncertainty of the experimental correction factor of a 2%. Discrepancies between simulation and measurements were found to be generally higher for the composite fields, which could be related with dose inhomogeneities in the treatment PTV. These discrepancies may not be significant if we take

PTW31014			
Calibration	$k^{f_{\mathrm{msr}},f_{\mathrm{ref}}}_{Q_{\mathrm{msr}},Q_0}$	$k^{f_{\mathrm{msr}},f_{\mathrm{ref}}}_{Q_{\mathrm{msr}},Q}$	–
f_{msr}	0.987(14)	0.993(22)	–
	$k^{f_{\mathrm{pcsr}},f_{\mathrm{ref}}}_{Q_{\mathrm{pcsr}},Q_0}$	$k^{f_{\mathrm{pcsr}},f_{\mathrm{ref}}}_{Q_{\mathrm{pcsr}},Q}$	$k^{f_{\mathrm{pcsr}},f_{\mathrm{msr}}}_{Q_{\mathrm{pcsr}},Q_{\mathrm{msr}}}$
f_{pcsr1}	0.993(12)	0.999(12)	1.006(11)
f_{pcsr2}	0.987(12)	0.992(12)	0.999(12)
Treatment	$k^{f_{\mathrm{clin}},f_{\mathrm{ref}}}_{Q_{\mathrm{clin}},Q_0}$ – $k^{f_{\mathrm{clin}},f_{\mathrm{ref}}}_{Q_{\mathrm{clin}},Q}$	$k^{f_{\mathrm{clin}},f_{\mathrm{msr}}}_{Q_{\mathrm{clin}},Q_{\mathrm{msr}}}$	$k^{f_{\mathrm{clin}},f_{\mathrm{pcsr1\&2}}}_{Q_{\mathrm{clin}},Q_{\mathrm{pcsr1\&2}}}$
brain	1.025(13) – 1.031(13)	1.038(12)	1.032(10) & 1.039(10)

CC13			
Calibration	$k^{f_{\mathrm{msr}},f_{\mathrm{ref}}}_{Q_{\mathrm{msr}},Q_0}$	$k^{f_{\mathrm{msr}},f_{\mathrm{ref}}}_{Q_{\mathrm{msr}},Q}$	–
f_{msr}	0.990(10)	0.994(10)	–
	$k^{f_{\mathrm{pcsr}},f_{\mathrm{ref}}}_{Q_{\mathrm{pcsr}},Q_0}$	$k^{f_{\mathrm{pcsr}},f_{\mathrm{ref}}}_{Q_{\mathrm{pcsr}},Q}$	$k^{f_{\mathrm{pcsr}},f_{\mathrm{msr}}}_{Q_{\mathrm{pcsr}},Q_{\mathrm{msr}}}$
f_{pcsr1}	0.992(10)	0.996(10)	1.0024(88)
f_{pcsr2}	0.994(10)	0.998(10)	1.004(10)
Treatment	$k^{f_{\mathrm{clin}},f_{\mathrm{ref}}}_{Q_{\mathrm{clin}},Q_0}$ – $k^{f_{\mathrm{clin}},f_{\mathrm{ref}}}_{Q_{\mathrm{clin}},Q}$	$k^{f_{\mathrm{clin}},f_{\mathrm{msr}}}_{Q_{\mathrm{clin}},Q_{\mathrm{msr}}}$	$k^{f_{\mathrm{clin}},f_{\mathrm{pcsr1\&2}}}_{Q_{\mathrm{clin}},Q_{\mathrm{pcsr1\&2}}}$
brain	0.994(13) – 0.998(13)	1.0041(88)	1.0017(81) &1.0004(90)

TABLE 4.10: Monte Carlo calculated correction factors for intermediate calibration fields f_{msr}, f_{pcsr1} and f_{pcsr2} and the brain clinical treatment. Associated uncertainties affecting last decimals are shown in brackets with two significant digits and coverage factor k=2.

into account that only type A uncertainties were considered in the calculation of Monte Carlo correction factors. Some works [145, 152] propose the introduction of type B uncertainties in the uncertainty budget of Monte

Carlo calculated absorbed dose, which would increase our expanded uncertainties.

It should be noted that Monte Carlo calculations lead to correction factors associated to the CC13 chamber that are very similar among them and compatible with unit for all the investigated fields. For PTW31014, similar correction factors, also compatible with unity, were obtained associated to intermediate calibration fields, but a 3.1% deviation was found between absorbed dose to water and the chamber measurement for the brain clinical treatment.

Water to alanine dose ratios calculated from simulations yielded values between 0.969 and 0.972, which agree well with previously reported data on water to alanine mass energy absorption coefficient and stopping power ratios for the photon beam energies under investigation [82].

4.2.2.7 Discussion

The applicability of the studied intermediate calibration fields for the relative dosimetry of clinical treatments has to be studied considering the dosimetric paths proposed for that purpose by the new formalism, Section 1.2.3.3. In Equation 1.15, $k_{Q_{\mathrm{clin}},Q_i}^{f_{\mathrm{clin}},f_i}$ values close to unity would imply a better representation of the clinical field by the corresponding intermediate reference field. In this context, and as we said in Section 4.2.2.5, measurements with PTW31014 chamber yielded clinical overall correction factors that would make f_{msr} a more representative field for the lung treatment, while both f_{pcsr1} and f_{pcsr2} would stand closer to the brain treatment. Although measured $k_{Q_{\mathrm{clin}},Q_{\mathrm{msr}}}^{f_{\mathrm{clin}},f_{\mathrm{msr}}}$ and $k_{Q_{\mathrm{clin}},Q_{\mathrm{pcsr}}}^{f_{\mathrm{clin}},f_{\mathrm{pcsr}}}$ are not compatible within uncertainties these differences may not be however significant, as results obtained through Monte Carlo simulation for the static and composite calibration fields for both chambers suggest the dosimetric equivalence between f_{msr} and any of the studied *pcsr* fields. Moreover, instabilities exhibited by the

PTW31014 ionization chamber might put under question the relevance of the differences observed in the measurements.

On the other hand, no significant correlation was found between the composite and clinical fields employing the same set of collimators, as correction factors associated to such fields were not found to be closer to unity than those associated with intermediate calibration fields delivered by other collimators.

Regarding clinical dosimetry, it should be again noted that general conclusions should not be drawn because other clinical treatments could be found to behave differently. Inhomogeneities arising in dose distributions and mispositionings affecting composite field measurements may be responsible in part for the discrepancies encountered between the different investigated fields, as these effects can cause substantial correction factor variations. Additionally, machine output variations due to the vented monitor chambers in the CyberKnife unit were corrected for, but small residual effects may persist.

Dose Inhomogeneities

Composite intermediate calibration field dosimetry can have high associated uncertainties due to the combination of measurement conditions with steep dose gradients or low dose regions (under which detectors may give misleading results) and the positioning of both the CyberKnife robotic arm and the detectors.

In order to estimate the effect that dose inhomogeneities can have in the determination of correction factors, absorbed dose in every alanine pellet was calculated by Monte Carlo simulation to estimate the averaging effect introduced by the use of three pellets for the determination of absorbed dose to water in every measurement. Relative standard deviations of the dose imparted to the three pellets were observed to be around 0.7% and

0.6% for f_{pcsr1} and f_{pcsr2}, while standard deviations compatible with zero within uncertainties were obtained for f_{msr} and the brain clinical treatment. Alternatively, the analysis of TPS dose distributions of the composite fields under investigation revealed dose inhomogeneities contributing to an average effect in the alanine that amounted to a 0.7% and a 0.5% for f_{pcsr1} and f_{pcsr2} and to a 0.5% and a 0.7% for the brain and lung clinical treatments respectively.

In an attempt to study the effect of dose inhomogeneities in plan class specific reference fields dose distributions, Chung *et al.* [137] proposed the quantification of dose homogeneity in *pcsr* fields target volumes by a homogeneity index, HI, defined as the ratio of $D_{2\%} - D_{98\%}$ to the average dose in the target volume, where $D_{2\%}$ and $D_{98\%}$ are the maximum values of dose achieved by at least 2% and 98% of the target volume. In this work, the study of correction factors versus the homogeneity index revealed that correction factors associated to Farmer type chambers depart more drastically from unity as the homogeneity index increases, due to the growing importance of gradient effects in large active volumes as the HI increases. Small volume chambers exhibit correction factors closer to unity but with higher variability due to the effect of positioning as the HI increases.

When TPS dose distributions from the CyberKnife *pcsr* fields proposed here were analyzed, HIs calculated in a spherical central target volume of 10 mm radius exhibited values of 13.8% and 6.9% for *pcsr1* and *pcsr2*, both above the 5% that was considered by Chung in TomoTherapy to be the value above which low homogeneity in the target volume may involve noticeable gradient effects or correction factors varying strongly with the positioning. We have to consider however that the establishment of such a threshold for acceptable homogeneity in *pcsr* fields may be delicate and can depend on the treatment technique. Since *pcsr* fields should deliver homogeneous dose distributions in order to ensure measurement reproducibility and minimize detector perturbation factors, the two composite fields proposed here, planned by the Accuray TPS with parameters and constraints described in section 4.2.2.2, may not perfectly match the requirements of an ideal intermediate calibration field as defined in the proposal for new protocol [30], although given the intrinsic characteristics of the CyberKnife delivery, they are probably a good example of the *pcsr* fields that can be established for this technique.

4.2.2.8 Review

As we made for Tomotherapy, an overview of the work that has been presented about the application of the new formalism to CyberKnife results useful to gain a more complete perspective and will be also presented here for CyberKnife.

Previous works on CyberKnife dosimetry studied total scatter factors for different detectors and collimators [28, 116], Monte Carlo calculated k_{Q_{msr},Q_0} values for different beam energies and detectors [117] and $k_{Q_{\mathrm{msr}},Q}^{f_{\mathrm{msr}},f_{\mathrm{ref}}}$ correction factors associated with different ionization chambers [144, 145]. Plan Class Specific reference field have not been proposed nor measured by other authors and thus the comparison will be restricted to *msr* fields, see the k_{Q_{msr},Q_0} correction factors presented in Figure 4.19.

All the authors employed the 6 cm diameter collimator for the definition of the *msr* field, all measured at 80 cm SCD but with some differences in the SSD: 70 cm in the work of Kawachi *et al.* [117], 75 cm in the work of Francescon *et al.* [145] and 78.5 cm in the work of Pantelis *et al.* [144], while our study was performed at 75 cm SSD.

In our study [153], both simulations and measurements yielded overall correction factors departing from unity by approximately 2%, with results for the PTW31014 chamber that are in agreement with those recently presented by Francescon *et al.* [145] for the f_{msr}, although the CC13 chamber

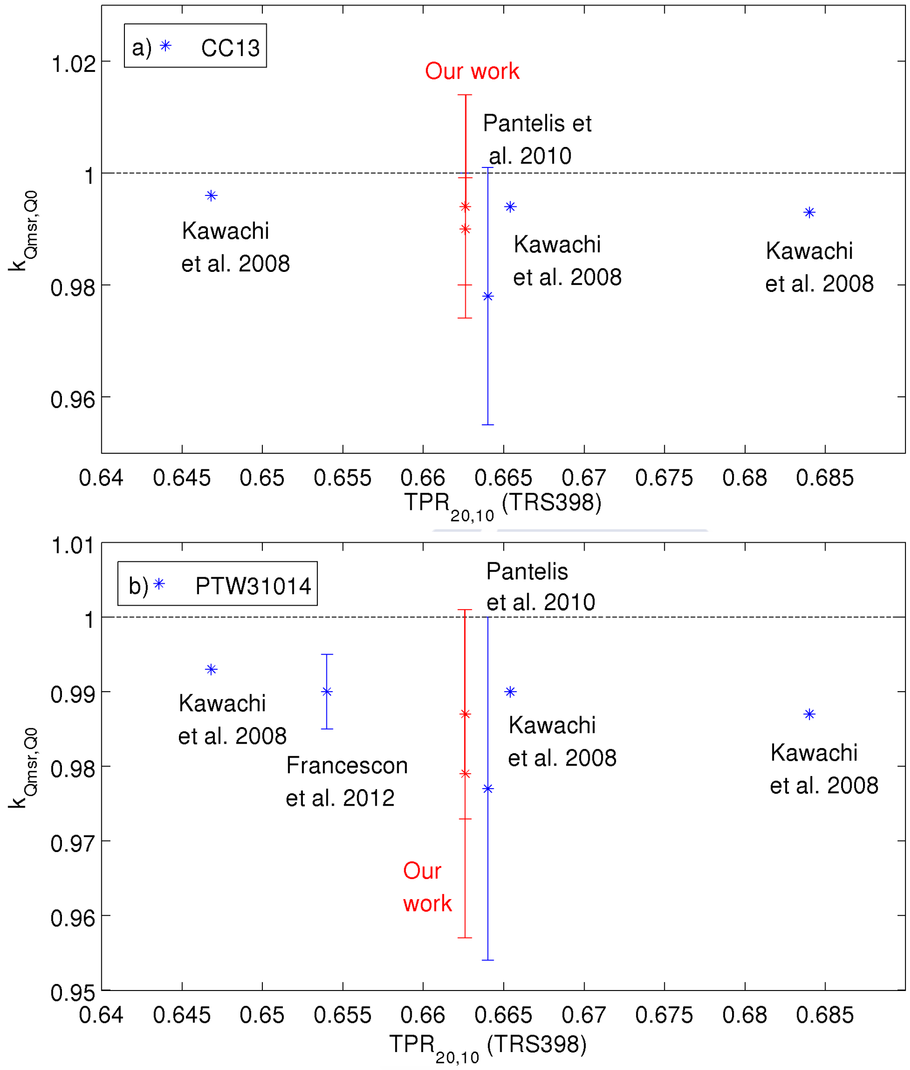

FIGURE 4.19: Summary of $k_{Q_{\mathrm{msr}},Q_0}^{f_{\mathrm{msr}},f_{\mathrm{ref}}}$ correction factors published to this date for CC13 (a), and PTW31014 (b) ionization chambers versus the estimated value of CyberKnife $TPR_{20,10}$ under reference conditions (10 cm ×10 cm field at 100 cm SCD).

was not studied in that work. Monte Carlo calculated correction factors presented by Kawachi *et al.* [117] for both PTW31014 and CC13 chambers and different beam qualities are also consistent with those presented here. In the work of Pantelis *et al.* [144], correction factors for these ionization chambers can be obtained from the k_{Q_{msr},Q_0} correction factor for a Farmer type chamber and Farmer to PTW3104 and CC13 dose ratios, finding also agreement with our results.

All the correction factors associated with the *msr* fields exhibit values sistematically below unity, although the uncertainties associated to the experimental measurements (only available in our work and that by Pantelis *et al.*) are high enough and do not discard compatibility with unity.

4.2.3 Conclusions.

In our studies about TomoTherapy and CyberKnife we have found that depending on the clinical treatment field and ionization chamber used, either the *msr* or *pcsr* fields proposed result in associated correction factors $k^{f_{\mathrm{clin}},f_i}_{Q_{\mathrm{clin}},Q_i}$ that are slightly closer to unity. Considering the uncertainties associated to our measurements, these differences do not seem to be significant, as all the measurements in clinical fields, with the exception of those performed in the lung treatment with PTW31014 in CyberKnife, yielded $k^{f_{\mathrm{clin}},f_{msr}}_{Q_{\mathrm{clin}},Q_{msr}}$ and $k^{f_{\mathrm{clin}},f_{pcsr}}_{Q_{\mathrm{clin}},Q_{pcsr}}$ correction factors that are compatible with each other within uncertainties. This agreement was also found between all the Monte Carlo calculated correction factors.

We cannot therefore see any strong indication showing the *pcsr* field as a more suitable intermediate calibration field for nonstandard field dosimetry than the *msr* field, both in TomoTherapy and CyberKnife. Taking into account that the requirement to have highly homogeneous PTV dose distributions on *pcsr* fields for the measurement of correction factors with low associated uncertainties is not always easily fulfilled, *msr* fields would seem to be a better intermediate calibration field candidate for the measurement of associated correction factors with low uncertainties.

The initial proposal of plan class specific intermediate calibration fields as composite field configurations lying closer to the clinical treatment conditions has not been demonstrated, at least for the cylindrical and spherical *pcsr* here studied. Measuring such simple composite field configurations could still result very useful for dosimetry quality assurance in certain techniques, as many treatment delivery features are included in *pcsr* fields but not in *msr* fields. However, the advantage obtained through their use for clinical dosimetry is not clear.

Further measurements of clinical fields and the study of their relationship with both *pcsr* and *msr* fields will of course help to strongly confirm that *msr* fields are an optimum path for the performance of clinical dosimetry in non standard fields. Reports will be published in the near future, hopefully by the beginning of 2014, by IAEA and AAPM that will compile all the results presented by the scientific community since 2008 on the application of the new dosimetry formalism to different radiotherapy techniques. The role that both *msr* and *pcsr* fields will finally play on the dosimetry of non standard beams will be then probably clarified.

Alternative strategies are also being studied and recommendations are being elaborated by other institutions like DIN, the German Institute for Standardization, which prefers the election of the most appropriate detectors, *i.e.* those that require the minimum correction, for each technique. This institution advocates for the use of an unshielded diode for the measurement of small fields. Diodes would be in this case cross-calibrated with an ionization chamber in a small reference field, large enough though to have associated k_Q factors not departing significantly from those published in conventional CoPs (4 cm×4 cm field for example). Measurements on smaller fields would be then performed with this diode once the change of response for smaller fields has been studied. For the measurement on clinical fields, DIN dispenses with the use of *pcsr* fields and recommends the use of exhaustive dosimetric verification through different methods including detector arrays, film dosimetry with an absolute dose measurement, etc.

On the other hand, the European Metrology Research Programme of EURAMET has some research lines under the project *Metrology for radiotherapy using complex radiation fields* exploring new quality indexes and calibration methods for Stereotactic Radiosurgery, covering static and dynamic fields and studying the option for a TPS beam model parameter. Other work packages include for example a proposal to verify TPS dose distributions in anthropomorphic phantoms following a methodology, similar to that proposed by González-Castaño [62] *et al.*, that includes the convolution of TPS dose distributions with the spatial response function of the detector employed in verification measurements.


USC
UNIVERSIDADE DE SANTIAGO DE COMPOSTELA

Appendix A

Resumen

El trabajo realizado en esta tesis abarca un conjunto de estudios relacionados con la dosimetría en radioterapia externa de fotones, presentando en primer lugar sus fundamentos, objetivos, procedimientos y las técnicas y maquinas empleadas en la radioterapia externa de fotones. En este contexto se analizarán diversos aspectos de la dosimetría en campos de radioterapia no estándar.

La magnitud empleada para cuantificar el efecto de la radiación ionizante en el tejido biológico es la dosis, definida como la energía depositada en el material por unidad de masa. La dosis depositada en agua se usa generalmente en radioterapia dado el buen conocimiento del transporte de radiación en este material, que permite obtener resultados con baja incertidumbre. Además, la dosis en agua está estrechamente relacionada con la dosis en tejido, dado que el cuerpo humano, formado en un 70% por agua y con una densidad media de 1 g cm^{-3}, muestra coefficientes másicos de absorción de la radiación muy similares a los del agua. Las bases de la dosimetría se presentan en el trabajo, resumiendo las carácterísticas ideales de un dosímetro y describiendo los mecanismos empleados por distintos detectores para la medida de dosis. Se pormenoriza también la dosimetría de haces de fotones en “condiciones de referencia”. Los procedimientos de este tipo de dosimetría son establecidps en protocolos internacionales como el TRS398 del Organismo Internacional de Energía atómica (OIEA), o el TG-51 de la Sociedad Americana de físicos médicos (AAPM). Este tipo de protocolos dictan recomendaciones estandarizadas para la medida de dosis en agua en los haces clínicos de radioterapia, contribuyendo a la aplicación de procedimientos dosimétros unificados en los hospitales y a una determinación de dosis en agua trazable a patrones (primarios o secundarios) de esta magnitud. La dosimetría de referencia en haces de radioterapia externa de fotones, provenientes de aceleradores lineales de electrones de megavoltage o unidades de colbaltoterapia, consiste en la determinacón de la dosis depositada en agua por un haz de radiación en un tanque de agua en condiciones de referencia, siendo éstas establecidas en los citados protocolos de dosimetría.

La dosis en condiciones de referencia debe ser conocida por el radiofísico hospitalario con una incertidumbre relativa que no supere el 1.5% para que éste pueda llevar a cabo las planificaciones de tratamientos cumpliendo las prescripciones del oncólogo y las recomendaciones de los organismos nacionales e internacionales competentes que establecen las normas reguladoras del control de calidad en radioterapia.

La dosimetría de referencia se realiza con cámaras de ionización de aire, donde la carga eléctrica generada en el volumen activo del detector por el campo de radiación es convertida en dosis depositada en agua a partir de un coeficiente de calibración y una serie de factores de corrección. Los coeficientes de calibración se determinan en laboratorios de calibración mediante la comparación de la carga registrada por la cámara con la dosis en agua, conocida mediante otro procedimiento de precisión, en igualdad de condiciones (las de referencia). Las condiciones de referencia permiten asegurar la reproducibilidad del procedimiento por parte de otro usuario o laboratorio de calibrabción, así como la fidelidad del valor obtenido con respecto al valor convencionalmente verdadero.

Los haces de radiación utilizados en los laboratorios de calibración para la determinación de los coeficientes de calibración son habitualmente haces de fotones de cobalto-60, dada la reproducibilidad del haz de un radioisótopo y la similitud entre la energía media del espectro de cobalto-60 y la energía media de los haces de fotones generados en los aceleradores lineales de electrones. Sin embargo, las diferencias espectrales entre el haz del laboratorio de calibración y los haces empleados en radioterapia, habitualmente haces de megavoltage, hacen necesaria la aplicación de un factor de corrección para la determinación de dosis en agua en los haces clínicos. Este factor, denominado factor de corrección por calidad de haz, depende no sólo del espectro del haz utilizado en la clínica, si no también de la cámara de ionización empleada para la medida (de la geometría y materiales de los que está compuesta). Los factores de corrección por calidad de haz aparecen tabulados en los protocolos de dosimetría para distintas cámaras de ionización y distintas calidades de haz. De este modo, la determinación de la dosis depositada en agua por un haz clínico se puede obtener como el producto de la carga registrada por la cámara en condiciones de referencia, el coeficiente de calibración y el factor de corrección por calidad de haz correspondiente al espectro de la máqina y a la cámara de ionización utilizada.

La evolución de la radioterapia externa de fotones ha dado lugar a técnicas que emplean campos de radiación de intensidad modulada, o campos más pequeños que el tamaño de campo utilizado en las condiciones de referencia de los protocolos de dosimetría convencionales anteriormente mencionados (de 10 cm x 10 cm). Estas técnicas permiten suministrar dosis más elevadas y confinadas al volumen del tumor que las técnicas de radioterapia conformada previamente existentes. Además, existe un conjunto de máquinas de radioterapia que utilizan este tipo de campos en la práctica clínica y que no pueden reproducir, por construcción, el campo de referencia establecido en los protocolos de dosimetría convencionales. La medida de dosis absoluta en los campos suministrados por este tipo de máquinas, denominados campos no estándar, está sujeta a mayores incertidumbres ya que no existe un procedimiento dosimétrico establecido para ser aplicado en estas condiciones de medida. Esto compromete la calidad de la planificación de los tratamientos de radioterapia al no conocerse con exactitud el error que se comete en la determinación de la dosis suministrada al paciente. Esta situación desencadenó la puesta en marcha de un Grupo de Trabajo de dosimetría en Campos de Radioterapia no Estándar, fruto de la colaboración de la OIEA y la AAPM, que publicó unas recomendaciones para el desarrollo de un nuevo protocolo de dosimetría: "A new formalism for reference dosimetry of small and non-standard fields" Medical Physics Volume 35, Issue 11, pp. 5179-5186 (November 2008). La realización de un nuevo protocolo exige la redefinición de condiciones de medida adecuadas para la dosimetría de referencia en las máquinas de radioterapia que lo requieran y la realización de medidas y simulaciones para el cálculo de los factores de corrección asociados a distintas cámaras de ionización en las calidades de haz habituales en dichas máquinas.

El cálculo de factores de corrección por calidad de haz en un campo de radiación implica la determinación de la desviación existente entre el valor absoluto de dosis depositada en agua por el campo de radiación y el valor de dosis depositada en agua obtenido a partir de la carga registrada en la cámara y el coeficiente de calibración en cobalto-60. En condiciones de no referencia, la falta de equilibrio transitorio de partículas cargadas y la importacia del promediado por efecto volumen en los dosímetros hacen que la medida de dosis absorbida en agua esté sometida a altas exigencias. El dosímetro empleado para esta medida debe ser de pequeño tamaño, presentar poca dependencia energética y ser equivalente a agua. La dosimetría de alanina es un patrón secundario de dosis en agua en radioterapia, empleado en laboratorios primarios como el National Physical Laboratory de

Inglaterra (NPL), el National Institute of Santards and Technology de Estados Unidos (NIST) o el Physikalisch-Technische Bundesanstalt de Alemania (PTB). Este sistema dosimétrico cumple los requerimientos anteriormente mencionados, siendo ampliamente utilizado para la medida de dosis en campos de radiación pequeños.

La dosimetría de referencia es tan sólo uno de los pilares del control de calidad en radioterapia. El control de calidad en radioterapia engloba una serie de procesos cuyo objetivo es asegurar el cumplimiento de la prescipción médica mediante la deposición de la dosis en el volumen objetivo dentro de una tolerancia, que habitualmente ronda el 5% de la dosis prescrita. Entre los objetivos centrales se encuentra además minimizar la dosis depositada en tejido sano y la exposición del personal sanitario, tratando de asegurar una adecuada monitorización del paciente que permita lograr y determinar el resultado del tratamiento. El control de calidad pretende la minimización general de las incertidumbres asociadas a todo el proceso radioterápico, intentando corregir y reducir la incidencia de errores. Para ello se establecen programas de control de calidad en los servicios de radioterapia de los hospitales a partir de las guías y recomendaciones publicadas por organismos como la Organización Mundial de la Salud, la Sociedad Europea de Radioterapia y Oncología o la Asociación Americana de Física Médica. Los programas de control de calidad de radioterapia definen las responsabilidades del personal y establecen protocolos documentados, el registro y control de fallos y procedimientos de auditoría interna y externa, promoviendo la educación y entrenamiento continuado.

Estos programas se dividen en pasos de control de calidad individuales, relacionados con cada uno de los pasos que forman parte del proceso radioterápico, donde se requieren determinados niveles de incertidumbre para lograr el cumplimiento de las tolerancias globales exigidas. En lo que concierne al físico médico, las actividades de control de calidad incluyen:

- La protección radiológica.
- El control de calidad del equipamiento tanto de diagnóstico como de tratamiento, donde se incluye la dosimetría de referencia.
- El control de calidad de la planificación de tratamientos.
- El control de calidad de la suministración del tratamiento.

Este último paso, generalmente denominado verificación del tratamiento, es un proceso de control de calidad final que trata de asegurar que las distribuciones de dosis suministradas coinciden con las planificadas. Además de todos los procedimientos realizados para comprobar los haces suministrados por la máquina y su consistencia con los simulados en el software de planificación de tratamientos, la verificación dosimétrica fue extensivamente incorporada a los programas de control de calidad debido a la complejidad de las técnicas de radioterapia modernas.

Los haces altamente conformados utilizados en las técnicas de radioterapia de intensidad modulada involucran campos pequeños de radiación y altos gradientes de dosis, con falta de equilibrio lateral de particulas cargadas e importantes efectos de promediado en volumen asociados a la medida de dosis con camára de ionización. Como los protocolos de dosimetría incluyen factores de corrección por calidad de haz asociados a campos de referencia estándar, la medida de dosis en las condiciones anteriormente descritas está sometida a incertidumbres relativas superiores, pudiendo alcanzar valores de hasta un 10%. Las técnicas modernas exigen además un control más estricto en la colocación del paciente y del posicionado colimadores multiláminas utilizados en las máquinas de radioterapia. Los algoritmos de cálculo de dosis utilizados en el software de planificación de tratamientos complejos deben presentar también una precisión mayor que la requerida por la radioterapia conformada tradicional. Esta situación aumenta la importancia y necesidad de una verificación dosimétrica previa a la suminstración del tratamiento al paciente, donde se evalúan los efectos de la propagación de incertidumbres asociadas a todos los pasos del proceso en la distribución de dosis finalmente suminsitrada.

Entre los distintos sistemas de dosimetría empleados para la verificación de tratamientos, las matrices de detectores son dispositivos que permiten una verificación exhaustiva y agilizan el proceso, un factor clave dada la alta demanda asistencial de los servicios de radioterapia. Estos dispositivos, de lectura directa, son fáciles de usar y posibilitan la rápida comparación de las distribuciones de dosis medidas con las calculadas por el planificador.

Distintas matrices de detectores comerciales aparecieron a lo largo de la última década respondiendo a la demanda clínica, estando formadas por un número determinado de detectores embebidos en posiciones fijas en un material equivalente a agua. Los mecanismos de detección más extendidos en las matrices de verificación son la cámara de ionización y el diodo, dada su robustez, facilidad de calibración y la baja incertidumbre asociada a sus medidas.

El trabajo presentado en esta memoria se divide en cuatro capítulos, cuyo contenido se resume a continuación.

- En el **capítulo uno** se realiza una introducción a la radioterapia externa de fotones, presentando sus fundamentos, objetivos y las máquinas y técnicas de radioterapia empleadas. Las bases de la dosimetría son descritas, incluyendo los procedimientos de la dosimetría de referencia en haces de radioterapia externa de fotones, y presentando la propuesta de un nuevo protocolo para haces de radioterapia no estándar. Se pone además en contexto el control de calidad en la suministración de tratamientos, describiendo los sistemas de dosimetría empleados en dicha tarea.

- En el **capítulo dos** se realiza un estudio sobre el uso de matrices de detección para la verificación dosimétrica de tratamientos de radioterapia. Tres soluciones comerciales, PTW729 (PTW-Freiburg, Alemania), MatriXX (IBA

Dosimetry, Louvain-La-Neuve, Bélgica) y MapCHECK2 (Sun Nuclear Corporation, Melbourne FL) son analizadas bajo una metodología común que permitirá la comparación de sus características y la obtención de conclusiones sobre el diseño óptimo de este tipo de detectores.

La respuesta espacial, F_ψ, de los detectores empleados en las distintas matrices, cámaras de ionización en los dos primeros casos y diodo en el caso de la última matriz, es definida como la respuesta registrada por el detector, estando éste situado a cierta profundidad z en un material equivalente a agua, ante la incidencia de un haz de fluencia infinitesimal. La función de respuesta F_ψ asociada a los tres detectores estudiados fue medida a cierta profundidad, z, mediante la irradiación del detector con un haz de pincel con un espectro de haz de megavoltaje de 6 MV y fue simulada mediante el método Monte Carlo. Para analizar el efecto de esta función de respuesta en la medida de distribuciones de dosis hemos de tener en cuenta que la deposición de dosis producida a cierta profundidad en un material ante la incidencia de una fluencia de radiación se puede calcular a partir de la convolución de esta fluencia con el kernel de deposición de dosis en el material. Este kernel describe la deposición de dosis a cierta profundidad, considerando las contribuciones de radiación dispersa, el transporte primario y secundario de electrones en el material y el ensanchamiento del haz a medida que éste penetra en el material. Cuando un detector es empleado para medir una distribución de dosis, la señal registrada por éste se puede obtener como la convolución de la distribución de dosis a cierta profundidad con una respuesta del detector, $F_D(x, y)$, que puede ser a su vez calculada a partir de la deconvolución de la función F_ψ del detector con el kernel de deposición de dosis correspondiente al haz de radiación empleado para la medida de F_ψ a profundidad z. Esta metodología, verificada en el trabajo, permitió modelizar la respuesta de los detectores ante la incidencia de fluencias arbitrarias, cuantificar las desviaciones existentes entre la distribución de dosis real y la medida por el detector y comparar los efectos introducidos por los distintos detectores estudiados en la medida de distribuciones de dosis representativas de tratamientos de radioterapia de intensidad modulada. Se observó una mayor fidelidad en la medida de dosis con diodo, aunque los efectos introducidos por las cámaras de ionización resultaron no ser significativos teniendo en cuenta los criterios de aceptación habituales de los programas de verificación de radioterapia, donde un 5% de puntos en la distribución mostrando desviaciones mayores que un 1.5% o 3% (dependiendo del servicio) con la distrución de referencia se suele considerar aceptable.

El trabajo realizado analizó también la capacidad de las distintas matrices para la detección de variaciones de fluencia, objetivo central de la verificación de tratamientos de radioterapia. En este estudio se observa que las matrices que utilizan cámaras de ionización, con respuestas espaciales, F_ψ, de 0.6 a 0.7 cm de anchura a mitad de altura y espaciado entre detectores de 0.8 a 1 cm, presentan una mayor capacidad para la detección de variaciones de fluencia que las matrices de diodos, cuya función F_ψ presenta una anchura a mitad de altura de 0.083 cm, siendo el espaciado entre detectores es de 0.7 cm. Esto es debido a la mayor área sensible efectiva presente en las matrices de detección que involucran detectores de mayor tamaño, lo que permite suponer un diseño optimizado para las matrices con tamaños de detetores de un área $\backsim$ 0.25 cm^2 y distancia entre detectores que dé lugar a un área sensible por encima de un 50% del área total de la matriz.

- En el **tercer capítulo** se presenta la puesta en marcha de un sistema de dosimetría con alanina en el rango de dosis de la radioterapia (1 a 20 Gy), pionero en España, involucrando la Resonancia Paramagnética Electrónica del servicio de Resonancia Magnética de la Red de Infraestructuras de Apoyo a la Investigación y al Desarrollo Tecnológico de la Universidad de Santiago de Compostela y trazado al patrón secundario de dosis absorbida en agua del Laboratorio de Radiofísca de la misma institución.

La alanina es uno de los aminoácidos más simples presentes en la naturaleza, con estructura molecular $CH_3CH(NH_2)COOH$. La incidencia de radiación ionizante produce la formación de radicales en este material, en una concentración proporcional a la energía depositada en un amplio rango de dosis (de 0.5 Gy a 5 kGy). La presencia de radicales en la alanina puede ser medida con resonancia paramagnética electrónica (RPE). La cantidad de radicales presentes en un dosímetro de alanina por unidad de masa se cuantifica a partir de su intensidad de señal en RPE, relacionando ésta con la dosis absorbida en agua, lo que permite la calibración de este sistema de dosimetría.

El capítulo presenta una introducción a los fundamentos teóricos de detección en Resonancia Paramagnética Electrónica (RPE), así como un estudio sobre el funcionamiento de este tipo de espectrómetros. La sensibilidad y estabilidad requeridas en el espectrómetro para obtener uncertidumbres por debajo de un 1% en la cuantificación de la señal de RPE de dosímetros de alanina irradiados en el rango de dosis de radioterapia son superiores a los necesarios en otras aplicaciones de RPE. Los parámetros óptimos de operación del espectrómetro pueden de este modo diferir de los empleados en otras aplicaciones donde se estudia la forma de los espectros en vez de quantificar su intensidad de señal.

Con el fin de mejorar la calidad de la cuantificación de señal RPE de los dosímetros de alanina se llevaron a cabo varias pruebas, lo que permitió optimizar la estabilidad y la sensibilidad del espectrómetro en la aplicación que nos ocupa. Además, se desarrolló e instaló en la unidad un sistema de posicionamiento específico para asegurar la optimización de la sensibilidad y un posicionamiento reproducible de los dosímetros de alanina en la cavidad de la RPE. La optimización de los parámetros de operación del espectrómetro y el estudio de la anisotropía en la señal RPE de la alanina permitió la definición de un protocolo de medida.

Una primera calibración de intensidad de señal de RPE de dosímetros de alanina en términos de dosis absorbida en agua se realizó mediante la irradiación de un lote de dosímetros en seis niveles de dosis en agua en la unidad^{60} Co en el Laboratorio de Radiofísica de la Universidad de Santiago de Compostela. Se investigaropm dos métodos de cuantificación de señal de RPE, y se realizó la substracción de la señal de fondo presente en dosímetros de alanina no irradiados para garantizar la calidad de la calibración. La estimación de las incertidumbres asociadas a todo el procedimiento permitió determinar la incertidumbre relativa asociada a la calibración, situándose ésta entre un 2.8% y un 1.2% (k=2) para dosímetros irradiados a una dosis en agua entre 10 y 50 Gy.

Varias mejoras fueron introducidas en el sistema tras esta calibración, incluyendo la instalación de un dispositivo de control de la temperatura en el sistema de refrigeración por agua del espectrómetro para mejorar la estabilidad. También se llevó a cabo una determinación más precisa de la dosis en agua correspondiente a la irradiación de los dosímetros.

Tras estas mejoras se construyó una nueva curva de calibración de dosis en agua frente a señal de RPE de dosímetros de alanina. En este caso se incluyeron dos pruebas ciegas en la irradiación de los dosímetros para comprobar la consistencia del sistema de dosimetría. La incertidumbre relativa asociada a esta calibración arrojó valores estimados entre un 1.7% y un 0.8% (k=2) para dosímetros irradiados entre 10 Gy y 50 Gy. Resultados satisfatorios fueron obtenidos en las pruebas ciegas, ya que se encontrÃş acuerdo entre los valores de dosis determinados con el sistema y los valores dosis en agua correspondientes a la irradiación de los pellets, con incertidumbres relativas de un 1.4% a 13.34 Gy y 1.3% a 15.19 Gy (k=2).

Posibles mejoras en el sistema de medida incluirían el diseño de un sistema de posicionado más adecuado para la irradiación o el refinamiento de la metodología empledada para la sustracción de fondo de la señal de ESR de los dosímetros, tareas que podrían ser abordadas en futuras calibraciones. La implantación de un servicio de dosimetría con alanina en la Universidad de Santiago de Compostela, requeriría establecer la variabilidad de las incertidumbres asociadas al sistema mediante la repetición continuada de la construcción de la curva de calibración.

- En el **cuarto capítulo** se estudia la aplicación de la propuesta del nuevo protocolo de dosimetría para campos de radiación no estándar a dos máquinas modernas de radioterapia, TomoTherapy y CyberKnife, ambas fabricadas por Accuray Inc., Sunnyvale, CA, Estados Unidos.

El objetivo de este trabajo consiste en la determinación de los factores de corrección asociados a distintas cámaras de ionización para la determinación de dosis absorbida en agua en unos campos de calibración intermedios, definidos en las máquinas con el propósito de establecer para ellas un nuevo protocolo de dosimetría. Dos tipos de campos de calibración intermedios son propuestos para cada una de las máquinas, siendo el primero de éstos un campo estático, específico para cada máquina y lo más cercano posible al campo de referencia definido en los protocolos de dosimetría convencionales. El segundo campo de calibración intermedio es un campo compuesto, denominado campo de plan de clase, que deposita una distribución de dosis homogénea con una forma sencilla (geometría cilíndrica en el caso de TomoTherapy y esférica en el caso de CyberKnife) en un maniquí equivalente a agua de geometría adecuada (cilíndrica y esférica para TomoTherapy y CyberKnife respectivamente). El campo de calibración compuesto se introdujo en la propuesta del protocolo con el objetivo de determinar la dosis absorbida en agua en condiciones más próximas a las de los tratamientos, ya que dada la complejidad de las técnicas de radioterapia asociadas a estas máquinas, éstas podrían diferir substancialmente de las correspondientes a los campos de calibración intermedios estáticos.

Los factores de corrección asociados a la medida de dosis en agua con cámara de ionización en los campos de calibración intermedios se determinó a partir de la relación entre la dosis absoluta absorbida en agua, obtenida mediante dosimetría de alanina, y el producto de la lectura corregida de la cámara y el coeficiente de calibración de la misma en cobalto-60. Los factores de corrección fueron también calculados mediante simulación Monte Carlo para el caso de CyberKnife. La dosimetría de alania se realizó en colaboración con el NPL de Inglaterra, ya que el sistema de dosimetría estudiado en el capítulo tres fue desarrollado de modo simultáneo a la realización de este trabajo.

Distintos tratamientos clínicos reales fueron investigados, determinando los factores de corrección asociados a la medida de las cámaras de ionización para la determinación de dosis absoluta en agua en un punto de una región de dosis homogénea del volumen planificado en cada uno de tratamientos. La relación entre los factores de corrección obtenidos en los tratamientos clínicos y en los campos intermedios de calibración permitió evaluar, aunque con estadística limitada, la idoneidad de los distintos campos de calibración para la práctica clínica.

En el estudio de TomoTherapy, los factores globales, $k^{f_i,f_{ref}}_{Q_i,Q_0}$, asociados a la cámara de ionización estudiada (Exradin A1SL de Standard Imaging) arrojaron valores por debajo de la unidad en todos los campos investigados, con desviaciónes entre un 1.6% y un 2.1%. Las incertidumbres relativas asociadas a estas medidas se situan sin embargo entorno al 2% (k=2), lo que hace que los valores sean compatibles entre sí y compatibles con la unidad, aunque la desviación sistemática resulta significativa en un test de hipótesis involucrando la t de student.

En el caso de CyberKnife no se encontraron desviaciones sistemáticas en los factores de corrección globales asociados a las cámaras estudiadas (CC13 de Scanditronix-Wellhofer y PTW31014 de PTW-Freiburg), que arrojaron valores por encima y por debajo de la unidad dependiendo del campo. Los factores de corrección para la cámara CC13 tomaron valores desviándose de la unidad entre un 0.6% y un 1.6% en las medidas experimentales, mientras que en la simulación Monte Carlo estas desviaciones variaron entre un 0.6% y un 1%. En el caso de la PTW31014, las desciaciones de la unidad medidas estuvieron entre un 0.8% y un 2.3%, y entre un 0.7% y un 2.5% según las simulaciones Monte Carlo.

La mayor desviación con respecto a la unidad observada en las medidas de la cámara PTW31014 son debidas a la mayor diferencia en el promediado por efecto volumen entre este detector y la alanina. Los factores obtenidos para los distintos campos son compatibles entre sí (excepto uno asociado a la medida de PTW31014 en un tratamiento clínico) dadas las incertidumbres relativas de las medidas, que rondan el 2% para la CC13 y el 2.4% para la PTW31014 (k=2), siendo ésta última ligeramente superior debido a la mayor intestabilidad de este detector. Los resultados obtenidos mediante cálculo Monte Carlo mostraron acuerdo dentro de incertidumbres con las medidas, siendo también equivalentes entre sí los factores asociados a distintos campos estudiados.

A raíz de estos resultados no se encuentra evidencia para afirmar que los campos intermedios de calibración compuestos (planes de clase) suponen una calibración intermedia más adecuada que los campos de intermedios de calibración estáticos para la dosimetría de campos no estándar estudiados, tanto en TomoTherapy como en CyberKnife.

Por otro lado, una alta uniformidad en las distribuciones de dosis de los planes de clase es requerida para la medida de factores de corrección con incertidumbres asociadas bajas, pero se ha visto que esto resulta, dependiendo de la técnica, difícil de cumplir. Este factor apoya la reivindicación de los campos intermedios de calibración estáticos como mejores candidatos para la calibiración en el marco del nuevo protocolo, ya que éstos permiten la medida de factores de corrección con incertidumbres asociadas más bajas.

La consideración inicial de campos de intermedios calibración compuestos como configuraciones más cercanas a las condiciones de tratamiento clínico no ha podido ser verificada, al menos para las propuestas de distribuciones de dosis cilíndricas y esféricas aquí estudiadas. La medida de las configuraciones de campo compuesto simple propuestas en los planes de clase podría resultar útil para el control de calidad de dosimetría en ciertas técnicas, al incluir éstos muchas características del suministro de tratamiento propio de cada técnica. Sin embargo, las ventajas obtenidas a meidante su uso como campos de calibración intermedios para la dosimetría clínica no ha sido demostrada.


USC
UNIVERSIDADE
DE SANTIAGO
DE COMPOSTELA

Bibliography

[1] J. Ferlay, E. Steliarova-Foucher, J. Lortet-Tieulent, S. Rosso, J.W.W. Coebergh, H. Comber, D. Forman, and F. Bray. Cancer incidence and mortality patterns in europe: Estimates for 40 countries in 2012. *European Journal of Cancer*, 49(6):1374–1403, April 2013. doi: 10.1016/j.ejca.2012.12.027.

[2] G. Delaney, S. Jacob, C. Featherstone, and M. Barton. The role of radiotherapy in cancer treatment: estimating optimal utilization from a review of evidence-based clinical guidelines. *Cancer*, 104(6): 1129–1137, September 2005. doi: 10.1002/cncr.21324.

[3] P. Mayles, A. E Nahum, and J. C. Rosenwald. *Handbook of radiotherapy physics: theory and practice*. Taylor & Francis, New York, 2007. ISBN 9780750308601 0750308605.

[4] *Radiation oncology: a physicist's-eye view*. New York, NY. ISBN 9780387726458 0387726454.

[5] *ICRU Report 50. Prescribing, Recording and Reporting Photon Beam Therapy*. International Commission on Radiation Units and Measurements. Bethesda, MD : ICRU, 1993. - 72 p.

[6] S. Webb. *The Physics of Conformal Radiotherapy: Advances in Technology (PBK)*. CRC Press, December 2010. ISBN 9781420050806.

[7] E. D. Podgorsak. *Radiation oncology physics: a handbook for teachers and students.* International Atomic Energy Agency, Vienna, 2005. ISBN 9201073046 9789201073044.

[8] S. Webb. The physical basis of IMRT and inverse planning. *British Journal of Radiology*, 76(910):678–689, 2003. doi: 10.1259/bjr/65676879.

[9] Ce. X. Yu and G. Tang. Intensity-modulated arc therapy: principles, technologies and clinical implementation. *Physics in Medicine and Biology*, 56(5):R31, 2011. doi: 10.1088/0031-9155/56/5/R01.

[10] T. R. Mackie. History of tomotherapy. *Physics in Medicine and Biology*, 51(13):R427–53, 2006. doi: 10.1088/0031-9155/51/13/R24.

[11] J. A. Bonnell. ICRU report 19. Radiation Quantities and Units. *British Journal of Industrial Medicine*, 29(4):464, October 1972. ISSN 0007-1072.

[12] A M Kellerer and D Chmelevsky. Concepts of microdosimetry. i. quantities. *Radiation and environmental biophysics*, 12(1):61–69, June 1975. ISSN 0301-634X.

[13] C. K. Ross and N. V. Klassen. Water calorimetry for radiation dosimetry. *Physics in Medicine and Biology*, 41(1):1, January 1996. doi: 10.1088/0031-9155/41/1/002.

[14] G. Shani. *Radiation Dosimetry: Instrumentation and Methods.* CRC Press, January 2001. ISBN 9780849315053.

[15] F. H. Attix. *Introduction to Radiological Physics and Radiation Dosimetry.* John Wiley & Sons, 1986. ISBN 9780471011460.

[16] *Absorbed dose determination in photon and electron beams : an international code of practice.* International Atomic Energy Agency, Vienna, 1997. ISBN 9201005970 9789201005977.

[17] Task Group 21, Radiation Therapy Committee, and AAPM. A protocol for the determination of absorbed dose from high-energy photon and electron beams. *Medical Physics*, 10(6):741–771, 1983. doi: 10.1118/1.595446.

[18] *Absorbed dose determination in external beam radiotherapy: an international code of practice for dosimetry based on standards of absorbed dose to water.* Number no. 398 in Technical reports series. International Atomic Energy Agency, Vienna, 2001. ISBN 920102200X.

[19] P. R. Almond, P. J. Biggs, B. M. Coursey, W. F. Hanson, M. S. Huq, R. Nath, and D. W. O. Rogers. AAPM's TG-51 protocol for clinical reference dosimetry of high-energy photon and electron beams. *Medical Physics*, 26(9):1847–1870, 1999. doi: 10.1118/1.598691.

[20] M Barboza-Flores, R Meléndrez, V Chernov, B Castañeda, M Pedroza-Montero, B Gan, J Ahn, Q Zhang, and S F Yoon. Thermoluminescence in CVD diamond films: application to actinometric dosimetry. *Radiation protection dosimetry*, 100(1-4):443–446, 2002. ISSN 0144-8420.

[21] S. Almaviva, M. Marinelli, E. Milani, G. Prestopino, A. Tucciarone, C. Verona, G. Verona-Rinati, M. Angelone, M. Pillon, I. Dolbnya, K. Sawhney, and N. Tartoni. Chemical vapor deposition diamond based multilayered radiation detector: Physical analysis of detection properties. *Journal of Applied Physics*, 107(1):014511–014511–7, January 2010. ISSN 00218979. doi: doi:10.1063/1.3275501.

[22] J. Andersson, F. J. Kaiser, F. Gómez, O. Jäkel, J. Pardo-Montero, and H. Tölli. A comparison of different experimental methods for general recombination correction for liquid ionization chambers. *Physics in Medicine and Biology*, 57(21):7161–7175, November 2012. ISSN 0031-9155, 1361-6560. doi: 10.1088/0031-9155/57/21/7161.

[23] B. Mijnheer and European Society for Therapeutic Radiology and Oncology. *Monitor unit calculation for high energy photon beams: practical examples.* ESTRO, Brussels, 2001.

[24] B. R. Muir, M. R. McEwen, and D. W. O. Rogers. Measured and Monte Carlo calculated k_Q factors: Accuracy and comparison. *Medical Physics*, 38(8):4600–4609, 2011. doi: 10.1118/1.3600697.

[25] M S. Huq, P. Andreo, and H. Song. Comparison of the IAEA TRS-398 and AAPM TG-51 absorbed dose to water protocols in the dosimetry of high-energy photon and electron beams. *Physics in Medicine and Biology*, 46(11):2985–3006, 2001. doi: 10.1088/0031-9155/46/11/315.

[26] F. Sánchez-Doblado, G. H Hartmann, J. Pena, R. Capote, M. Paiusco, B. Rhein, A. Leal, and J. I. Lagares. Uncertainty estimation in intensity-modulated radiotherapy absolute dosimetry verification. *International Journal of Radiation Oncology, Biology, Physics*, 68(1):301–310, 2007. doi: 10.1016/j.ijrobp.2006.11.056.

[27] D. González-Castaño, J. Pena, F. Sánchez-Doblado, G. H. Hartmann, F. Gómez, and A. Leal. The change of response of ionization chambers in the penumbra and transmission regions: impact for IMRT verification. *Medical & Biological Engineering & Computing*, 46(4): 373–380, 2008. doi: 10.1007/s11517-007-0249-z.

[28] P. Francescon, S. Cora, and C. Cavedon. Total scatter factors of small beams: A multidetector and monte carlo study. *Medical Physics*, 35 (2):504–513, 2008. doi: 10.1118/1.2828195.

[29] H. Bouchard, J. Seuntjens, and H. Palmans. On charged particle equilibrium violation in external photon fields. *Medical Physics*, 39 (3):1473, 2012. doi: 10.1118/1.3684952.

[30] R. Alfonso, P. Andreo, R. Capote, M. Saiful Huq, W. Kilby, P. Kjäll, T. R. Mackie, H. Palmans, K. Rosser, J. Seuntjens, W. Ullrich, and

S. Vatnitsky. A new formalism for reference dosimetry of small and nonstandard fields. *Medical Physics*, 35(11):5179–5186, 2008.

[31] H. Palmans. Small and composite field dosimetry: the problems and recent progress. *Proceedings IAEA International Symposium on Standards, Applications and Quality Assurance in Medical Radiation Dosimetry*, 2010, Vienna, Austria.

[32] A new protocol for the dosimetry of non standard beams. *World Congress On Medical Physics and Biomedical Engineering*, 103, 2012, Beijing.

[33] F. C. Abrego, C. S. G. Calcina, A. de Almeida, C. E. de Almeida, and O. Baffa. Relative output factor and beam profile measurements of small radiation fields with an l-alanine/K-Band EPR minidosimeter. *Medical Physics*, 34(5):1573–1582, 2007. doi: 10.1118/1.2717414.

[34] M. Anton, A. Krauss, R. P. Kapsch, and T Hackel. Response of alanine dosimeters in small photon fields. *Book of extended abstracts, IDOS conference (IAEA Vienna)*, page 267, 2010.

[35] B. Schaeken *et al.* BELdART: Implementation of a quality assurance audit for photon and electron beams based on alanine emr dosimetry. *Proceedings of IAEA International Symposium on Standards, Applications and Quality Assurance in Medical Radiation Dosimetry (IDOS) (Vienna)*, page 267, 2010.

[36] World Health Organization. *Quality assurance in radiotherapy.* WHO Publications Center USA, Geneva: Albany, NY, 1988. ISBN 9241542241. Bibliography: p. [51]-52.

[37] *Estro Booklet 4, Practical Guidelines for the Implementation of a Quality System in Radiotherapy.* European Society for Therapeutic Radiology and Oncology.

[38] G. J. Kutcher, L. Coia, M. Gillin, W. F. Hanson, S. Leibel, R. J. Morton, J. R. Palta, J. A. Purdy, L. E. Reinstein, G. K. Svensson, M. Weller, and L. Wingfield. Comprehensive QA for radiation oncology: Report of AAPM radiation therapy committee task group 40. *Medical Physics*, 21(4):581–618, 1994. doi: 10.1118/1.597316.

[39] W. L. Mclaughlin and M. F. Desrosiers. *Physics aspects of quality control in radiotherapy.* The Institute of Physics and Engineering in Medicine.

[40] L. R. Aarup, A. E. Nahum, C. Zacharatou, T. Juhler-NÃÿttrup, T. Knöös, H. Nyström, L. Specht, E. Wieslander, and S. S Korreman. The effect of different lung densities on the accuracy of various radiotherapy dose calculation methods: implications for tumour coverage. *Radiotherapy and oncology: journal of the European Society for Therapeutic Radiology and Oncology*, 91(3):405–414, June 2009. ISSN 1879-0887. doi: 10.1016/j.radonc.2009.01.008.

[41] P. Carrasco, N. Jornet, M. A. Duch, L. Weber, M. Ginjaume, T. Eudaldo, D. Jurado, A. Ruiz, and M. Ribas. Comparison of dose calculation algorithms in phantoms with lung equivalent heterogeneities under conditions of lateral electronic disequilibrium. *Medical Physics*, 31(10):2899–2911, 2004. doi: 10.1118/1.1788932.

[42] R. Capote, F. Sanchez-Doblado, A. Leal, J. I. Lagares, R. Arrans, and G. H. Hartmann. An EGSnrc monte carlo study of the microionization chamber for reference dosimetry of narrow irregular IMRT beamlets. *Medical Physics*, 31(9):2416–2422, 2004. doi: 10.1118/1.1767691.

[43] *Estro Booklet 9, Guidelines for the verification of IMRT.* European Society for Therapeutic Radiology and Oncology., 2008-First Edition. ISBN 90-804532-9. Brussels (Belgium).

[44] S. Pai, I. J. Das, J. F. Dempsey, K. L. Lam, T. J. LoSasso, A. J. Olch, J. R. Palta, L. E. Reinstein, D. Ritt, and E. E. Wilcox. TG-69:

radiographic film for megavoltage beam dosimetry. *Medical Physics*, 34(6):2228–2258, 2007. doi: 10.1118/1.2736779.

[45] S. Devic. Radiochromic film dosimetry: Past, present, and future. *Physica Medica*, 27(3):122–134, July 2011. ISSN 1120-1797. doi: 10.1016/j.ejmp.2010.10.001.

[46] M. Donetti, E. Garelli, F. Marchetto, A. Boriano, F. Bourhaleb, R. Cirio, I. Cornelius, S. Giordanengo, A. La Rosa, U. Nastasi, and C. Peroni. A method for the inter-calibration of a matrix of sensors. *Physics in Medicine and Biology*, 51(3):485, 2006. doi: 10.1088/0031-9155/51/3/002.

[47] S. Amerio, A. Boriano, F. Bourhaleb, R. Cirio, M. Donetti, A. Fidanzio, E. Garelli, S. Giordanengo, E. Madon, F. Marchetto, U. Nastasi, C. Peroni, A. Piermattei, C. J. Sanz Freire, A. Sardo, and E. Trevisiol. Dosimetric characterization of a large area pixel-segmented ionization chamber. *Medical Physics*, 31(2):414–420, 2004. doi: 10.1118/1.1639992.

[48] M. Stasi, S. Giordanengo, R. Cirio, A. Boriano, F. Bourhaleb, I. Cornelius, M. Donetti, E. Garelli, I. Gomola, F. Marchetto, M. Porzio, C. J. Sanz Freire, A. Sardo, and C. Peroni. D-IMRT verification with a 2D pixel ionization chamber: dosimetric and clinical results in head and neck cancer. *Physics in Medicine and Biology*, 50(19):4681, 2005. doi: 10.1088/0031-9155/50/19/017.

[49] E. Spezi, A. L. Angelini, F. Romani, and A. Ferri. Characterization of a 2D ion chamber array for the verification of radiotherapy treatments. *Physics in Medicine and Biology*, 50(14):3361, 2005. doi: 10.1088/0031-9155/50/14/012.

[50] B. Poppe, A. Blechschmidt, A. Djouguela, R. Kollhoff, A. Rubach, K. C. Willborn, and D. Harder. Two-dimensional ionization chamber

arrays for IMRT plan verification. *Medical Physics*, 33(4):1005–1015, 2006. doi: 10.1118/1.2179167.

[51] B. Poppe, A. Djouguela, A. Blechschmidt, K. Willborn, A. RÃijhmann, and D. Harder. Spatial resolution of 2D ionization chamber arrays for IMRT dose verification: single-detector size and sampling step width. *Physics in Medicine and Biology*, 52(10):2921, 2007. doi: 10.1088/0031-9155/52/10/019.

[52] P. A. Jursinic and B. E. Nelms. A 2-d diode array and analysis software for verification of intensity modulated radiation therapy delivery. *Medical Physics*, 30(5):870–879, 2003. doi: 10.1118/1.1567831.

[53] F. Banci Buonamici, A. Compagnucci, L. Marrazzo, S. Russo, and M. Bucciolini. An intercomparison between film dosimetry and diode matrix for IMRT quality assurance. *Medical Physics*, 34(4):1372–1379, 2007. doi: 10.1118/1.2713426.

[54] K. Eklund and A. Ahnesjö. Modeling silicon diode dose response factors for small photon fields. *Physics in Medicine and Biology*, 55 (24):7411, 2010. doi: 10.1088/0031-9155/55/24/002.

[55] J. F. Dempsey, H. E. Romeijn, J. G. Li, D. A. Low, and J. R. Palta. A fourier analysis of the dose grid resolution required for accurate IMRT fluence map optimization. *Medical Physics*, 32(2):380–388, 2005. doi: 10.1118/1.1843354.

[56] A. Gago-Arias, L. Brualla-González, D. M. González-Castaño, F. Gómez, M. Sánchez García, V. Luna Vega, J. Mosquera Sueiro, and J. Pardo-Montero. Evaluation of chamber response function influence on IMRT verification using 2D commercial detector arrays. *Physics in Medicine and Biology*, 57(7):2005, April 2012. doi: 10.1088/0031-9155/57/7/2005.

[57] A. Djouguela, D. Harder, R. Kollhoff, S. Foschepoth, W. Kunth, A. Rühmann, K. Willborn, and B. Poppe. Fourier deconvolution reveals the role of the lorentz function as the convolution kernel of narrow photon beams. *Physics in Medicine and Biology*, 54(9):2807, 2009. doi: 10.1088/0031-9155/54/9/015.

[58] C. Ma and A. E. Nahum. Bragg-gray theory and ion chamber dosimetry for photon beams. *Physics in Medicine and Biology*, 36(4):413, 1991. doi: 10.1088/0031-9155/36/4/001.

[59] I. Kawrakow, E. Mainegra-Hing, F. Tessier, D. W. O. Rogers, and B. R. B. Walters. The EGSnrc code system: Monte carlo simulation of electron and photon transport. *Technical Report No. PIRS-701 (National Research Council of Canada, Ottawa, Canada, 2011).*, .

[60] I. Kawrakow, E. Mainegra-Hing, F. Tessier, and B. Walters. EGSnrc c++ class library. *Technical Report No. PIRS-898 (National Research Council of Canada, Ottawa, Canada, 2005)*, .

[61] D. W. O. Rogers, B. R. B. Walters, and I Kawrakow. BEAMnrc users manual. *NRCC Report No. PIRS 509(A) revL (National Research Council of Canada, Ottawa, Canada, 2011).*

[62] D. M. González-Castaño, L. González Brualla, M. A. Gago-Arias, J. Pardo-Montero, F. Gomez, V. Luna-Vega, M. Sanchez, and R. Lobato. A convolution model for obtaining the response of an ionization chamber in static non standard fields. *Medical Physics*, 39(1):482–491, 2012. doi: 10.1118/1.3666777.

[63] D. A. Low, W. B. Harms, S. Mutic, and J. A. Purdy. A technique for the quantitative evaluation of dose distributions. *Medical Physics*, 25 (5):656–661, 1998. doi: 10.1118/1.598248.

[64] B. E. Nelms and J. A. Simon. A survey on IMRT QA analysis. *Journal of Applied Clinical Medical Physics*, 8(3), 2007. doi: 10.1120/jacmp.v8i3.2448.

[65] B. E. Nelms, H. Zhen, and W. A. Tome. Per-beam, planar IMRT QA passing rates do not predict clinically relevant patient dose errors. *Medical Physics*, 38(2):1037–1044, 2011. doi: 10.1118/1.3544657.

[66] C. Martens, C. De Wagter, and W. De Neve. The value of the LA48 linear ion chamber array for characterization of intensity-modulated beams. *Physics in Medicine and Biology*, 46(4):1131, 2001. doi: 10.1088/0031-9155/46/4/316.

[67] J. Pardo, J. V. Roselló, F. Sánchez-Doblado, and F. Gómez. Verification of intensity modulated profiles using a pixel segmented liquid-filled linear array. *Physics in Medicine and Biology*, 51(11):N211, 2006. doi: 10.1088/0031-9155/51/11/N01.

[68] J. Pardo, L. Franco, F. GÃşmez, A. Iglesias, A. Pazos, J. Pena, R. Lobato, J. Mosquera, M. Pombar, and J. SendÃşn. Development and operation of a pixel segmented liquid-filled linear array for radiotherapy quality assurance. *Physics in Medicine and Biology*, 50(8):1703, 2005. doi: 10.1088/0031-9155/50/8/006.

[69] L. Brualla-González, F. Gómez, A. Vicedo, D. M. González-Castaño, M. A. Gago-Arias, A. Pazos, M. Zapata, J. V. Roselló, and J. Pardo-Montero. A two-dimensional liquid-filled ionization chamber array prototype for small-field verification: characterization and first clinical tests. *Physics in Medicine and Biology*, 57(16):5221, 2012. doi: 10.1088/0031-9155/57/16/5221.

[70] C. K. McGarry, B. F. O'Connell, M. W. D. Grattan, C. E. Agnew, D. M. Irvine, and A. R. Hounsell. Octavius 4D characterization for flattened and flattening filter free rotational deliveries. *Medical Physics*, 40(9):091707, 2013. doi: 10.1118/1.4817482.

[71] S. Stathakis, P. Myers, C. Esquivel, P. Mavroidis, and N. Papanikolaou. Characterization of a novel 2D array dosimeter for patient-specific quality assurance with volumetric arc therapy. *Medical physics*, 40(7):071731, 2013. doi: 10.1118/1.4812415.

[72] B. Poppe, T. S. Stelljes, H. K. Looe, N. Chofor, D. Harder, and K. Willborn. Performance parameters of a liquid filled ionization chamber array. *Medical Physics*, 40(8):082106, 2013. doi: 10.1118/1.4816298.

[73] M. Z. Heydari, E. Malinen, E. O. Hole, and E. Sagstuen. Alanine radicals. 2. the composite polycrystalline alanine EPR spectrum studied by ENDOR, thermal annealing, and spectrum simulationsâĂă. *The Journal of Physical Chemistry A*, 106(38):8971–8977, 2002. doi: 10.1021/jp026023c.

[74] E. Malinen, M. Z Heydari, E. Sagstuen, and E. O Hole. Alanine radicals, part 3: properties of the components contributing to the EPR spectrum of x-irradiated alanine dosimeters. *Radiation Research*, 159 (1):23–32, 2003. ISSN 0033-7587.

[75] H. C. Box and H. G. Freund. Paramagnetic resonance shows radiation effects. *Nucleonics (U.S.) Ceased publication*, Vol: 17, No. 1, January 1959.

[76] W. W. Bradshaw, D. G. Cadena, G. W. Crawford, and H. A. W. Spetzler. The use of alanine as a solid dosimeter. *Radiation Research*, 17:11, 1962.

[77] J Rotblat and J A Simmons. Dose-response relationship in the yield of radiation-induced free radicals in amino acids. *Physics in Medicine and Biology*, 7(4):489–497, 1963. doi: 10.1088/0031-9155/7/4/310.

[78] D.F. Regulla and U. Deffner. Dosimetry by ESR spectroscopy of alanine. *The International Journal of Applied Radiation and Isotopes*, 33(11):1101–1114, 1982. doi: 10.1016/0020-708X(82)90238-1.

[79] P. Sharpe, K. Rajendran, and J. Sephton. Progress towards an alanine/ESR therapy level reference dosimetry service at NPL. *Applied Radiation and Isotopes*, 47(11–12):1171–1175, 1996. doi: 10.1016/S0969-8043(96)00174-1.

[80] W. L. Mclaughlin and M. F. Desrosiers. Dosimetry systems for radiation processing. *Radiation Physics and Chemistry*, 46(4âĂŞ6, Part 2):1163–1174, 1995. doi: 10.1016/0969-806X(95)00349-3.

[81] Dosimetry systems. *Journal of the ICRU*, 8(2):29–70, 2008. doi: 10.1093/jicru/ndn027.

[82] P. Sharpe and J. Sephton. Alanine dosimetry at the NPL- The development of a mailed reference dosimetry service at radiotherapy dose levels. *IAEA-SM-356/R6 Proc. International symposium on techniques for high dose dosimetry in Industry, Agriculture and Medicine*, 8(2):1–7, 1998.

[83] V. Nagy. Accuracy considerations in EPR dosimetry. *Applied Radiation and Isotopes*, 52(5):1039–1050, 2000. doi: 10.1016/S0969-8043(00)00052-X.

[84] E. S. Bergstrand, K. R. Shortt, C. K. Ross, and E. O. Hole. An investigation of the photon energy dependence of the EPR alanine dosimetry system. *Physics in Medicine and Biology*, 48(12):1753, 2003. doi: 10.1088/0031-9155/48/12/306.

[85] G G Zeng, M R McEwen, D W Rogers, and N V Klassen. An experimental and monte carlo investigation of the energy dependence of alanine/EPR dosimetry: I. clinical x-ray beams. *Physics in Medicine and Biology*, 49(2):257–270, 2004. ISSN 0031-9155.

[86] E. Waldeland and E. Malinen. Review of the dose-to-water energy dependence of alanine and lithium formate EPR dosimeters and LiF TL-dosimeters âĂŞ comparison with monte carlo simulations. *Radiation Measurements*, 46(9):945–951, 2011. doi: 10.1016/j.radmeas.2011.03.014.

[87] P. Sharpe. Progress report on radiation dosimetry at NPL. *BIPM Report CCRI(I)-03-14*.

[88] M.F. Desrosiers and J.M. Puhl. Absorbed-dose/dose-rate dependence studies for the alanine-EPR dosimetry system. *Radiation Physics and Chemistry*, 78(7âĂŞ8):461–463, 2009. doi: 10.1016/j.radphyschem.2009.03.025.

[89] M. F. Desrosiers, S. L. Cooper, J. M. Puhl, and McBain. A study of the alanine dosimeter irradiation temperature coefficient in the -77°C to +50°C range. *Radiation Physics and Chemistry*, 71(1âĂŞ2). doi: 10.1016/j.radphyschem.2004.04.066.

[90] F. J. Ahlers and C. C. J. Schneider. Alanine ESR dosimetry: An assessment of peak-to-peak evaluation. *Radiation Protection Dosimetry*, 37(2):117–122, 1991. ISSN 0144-8420, 1742-3406.

[91] J. Millman and C. C. Halkias. *Electronic devices and circuits*. McGraw-Hill, 1967. ISBN 978-0070423800.

[92] M. Anton. Development of a secondary standard for the absorbed dose to water based on the alanine EPR dosimetry system. *Applied Radiation and Isotopes*, 62(5):779–795, 2005. doi: 10.1016/j.apradiso.2004.10.009.

[93] V. Y. Nagy and M. F. Desrosiers. Complex time dependence of the EPR signal of irradiated l-Îś-alanine. *Applied Radiation and Isotopes*, 47(8):789–793, 1996. doi: 10.1016/0969-8043(96)00053-X.

[94] L. B. Rockland. Saturated salt solutions for static control of relative humidity between 58 and 408c. *Analytical Chemistry*, 32(5):1375–1376, 1960.

[95] O. F Sleptchonok, V. Nagy, and M. F. Desrosiers. Advancements in accuracy of the alanine dosimetry system. part 1. the effects of environmental humidity. *Radiation Physics and Chemistry*, 57(2): 115–133, 2000. doi: 10.1016/S0969-806X(99)00338-2.

[96] J. A. Weil and J. R. Bolton. *Electron Paramagnetic Resonance: Elementary Theory and Practical Applications.* John Wiley & Sons, January 2007. ISBN 9780470084977.

[97] T. Garcia and J. M. Dolo. Study of the influence of grain size on the ESR angular response in alanine radicals. *Radiation Measurements*, 42(6âĂŞ7):1207–1212, July 2007. doi: 10.1016/j.radmeas.2007.05.039.

[98] V. Nagy, S. V. Sholom, V. V. Chumak, and M. F. Desrosiers. Uncertainties in alanine dosimetry in the therapeutic dose range. *Applied Radiation and Isotopes*, 56(6):917–929, June 2002. doi: 10.1016/S0969-8043(01)00271-8.

[99] J. M. Dolo and T. Garcia. Angular response of alanine samples: From powder to pellet. *Radiation Measurements*, 42(6âĂŞ7):1201–1206, July 2007. doi: 10.1016/j.radmeas.2007.05.020.

[100] V. Nagy, O. F. Sleptchonok, M. F. Desrosiers, R. T. Weber, and A. H. Heiss. Advancements in accuracy of the alanine EPR dosimetry system: Part III: usefulness of an adjacent reference sample. *Radiation Physics and Chemistry*, 59(4):429–441, 2000. doi: 10.1016/S0969-806X(00)00275-9.

[101] ISO/IEC guide 98-3:2008 uncertainty of measurement, part 3: Guide to the expression of uncertainty in measurement (GUM:1995). http://www.bipm.org/en/publications/guides/gum.html.

[102] NIST US Department of Commerce. NIST radionuclide half-life measurements (HTML). http://www.nist.gov/pml/data/halflife-html.cfm.

[103] D. York, N. M. Evensen, M. Martínez López, and J. De Basabe Delgado. Unified equations for the slope, intercept, and standard errors of the best straight line. *American Journal of Physics*, 72(3):367, 2004. doi: 10.1119/1.1632486.

[104] E. Waldeland, J. Helt-Hansen, and E. Malinen. Characterization of lithium formate EPR dosimeters for high dose applications âĂŞ comparison with alanine. *Radiation Measurements*, 46(2):213–218, February 2011. doi: 10.1016/j.radmeas.2010.11.015.

[105] A. V. D. Kogel and M. Joiner. *Basic Clinical Radiobiology*. Hodder Arnold, March 2009. ISBN 9780340929667.

[106] M. Dalaryd, G. Kragl, C. Ceberg, D.r Georg, B. McClean, S. af Wetterstedt, E. Wieslander, and T. Knöös. A monte carlo study of a flattening filter-free linear accelerator verified with measurements. *Physics in Medicine and Biology*, 55(23):7333, 2010. doi: 10.1088/0031-9155/55/23/010.

[107] J. Hrbacek, S. Lang, and S. Klöck. Commissioning of photon beams of a flattening filter-free linear accelerator and the accuracy of beam modeling using an anisotropic analytical algorithm. *International Journal of Radiation Oncology*Biology*Physics*, 80(4):1228–1237, 2011. doi: 10.1016/j.ijrobp.2010.09.050.

[108] G. Kragl, S. af Wetterstedt, B. Knäusl, M. Lind, P. McCavana, T. Knöös, B. McClean, and D. Georg. Dosimetric characteristics of 6

and 10 MV unflattened photon beams. *Radiotherapy and Oncology*, 93(1):141–146, 2009. doi: 10.1016/j.radonc.2009.06.008.

[109] F. Ponisch, U. Titt, O. N. Vassiliev, S. F. Kry, and R. Mohan. Properties of unflattened photon beams shaped by a multileaf collimator. *Medical Physics*, 33(6):1738–1746, 2006. doi: 10.1118/1.2201149.

[110] X. R. Zhu, Y. Kang, and M. T. Gillin. Measurements of in-air output ratios for a linear accelerator with and without the flattening filter. *Medical Physics*, 33(10):3723–3733, 2006. doi: 10.1118/1.2349695.

[111] G. Kragl, F. Baier, S. Lutz, D. Albrich, M. Dalaryd, B. Kroupa, T. Wiezorek, T. Knöös, and D. Georg. Flattening filter free beams in SBRT and IMRT: dosimetric assessment of peripheral doses. *Zeitschrift für Medizinische Physik*, 21(2):91–101, 2011. doi: 10.1016/j.zemedi.2010.07.003.

[112] M. T. Romero Expósito, F. Sánchez-Doblado, J.A. Terrón, C. Domingo, K. Amgarou, M.J. García-Fuste, X.L. González Soto, J.I. Lagares, and F. Gómez. Comparison of photo-neutron fluence for different energies, manufacturers and models of linacs. *Radiotherapy and Oncology*, 99, Supplement 1:S168, 2011. doi: 10.1016/S0167-8140(11)70544-8.

[113] A. Mesbahi. A monte carlo study on neutron and electron contamination of an unflattened 18-MV photon beam. *Applied Radiation and Isotopes*, 67(1):55–60, 2009. doi: 10.1016/j.apradiso.2008.07.013.

[114] D. S. Followill, F. Nüsslin, and C. G. Orton. IMRT should not be administered at photon energies greater than 10 MV. *Medical Physics*, 34(6):1877–1879, 2007. doi: 10.1118/1.2734751.

[115] G. Xiong and D. W. O. Rogers. Relationship between %dd$(10)_x$ and stopping-power ratios for flattening filter free accelerators: A

monte carlo study. *Medical Physics*, 35(5):2104–2109, 2008. doi: 10.1118/1.2905028.

[116] E. Pantelis, C. Antypas, L. Petrokokkinos, P. Karaiskos, P. Papagiannis, M. Kozicki, E. Georgiou, L. Sakelliou, and I. Seimenis. Dosimetric characterization of CyberKnife radiosurgical photon beams using polymer gels. *Medical Physics*, 35(6):2312–2320, 2008. doi: 10.1118/1.2919099.

[117] T. Kawachi, H. Saitoh, M. Inoue, T. Katayose, A. Myojoyama, and K. Hatano. Reference dosimetry condition and beam quality correction factor for CyberKnife beam. *Medical Physics*, 35(10):4591–4598, 2008. doi: 10.1118/1.2978228.

[118] K. M. Langen, N. Papanikolaou, J. Balog, R. Crilly, D. Followill, S. M. Goddu, W. III Grant, G. Olivera, C. R. Ramsey, and C. Shi. QA for helical tomotherapy: Report of the AAPM task group 148. *Medical Physics*, 37(9):4817–4853, 2010. doi: 10.1118/1.3462971.

[119] R. Rodríguez-Romero and P. Sánchez-Rubio. Experimental estimation of beam quality conversion factor under non standard condition for helical tomotherapy (physics and technology: Applied dosimetry quality assurance). *Radiotherapy and Oncology*, 96, Supplement 1: S444–S467, 2010. doi: 10.1016/S0167-8140(10)80072-6.

[120] H. Palmans. Determination of the beam quality index of high-energy photon beams under nonstandard reference conditions. *Medical physics*, 39(9):5513–5519, 2012. doi: 10.1118/1.4745565.

[121] P. Sharpe and J. Sephton. An automated system for the measurement of alanine/EPR dosimeters. *Applied Radiation and Isotopes*, 52(5): 1185–1188, 2000. doi: 10.1016/S0969-8043(00)00068-3.

[122] S. Duane, D. Nicholas, H. Palmans, B. Schaeken, J. Sephton, P. Sharpe, R. Thomas, M. Tomsej, K. Tournel, D. Verellen, and

S. Vynckier. SU-FF-T-195: dosimetry audit for tomotherapy using Alanine/EPR. *Medical Physics*, 33(6):2093–2094, 2006. doi: 10.1118/1.2241118.

[123] C. J. Bailat, T. Buchillier, M. Pachoud, R. Moeckli, and F. O. Bochud. An absolute dose determination of helical tomotherapy accelerator, TomoTherapy high-art II. *Medical Physics*, 36(9):3891–3896, 2009. doi: 10.1118/1.3176951.

[124] International Electrotechnical Commission. *Radiotherapy Equipment: Coordinates, Movements and Scales*. IEC, 2008.

[125] S. D. Thomas, M. Mackenzie, D. W. O. Rogers, and B. G. Fallone. A monte carlo derived TG-51 equivalent calibration for helical tomotherapy. *Medical Physics*, 32(5):1346–1353, 2005. doi: 10.1118/1.1897084.

[126] R. Jeraj, T. R. Mackie, J. Balog, and G. Olivera. Dose calibration of nonconventional treatment systems applied to helical tomotherapy. *Medical Physics*, 32(2):570–577, 2005. doi: 10.1118/1.1855015.

[127] C. J. Bailat, T. Buchillier, M. Pachoud, R. Moeckli, and F. O. Bochud. An absolute dose determination of helical tomotherapy accelerator, TomoTherapy high-art II. *Medical Physics*, 36(9):3891–3896, 2009. doi: 10.1118/1.3176951.

[128] O. A. Sauer. Determination of the quality index (q) for photon beams at arbitrary field sizes. *Medical Physics*, 36(9):4168–4172, 2009. doi: 10.1118/1.3197062.

[129] BJR, Central axis depth dose data for use in radiotherapy. *The British journal of radiology*, Suppl. 25:84–151, 1996.

[130] Depth dose tables for use in radiotherapy. a survey, prepared by the scientific sub-committee of the hospital physicist's association, of central axis depth-dose data measured in water or equivalent media. *The British journal of radiology*, 10 Suppl:1–96, 1961. ISSN 0007-1285.

[131] H. Palmans, R. A. S. Thomas, S. Duane, E. Sterpin, and S. Vynckier. Ion recombination for ionization chamber dosimetry in a helical tomotherapy unit. *Medical Physics*, 37(6):2876–2889, 2010. doi: 10.1118/1.3427411.

[132] A. Gago-Arias, R. Rodríguez-Romero, P. Sánchez-Rubio, D. M. González-Castaño, F. Gómez, L. Nuñez, H. Palmans, P. Sharpe, and J. Pardo-Montero. Correction factors for A1SL ionization chamber dosimetry in TomoTherapy: machine-specific, plan-class, and clinical fields. *Medical Physics*, 39(4):1964–1970, 2012. doi: 10.1118/1.3692181.

[133] E. Sterpin, T. Mackie, W. Lu, G. Olivera, and S. Vynckier. SU-FF-T-407: full monte carlo computation of k correction factors calculated in tomotherapy static and helical deliveries for future ion chamber reference dosimetry protocols of non standard beams. volume 36, pages 2615–2616. AAPM, 2009. doi: 10.1118/1.3181889.

[134] B. De Ost, B. Schaeken, S. Vynckier, E. Sterpin, and D. Van den Weyngaert. Reference dosimetry for helical tomotherapy: Practical implementation and a multicenter validation. *Medical Physics*, 38 (11):6020–6026, 2011. doi: 10.1118/1.3651496.

[135] M. Zeverino, S. Agostinelli, F. Pupillo, and G. Taccini. Determination of the correction factors for different ionization chambers used for the calibration of the helical tomotherapy static beam. *Radiotherapy and Oncology*, 100(3):424–428, 2011. doi: 10.1016/j.radonc.2011.08.044.

[136] E. Chung, E. Soisson, H. Bouchard, and J. Seuntjens. Advanced dosimetry techniques for accurate verification of nonstandard beams.

Proceedings IAEA International Symposium on Standards, Applications and Quality Assurance in Medical Radiation Dosimetry, 2010, Vienna, Austria.

[137] E. Chung, E. Soisson, and J. Seuntjens. Dose homogeneity specification for reference dosimetry of nonstandard fields. *Medical Physics*, 39(1):407–414, 2012. doi: 10.1118/1.3669487.

[138] S. Duane, D. Nicholas, H. Palmans, B. Schaeken, J. Sephton, P. Sharpe, R. Thomas, M. Tomsej, K. Tournel, D. Verellen, and S. Vynckier. SU-FF-T-195: dosimetry audit for tomotherapy using Alanine/EPR. *Medical Physics*, 33(6):2093–2094, 2006. doi: 10.1118/1.2241118.

[139] H. Bouchard, J. Seuntjens, J.-F. Carrier, and I. Kawrakow. Ionization chamber gradient effects in nonstandard beam configurations. *Medical Physics*, 36(10):4654, 2009. doi: 10.1118/1.3213518.

[140] I. J. Das, C. W. Cheng, R. J. Watts, A. Ahnesjo, J. Gibbons, X. A. Li, J. Lowenstein, R. K. Mitra, W. E. Simon, and T. C. Zhu. Accelerator beam data commissioning equipment and procedures: Report of the TG-106 of the therapy physics committee of the AAPM. *Medical Physics*, 35(9):4186–4215, 2008. doi: 10.1118/1.2969070.

[141] S. Dieterich, C. Cavedon, C. F. Chuang, A. B. Cohen, J. A. Garrett, C. L. Lee, J. R. Lowenstein, M. F d'Souza, Jr Taylor, D. D, X. Wu, and C. Yu. Report of AAPM TG 135: quality assurance for robotic radiosurgery. *Medical physics*, 38(6):2914–2936, 2011. ISSN 0094-2405.

[142] D. McDonald, C. Yount, N. Koch, M. Ashenafi, J. Peng, and K. Vanek. Calibration of the gamma knife perfexion using TG-21 and the solid water leksell dosimetry phantom. *Medical Physics*, 38 (3):1685–1693, 2011. doi: 10.1118/1.3557884.

[143] National Electrical Manufacturers Association. Digital imaging and communications in medicine (DICOM) part 3: Information object definitions. *NEMA PS 3.3-2003*, (Rosslyn, VA, NEMA, 2004).

[144] E. Pantelis, A. Moutsatsos, K. Zourari, W. Kilby, C. Antypas, P. Papagiannis, P. Karaiskos, E. Georgiou, and L. Sakelliou. On the implementation of a recently proposed dosimetric formalism to a robotic radiosurgery system. *Medical Physics*, 37(5):2369–2379, 2010. doi: 10.1118/1.3404289.

[145] P. Francescon, W. Kilby, N. Satariano, and S. Cora. Monte carlo simulated correction factors for machine specific reference field dose calibration and output factor measurement using fixed and iris collimators on the CyberKnife system. *Physics in Medicine and Biology*, 57(12):3741, 2012. doi: 10.1088/0031-9155/57/12/3741.

[146] S. Agostinelli, S. Garelli, M. Piergentili, and F. Foppiano. Response to high-energy photons of PTW31014 PinPoint ion chamber with a central aluminum electrode. *Medical Physics*, 35(7):3293–3301, 2008. doi: 10.1118/1.2940190.

[147] F. DeBlois, C. Zankowski, and E. B. Podgorsak. Saturation current and collection efficiency for ionization chambers in pulsed beams. *Medical Physics*, 27(5):1146–1155, 2000. doi: 10.1118/1.598992.

[148] B. Walters, I. Kawrakow, and D. W. O. Rogers. DOSXYZnrc users manual. *NRCC Report No. PIRS-794 revB (National Research Council of Canada, Ottawa, Canada, 2011).*

[149] D. Sheikh-Bagheri and D. W. O. Rogers. Sensitivity of megavoltage photon beam monte carlo simulations to electron beam and other parameters. *Medical Physics*, 29(3):379–390, 2002. doi: 10.1118/1.1446109.

[150] J. Pena, D. M. Gonzalez-Castano, F. Gomez, F. Sanchez-Doblado, and G. H. Hartmann. Automatic determination of primary electron beam parameters in monte carlo simulation. *Medical Physics*, 34(3): 1076–1084, 2007. doi: 10.1118/1.2514155.

[151] C.-M. Ma, J. S. Li, J. Deng, and J. Fan. Implementation of monte carlo dose calculation for CyberKnife treatment planning. *Journal of Physics: Conference Series*, 102(1):012016, 2008. doi: 10.1088/1742-6596/102/1/012016.

[152] B. R. Muir, M. R. McEwen, and D. W. O. Rogers. Measured and monte carlo calculated k[sub q] factors: Accuracy and comparison. *Medical Physics*, 38(8):4600–4609, 2011. doi: 10.1118/1.3600697.

[153] A. Gago-Arias, E. Antolín, F. Fayos-Ferrer, R. Simón, D. M. González-Castaño, H. Palmans, P. Sharpe, F. Gómez, and J. Pardo-Montero. Correction factors for ionization chamber dosimetry in CyberKnife: machine-specific, plan-class, and clinical fields. *Medical Physics*, 40(1):011721, 2013. doi: 10.1118/1.4773047.